Feasibility Study of a Fission-Suppressed Tandem-Mirror Hybrid Reactor

J. D. Lee, R. W. Moir, W. L. Barr, R. S. Devoto, G. W. Hamilton,

W. S. Neef, D. H. Berwald, J. A. Maniscalco, W. D. Bjorndahl,

R. B. Campbell, J. K. Garner, J. Ogren, R. H. Whitley, N. Ghoniem,

M. Youseff, K. R. Schultz, E. T. Cheng, R. L. Creedon, I. Maya,

P. W. Trester, C. P. C. Wong, R. P. Rose, D. L. Chapin, J. W. H. Chi,

J. S. Karbowski, and W. R. Grimes

April 1982

DISCLAIMER

This document was prepared as an account of work sponsored by an agency of the United States Government. Neither the United States Government nor the University of California nor any of their employees, makes any warranty, express or implied, or assumes any legal liability or responsibility for the accuracy, completeness, or usefulness of any information, apparatus, product, or process disclosed, or represents that its use would not infringe privately owned rights. Reference herein to any specific commercial products, process, or service by trade name, trademark, manufacturer, or otherwise, does not necessarily constitute or imply its endorsement, recommendation, or favoring by the United States Government or the University of California. The views and opinions of authors expressed herein do not necessarily state or reflect those of the United States Government thereof, and shall not be used for advertising or product endorsement purposes.

Page Range	Domestic Price	Page Range	Domestic Price
001-025	$ 5.00	326-350	$ 18.00
026-050	6.00	351-375	19.00
051-075	7.00	376-400	20.00
076-100	8.00	401-425	21.00
101-125	9.00	426-450	22.00
126-150	10.00	451-475	23.00
151-175	11.00	476-500	24.00
176-200	12.00	501-525	25.00
201-225	13.00	526-550	26.00
226-250	14.00	551-525	27.00
251-275	15.00	526-550	28.00
276-300	16.00	601-up [1]	
301-325	17.00		

[1] Add 2.00 for each additional 25 page increment from 601 pages up.

FEASIBILITY STUDY OF A FISSION-SUPPRESSED TANDEM MIRROR HYBRID REACTOR

J. D. Lee, R. W. Moir, W. L. Barr,
R. S. Devoto, G. W. Hamilton, W. S. Neef
Lawrence Livermore National Laboratory,
Livermore, CA 94550

D. H. Berwald, J. A. Maniscalco, W. D. Bjorndahl,
R. B. Campbell, J. K. Garner, J. Ogren, R. H. Whitley,
N. Ghoniem and M. Youseff (Consultants),
TRW, Inc., Redondo Beach, CA 90278

K. R. Schultz, E. T. Cheng, R. L. Creedon, I. Maya,
P. W. Trester, C. P. C. Wong
General Atomic Co., San Diego, CA 92138

R. P. Rose, D. L. Chapin, J. W. H. Chi, J. S. Karbowski,
Westinghouse Electric Corp., Pittsburgh, PA 15236

W. R. Grimes
Oak Ridge National Laboratory, Oak Ridge, TN 37830

CONTENTS

ILLUSTRATIONS

TABLES

FEASIBILITY STUDY OF A FISSION-SUPPRESSED
TANDEM-MIRROR HYBRID REACTOR

ABSTRACT

Results of a conceptual design study of a U-233 producing fusion breeder consisting of a tandem mirror fusion device and two types of fission-suppressed blankets are presented. The majority of the study was devoted to the conceptual design and evaluation of the two blankets. However, studies in the areas of fusion engineering, reactor safety, fuel reprocessing, other fuel cycle issues, economics, and deployment were also performed.

The first blanket studied uses an inner zone of depleted lithium for tritium breeding and cooling, with an outer zone containing molten salt for fissile breeding and cooling. This concept features on-line lithium and molten-salt fuel processing. Neutrons in excess of that needed for tritium breeding are available for fissile breeding by virtue of the ^{7}Li(n,n't) reaction. The second blanket studied uses beryllium for neutron multiplication, a LiPb suspension of ThO_2 for tritium and U-233 breeding, helium for cooling, and features aqueous (thorex) fuel reprocessing. The beryllium resource, while possibly too limited for extensive pure fusion application, will be adequate (with carefully planned industrial expansion) for the fusion breeder application because of the large support ratio; hence few fusion breeders required. Fabrication and radiation damage of beryllium remain issues to be resolved by further study and experimentation.

Molten salt reprocessing economics were compared to aqueous reprocessing (thorex). The predicted cost (levelized) for molten-salt reprocessing is $1.9/g fissile, whereas the aqueous reprocessing cost estimate is $23/g fissile for thorium metal and 28 to 42 $/g fissile for ThO_2. Molten salt handling and processing appear to be attractive but require more development.

The fusion driver for these fusion breeders is a 3000-MW axicell tandem mirror operating in the thermal barrier mode with 20-tesla barrier coils. The

Li- and Be-based blankets are predicted to produce 4.5 and 6.6 tonnes/y of U-233, respectively, in addition to the tritium required to fuel the DT fusion reaction. When used as makeup to conventional light water reactors (LWRs),15 GW and 22 GW of electric power can be supported. Both fission-suppressed blankets are predicted to be significantly safer than fission systems by virtue of much lower radioisotope inventories and afterheat. Initial studies indicate that both blankets have very low probability of radioactivity release.

The electricity generation cost from fusion-fission systems consisting of these fusion breeders and conventional LWRs being supplied make fuel is predicted to be 13% and 8.9% above that of an LWR fueled with mined uranium. A 100$/kg U_3O_8 fuel cost, 3% real U_3O_8 cost escalation, and full fissle recycle in the LWR, is assumed. The electrical output from the breeders accounts for only 8% and 5% of total system output. The cost of bred fissile material (U-233), expressed as an equivalent U_3O_8 cost, was $91/lb for the Li case with molten-salt reprocessing and $76/lb for the beryllium case with aqueous reprocessing.

In 1982 we plan to pursue a relatively low technology hybrid which uses beryllium and thorium (or uranium) pebbles cooled by liquid lithium with equivalent U_3O_8 costs expected to be $75/lb or less. At a lower level we plan to pursue a higher technology hybrid which uses beryllium and molten salt with an equivalent U_3O_8 cost of $60/lb. All costs are in 1980 dollars. These results are based on the hybrid costing approximately 3.5 times a light water reactor for the same nuclear power. Advances which lower the cost of the fusion reactor will lower the cost of fissile material produced.

High support ratio results in attractive deployment scenarios. Only a relatively small number of fusion breeders are needed to support a large-scale fission economy. In a specific fusion breeder/LWR deployment example, only 81 fusion breeders would be required to support the LWR nuclear capacity required to meet 50% of U.S. electrical demand (1600-GWe nuclear) in the year 2050. If LWRs and LMFBRs are included in the fission reactor mix, only 40 fusion breeders would be required.

EXECUTIVE SUMMARY

ii-A   INTRODUCTION

This executive summary section summarizes our FY81 (October 1980 through September 1981) fusion-fission study of tandem mirror fusion reactors designed to produce fissile fuel for light-water reactors (LWRs) and for more advanced fission reactors. If the U.S. is to rely on fission power for a significant fraction of its electrical power (25 to 50%) in the year 2000 to 2050 time frame, a new and reliable source of fissile fuel may be needed. Fusion breeder reactors offer a potentially economical, timely, and virtually inexhaustible source of fissile fuel for fission reactors.

The goal of the U.S. fusion program is to develop fusion technology so that it is available in about 20 years. While fusion may not be sufficiently advanced at that time to produce electrical power at an acceptable cost, fusion will likely be sufficiently developed to work well as a neutron source for breeding fissile fuel: ^{233}U from ^{232}Th or ^{239}Pu from ^{238}U. A fusion breeder could cost several times that of its fission counterparts--and still be economically attractive by producing fissile fuel for consumption in relatively inexpensive fission power reactors.

The prospect for developing a fusion reactor with adequate performance for a hybrid (fusion-fission) system is quite good. The cost and safety aspects of the bulk of the power system (i.e., the LWRs) are relatively well known and need little development other than closing the fuel cycle. Also, the introduction of new capacity is not inhibited by doubling time constraints, because the fusion breeder requires no initial fissile inventory.

Electrical power is the ultimate goal of the U.S. fusion development program, however a nearer term goal could be to develop the fusion breeder to the point where a relatively small number of them (one-tenth or less of the number of supported fission reactors) could be built should a severe uranium shortage develop. This strategy fits well into an evolutionary philosophy of fusion. The application of fusion would logically evolve from the fusion

breeder to pure deuterium-tritium (D-T) fusion, to the ultimate objective of advanced fuel (D-D) fusion as plasma confinement capability improves.

While this study is based on the tandem mirror as the fusion part of the fusion breeder, any successful fusion concept could be used. The tandem mirror does have desirable features, such as steady-state operation, simple cylindrical geometry, low first-wall surface heat load, and a significant development program underway.

The principal emphasis this year was on the fission suppressed class of fissile-producing blankets. The objective was to develop one or two-blanket design concepts that performed well, but did not have the materials questions encountered with beryllium/molten salt (Be/MS) design worked on in FY 1979. To this end, two-blanket designs were conceived and analyzed in some detail. The first (the Li/MS design) uses a lithium zone depleted in ^{6}Li to produce tritium plus excess neutrons, followed by a molten-salt zone for fissile breeding. Molten salt is attractive because of its potential for low fuel cycle costs. The second (the Be/LiPb + ThO_2 design) uses Be to multiply neutrons and LiPb + ThO_2 particles in which to produce T and U233. The LiPb also acts as a thermal coupler to helium coolant tubes. The net fissile plus fusile breeding ratios (atoms/14-MeV DT neutron) calculated for these two blankets are 1.49 and 1.73, respectively. Blanket energy multiplication, M [M = (Blanket energy/DT neutron) ÷ 14 MeV] is 1.5 and 1.8, respectively.

A second objective of this study was to conceptually design and analyze the performance of fusion-fission systems consisting of fission-suppressed blankets, driven by "mainline" tandem mirrors, providing fuel to conventional LWRs. The "mainline" tandem mirror employs thermal barriers and axisymmetric end-plug magnets followed by yin-yang magnets to produce a magnetic well for radial stability of the entire plasma column. This is "mainline" because it is the main route the mirror program is taking. The optimized plasma performance calculated for the reference case is a Q of 15 at a neutron first-wall loading of 2 MW_n/m^2 and a central-cell fusion power level of 3 GW.

Our estimate of the overall performance of these fusion-fission systems with the two different blankets is summarized in Table ii.A-1. Subsequent sections of this chapter summarize the major topics addressed in this study in the order they appear in the main body of this report.

It is important to emphasize that this report does not describe a final design. It is more of a progress report describing where we presently are in

our efforts to conceptually develop and assess the feasibility of a fusion breeder based on tandem-mirror fusion and fission-suppressed blankets. Because of this there are inconsistencies that will be address in future design iterations. For example, blanket design work was done assuming a first-wall radius of 2.0 m, while the tandem driver was found to optimize with a first-wall radius of about 1.5 m. The later value is used to estimate economic performance as listed in Table iiA-1. Figure iiA-1 shows one end of the tandem mirror driver configuration. The blanket modules are located between the central-cell plasma and the solenoidal coils.
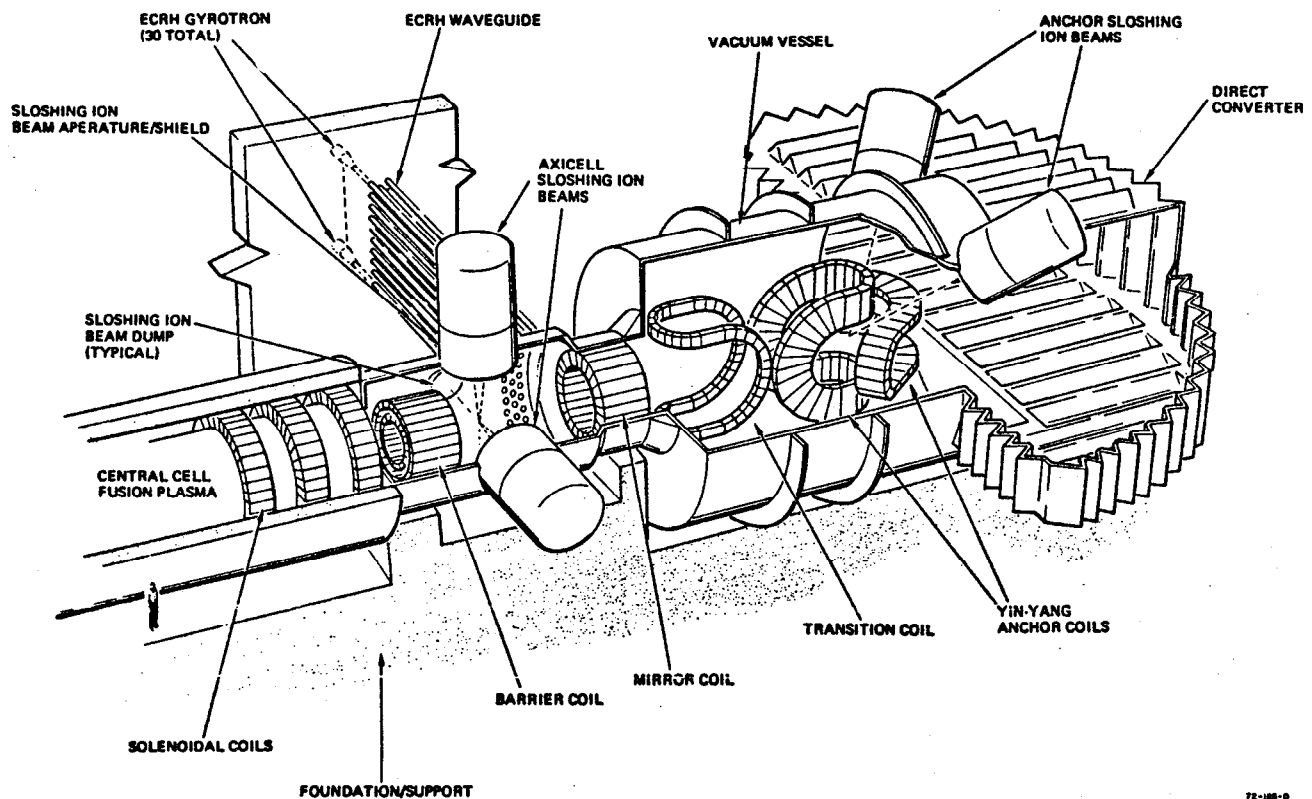
Fig. ii.A-1 Tandem mirror driver configuration (one end).

TABLE ii.A-1

SUMMARY OF REFERENCE FUSION-FISSION SYSTEM PERFORMANCE

FUSION BREEDER PARAMETERS

Fusion Driver

Fusion power (MW)	3000	
Wall loading (MW/m^2)	2	
Wall radius (m)	1.5	
Central-cell length (m)	129	
Plasma Q	15	

Blanket	Li/MS	Be/PbLi + ThO$_2$
Fissile breeding ratio (net), F	0.49	0.73
Energy multiplication, M	1.5	1.8
Total Nuclear Power (MW)	4,300	5,000
Net Electric Power (MW)	1,300	1,100
Fissile Production (kg/y) (@ 70% CF)	4,500	6,600
FISSION REACTOR (LWR'S) POWER SUPPORTED (MWe)	15,000	22,000

FUSION-FISSION SYSTEM ECONOMICS

	Li/MS	Be/PbLi + ThO$_2$
Breeder Capital Cost (PER KW$_{nuclear}$ relative to LWR)	3.7	3.0
Electricity Cost (% above current technology LWR electricity cost)	13.2	8.9
Equivalent U$_3$O$_8$ Cost (1980 dollars/kg)	201	168

Current Technology LWR on the denatured uranium-thorium fuel cycle, levelized electricity cost for conventional uranium fueling = 49 mil/KW$_e$H (at 100 \$/Kg U$_3$O$_8$ with full reprocessing and 3%/yr real U$_3$O$_8$ cost escalation).

LWR DATA: Capital Cost = 378 \$/KW$_{nuclear}$, Net Electrical Efficiency = 33%, Fissile Consumption Rate = 0.141 g/KW$_{nuclear}$-yr.

The plasma physics baseline case used in this study is summerized in Table ii.B-1 and shown pictorially in Fig. ii.B.1. The design features the use of an "axicell" end plug which uses thermal barriers to improve the performance over that of tandem mirror models for previous TMHRs. The plasma Q of the 1981 TMHR is about 15, compared to about 2 for the 1979 TMHR. This higher Q is maybe necessary for the production of competitively priced fuel because of higher estimates of supplementary heating costs obtained recently, particularly ECRH. The required plasma performance of the TMHR in a breeder/LWR burner system producing economic electricity is still considerably less than that required for fusion to have a stand-alone electricity generating capability. With the same fusion performance the cost of electricity is more than a factor of two less. This has been shown quantitatively in Chapter IX.

Thermal barriers were invented to allow the electrons in the end plug to be insulated from those in the central cell. The reason for this is to produce a high electron temperature in the plug (central-cell ion confining potential scales with T_e) by only heating a comparatively small volume. This results in an injected power savings and, therefore, an increase in plasma power out per unit of power in.

The sensitivity of plasma physics performance to changes in magnetic field strengths, plasma beta limits, neutral-beam injection energies, and other physics related variables is also assessed. The performance is altered the most by changing the magnetic field strength in the barrier coil, plasma Q(power out divided by power in) can change by 60% when this field is changed by 30%.

Issues related to the operation of the tandem mirror, including startup and shutdown of the plasma, production of a protective "halo" plasma, controlling the influx of high-Z impurities, and removing alpha particle "ash" produced by the D-T fusions are also examined. The halo plasma is presumed to be fed externally with D_2 gas, and heated by alpha particles produced at the edge of the fusion grade plasma. This halo plasma shields the hot plasma from gas and sputtered atoms which come from the walls. The halo also flushes away alpha particles which have diffused radially by some means.

TABLE ii.B-1. Physics Parameters for the Baseline Axicell Case

Parameter	Value
Central Cell	
Density, n_c (cm^{-3})	1.6×10^{14}
Ion Temperature, T_c (keV)	40
Electron Temperature, T_{ec} (keV)	32
Plasma Radius, r_{cc} (cm)	104
Vacuum Magnetic Field, $B_{c,vac}$ (T)	3
Beta, β_c	0.7
Floating Potential, ϕ_e (keV)	234
Cold Fueling Current, I_c (kamps)	1.6
Ion Confinement Parameter, $(n\tau)_i$ (s cm^{-3})	1.3×10^{15}
Electron Confinement Parameter, $(n\tau)_i$ (s cm^{-3})	1×10^{15}
First Wall Radius (cm)	150
Central Cell Length (m)	129
Axicell/Barrier	
Maximum Hybrid Coil Field B_{max} (T)	20
Sloshing Ion Injection Energy, $E_{inj,a}$ (keV)	250
Vacuum Magnetic Field at Barrier Minimum (point b) (T)	1.69
Total Barrier Beta ($\beta + \beta$)	1.2
Perpendicular Barrier Beta, β	0.56
Passing Ion Density at Point "b", $n_{pass,b}$ (cm^{-3})	2.84×10^{12}
Hot Electron Energy at Point "b", E_{eh} (keV)	361
Warm Electron Energy at Point "a", T_{ew} (keV)	93
Barrier Length, L_B (m)	12
Cold Electron Density Fraction, F_{ec} (%)	2.54
Sloshing Beam Trapping Fraction (%)	23
Pump Beam Trapping Fraction (%)	70
Beta at Point "a", β_a	0.35
Barrier Potential Dip, ϕ_b (keV)	192
Ion Confining Potential, ϕ_c (keV)	137

Fig. ii.B-1. Ideal end plug with a thermal barrier.

Also discussed are some possible scenarios for a plasma disruption to occur and the different forms of energy produced during normal operation in the plasma which will appear on the first wall as a heat source. A plasma disruption could dump up to 5 GJ of plasma energy onto material walls. The plasma could dump axially if for some reason the input power to one of the plugs was interrupted for a sufficiently long time. This time would have to be long enough so that the potential peak would collapse. The problem here is thought to be not one of increased heat load at the ends, but one of induced forces in structures because of the changing plasma diamagnetism. Another scenario supposes that a flute mode could be spontaneously excited and driven by bad curvature at the ends of the central cell. This could move the plasma radially to the wall. The worse case for this mode is that wall protectors would be located every 8 meters. In a steady-state mode, three sources of energy comprise wall bombardment. Bremsstrahlung dominates, cyclotron and line radiation are small, radially diffusing alpha particles are unimportant; and charge-exchange neutrals and radially diffusing plasma are negligible. Bremsstrahlung, the largest contributor, producing a 10 kW/m^2 heat load.

The fusion power produced in the end cell regions where no tritium breeding blanket is present represents a loss of tritium which must be recovered at the expense of fissile material breeding in the blanket. This fusion power has been evaluated for the baseline case and is found to be about 120 MW, which decreases the total breeding T+F in the rest of the blanket by about 3%. The same analysis was performed on an MFTF-B "A-cell" end plug and 400 MW of fusion power was produced, reducing T+F by 10%, a substantially greater penalty.

The fact that there are a finite number of central-cell coils produces field ripple which can reduce the amount of plasma pressure which can be stably sustained. A set of interchange stability cases were considered, with varying ripple, and it was found that if the $\Delta B/B$ did not exceed 5%, the pressure limit could be recovered with only a modest increase in the pressure in the MHD anchor.

Also addressed are developments and plans in the areas of tandem mirror experiments and theoretical support. The two major experiments which are intended to test for microstability of improved plug distribution functions, as well as demonstrate thermal barriers are TMX-U and MFTF-B. The TMX-U experiment is intended to come online in early 1982, and MFTF-B is planned to

being operation at the end of 1984. The two major areas of theoretical
support are in the areas of microstability of both hot ions and electrons in
the end plug as well as providing a realistic estimate for the maximum plasma
pressure attainable in the central cell for a given magnetic field.

This topic deals with aspects related to the fusion related technologies needed for the realization of the fusion driver of the TMHR. The major technologies necessary are: high field magnets, neutral-beam injectors, sources of microwave energy, direct converters, and vacuum pumping systems. It is important to know what performance can be expected from a given technology at the time at which the hybrid could be introduced competitively (about the year 2015). The only way to know this is to study the individual technologies, and the current plans in place to develop the technologies.

There are several requirements for high field magnets in the TMHR. (see Fig. iiB.1) Super conducting magnets made of NbTi, which produce three tesla on axis, are necessary for the central-cell magnets. Magnets also made of NbTi in the yin-yang configuration are necessary for the MHD anchors at the end of the machine. A solenoid made of Nb_3Sn is necessary to produce the 9 T on axis field, which forms the outboard mirror of the axicell. The coil with the highest magnetic field is the "barrier" coil which forms the inboard mirror of the axicell. It needs to produce 20 T on axis. This is accomplished by constructing the coil using layers of superconductor and water-cooled normal copper, NbTi taking the lowest fields on the outside, Nb_3Sn taking the "moderate" fields (12 T) and the copper exposed to the highest fields (21 T). There is no formal plan in place to develop these layered hybrid coils, but there is work by several groups intended to define a conceptual design of a workable coil.

The neutral-beam requirement for the hybrid will call for beams with various energies and current requirements. The "pump" beams used to remove trapped ions in the thermal barriers represent the most challenging beam requirement, because they require both high current and from low to high energy (30-200 keV). Divided among three beams, the low, medium, and high energy pump beams, a total of 170 MW of beam power is needed. The "sloshing" beams in the axicell help to produce velocity space distributions having favorable microstability properties. They have energies around 250 keV, and will probably need to be produced by negative ions. If energy conservation of an unneutralized positive ion beam is possible the overall efficiency is high enough (35%) at 200 keV, that a positive ion system could be used on a TMHR

without serious economic penalty. In any event, a total of 74 MW will have to be produced by these sloshing-ion beamlines. There are also sloshing beams in the yin-yang "anchor" which can be produced with positive ion neutral beams (~150 keV), requiring moderate current.

The design of the TMHR is facilitated by having sources of microwave radiation in 1 MW sizes, and requires frequencies in the range from between 30 GHz and 100 GHz. The current development plan (section XI.B.2) calls for these sources to be available by 1990, in plenty of time for the hybrid application. Two frequencies are necessary for heating the end cell region, because we must heat at two locations where the magnetic field strengths are different. The power requirement at both frequencies is about 30 MW. Because the plasma alters the magnetic field through its diamagnetism, the resonant heating zone will move at a fixed frequency. This suggests that the source should be tunable. Gyrotrons, the presently envisioned microwave source, are not tunable. A promising alternate source of microwave energy not highly developed is the free electron laser (FEL). Along with the feature of tunability, FELs have the capability of operating efficiently at very high frequencies, (>300 GHz). This may be advantageous if studies in electron heating physics show that heating at harmonics of the electron gyrofrequency has desireable aspects.

The technology of direct conversion of both neutral beams and charged particle beams is well in hand. This is due primarily to the pioneering work at LLNL in the late 1970s, culminating in 1979 when a plasma direct converter was tested at high energy flux ($70W/cm^2$) for a long period of time (~70 hours) with no apparent material degradation. A 100 keV ion beam with a power of 170 KW was recovered at 70% efficiency. A plasma direct converter on TMX was successfully tested in 1980. Future experimental efforts will be directed at greater power handling capability and testing on tandem mirror experiments. The TMHR baseline reactor case will need to convert 800 MW of charged particle power flowing out the ends.

The area of vacuum pumping is particularly challenging for a device which must operate in the steady state. In this case, a certain fraction of the cryopanels must be isolated from the vacuum and warmed while the rest continue the pumping job. There is a rapid cycling pumping technique being developed at LLNL which is intended to accomplish this task, and will be tested in 1982. The pumping of helium ash is also difficult to do on standard cryo-panels, because the helium will not stick. A way that is being developed to

pump helium is to trap it between layers of frozen argon gas. This method is currently undergoing development at LLNL.

The performance expected to be achieved for the major fusion components is largely consistent with the requirements necessary for the fusion breeder introduction in 2015. The only exception seems to be the lack of a program to develop 20-T layered S.C./Cu coils. In the next few years, a program to study these coils should be in place. Since these coils are small, successful tests can be expected within a few years after starting their development.

The reference lithium/molten salt (Li/MS) blanket design, shown in Fig. ii.D-1, is a two-zone design which employs ^{6}Li depleted liquid lithium in the inner zone to cool the first wall and inner region structure and provide tritium breeding and excess neutrons for fissile breeding [via ^{7}Li(n,n'α) reactions]. The outer region contains a thorium-breeding molten-salt coolant that breeds ^{233}U and is slowly circulated for on-line fuel processing. The design employs a frozen layer of the salt to protect the stainless-steel blanket structure from the corrosive action of the molten salt.

In this blanket design, fast and thermal fissioning are suppressed by three methods:

o A 50-cm front region of lithium moderates the fission neutron flux to lower energies

o Fissile ^{233}U is discharged from the blanket at very low concentration (0.11% in thorium)

o The fertile thorium in the back of the blanket is diluted in the sense that only one atom of 22 in the molten salt is thorium. These result in a blanket fission rate which is reduced 1 to 2 orders of magnitude relative to fast-fission blankets considered in previous studies.

Both liquid helium and molten salts are uniquely qualified for the suppressed fission environment. Concerning ^{6}Li-depleted lithium, it is the only single material that provides substantial neutron enhancement, in situ tritium breeding, and has excellent coolant properties. Unfortunately, liquid lithium has two well-known drawbacks: it is chemically reactive with water and other materials and, because it is a liquid metal, MHD pressure drop effects must be considered. Concerning the molten salt, the principal advantage is a potential for low-cost reprocessing at low ^{233}U concentration in thorium--a necessary ingredient for good economic performance. Its principal drawbacks are its corrosive nature at high temperature and the lack of commercially demonstrated molten-salt reprocessing and primary loop technologies.

The present design concept introduces several novel design features that can mitigate concerns due to both MHD effects on liquid lithium and materials compatibility issues for the molten salt.

First, as shown in Fig. ii.D-1, the two-zone design features a cylindrical inner first wall and a concentric intermediate wall (both of which

FIGURE ii.D-1. Component arrangement and dimensions for the reference lithium/molten salt TMHR blanket module assembly.
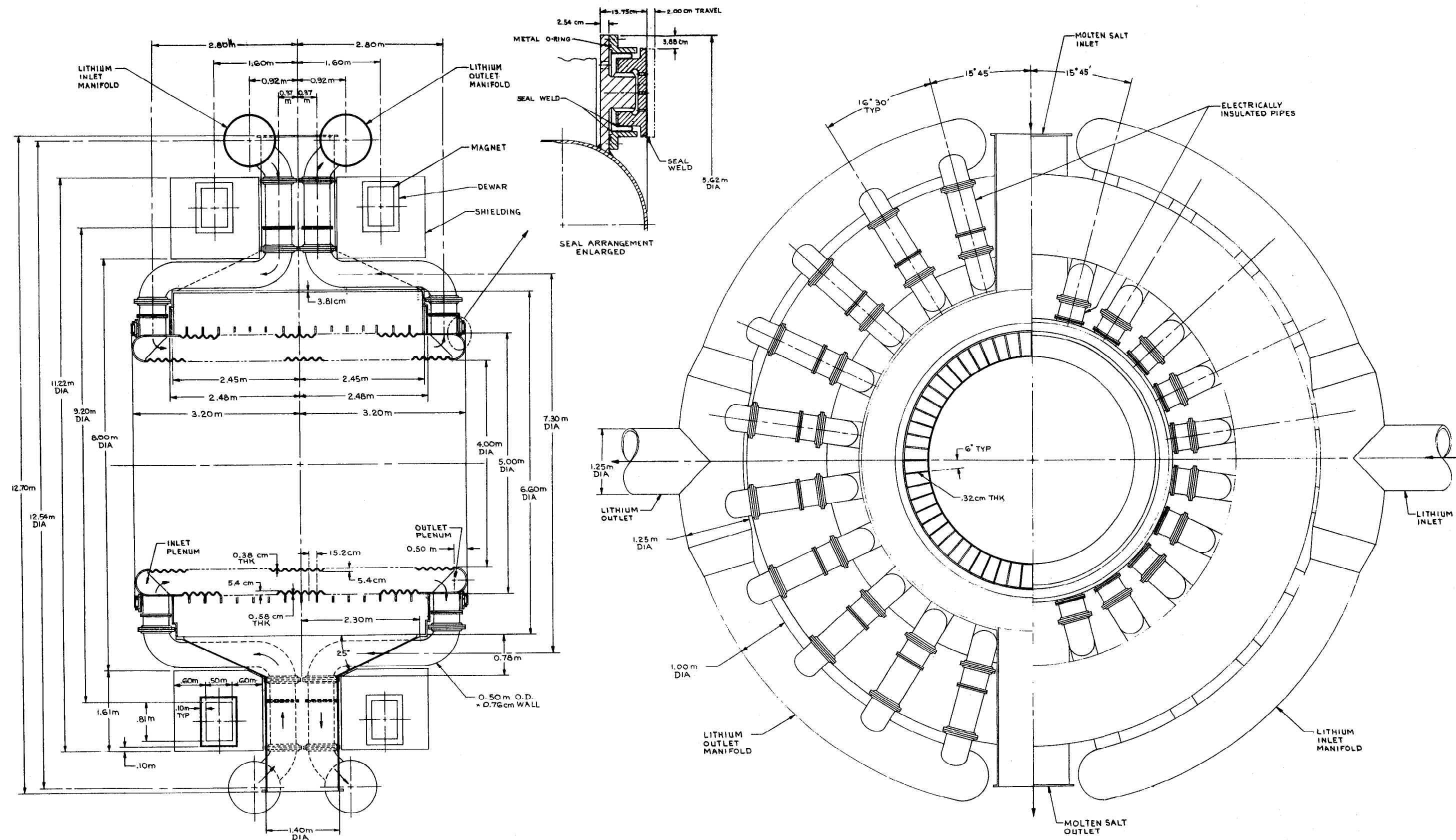
are corrugated to minimize the structure thickness and accommodate swelling).
The intermediate wall separates the inner zone and the outer molten-salt
zone. Radial ribs, equally spaced around the perimeter of the inner blanket
zone are connected to the two concentric shells to provide structural support
so that the shells can withstand the pressure loads from the coolant and
molten salt. The outer molten-salt zone extends radially outward from the
intermediate wall to the back wall of the blanket. Since the active volumes
of both zones also serve as the coolant materials, internal piping is
eliminated, structure is minimized, and high reliability should result from
the simple coolant circuits which are employed.

Second, the design features minimal MHD-induced pressure drops ($\approx$200 psi).
This results because the liquid metal flow within the blanket is parallel to
the central-cell field. The liquid metal does flow perpendicular to the field
in 20 inlet/outlet ducts which direct the coolant into and out of the
blanket. This flow component would normally produce large MHD pressure
drops. However, by a combination of design features including
electrically-insulated duct walls and large cross-sectional flow areas, the
pressure drop can be greatly reduced. Westinghouse has proposed a
low-conductivity pipe design incorporating a thin-metal wall and ceramic or
refractory-textile insulator materials to accomplish the above purpose.

The method used to contain molten salts in this design is also novel.
Since the maximum lithium-coolant temperature (400°C) is significantly
cooler than the salt (composition 72 LiF - 16 BeF$_2$ - 12 ThF$_4$) melting
point (500°C), it is possible to freeze a thin layer of the thorium-bearing
salt on the intermediate wall and other common surfaces which can be cooled by
the liquid lithium. This approach eliminates problems associated with the use
of Hastelloy or molybdenum alloys (e.g., TZM) as structural materials
throughout the blanket (i.e., radiation damage for Hastelloy, poor
fabricability for TZM). A Hastelloy structural option has also been
investigated as a backup and for use as a back-wall containment material where
neutron flux levels are considerably depressed.

Design issues associated with the reference lithium/molten-salt blanket
are discussed in Section ii.K.

Blanket Design and Performance Overview

Table ii.D-1 is an overview of several key design and performance parameters for the lithium/molten-salt TMHR blanket. These parameters are discussed in more detail throughout Chapter IV of the report. Additional data relating to a reference TMHR based upon the lithium/molten-salt blanket is presented elsewhere in the report.

TABLE ii.D-1. Key design and performance parameters for the reference
lithium/molten-salt blanket.
(Design basis: 3000-MW fusion power)

Mechanical Design

Central-cell length, m	96
First-wall radius, m	2
Number of blanket modules	15
Fraction of module axial length used for molten-salt zone,[a] %	77
First-wall thickness, cm	0.5 (avg.)
Lithium-zone thickness, cm	50
Molten-salt zone thickness, cm	80
Total blanket thickness, cm	130
Shield thickness, cm	50
Magnet inner bore (diameter), m	9.2
Magnet width, cm	50
Magnet pitch, m	3.2
Magnetic-field centerline, T	3
Blanket structural material	316 stainless steel (modified)

Power Flow and Thermal Hydraulic Design

Central-cell fusion power, MW	3000
First-wall surface heat load,[b] MW/m^2	0.01
First-wall neutron loading, MW/m^2	2.0
Total thermal power removed by blanket coolants, MW	3658
Thermal power deposited in liquid-lithium zone,[c] MW	2233
Lithium inlet/outlet temperatures, °C	220/390
Design liquid-lithium coolant pressure, psia at first wall	120
Number of 0.5-m-dia. liquid-lithium inlet/outlet pipes per module	20/20
Thermal power deposited in molten-salt zone, MW	1425
Molten-salt inlet/outlet temperature, °C	550/650
Molten-salt coolant pressure, psia	<80
Number of 1.4-m dia. molten-salt coolant inlet/outlet pipes per module	1/1

Nuclear Design and Performance[d]

^{6}Li enrichm,ent in liquid lithium, %	0.2
Tritium breeding ratio[e]	1.05
Lithium processing rate for tritium recovery, m^3/hr	43
Tritium inventory in liquid lithium, kg	1.0
^{233}U equilibrium concentration per atom of molten-salt thorium, %	0.11
^{233}Pa equilibrium concentration per atom of molten-salt thorium, %	0.03
Net fissile breeding ratio	0.49
Net fissile production rate,[f] kg/yr	6360

TABLE ii.D-1 (Continued)

Molten-salt processing rate for uranium recovery,[g] m^3/hr	0.46
Fissions in ^{232}Th per fusion	0.003
Fissions in ^{233}U per fusion	0.024
Fission power, MW	786
Blanket energy multiplication[h]	1.51

[a]Remainder of axial length used for lithium coolant piping
[b]Dominated by Bremsstrahlung radiation
[c]Includes first-wall surface heat contribution
[d]Includes 2-D leakage effects
[e]Must breed at least 1.027 to make up for breeding losses due to 80-MW fusion in end plugs
[f]At 100% plant capacity
[g]"Fluorination only" process removes only uranium from molten salt
[h]Defined as (energy-per-fusion deposited in blanket)/14.1

Concept Description and Motivation

The reference beryllium/thorium oxide (Be/ThO$_2$) suspension blanket is a two-zone design which is helium cooled, uses beryllium as a neutron multiplier, thorium oxide as a fertile fuel, and Li$_{17}$Pb$_{83}$ as a tritium breeding and heat transfer material. A perspective view of a section of the reference blanket is shown in Fig. ii.E-1. The first zone of this design employs nonstressed beryllium blocks located immediately behind the first wall. The volume between the blocks is filled with a liquid suspension including the lead-lithium eutectic and thorium oxide particles of approximately equal density. Also located between the beryllium blocks are concentric helium coolant tubes which remove heat generated in the blocks and the suspension. The second zone, composed of silicon carbide blocks, serves as a reflector and is also cooled by the helium carrying tubes. A split inlet/outlet helium distribution plenum is located outside of the reflector region.

As a result of the use of beryllium metal as a neutron multiplier, this design achieves excellent breeding performance (fissile breeding ratio of 0.74 for tritium breeding ratio of 1.05) with a very low fission rate (0.03 per fusion). Fast and thermal fissioning in the beryllium/thorium oxide suspension blanket is suppressed in several ways. Most importantly, the concept of fertile dilution is used. In particular, the thorium oxide volume fraction in the blanket is less than 3%. As a result, the macroscopic fast fission cross section for thorium above the fission threshold energy ($\approx$1.2 MeV) is only a small fraction of the total macroscopic cross section (which in this case is dominated by ^{9}Be(n,2n). Below the fast fission threshold (i.e., in the resonance region) the thorium (n,γ) cross section is large enough, however, to provide the desired level of fissile breeding at very low thorium concentrations. Fast fissioning is also reduced due to the strong neutron energy moderation properties of the beryllium multiplier.

Fissioning of ^{233}U in this blanket is suppressed in three ways. First, the fissile fuel bred in the blanket is discharge at very low concentration (typically 0.2% ^{233}U + 0.5% ^{233}Pa in thorium). Second, for a fixed fissile discharge concentration, a consequence of fertile dilution is a very low-volume fraction of fissile material (e.g., 0.5% x 3% = 0.015% by volume)
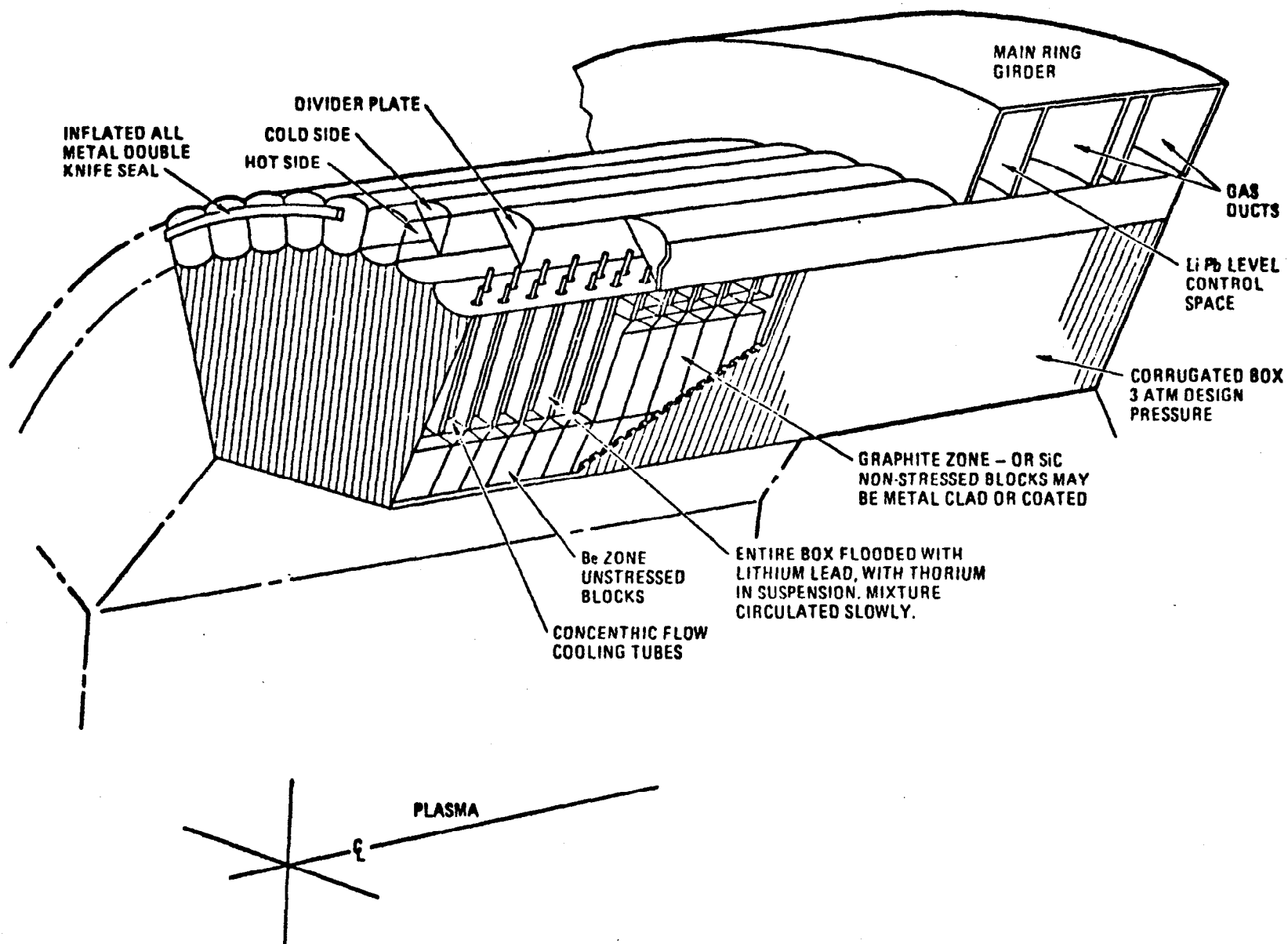
FIGURE ii.E-1.   Reference beryllium/thorium oxide suspension blanket

in the blanket. Third, in the reference system, the above fissile discharge enrichment can be achieved during a 1-2 month fuel residence time. As a result, ^{233}Pa($T^{1/2}$=27d) does not reach isotopic equilibrium during the fuel residence time and, consequently, most of the bred material (60%) prior to discharge from the blanket, will be in the form of ^{233}Pa rather than ^{233}U. This effect reduces the amount of thermal fissioning, improves the net fissile breeding ratio, and improves the isotopic quality of the bred fuel (i.e., less ^{232}U production).

In addition to its suppressed fission characteristics, this concept introduces several novel design features. To begin, pressurization of the entire blanket module is not required since the helium coolant is confined to concentric high pressure (50 Atm) tubes which penetrate the blanket. The coolant flows from the inlet manifold through the center of each tube, turns near the first wall, and exits to the outlet manifold along the outside annulus of each tube. This concept results in a considerable savings in structural materials and improved neutronics and safety aspects relative to previous pressurized module designs. The average thickness of the corrugated first wall is only 0.3 cm and the volume fraction of HT-9 ferritic steel in the blanket is only 4%. As a result of the radial orientation of the coolant tubes and the corrugated construction of the blanket submodules, this design is expected to be quite tolerant of neutron induced swelling.

Another novel design feature is the use of beryllium and the lead-lithium eutectic/thorium oxide suspension in this design. Since beryllium is predicted to swell up to 10% by volume during a 10-year irradiation at 2-MW/m^2 wall loading, space must be provided to accommodate such swelling. The suspension solves four problems. First, it fills the entire void between the fixed, unstressed, beryllium blocks and the pressurized coolant tubes. Second, it provides conductive heat transfer between the beryllium blocks, thorium oxide fuel (0.5-mm-dia. particles) and the coolant tubes. Third, it provides an excellent breeding material for both tritium and ^{233}U. Finally, it is expected that the lead-lithium density can be closely matched to that of thorium oxide so that the physical characteristics of the suspension can resemble those of a liquid if only a modest recirculating flow is incorporated into the system. Provision for such flow also allows for on-line fuel management. During the lifetime of the blanket, the beryllium blocks will swell and will displace 50% of the original volume of the suspension. Nevertheless, the heat transfer and breeding characteristics of the blanket

can be preserved. The latter is accomplished by varying both the volumetric concentration of thorium in the suspension as well as the ^{6}Li enrichment in the lithium component of the suspension.

A unique advantage associated with this design is the use of materials which are not chemically reactive with water or other common materials while achieving excellent breeding performance. Therefore, safety and design concerns normally associated with liquid metal and some solid lithium compounds (e.g., Li_7Pb_2) are avoided.

Design issues associated with the reference beryllium/thorium oxide blanket are discussed in Section ii.K.

Blanket Design and Performance Overview

Table ii.E-1 is an overview of several key design and performance parameters for the beryllium/thorium oxide suspension TMHR blanket. These parameters are discussed in more detail in Chapter V of the report. Additional data relating to a reference TMHR based upon the beryllium/thorium oxide suspension blanket is presented elsewhere in the report.

TABLE ii.E-1. Key design and performance parameters for the reference beryllium/thorium oxide suspension blanket.
(Design Basis: 3000-MW fusion)

Mechanical Design

Central-cell length, m	96
First-wall radius, m	2
Number of blanket modules	24
Number of blanket submodules per blanket module[a]	8
First-wall thickness,[b] cm (Avg.)	0.3
Beryllium multiplier zone thickness,[c] cm	30
Silicon-carbide reflector-zone thickness,[c] cm	30
Total blanket thickness, cm	63
Shield thickness, m	1
Magnet inner bore (diameter), m	7.9
Magnet width, cm	50
Magnet pitch, m	4
Blanket structural material	HT-9 ferritic steel

Power Flow and Thermal Hydraulic Design

Central-cell fusion power, MW	3000
First-wall surface heat load,[d] MW/m^2	0.01
First-wall neutraon loading, MW/m^2	2.0
Total thermal power removed by helium coolant,[e] MW	4460
Helium inlet/outlet temperatures, ^oC	250/450
Helium coolant pressure,[f] atm	50 (735 psia)
Pressure tube pitch separation, cm	4
Number of pressure tubes per unit area/m^2	800
$Li_{17}Pb_{83}/ThO_2$ suspension operating temperature, ^oC	663
Beryllium operating temperature,[f] ^oC	596
HT9 pressure tube operating temperature,[f] ^oC	514
HT9 first-wall operating temperature,[f] ^oC	600

Nuclear Design and Performance[g]

^6Li enrichment in lithium component of lead-lithium, %	10 to 25
Tritium breeding ratio[h]	1.05
^{233}U discharge enrichment in thorium,[i] %	0.20
^{233}Pa discharge enrichment in thorium,[u] %	0.38
Net fissile breeding ratio	0.73
Net fissile production rate,[i] kg/yr	9475
Fuel residence time,[i] days	36

TABLE ii.E-1 (Continued)

Fissions in ^{232}Tn per fusion[j]	0.007
Fissions in ^{233}U per fusion[j]	0.019
Fission power,[j] MW	840
Blanket energy multiplication[j]	1.86

[a]These are aziumuthally oriented and make the first wall octagonal in shape
[b]Effective thickness for corrugated first wall
[c]Also contains $Li_{17}Pb_{83}/ThO_2$ suspension for breeding and heat transfer
[d]Dominated by Bremsstrahlung radiation
[e]Includes first-wall surface-heat contribution
[f]Maximum steady state quantities
[g]Includes 2-D leakage and other adjustments to 1-D calculations
[h]Must breed at least 1.027 to compensate for breeding losses due to 80-MW fusion power in end plgs
[i]At 100% plant capacity
[j]Average over blanket lifetime

ii.F   TMHR FUEL CYCLE ISSUES

The principal role of the suppressed fission TMHR is to provide an external source of fissile fuel to support a fission power reactor economy composed of LWRs or other fission reactors. In this capacity, illustrated in Fig. ii.F-1, the TMHR fusion breeder is operationally similar to a fissile enrichment plant which requires no fissile feed stream and is an electricity producer rather than a consumer. As in the case for fission breeder reactors (e.g., LMFBR) the TMHR requires a closed fuel cycle with fuel reprocessing and fissile recycle to become practical and economically attractive. TMHR fuel cycle related issues will, in general, depend upon the particular breeding blanket design, the choice of a fertile fuel form, and the choices of a client reactor type and its associated fuel cycle. These issues can have potentially large impact on the cost of bred fuel, the cost of electricity generation, and overall feasibility of the TMHR. A more detailed discussion of fuel cycle issues is provided in Chapter VII of the report.

Fuel cycle information for the reference beryllium/thorium oxide (Be/ThO$_2$) and the lithium molten salt (Li/MS) designs is shown in Table ii.F-1. Most importantly, in comparison with the Li/MS blanket TMHR, the Be/ThO$_2$ blanket TMHR produces 50% more fissile fuel. Thorium oxide fuel Be/ThO$_2$ blanket TMHR produces 50% more fissile fuel. Thorium oxide fuel discharged by the gas cooled Be/ThO$_2$ blanket TMHR is unclad and is characterized by a very low fission burnup (250 MWD/MTHM) and a very large throughput (1326 MTHM/yr). The latter results due to the low fissile discharge concentration (0.5% in thorium). To estimate fuel cycle cost for this blanket, an earlier conceptual design and cost study for a dedicated thorium metal fuel processing plant based upon the thorex process was adapted. Similar product specifications were considered in the earlier study and differences between thorium metal and thorium oxide reprocessing were considered during the present study.

For the Li/MS blanket, two molten-salt processing options were considered n the new conceptual designs. The first, a "fluorination only" process, is shown schematically in Fig. ii.F-2. In this process, fluorination is used to recover bred ^{233}U fuel from the salt by volatilization as UF$_6$. The fluorination only process does not recover protactinium and fission products from the salt, but features only one major process component and eliminates many of the developmental requirements associated with molten-salt processing for fission systems (e.g., the molten-salt breeder reactor). A second process
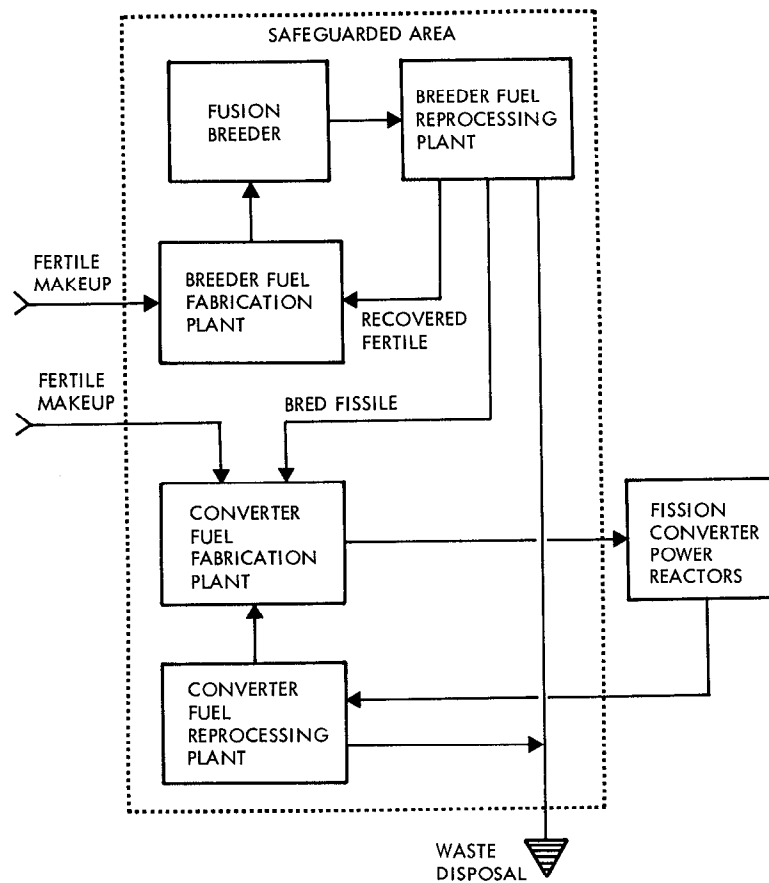
FIGURE ii.F-1. General schematic of the fusion breeder/fission burner reactor fuel cycle.

TABLE ii.F-1. Fuel cycle summary for thorium oxide and molten-salt reference-blanket designs.
(Basis: 3000-MW fusion)

	Thorium oxide	Molten salt Fluorination only[a]	Molten salt Full processing[b]
Thorium inventory, MT	157	1680[c,g]	1680[c,g]
Fissile inventories, Kg			
$^{233}U + ^{233}Pa$ in-core	408	2270[c,g]	2185[c,g]
$^{233}U + ^{233}Pa$ ex-core[d]	3315	2225	2225
Fuel management mode	batch	continuous	continuous
Fuel residence time,[e] yr	0.123	30	30
Net fissile production,[f] Kg/yr ^{233}U	6630	4450	4450
Reprocessing plant thorium throughput,[f] MT/yr	1326	5400	3340
Blanket discharge concentrations in thorium,[e] atom %			
^{233}U	0.20	0.107	0.107
^{233}Pa	0.32	0.028	0.023
Fission products	0.025	0.238	0.214
^{228}Th	$4.65 \cdot 10^{-8}$	$3.23 \cdot 10^{-6}$	$4.31 \cdot 10^{-6}$
^{232}U	$9.78 \cdot 10^{-5}$	$3.28 \cdot 10^{-4}$	$1.64 \cdot 10^{-4}$
Reprocessing plant discharge product concentrations,[e] atom %			
^{232}U in ^{233}U	0.0157^{d}	0.236	0.099
^{228}Th in thorium	$4.67 \cdot 10^{-7\,d}$	$8.23 \cdot 10^{-6}$	$4.31 \cdot 10^{-6}$

[a]Fluorination only process removes uranium only. Continuous process rate = 0.42 m^3/hr. Reprocessing plant capacity = 0.60 m^3/hr.

[b]Full processing removes uranium, protactinium and a small fraction of rare earth fission products. Continuous process rate = 0.24 m^3/hr. Reprocessing plant capacity = 0.35 m^3/hr.

[c]In-core fraction = 91%. Fraction in primary loop = 9%.

[d]0.5 yr delay between discharge and reprocessing assumed.

[e]Isotopic accumulation for molten-salt blanket based upon 30 year residence time. Thorium is replaced at the rate it is depleted and notes (a) and (b), above, apply.

[f]70% average plant capacity factor included.

[g]Molten salt inventories could be reduced many fold by adding graphite to molten-salt zone.

TO PRODUCT RECOVERY
F_2 9100 g/day
UF_6 25,990 g/day

TO GAS MANAGEMENT
SYSTEM

ThF$_4$ 24,600 g/day
NATURAL LiF 790 g/day

FLUORINATOR

F_2
12,250 g/day
H_2 485 g/day
HF 350 g/day

LiF and ThF$_4$
ADDITION

FILTER   FILTER

FEED
TANK
90-min
HOLDUP

H_2

PURGE
COLUMN H_2
643 g/day

SAMPLING
TANK
30-min
HOLDUP

SAMPLING
TANK
30-min
HOLDUP

SURGE
TANK

from BLANKET
0.6 m^3 Salt/h

0.6 m^3/h
Salt
Return to
BLANKET
SYSTEM

FIGURE ii.F-2. Molten salt processing schematic for fluorination in only option.

option, designated as "full processing" was also investigated. This, more complex process involves the reductive extraction of protactinium, zirconium, and possibly the rare earth fission products into bismuth. The reductive extraction process requires a lower overall salt process rate and provides for less radioactive hazard since ^{231}Pa, a percent of the undesirable isotopes ^{232}U and ^{228}Th, is removed to a holding tank. Although the difference in process cost between the two options is small, the fluorination only process was chosen as the reference process due to fewer anticipated developmental requirements. For either option, tritium, xenon, and krypton generated in the salt would be recovered by a helium purge and cleanup in a separate process.

The recovery cost of bred fissile fuel at low discharge concentration is an important economic factor in determining the relative merits of a TMHR fuel factory. This observation is illustrated in Fig. ii.F-3 where the allowable fuel reprocessing cost for a given increment in the overall cost of bred fuel is shown as a linear function of the fissile discharge concentration. For instance, a 20 $/gm impact up on the cost of bred fuel requires that the fuel reprocessing cost for the beryllium/thorium oxide and lithium/molten-salt TMHRs be below 104 $/kgHM and 47 $/KgHM, respectively.

Our estimates of reprocessing costs for thorex and molten-salt reprocessing, shown in Table ii.F-2, indicate that thorex process costs can not easily satisfy a 20 $/gm added cost goal while the cost of molten-salt reprocessing is an order of magnitude less expensive than needed to satisfy such a goal. As shown in Fig. ii.F-4, a representative trade study comparing relative economic performance for the three fuel cycle options shown in Table ii.F-2, the higher cost of thorex reprocessing for thorium oxide fuels is disincentive, but does not necessarily preclude the use of such fuel in a TMHR. Note that the cases shown in the above figure do not represent the reference beryllium/thorium oxide and lithium/molten-salt blankets, but rather a crude adaptation of the various fuel forms to a single blanket without regard for detailed blanket design.

As shown in Table ii.F-1, the Be/ThO$_2$ oxide blanket TMHR is characterized by much lower ^{232}U and ^{228}Th concentrations than the Li/MS blanket TMHR. The latter quantities determine the extent of remote fuel fabrication processes which are required for thorium recycle in the TMHR and LWR fuel fabrication. In particular, it is expected that a 10 year cooloff will be required prior to hands-on refabrication of thorium for reuse in the
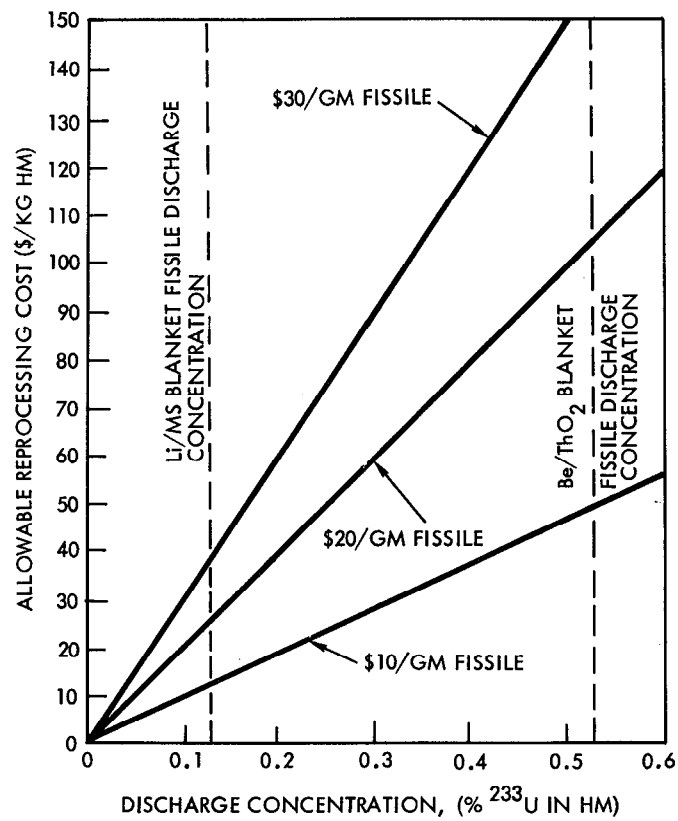
FIGURE ii.F-3. Allowable reprocessing cost to obtain a fixed contribution to the overall cost of bred fuel.

TABLE ii.F-2. Comparative results for various fuel forms and reprocessing technologies (1980 dollars).

	Fuel type/reprocessing option			
	Thorium metal	Thorium oxide	Reference molten salt[b]	Molten salt with Pa recovery
Total fissile discharge assay in thorium,[a] %	0.55	0.55	0.14	0.13
Uranium discharge assay in thorium, %	0.25	0.25	0.11	0.11
Process rate, MT/yr	1200	1200	5440	3160
Levelized cost per Kg thorium, $	127	152 to 233	1.59	5.06
Levelized cost per gm uranium, $	23	28 to 42	1.93	3.90

[a]Uranium plus protactinium.
[b]For this system only uranium is recovered and recovery efficiency is 75%. So cost per gram = 1.59/(1.1·0.75) = 1.93 $/gm.

beryllium/thorium oxide blanket. This issue does not apply to continuous operation of the molten-salt processing plant. Regarding LWR fuel fabrication, the 147 appm ^{232}U concentration in ^{233}U for the Be/ThO$_2$ blanket is encouraging and indicates that extensive shielding may not be required. However, the 2360 appm level of ^{232}U in fuel discharged by the molten-salt reprocessing plant will require fully remote fabrication of the LWR fuel charge.
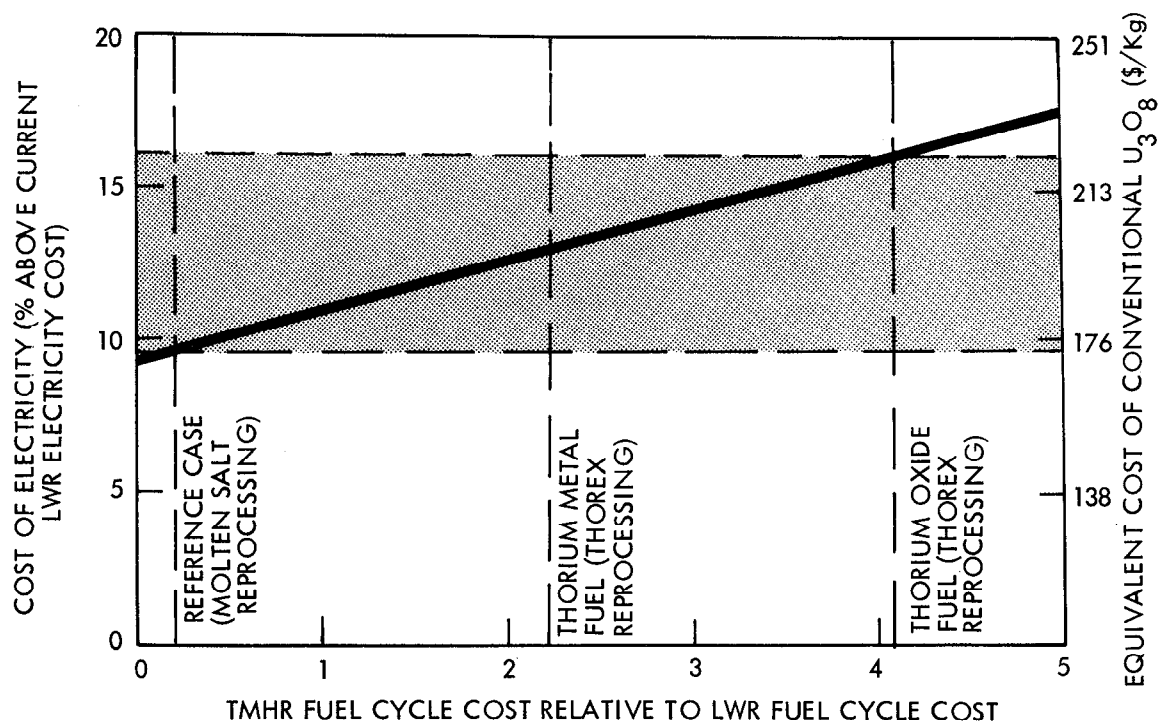
FIGURE ii.F-4. Trade study comparison of thorium oxide, thorium metal, and molten-salt fuel forms.

In this section an overview of safety considerations for suppressed fission blankets is provided and a summary of the safety analysis for both reference blanket concepts is presented. A more detailed presentation of the analysis and our results is provided in Chapter VI of the report.

Figures of Merit for Fission-Suppressed Blanket Safety Analysis

On the basis of past works on hybrid reactor safety, a number of safety characteristics were selected for evaluation for the TMHR with the intent of obtaining figures-of-merit and establishing safety criteria.

The figure-of-merit used to quantify the potential isotopic hazard in the TMHR is the Biological Hazard Potential (BHP). BHP is defined as the ratio of the total radionuclide activity to the maximum permissible concentration (MPC) of a specific isotope. Total BHP is the sum of the BHPs of each radionuclide present such that the BHP provides an acceptable measure of the total potential radiological hazard present in the system. Although the BHP does not suggest a hazard release mechanism, fission suppression has been shown to offer a factor of 10 to 20 improvements in shutdown BHP over fast-fission and LMFBR systems when compared on an equal thermal power basis. When compared on an equal fuel production basis, the copious quantity of fuel produced by the fission-suppressed hybrid results in an improvement in shutdown BHP/kg/yr to a factor of over 500 compared to the LMFBR.

An additional consideration has emerged as a result of this year's work; the isotopic distribution of the hazard. In the production of ^{233}U from fertile ^{232}Th, the concomitant production of the intermediate nuclides ^{233}Th and ^{233}Pa is inherent. Though these isotopes dominate the BHP at shutdown, they decay away relatively rapidly, leaving the hazard to be dominated by nuclides produced via parasitic captures and fissions. A computation of BHP as a function of time after shutdown would demonstrate this fact and permit comparisons of the hazard subsequent to the initial transient.

A second figure-of-merit proposed is the time-to-melt. The results of thermal analyses performed this year and comparisons to past work indicate that the computation of the time-to-melt is sensitive to the assumptions made in formulating the thermal model. Adiabatic models offer overly pessimistic indications of melting potential and two-dimensional models, although more

realistic, are quite costly and do not permit extensive parametric analyses. This year's results have shown that indications of melting (obtained with pessimistic assumptions), along with the attendant safety implications, were not observed after analysis with realistic two-dimensional configurations. The 2-D analyses showed that the gas-cooled beryllium/thorium oxide blanket does not melt under the postulated loss-of-cooling capability events.

An additional consideration arises in the use of time-to-melt in conjunction with structural members under stress. The allowable material working stress decreases rapidly at elevated temperatures. It is therefore necessary to consider the possibility of a material buckling before it has reached its melting temperature and a time-to-fail analysis may be more appropriate. This is a safety consideration that must enter into the design process, although the analysis of a realistic configuration is quite complex.

The third figure-of-merit, relative risk, was evaluted using the techniques of probabilistic risk assessment (PRA). Risk is defined as the product of the probability of an event times its consequence. The probability that a component will fail at a particular time when called upon to function depends upon both the failure rate for a particular failure mode and the availability of that particular component. Since many TMHR plant systems are unique, failure probabilities have been estimated using available data for more conventional systems (e.g., LWR).

The unit of consequence used in this report is effective dose. The effective dose equivalent assigns a biological consequence factor to the exposure of each organ based upon the likelihood of inducing biological damage. Since equal exposures to different organs have significantly different dose consequences, this formulation permits exposure to a number of different organs to be algebraically combined.

For the purposes of the present study, the product of probability and consequence can be used to identify the major risk contributors of a proposed design configuration. This is accomplished via construction of event trees--a logical display of the sequence of component and system failures and successes that result in, or prevent, a radioactive release. Example event trees resulting from this year's analysis of the lithium/molten salt and beryllium/thorium oxide blankets are shown in Figs. 1 and 2, and described in more detail in Chapter VI. The identification of the major risk contributors

then suggests design modifications that can reduce the overall risk. Design
guidance through which the risk can be reduced has been offered in the
appropriate sections for this year's reactor designs.

As noted above, the probabilities used in the risk analysis are
approximations based on generically similar components, mature instrumentation
and detection systems, fission industry service and maintenance procedures,
redundancy in the heat removal systems, etc. The results of the event trees
show that most sequences of events are inconceivable and/or have very low
consequences. This means that either the major risk-contributing sequences
have not been identified or that a large margin of safety exists due to
multi-tier engineered safety systems incorporated in the design. Due to the
design dependence of the probabilities, only relative comparisons within a
given design are possible. Extensions to comparisons among dissimilar systems
is risky. The failure probabilities, however, can be used as targets as the
system definition and design details emerge. As such, the relative risk has
indeed served as a useful figure-of-merit in the present designs and can
continue to serve as the designs evolve and the risk computation is refined.

Liquid Metal-Cooled Blanket

The engineered safety features incorporated into the reference
lithium/molten-salt blanket result in a design with very low probabilities of
radio-activity releave. These safety features include:

- up to 15 separate, parallel molten-salt loops
- molten salt and lithium dump tanks
- semipassive freeze-type drain valves
- argon-inerted sealed cells
- fluid pressure differentials directing potential lithium leaks into
  the molten salt

These features and others present a sequence of barriers whose probabilities
of successive failures are in most cases inconceivable.

In addition, the consequence can be reduced by proper design. The BHP
present at shutdown is approximately one order of magnitude lower than that of

an LMFBR. The use of a separate loop for each blanket module serves to reduce the consequences of an event an additional order of magnitude.*

Concerning lithium safety, it has been assumed that accident events involving the liquid lithium loop only would have little effect on the molten-salt loop. Lithium burns in air and reacts strongly with water and concrete. Upper limits on the adiabatic flame temperature of a lithium fire can be computed from thermochemical considerations to be from 2100 to 2500 K. Although this temperature range would appear to permit melting and failure of stainless steel components, analysis of realistic configurations with engineered safeguards may indicate otherwise. In particular, the use of inerted, steel-lined sealed cells, an inert reactor building, and lithium dump tanks will with semi-passive freeze valves reduce the possibility of a lithium fire and radioactive releases such as those pessimistically assumed and analyzed by Holdren. These safety features are common in LMFBR and MSBR plant designs.

The liquid lithium-cooled first wall may have an inherent safety feature; namely, the first wall might be adequately cooled by natural convection in the event of a loss-of-flow. In this case, the afterheat generated in the first wall (estimated to be $\sim$ 3.6 W/cm^3) could be transferred to the molten salt and to the adjacent modules. The depressurized lithium would reduce the pressure stresses on the containment walls, thereby permitting higher temperatures. In the event of a loss of liquid lithium as a result of a large breach of the first wall, the first wall will melt. However, the blanket module affected and the first wall would have to be replaced in any case. The molten stainless steel will flow and contact other intact blankets in which liquid lithium continues to flow. Thus the molten steel would solidify and result in no release of activation products outside the reactor. The possibility that the adjacent intact modules may serve as effective heat sinks needs to be analyzed.

---

* It must be noted that the analysis of loss of cooling capability events outside of the secondary containment (e.g., feedwater flow disruption or steam generator failure) are beyond the scope of the present work. This type of event could have more serious consequences since all molten-salt loops might be affected simultaneously.

Gas-Cooled Blanket

The safety features of the reference beryllium/thorium oxide blanket have been evaluated and the results indicate that the gas cooled blanket possesses very attractive safety characteristics. These characteristics include the following:

● Although loss of structural integrity is a concern requiring further analysis, blanket melting does not occur from decay afterheat under any postulated loss of heat removal capability event. Only as a result of the plasma remaining on during an undetected heat removal system failure will the radioactive inventory be released to a functional secondary containment.

● The BHP present at shutdown in the blanket is approximately a factor of 20 lower than that of an LMFBR. This advantage rapidly increases after shutdown as the major BHP contributors of the gas-cooled blanket (^{233}Th, ^{233}Pa, and the iodine isotopes) quickly decay while those of the LMFBR and the fast fission hybrids do not.

● The consequences of the maximum credible release using conservative release fractions and medium U.S. site meteorology are below the 10CRF100 guidelines for accident conditions.

Having performed the safety analysis integral with the design of the blanket, a number of conceptual engineered safety systems have been incorporated into the design. These include a fertile suspension flow control mechanism, a fertile suspension drain tank with semipassive frozen drain valves, and consideration of a submodule pressure relief system. These should be further analyzed and improved in future studies. In addition, the results of the risk analysis demonstrate the adequate plasma disruption protection devices and a method for limiting spills of the fertile suspension (as in a pipe rupture) need to be included and analyzed in subsequent design iterations. Finally, the results of the thermal analyses show that a blocked cooling tube may be tolerable for short periods of time. That analysis should be refined and a detection system to locate such blockages should be devised.

ii.H TMHR PLANT POWER FLOW AND COST ANALYSIS

A summary of TMHR flow and cost estimates for plants based upon the reference lithium/molten salt (Li/MS) and beryllium/thorium oxide (Be/ThO$_2$) blanket concepts is provided in this section. A more detailed presentation of related information is provided in Chapter VIII of this report.

Two computer models were used to generate the tandem mirror hybrid reactor performance and cost data. The first of these, the LLNL Tandem Mirror Physics Code (TMPC) was used to estimate the fusion and injected power flow and the central-cell configuration given the fusion power, neutron wall loading, end-plug configuration and other quantites. The fusion power flow and configuration are then input to the Tandem Mirror Reactor Design Code (TMRDC). TMRDC provides estimates of the direct capital cost and power flow parameters associated with fusion driver components, the first wall/blanket/ shield, power conversion, balance of plant systems, and site building and facilities. The TMRDC cost and performance estimates, which relate to a tenth-of-a-kind commercial fusion facility, are highly uncertain. Therefore, these estimates are represented to be reasonable rather than correct in an absolute sense.

Power Flow

The power flow characteristics of the two reference TMHR designs can be separated into three principal categories: the fusion plasma power flow, the fusion component (e.g., plasma heating system) power flow, and the thermal conversion and balance of plant power flow. Concerning the first category, the fusion plasma power flow assumptions were identical for both designs and are shown in Table ii.H-1. An axicell tandem mirror configuration operating at a 3000 MW$_{fusion}$ power level with a 2 MW/m^2 wall loading is estimated to achieve a plasma Q of 15.3. Considering a 60.5% net trapping fraction, 324 MW of injected power will be required to maintain steady state plasma conditions. The power level of the more expensive heating component, rf microwave heating, is 59 MW, or 18% of the total.

Assumptions concerning the power flow characteristics of fusion components were also identical for both reference designs, and are shown in Table ii.H-2. For the purpose of this study we have estimated the wall plug efficiencies of negative ion neutral beams, rf gyrotrons, and direct converter

TABLE ii.H-1. Fusion plasma power-flow data.

Fusion power, MW	3000
Plasma Q[a]	15.3
Net injected power absorbed in plasma, MW	196
Net injected power trapping fraction	0.605
Gross injected power, MW	324
RF heating power, MW	59
Neutral beam power, MW	265
Neutron wall loading, MW/m^2	2.0

[a]20-T barrier coil in axicell configuration with 1.5-m first-wall radius and 129-m central-cell length.

TABLE ii.H-2. Fusion component power flow parameters.

	Base	(Variations)
Neutral beam wall plug efficiency	0.60	(.30 to .80)
Fraction of unconverted neutral-beam thermal power input to thermal converter power cycle	0.70[a]	(0.0)
RF wall plug efficiency	0.50	(.3 to .6)
Fraction of unconverted rf thermal power input to thermal converter power cycle	0.70[a]	(0.0)
Plasma dump direct conversion efficiency	0.50	(.35 to .65)
Fraction of unconverted plasma dump thermal power input to thermal converter power cycle	0.50[a]	(0.0)
Auxilliary electric power as fraction of fusion power	0.0433[b]	

[a]Thermal power assumed to be extracted at 450°C to enable efficient conversion to electricity.
[b]Principal component is 100 MW$_e$ for resistive power losses (I^{2}R) in copper barrier coils at 20 Tesla.

plasma dump systems to be 60, 50 and 50% respectively. Reasonable variations about these values are shown in the table and the effect of such variations on system economics was investigated.

We have also recognized that a sgnificant amount of potentially recoverable thermal power (634 MW_t) is deposited in the plasma dump, neutral beams, and rf gyrotron tubes and we have assumed that 57% (364 MW_t) of the otherwise wasted thermal power deposited in the above components can be collected at high enough temperature to permit efficient thermal conversion. An additional 128 MW_t deposited in the neutral-beam dumps is not assumed to be recoverable. The ability to utilize power deposited in components such as gyroteon tubes requires further study, but our parametric results indicate that such use, although desirable, has little effect upon overall economics.

In addition to the 560 MW_e of gross recirculating power required to drive the plasma heating systems, other fusion related systems are estimated to consume 130 MW_e of recirculating power. Of this, 100 MW_e is required to compensate for resistive power losses (I^2R) in the copper inserts of the 20 tesla barrier coils. The remaining 30 MW should conservatively serve other power requirements (e.g., pumps and the cryoplant).

Overall power flow diagrams for both the Li/MS blanket and Be/ThO_2 blanket TMHR reference designs are shown in Fig. ii.H-1(a) and (b), respectively. As both systems utilize the same 3000 MW_{fusion} driver, many of the power flow parameters are identical. In comparison, the Li/MS blanket TMHR produces 17% more net electrical power due to a higher thermal conversion efficiency due to a higher maximum coolant outlet temperature (650^oC vs. 450^oC for the Be/ThO_2 blanket) and a lower coolant pump power requirement. Nevertheless, the symbiosis with LWR client reactors, the overall system electricity production is 30% lower for the Li/MS TMHR compared with the Be/ThO_2 TMHR; a superior fissile fuel producer.

Plant Cost

A rough costing analysis for each of the two reference blanket TMHR designs was performed using the TMRDC code. A breakout of this analysis for the direct cost of both reactor plant systems, by major PNL cost account number, is shown in Table ii.H-3. Despite a large heat transport system, the Be/ThO_2 TMHR achieves a 150 $M lower direct cost. This results due to lower central-cell magnet costs (smaller bore) and lower reactor plant equipment
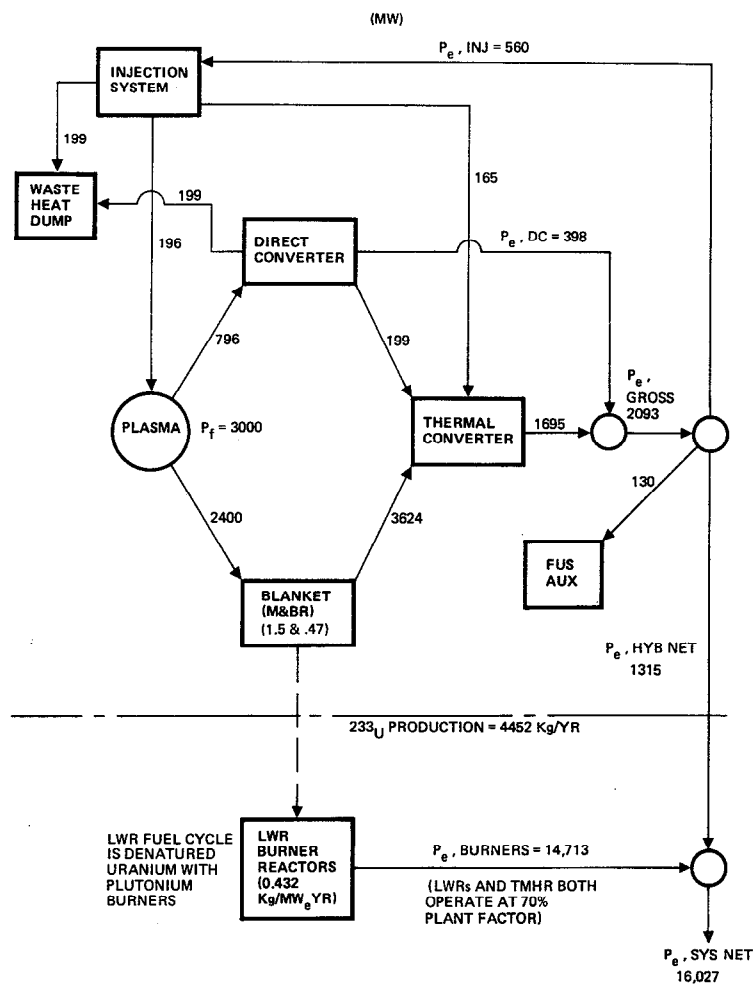
(a) Lithium/molten salt blanket TMHR.
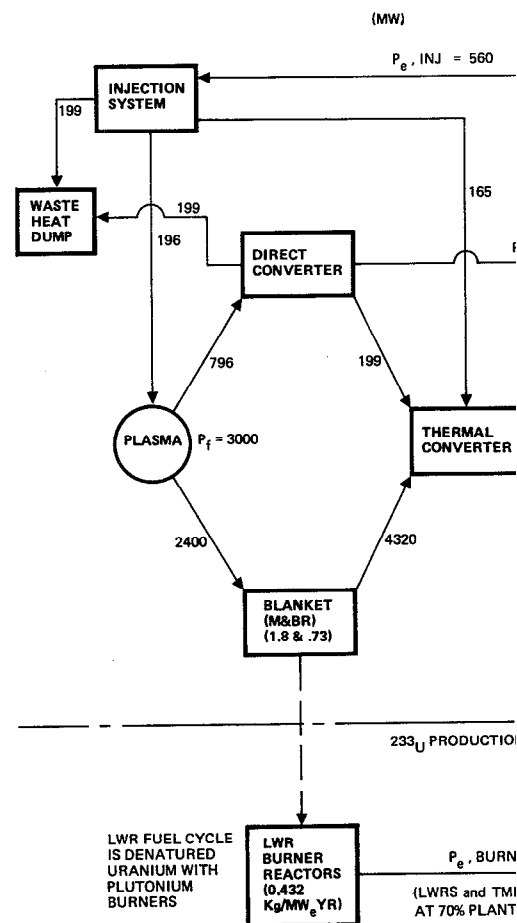
(b) Beryllium/thorium oxide

FIGURE ii.H-1. System power flow for TMHR power plants.

TABLE ii.H-3. TMHR direct cost breakout by cost account number.
($ Million)

Account number			Account title	Blanket Type Li/Ms	Blanket Type Be/ThO$_2$
20			Land and land rights	5.0	5.0
21			Buildings and structures	337.9	337.2
	21.1		Site improvements and facilities	12.5	12.5
	21.2		Reactor containment building	106.2	99.6
	21.3		Turbine generator building	47.0	46.1
	21.4		Cooling system structure	7.1	7.8
	21.5		Power supplies and energy storage	0.0	0.0
	21.6		Other plant buildings	165.1	171.2
		21.6.1	Reactor auxiliary building, R	22.2	22.5
		21.6.2	Reactor auxiliary building, NR	5.5	5.6
		21.6.3	Reactor service building	28.1	28.4
		21.6.4	Steam generator building	35.0	40.2
		21.6.5	Control building	19.4	19.5
		21.6.6	Direct converter building	42.4	42.4
		21.6.7	Miscellaneous structures	12.5	12.6
22			Reactor plant equipment	1967	1764
	22.1		Fusion reactor equipment	1627	1576
		22.1.1	NA		
		22.1.2	Blanket/shield	365.7	350.3
		22.1.3	Magnets	532.5	496.2
		22.1.3.1	End cell magnets	392.0	392.0
		22.1.3.2	Central-cell magnets	140.5	104.2
		22.1.4	Plasma heating systems	574.6	574.6
		22.1.4.1	Neutral beams (@ 1.5 $/W)	398.1	398.1
		22.1.4.2	RF heating (@ 3.0 $/W)	176.5	176.5
		22.1.5	NA		
		22.1.6	Vacuum vessels	0.9	0.9
		22.1.7	Other driver components	50.0	50.0
		22.1.8	NA		
		22.1.9	Direct converters (@ 0.13 $/W)	103.5	103.5
	22.2		Reactor plant equipment	339.4	188.7
23			Turbine plant equipment	227.2	237.2
	23.1		Turbine generators	125.6	119.2
	23.2		Main steam system	9.5	11.2
	23.3		Heat rejection system	25.7	32.8
	23.4		Condensing system	17.2	22.7
	23.5		Feed heating system	30.2	33.2
	23.6		Other equipment	19.0	18.1

TABLE ii.H-3 (Continued)

Account number	Account title	Blanket Type Li/Ms	Blanket Type Be/ThO$_2$
24	Electric plant equipment	162.4	206.8
24.1 thru 24.3	Switch gear and related equipment	23.3	36.4
24.4	Protective equipment	2.1	2.1
24.5 thru 24.6	Electrical bulks	133.6	164.9
24.7	Electrical lighting	3.4	3.4
25	Miscellaneous plant equipment	12.0	12.0
90	Total plant direct capital cost	2712	2562

costs (single coolant). In this analysis, the cost of neutral beams, rf heating, and plasma dump systems were taken to be 1.5 \$/W, 3.0 \$/W, and 0.13 \$/W, respectively. Variations about these costs (i.e., 1-2 \$/W for neutral beams, 1-5 \$/W for rf, and 0.065-0.195 \$/W for plasma dumps) were considered in the economics analysis. For both TMHR designs the cost for fusion reactor equipment (cost account 22.1) represents about 60% of the total direct capital cost.

Our estimates of the total (direct plus indirect) cost for both TMHR plants (including dedicated fuel processing plants) are shown in Table ii.H-4. These estimates are typical of private utility financing based upon light water reactor power plant construction experience. All costs are referenced to 1980 dollars.

TABLE ii.H-4. Summary of reference TMHR charges.

	Blanket type (in 10^6 dollars) Li/MS	Blanket type (in 10^6 dollars) Be/ThO$_2$
TMHR direct cost[a]	2711	2561
Fuel processing plant direct cost	75	541
Total direct cost	2786	3102
Indirect cost[b]	2365	2634
Time related cost[c]	917	1020
Total capital cost	6068	6756

[a]1980 dollars.
[b]Field indirect cost multiplier = 1.2, home office cost multiplier = 1.2, contingency factor = 1.2 (or 1.10 for LWR), owner's cost factor = 1.07 (or 1.10 for LWR).
[c]Inflation = 7%, escalation = 7%, construction period = 10 years results in 1.178 cost multiplier.

ii.I   SYSTEMS AND ECONOMIC ANALYSIS

A summary of results related to systems and economics analysis performed for symbiotic electricity generation systems composed of TMHRs and LWR clients is provided in this section. The TMHR fuel cycle center concept is introduced, figures of merit for symbiotic electricity generation are reviewed, these figures of merit are applied to TMHRs based upon the reference lithium/molten salt (Li/MS) and beryllium/thorium oxide (Be/ThO$_2$) blankets, parametric studies relating economic performance to uncertainties associated with the performance and cost of the TMHR are reviewed. A more detailed presentation of related information is provided in Chapter IX and Section X.B of this report.

In addition to the Tandem Mirror Physics Code (TMPC) and the Tandem Mirror Reactor Design Code (TMRDC), a third computer code, PERFEC, was used in the performance of the systems and economic analysis. PERFEC combines the TMRDC output with fission reactor, fission fuel cycle, and financial data to estimate the economic performance of the entire symbiotic electricity generation system. One net product, electricity, is considered.

Fuel Cycle Center Concept

As shown in Fig.s ii.I-1 and ii.I-2, TMHRs are ideally suited for siting in remotely-located fuel-cycle centers which would provide fuel cycle services for a large number of client LWRs. In particular, only three Be/ThO$_2$ blanket TMHRs are required to provide fuel to support a 69-GWe electric generation system with only 4.6% of the total electricity generated within the fuel cycle center itself. Similarly, four Li/MS blanket TMHRs can support a 63-GWe electric generation system with 8.2% of the total electricity generated within the fuel cycle center.

Suppressed fission blanket TMHRs can be logically considered as a replacement for the current uranium mining and fissile enrichment technologies since LWR fuel cycles based upon TMHR fuel supply can utilize a minimal number of facilities to provide sufficient quantities of enriched fuel to support large numbers of light water reactors. TMHRs would provide only a small fraction of the grid power, but differ from the mines, mills and enrichment plants in that they produce, rather than consume, net power. Like the LMFBR, another difference is that the TMHR fuel cycle center represents an inexhaustable energy source.
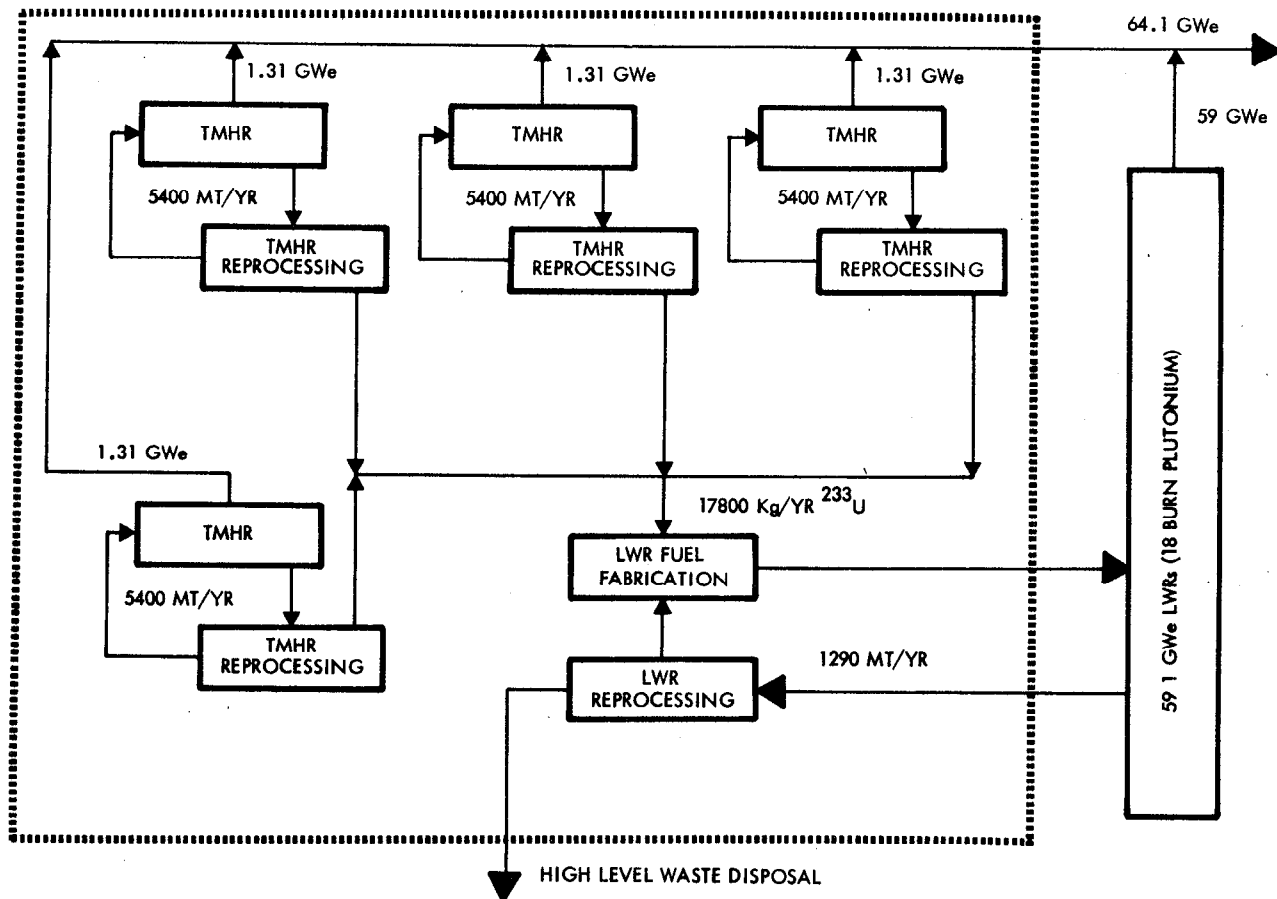
FIGURE ii.I-1. Fuel-cycle center concept for lithium/molten salt-blanket TMHR with LWR-denatured uranium (and plutonium) clients.
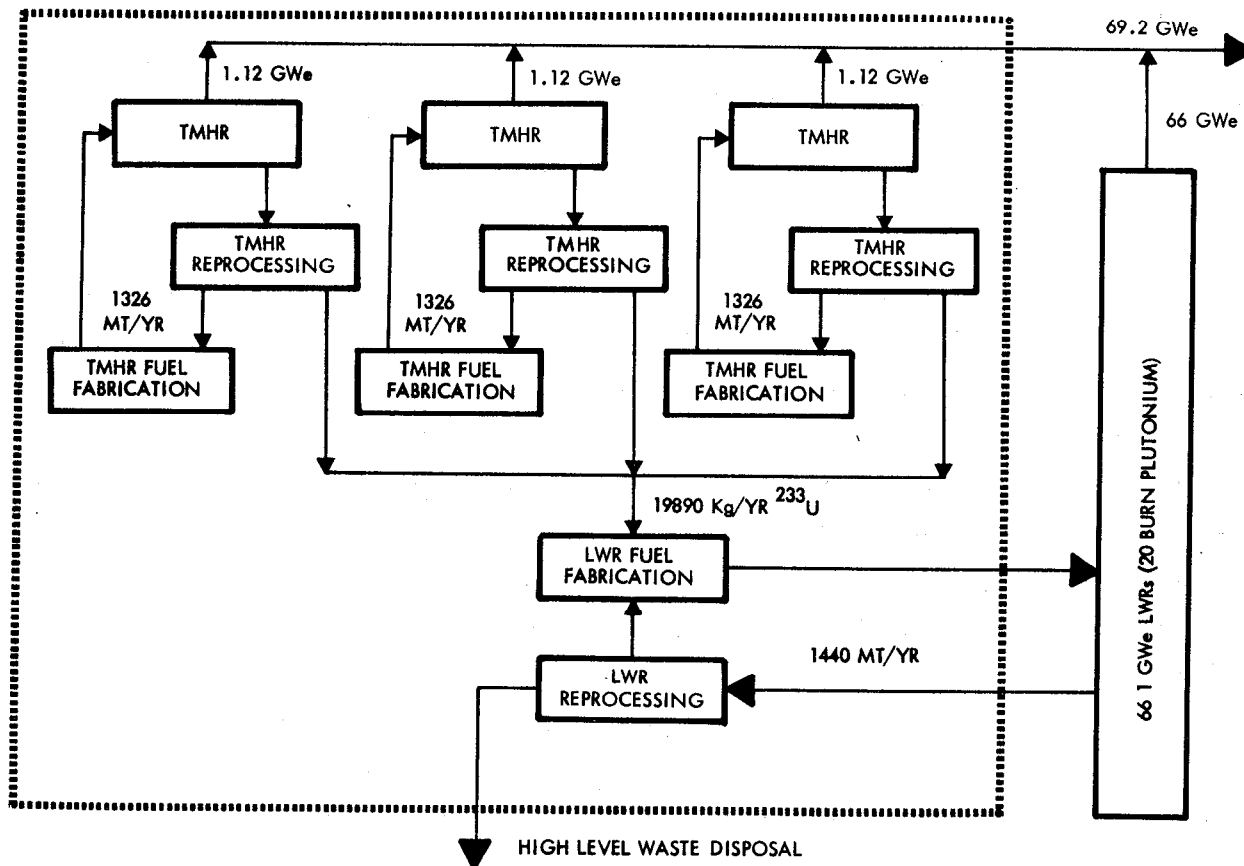
FIGURE ii-I.2. Fuel-cycle center concept for beryllium/thorium blanket TMHR
with LWR-denatured thorium (and plutonium) clients.

However, this option does require a closed fuel cycle with reprocessing. The ability to contain all potentially sensitive fuel cycle operations in remotely sited and safeguarded centers is viewed as an advantage with respect to proliferation (i.e., fissile diversion) resistance. The use of "denatured" fuel cycles for the majority of LWRs is an additional barrier to proliferation.

System Figures of Merit

Three system figures of merit are most important in characterizing the performance and economics of fusion-fission electricity generation systems. These are: the nuclear support ratio, the system electricity cost, and the year zero equivalent cost of U_3O_8 (i.e., natural uranium). These are briefly defined below.

The nuclear support ratio, R, is defined as the nuclear power of the client fission reactors divided by the nuclear power of the TMHR (i.e., fusion power x (0.8M + 0.2) where M is the blanket energy per source neutron divided by 14.1). A high nuclear-support ratio is advantageous because only a small fraction of the symbiotic system's cost and electricity generation comes from the TMHR (typically, about 15% of the overall capital cost and about 5% of the overall electricity generation). As a result of the high support ratio, system electricity costs can be relatively insensitive to uncertainties in the performance and cost of the fusion system while preserving a low average capital cost for the entire fusion-fission electricity generation system. Because a large fraction of the existing nuclear electric grid can be fueled from a small amount of fusion hybrid reactor capacity, TMHRs with high support ratios can have larger commercial impacts at earlier dates.

Variations in support ratio estimates are dependent on the specifics of the fusion hybrid-reactor designs, the type of client fission reactor, and fuel cycle choices. Typically, the highest nuclear support ratios are achieved by suppressed fission-blanket TMHRs. In this study our consideration of only LWR clients is motivated by our perception that LWRs will dominate nuclear power generation during the first decades of the next century when TMHRs can be introduced commercially. The nuclear support ratios estimated for the reference TMHR plants with denatured uranium or denatured thorium fuel cycle clients are shown in Table ii.I-1.

TABLE ii.I-1. Nuclear support ratios for reference TMHR plants.

	Blanket type	
	Li/MS	Be/ThO$_2$
Denatured-uranium fuel cycle[a]	10.5	13.4
Denatured-thorium fuel cycle[b]	13.7	17.5

[a]30% of LWRs in this system burn excess plutonium generated in (3% ^{233}U/ 97% ^{238}U) LWR fuel.

[b]14% of LWRs in this system burn excess plutonium generated in (3% ^{233}U, 19% ^{238}U, 19% ^{238}U, 79% ^{232}Th) LWR fuel.

These nuclear support ratios can be put in perspective by comparing them to those of an LMFBR. LMFBRs can produce enough excess fissile fuel to support about one LWR of equivalent nuclear power. Even so, the LMFBR must also produce fissile fuel to satisfy the fissile inventory requirement of additional LMFBRs. Consequently, LWR support is not a likely mode of LMFBR operation.

System electricity cost is an important figure of merit for a fusion fuel factory-fission burner system because the only real product of the symbiotic system is electricity. The system electricity cost is most useful when compared to a similar calculation of the cost of electricity produced by a "current technology LWR" fueled with ^{235}U derived from conventional mined uranium. Such a comparison is shown in Fig. ii.I-3 for typical fusion-fission electricity generation systems featuring several generic blanket and fuel cycle options. These options assume lower cost and improved power flow characteristics for the fast fission blankets relative to the suppressed fission blankets investigated in this report, but fast-fission blankets are characterized by lower fissile production and higher blanket energy multiplication. These result in a lower LWR support ratio. In this analysis the current technology LWR burns mined U$_3$O$_8$ costing 100 $/kg (1980 dollars) during its first year of operation* and assumes fissile recycle via fuel reprocessing. As shown in the figure, most blanket/fuel cycle options have potential to provide electricity for less than 15% above the cost of electricity for the current technology LWR.

---

*U$_3$O$_8$ escalation assumed to be 3%/year above general inflation for 30 year subsequent plant life.

Once the system electricity cost is known, it is possible to determine the bred fuel cost by subtracting the fusion fuel factory's electricity sales revenues from its operating expense. More importantly, the system electricity cost can be expressed in terms of an equivalent U_3O_8 cost. This is the year zero U_3O_8 price for which a new LWR, using mined U_3O_8, would generate electricity at the same levelized cost over its lifetime as the fusion fuel factory-fission burner system. Included in calculations for both the system electricity cost and the equivalent U_3O_8 cost are cost and cost escalation estimates for uranium,* uranium enrichment, fuel fabrication and fuel reprocessing.

Typical year zero equivalent U_3O_8 costs (1980 dollars) are also shown in Fig. ii.I-3. These indicate that equivalent U_3O_8 costs of less than 200 $/kg (about 90 $/lb) are possible. When compared with the NASAP U_3O_8 cost projections shown in Fig. ii.I-3 these indicate economic breakeven for the hybrid in the 2000 to 2020 timeframe.

More specific system economics results for TMHRs based upon the two reference blanket design concepts are shown in Table ii.I-2. As shown, the Be/ThO$_2$ TMHR results provide agreement with the results presented in Fig. ii.I-4. In particular, a system electricity cost of about 9% above the cost of electricity from the current technology LWR is estimated. The year zero U_3O_8 cost equivalent to a 9% electricity cost increase is 168 $/Kg-- about 2.5 times the current price of mined uranium ore.

The Li/MS blanket TMHR is estimated to result in system economic performance which is only slightly less attractive than that of the Be/ThO$_2$ blanket TMHR--namely, a system electricity cost 13% above that of the current technology LWR and a year zero equivalent U_3O_8 cost of 201 $/kg.

Although the system electricity costs presented above are encouraging, it would be misleading to indicate that cost, performance, and economics parameters are known to an acceptable degree of accuracy. In particular, we might expect that while the LWR data are reasonably accurate and well known, fusion breeder related cost and performance data is largely uncertain (despite the best efforts in conceptual design and costing). To address this issue, we have performed several parametric analysis relating the cost of system electricity and the year zero equivalent cost of U_3O_8 to various cost and performance uncertainties. Five analyses which are representative of our results are shown in Figs. ii.I-5, -6, -7, and -8. These are discussed in more detail in Chapter IX of the report.
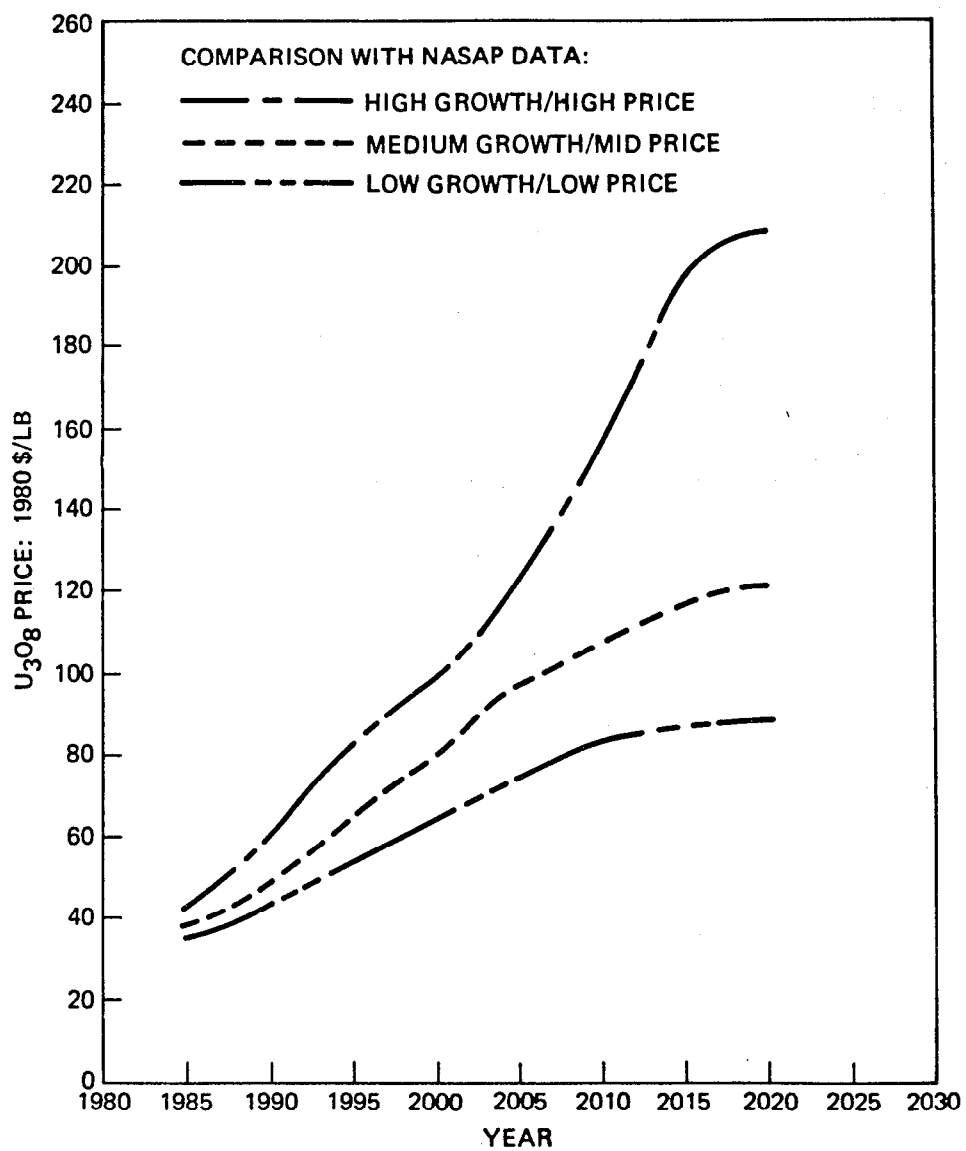
FIGURE ii-I-3. NASAP U_3O_8 price projections versus year for different nuclear growth rates and prices.

TABLE ii.I-2. Summary of system economics results for two reference TMHR concepts.

	TMHR blankets	
	Li/MS	Be/ThO$_2$
Plant capital cost, $ million (1980 dollars)[a]	6068	6756
Cost relative to LWR[b]	3.70	3.01
Elec. production, MWe	1310	1120
Net elec. efficiency, %	31	23
Fissile production, kg/yr[c]	4450	6630
Nuclear support ratio[d]	10.51	13.4
Levelized system electricity cost, mill/kWeh	56	54
System electricity cost, % above current technology LWR	13	9
Year zero equivalent U$_3$O$_8$ cost, $/kg	201	168

[a] Includes dedicated fuel reprocessing facility.
[b] Basis: $/kW(nuclear)
[c] 70% plant factor included.
[d] Denatured uranium fuel cycle LWRs with plutonium burning LWR.
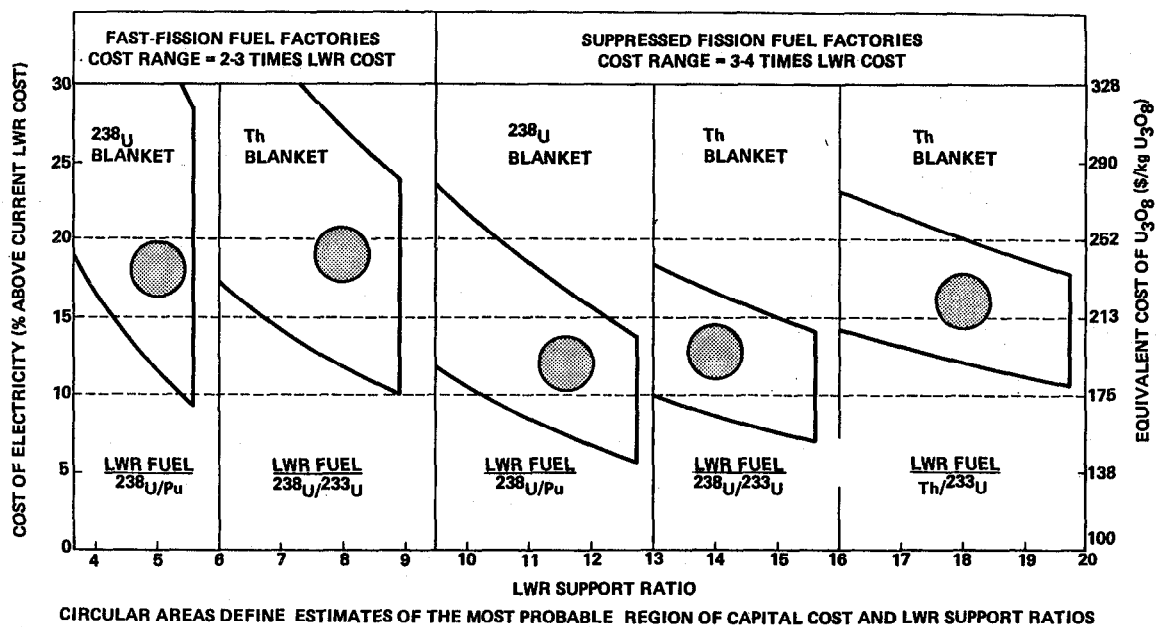
FIGURE ii-I-4. The economics of typical fusion fuel factory--fission burner systems.

Figure ii.I-5 illustrates changes in the equivalent U_3O_8 cost that would result from changes in the cost of fusion related reactor subsystems. In this analysis, the cost of the end cell (magnets, vessel, shielding) is the largest single cost driver--a 50% increase results in a 10% increase in the equivalent U_3O_8 cost and a 2.4% increase in the cost of electricity. The pessimistic case (see "ALL" in Fig. ii.I-5) results in a 21% increase in the equivalent U_3O_8 cost and a 7% increase in the electricity cost.

Figure ii.I-6 illustrates similar results when the efficiency of fusion related subsystems is varied. In this case, the neutral-beam efficiency is the largest cost driver--a 50% decrease results in a 24% decrease in net power production with an 18% increase in the equivalent U_3O_8 cost and a 4.1% increase in the electricity cost. The pessimistic case (see "ALL" in Fig. ii.I-5) results in a 60% decrease in net electricity with a 36% increase in the equivalent cost of U_3O_8 and an 8.4% increase in the cost of electricity.

Figure ii.I-7 illustrates changes in the equivalent cost of U_3O_8 when the fusion power is varied (for fixed wall loading). The dramatic decrease in U_3O_8 cost which results from increasing the fusion power is expected since cost and recirculating power requirements associated with the end cells remain fixed regardless of the fusion power. Our studies clearly indicate a substantial benefit at fusion power levels above 3000 MW, but the power level was arbitrarily fixed at this level.

Figure ii.I-8 illustrates an optimization of the neutron wall loading for a fixed fusion power of 3000 MW. This result reflects a balance between higher plasma Q (resulting in reduced recirculating power and reduced heating system costs) at low wall loading and lower blanket, central-cell magnet, building, and BOP costs at high wall loading. Optimum performance is achieved at wall loadings between 1.5 and 1.8 MW/m^2.

In conclusion, our parametric results indicate that TMHR driven electricity system is quite robust in that most and/or performance uncertainties result in less than a 10% increase in the cost of system electricity.
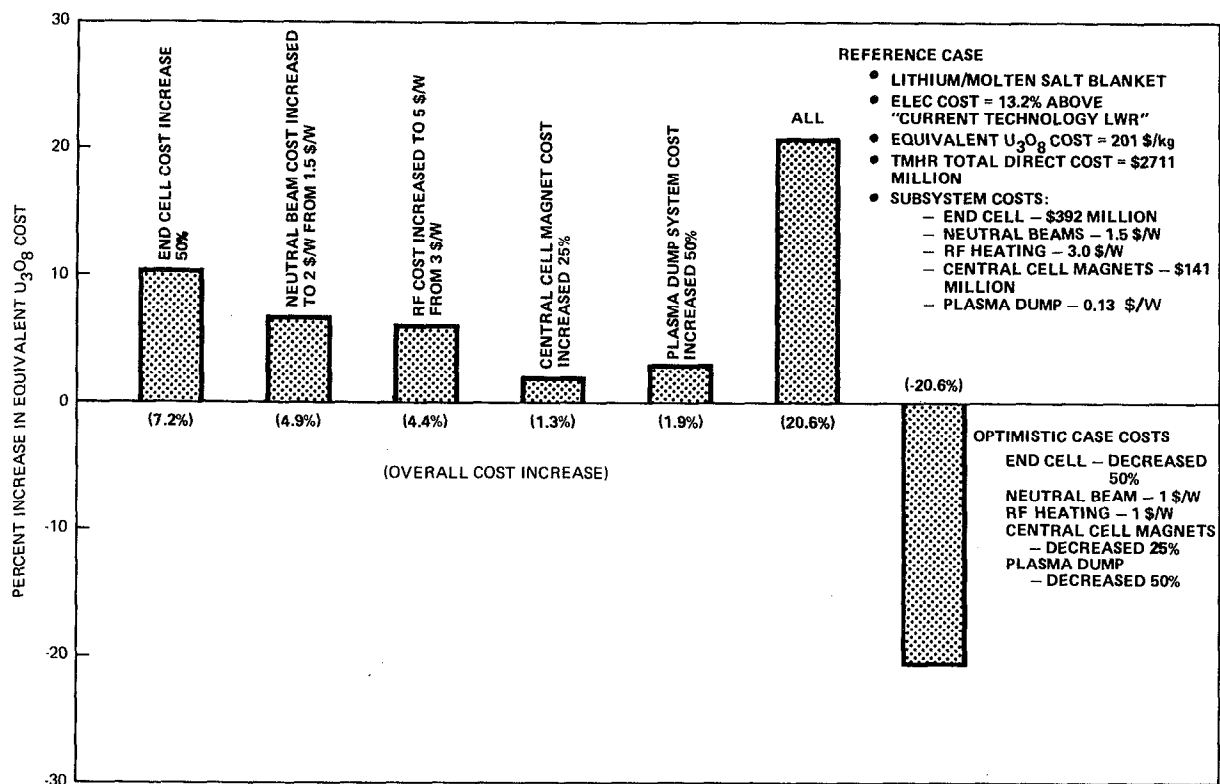
FIGURE ii.I-5. Equivalent U_3O_8 cost versus TMHR component cost uncertainty
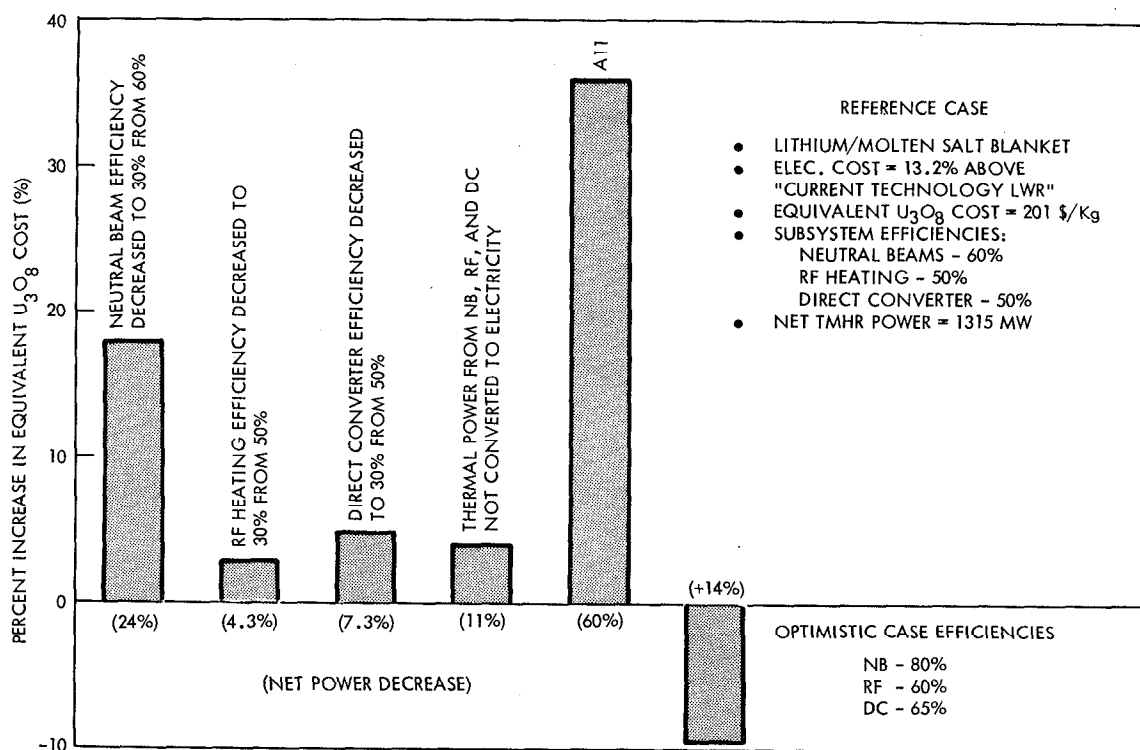
FIGURE ii.I-6. Equivalent U_3O_8 cost versus TMHR component performance uncertainty
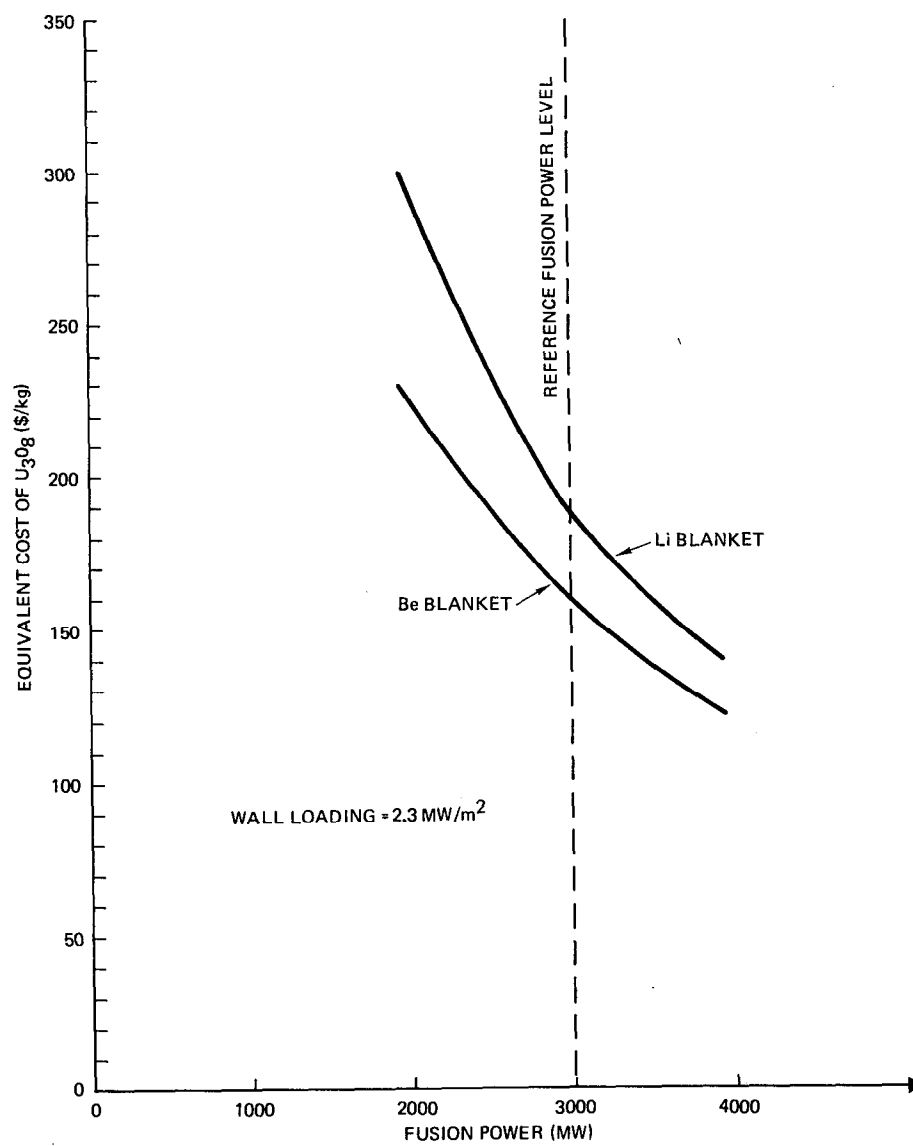
FIGURE ii.I-7. Year zero equivalent U_3O_8 cost as a function of fusion power.

PLASMA POWER INPUT

BARRIER FIELD, T	14	20
RF POWER, MW	180	50
NB POWER, MW	270	140
PLASMA GAIN, Q	6.7	15.8

3000 MW FUSION

Li, 14T

Be, 14T

Li, 20T

Be, 20T

REFERENCE WALL LOADING

EQUIVALENT COST OF U_3O_8 ($/Kg)

NEUTRON WALL LOADING (MW/m^2)
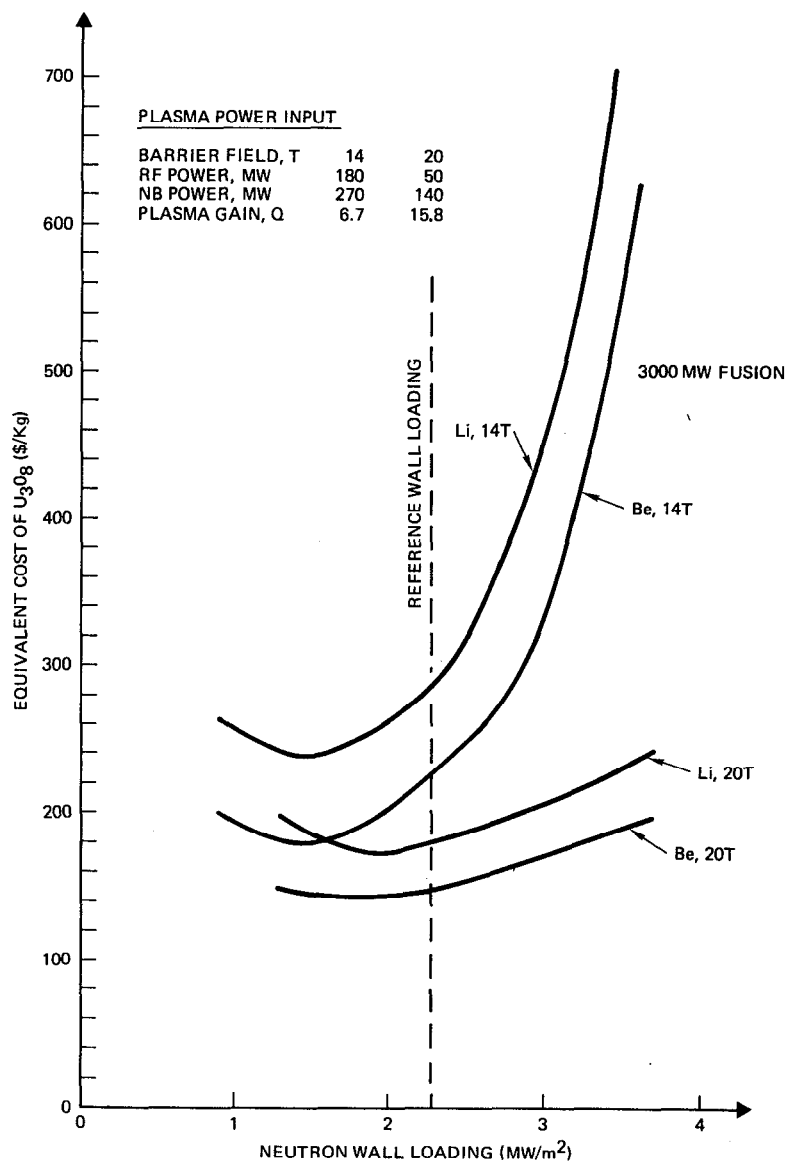
FIGURE ii.I-8. Comparison of equivalent U_3O_8 cost versus wall loading for different maximum magnetic field strengths and blanket designs.

ii-I-13

In the 2030 timeframe, our relatively inexpensive gasd, oil and conventional U_3O_8 resources will, most likely, be exhausted. Considering the remaining fossil resources which appear to be able to supply a substantial fraction of electrical energy in this timeframe (i.e., coal, shale oil), our ability to provide sufficient electrical generation capacity could be limited by allowable CO_2 concentrations, mining restrictions, or other concerns. It is therefore prudent to ask whether nuclear power (of all varieties) can provide a major fraction (50%) of the U.S. electrical demand by the middle of the next century.

In this section we consider deployment questions involving a suppressed fission blanket TMHR which produces enough fissile fuel to supply the makeup requirements of the 17 LWRs of equivalent nuclear power. A confirmation of the commercial feasibility of the TMHR option, before conventional U_3O_8 resources for new LWRs begin to become scarce, could accelerate LWR deployment by removing the current requirement to secure U_3O_8 resources for new plants for their entire 30 year operating lifetimes prior to commitment to plant construction and thus provide a means to economically preserve the LWR option. A more detailed presentation of the deployment analysis (including parametric variations) is provided in Chapter X of the report.

To quantify the potential energy impact of the fusion fuel factor, we must project the U.S. electrical demand into the next century and make some assumptions about fission reactor deployment and uranium resources. The electrical demand projection shown in Fig. ii.J-1 follows EPRI's intermediate growth projection through 2020 and then a lower growth rate of 1.5%/year thereafter. The EPRI intermediate forecast assumes that electrical generation requirements will increase from 540 GWe in 1980 at the rate of 4.4%/year to 2000 and 2.8%/year from 2000 to 2020. The EPRI projections assume that electrical energy will continue to account for a larger fraction of the total energy--increasing from 32% in 1978 to 48% in 2000 and 57% in 2020.

---

*This work results from an independent IR&D project performed at TRW, but is included in the TMHR report due to its applicability and general interest.
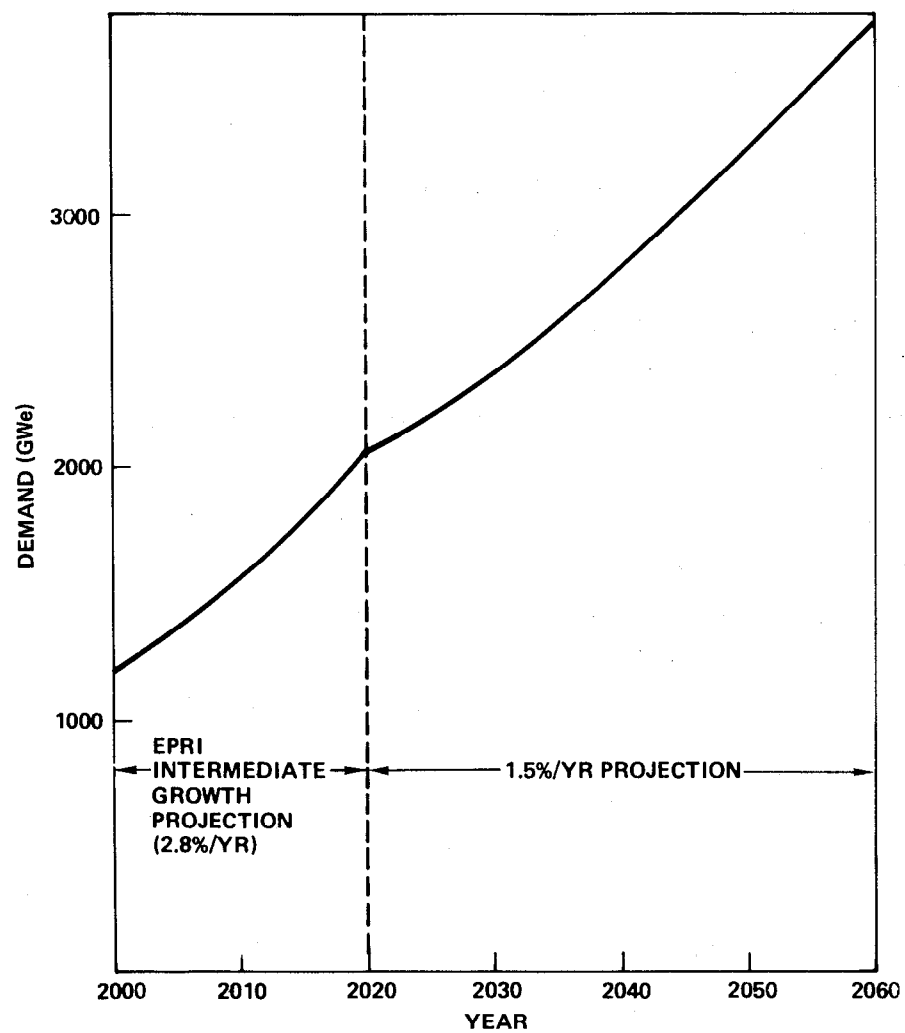
FIGURE ii-J-1. Electrical demand (year 2000 to 2060)

The guidelines and assumptions used to project nuclear energy growth in the first half of the next century from a base of 250 GWe LWR capacity in 2000 are presented in Table X.C-1 of Chapter X. Three nuclear technology options are considered in an attempt to define the combinations of conventional and advanced reactors that can satisfy the above generation goals: Case 1--LWR only: Case 2--LWR and LMFBR (int oduced in 2005); and Case 3--LWR and TMHR (introduced in 2015). In this analysis, it is assumed that the LWRs burn up to 3.0 million metric tons of U_3O_8. This is at the high end of estimates of economically recoverable reserves of U_3O_3 in the U.S. which range from 1.8 to 3.5 million tons. It is also assumed that all of the LWR generated plutonium is recovered and stockpiled for use in LMFBRs which are deployed at a high rate of growth (i.e., up to 25%/yr).

The results of this deployment analysis for Cases 1 and 2 are presented in Fig. ii.J-2. As shown by the dashed curve, after 2000 the LWR alone can increase capacity such that in 2034, LWRs supply about 33% of the total electrical demand. However, after 2034, the $3 \cdot 10^6$ MT U_3O_8 resource is entirely committed, new LWR plants are not built, and the nuclear capacity decreases rapidly as plants built in the post-2005 timeframe are retired. By 2050, nuclear power supplies only about 17% of the electrical demand.

The situation is somewhat improved for Case 2 with the addition of the LMFBR, which begins to make a significant contribution to electricity generation in the same timeframe as the LWR contribution decreases due to U_3O_8 limits. Nevertheless, due to the rapid LWR retirement during the period 2030-2040, the total nuclear capacity remains at, or slightly below, 30% of the total electrical demand. In 2040, the nuclear fraction quickly increases again, but in 2050 the nuclear fraction is only 36.5% of the electrical demand--or 73% of the 50% goal.

The deployment of LWRs and TMHR fusion breeders (Case 3) is shown in Fig. ii.J-3. The fraction of electricity generated by nuclear power increases in every year through 2050 when the 50% goal is achieved, but this system is not excessively stressed with respect to either the amount of U_3O_8 resources consumed or the number of fusion fuel factories required. In total, $2.2 \cdot 10^6$ MT of the $3.0 \cdot 10^6$ MT U_3O_8 limit are consumed by LWRs. The total required TMHR capacity through 2050 is 81 plants and, in 2050, LWRs provide 1508 GWe of electricity (nuclear support ratio = 15).
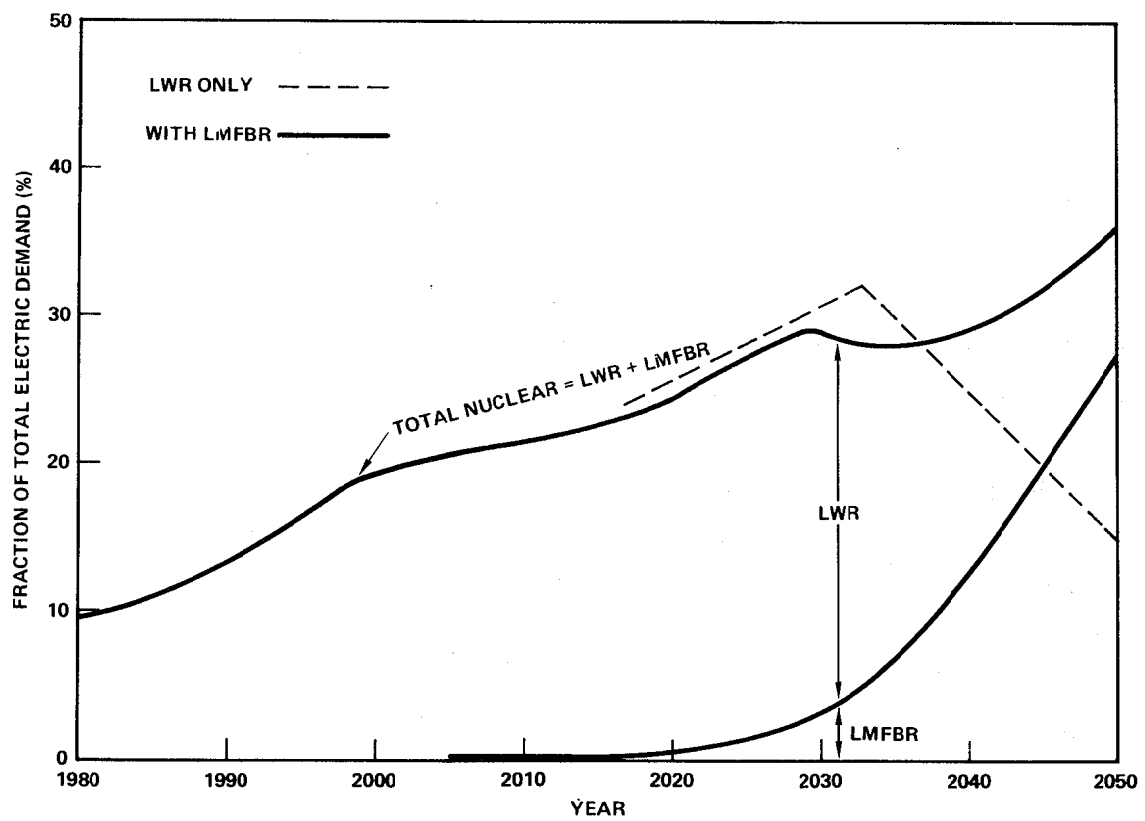
FIGURE ii.J-2. Deployment cases 1 (LWR only) and 2 (LWR and LMFBR).
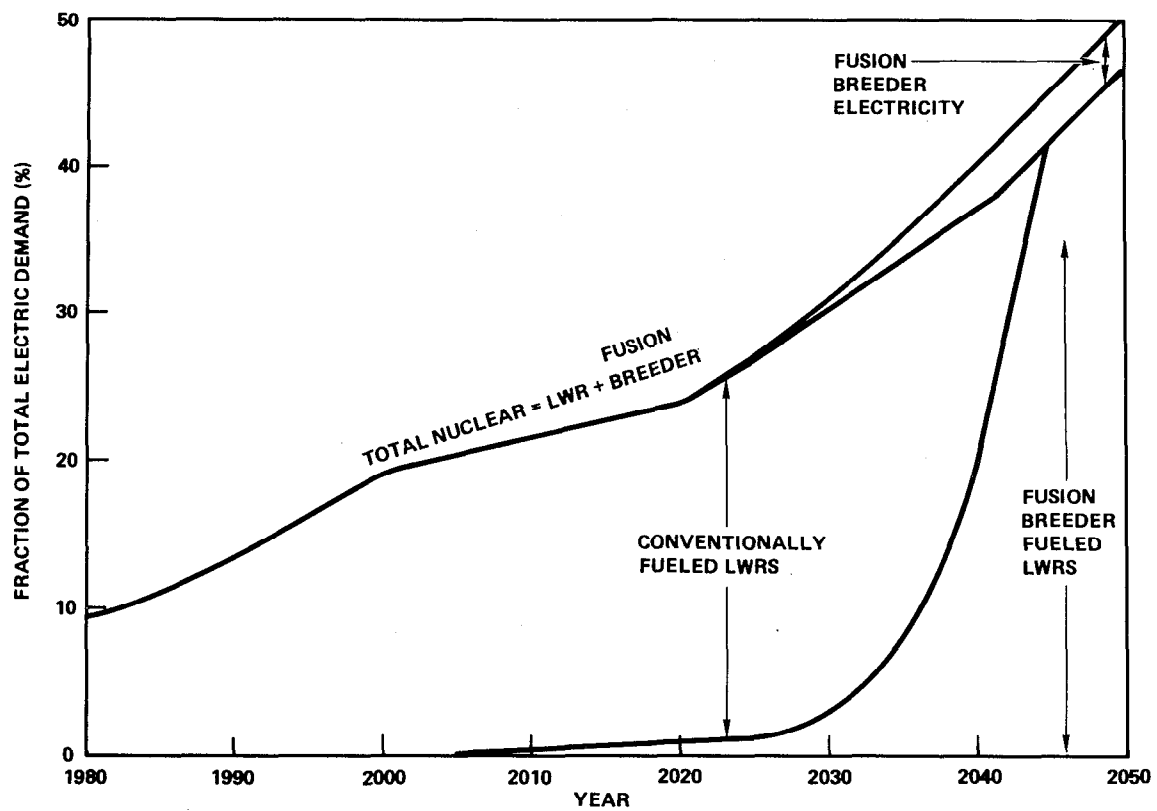
FIGURE ii.J-3. Deployment case 3 (LWR and fusion breeder).

A fourth case, the deployment of LWRs, LMFBRs, and TMHRs was also considered. This combination also satisfies the 50% goal in 2050 without a decrease in the total nuclear fraction during any two successive years, but slightly more U_3O_8 is required ($2.5 \cdot 10^6$ vs. $2.2 \cdot 10^6$ MT) because plutonium is not recycled in the LWRs, but stockpiled for future LMFBR inventories. The LWRs dominate electricity generation until 2046 and, the number of fusion fuel factories required through 2050 is only 40. If the fissile fuel production capabilities of the TMHR were reduced, the number of required facilities would increase correspondingly but the above generation goals can still be satisfied.

Additional parametric studies indicate that the TMHR driven electricity generation system can meet ambitious generation goals under even more difficult conditions. Specifically, the 50% nuclear electricity goal can be met in 2050 if U_3O_8 resources decrease from $3.0 \cdot 10^6$ MT to $2.0 \cdot 10^6$ MT. Also, a 50% nuclear electricity goal for the TMHR/LWR system as early as 2030 appears to be possible.

ii.K   TMHR REFERENCE BLANKET DESIGN ISSUES

In this section an overview of design issues associated with future
development of the reference lithium/molten salt (Li/MS) and beryllium/thorium
oxide (Be/ThO$_2$) blankets is presented. Both concepts appear to be worthy of
future consideration.

Lithium/Molten Salt Blanket Design Issues

The molten-salt blanket design described in Section ii.D and Chapter IV
of the report is much like a liquid lithium blanket for a fusion electric
plant, but features the addition of a molten-salt zone for fissile breeding.
It combines the economic advantage of on-line molten-salt reprocessing
technology with the mechanical design, thermal hydraulic, and neutronic
advantages of liquid lithium. Two novel features, the active maintenance of a
protective frozen salt layer and a design concept for electrically insulated
pipes for liquid lithium, enable the blanket to be fabricated from modified
316 stainless steel and to operate at relatively low pressure with minimal
internal piping. The molten-salt blanket also preserves the perceived safety,
reliability, fissile inventory, and developmental advantages of low power
density suppressed fission blanket design.

During the course of the FY81 TMHR design study, several design issues
have been explored in some detail, but others will require further resolution.
First is the issue of liquid lithium. The development of electrically
insulated pipes could result in lower MHD pressure drops than have been
assumed in our mechanical design. Several concepts which offer wide
flexibility in design and appear to be suited to immediate development are
proposed. The issue of electrically insulated piping is also of importance
for fusion electric blankets which utilize a flowing lithium or lead-lithium
coolant. Concerning liquid lithium safety issues (more detailed discussion in
Section ii.G and Chapter VI of the report), the lithium and salt are not
mutually reactive and many of the same protection systems proposed for the
LMFBR (e.g., cover gas, steel liners for concrete) are applicable to this
system. Dump tanks and semi-passive freeze valves for both the liquid lithium
and molten-salt coolants are provided.

Two global issues relating to the molten-salt features of this blanket are of interest. The first relates to the state-of-the-art for molten-salt fuel processing and energy conversion technologies. The required fuel processing technology is expected to be less demanding than that required for the Molten Salt Breeder Reactor (see Section ii.F and Chapter VII of the report), but a technology development program is required. The second issue relates to the selection of structural materials that are compatible with the molten salt. The frozen salt protection concept is promising, but is difficult to model analytically. Although the scoping studies provide favorable indications, an experimental determination will be required. The mechanical properties of Hastelloy in a fusion environment require further study.

In comparison with blankets utilizing a beryllium multiplier, the lithium multiplier blanket produces about 65% as much ^{233}U per fusion. This disadvantage is somewhat compensated by low cost fuel reprocessing, but several ideas for incorporating beryllium multipliers have been proposed. A preliminary design concept featuring a one zone packed bed of thorium and beryllium pebbles is presented in Appendix A. A more conventional two zone design replacing the molten-salt zone with a packed bed of thorium balls is also presented in Appendix A. It is believed that the liquid metal cooled blanket concept for the TMHR represents an acceptably low development risk because most design issues allow several possible design solutions within the same overall design framework.

Beryllium/Thorium Oxide Blanket Design Issues

The helium cooled beryllium/thorium oxide blanket design described in Section ii.E and Chapter V of the report has several attractive design and performance characteristics. The reference design results in an efficient capability for fissile fuel production as well as an excellent potential for reactor safety. For this design, excellent breeding performance results from both the use of beryllium as a neutron multiplier as well as a novel design configuration. In particular, the pressure tube blanket concept results in a low structural volume fraction and the fertile dilute lead-lithium/ThO$_2$ suspension permits adequate fissile breeding, but effectively limits fissioning in the blanket. Attractive reactor safety characteristics result because of the use of non-reactive materials(e.g., helium coolant and

lead-lithium eutectic) and because the blanket melting does not occur from decay afterheat under postulated accident scenarios.

During the course of the design study, several design issues have been explored in some detail, but others will require further resolution in future studies, and/or development programs. These are briefly described below.

The first set of issues requiring further resolution relates to the behavior of un-stressed beryllium blocks upon irradiation (see Section V.C of the report). In particular the physical integrity of the blocks, considering an accumulation of 10% or more swelling (by volume), must be confirmed. These blocks will also be subject to a substantial temperature gradient as well as some temporal cycling due to power level adjustments, start-up, and shutdown (similar to that occuring in LWR fuel rods). The solution to this problem will require an experimental program.

A second set of issues concerns design solutions to accommodate the failure of one or more high pressure coolant tubes. Two issues are involved. First, due to the large number of coolant tubes ($\sim 800/m^2$) small leaks are expected (in analogy to the small fraction of coolant tubes in a steam generator whicxh are expected to leak at any given time). There is a reasonable level of confidence that such leaks can be accommodated routinely, without having to shut the system down, by providing a purge relief mechanism at the back of the blanket.

A second concern involves a gross failure of a coolant pipe near the first wall which could result in a sudden over-pressurization of a local area of the blanket module followed by a rupture of the module. This situation is a particular concern since the module itself is designed for low pressure operation, the lead-lithium eutectic is a heavy and incompressable fluid, and the flow area in the neighborhood of the first wall is constricted by the corrugated wall and the beryllium blocks. It seems possible to remedy this situation via the use of simple burst tubes however, the number and location of such tubes and the actual behavior of the tubes (i.e., they might fill with lead-lithium before helium) requires further study and, possibly, an experimental program.

A third set of issues concerns the lead-lithium/ThO_2 suspension. In particular, the suspension requires a balance in the densities of the lead-lithium and the ThO_2. This balance must exist under the conditions of accumulated neutron fluence, different temperature regimes in different parts of the blanket, temporal cycling, and limited convective flow. Another issue

concerning the suspension is related to chemical compatibility issues (see Section V.C of the report) which require resolution.

A fourth set of issues concerns heat transfer in the blanket. The predicted first-wall temperature of 600°C is acceptable but a multi-dimensional thermal analysis is required to better predict these temperatures. As a result, design modification might be needed to be reduced to limit the first-wall temperature.

A fifth set of issues concerns fuel reprocessing for this design. Most importantly, as discussed in Section ii.F and Chapter VII of the report, an inexpensive ($200/kg thorium) thorex reprocessing technology for low burn-up (100 MWD/MT), high surface/volume ratio, un-clad ThO_2 particle fuels must be identified. A key question relating to the economics of such a process is the ability to adequately dissolve ThO_2 with minimal additional fluorine--a highly corrosive agent.

Two secondary reprocessing issues are also of importance. The first concerns tritium bred in the lead-lithium eutectic that reacts with the thorium oxide or otherwise becomes entrapped within thorium oxide fuel that is to be reprocessed. The magnitude of this transfer and its effect upon the reprocessing plant require additional study. Finally, separation of ThO_2 particles from the lead-lithium carrier fluid prior to reprocessing requires study to determine if this step would adversely impact overll economics.

In conclusion, both the lithium/molten-salt blanket and the gas-cooled beryllium/thorium oxide blanket feature attractive performance and safety characteristics but several technological issues must be explored in greater depth before the attainment of this level of performance is assured in a feasible design.

ii.L   OVERVIEW OF APPENDICES

    This section provides a brief overview of the contents of the appendices
of the FY81 TMHR design study report. The reader is referred to appendices A,
B and C in the body of the report.

Appendix A

    Appendix A, "Alternative Liquid Metal Cooled Blanket Options" provides a
summary of liquid metal cooled blankets considered during the initial scoping
phase of the study as well as a second generation liquid metal cooled design
developed for further study during FY82. The later design shown in
Fig. ii.L-1, features a one zone randomly packed bed containing a mixture of
beryllium and fertile pebbles (thorium or uranium) and a sodium heat transfer
medium. The bed in the figure is cooled by axially directed tubes containing
a lithium breeder/coolant. Several possible variations on this general design
theme are possible including beds with and without cooling tubes (i.e., for a
packed bed blanket without cooling tubes, the sodium would be replaced by
lithium which would be pumped directly through the bed). In addition, at
least one other coolant tube arrangement has also been proposed and lithium
lead could be substituted for lithium.

    This packed bed design is a preliminary attempt to combine the attractive
features of beryllium neutron multiplication with the design simplicity
associated with liquid metal coolant. (The one zone blanket configuration is
similar to the breeding zone of an earlier packed bed design also discussed in
Appendix A). On a volumetric basis, the breeding zone consists of the
following materials: 15% lithium coolant, 4.4% steel structure, 45% beryllium
pebbles, 3.4% thorium pebbles (or, alternatively uranium oxide pebbles), 32.2%
sodium heat transfer fluid. The beryllium and thorium pebbles would be
randomly mixed in the bed and the pebble diameter (for either type) would be
less than 1/8 of the minimum clearance between tubes in the blanket (4 cm).
As such, the design has been calculated to achieve the following F.M.T.
performance with thorium fuel: F = 0.75, M = 1.52, T = 1.05. Fuel management
for this design would be a batch process performed on-line by backfilling the
temporarily null blanket module with sodium alone.

    In this concept, beryllium swelling and refabrication are less of a
concern because the beryllium spheres do not swell appreciably during the 3

MAGNET

MAGNET SHIELD

LITHIUM
INLET
PIPING

Be/Na/FUEL INLET

LITHIUM
OUTLET
PLENUM

MAGNET AND
SHIELD

LITHIUM
INLET
PIPING

LITHIU
OUTLE
PIPING

Be BALLS,
FUEL BALLS,
Na CONTACT
COOLANT

CORRUGATED
FIRST WALL

FIRST WALL
COOLANT
CHANNEL

FIRST WALL
SUPPORT
STRINGER

LITHIUM COOLING
TUBES

REFLECTOR

Be/Na/FUEL OUTLET

LITHIUM INLET PLENUM
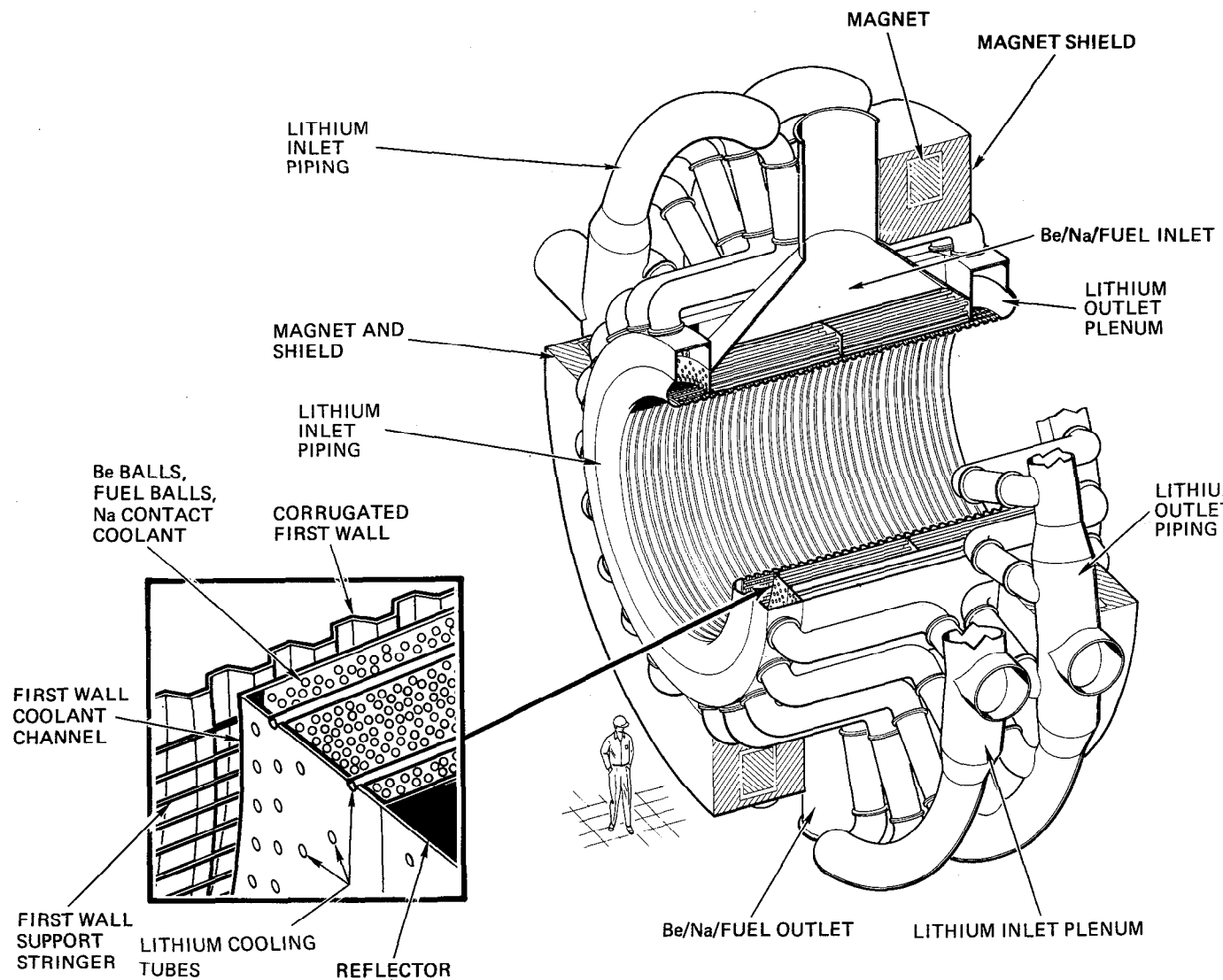
FIGURE ii.L-1. Packed bed blanket with beryllium multiplier.

month exposure time. Also, it is possible to allow the pebbles to readjust to any swelling semi-continuously by removing some pebbles from the bottom and adding pebbles to the top. The beryllium pebbles can, therefore, swell significantly over several cycles. Their lifetime is limited only by possibly losses in their physical integrity. These pebbles require no high tolerance machining and can, most likely, be refabricated using press sintering technology.

This design concept benefits due to the thermal characteristics of the Li coolant and Na heat transfer medium. Nevertheless, the reactive liquid metals cause some concern. To address this concern, a semi-passive dump tank system can be incorporated into the plant design philosophy (in addition to multiple barriers, inert cover gasses, etc.) and other safety systems can be adapted from the LMFBR program.

The potential benefits of this new design concept are excellent neutrons in a low risk mechanical design that offers conventional technologies.

Appendix B

Appendix B, "Alternative Gas-Cooled Blanket Options" provides a summary of gas cooled blankets considered during the initial scoping phase with detailed emphasis on neutronics issues associated with the use of beryllium as a neutron multiplier. A novel blanket concept, the fertile-in-tubes design, is described. The latter concept is, in many respects, similar to the reference beryllium/thorium oxide blanket, but rather than distributing the ThO_2 in suspension throughout the blanket, the fertile fuel is in the form of spheres which are carried in tubes. Mechanical and thermal issues associated with this configuration are described in the appendix.

Appendix C

Appendix C, "Beryllium/Molten-Salt Blanket Option," describes a second generation design for a molten-salt cooled blanket with beryllium pebbles for neutron multiplication. The design employs a frozen salt layer for protection of a steel blanket structure with the molten-salt coolant circulated radially between the beryllium pebbles. The back of the blanket is fabricated from Hastelloy.

The beryllium/molten-salt blanket is an advanced option which can provide excellent fissile breeding (0.8 fissile atoms per source neutron) with low cost fissile recovery (4 $/gm). However, several technology development issues (including a method to protect the beryllium pebbles from salt corrosion) are outstanding. This design will be pursued at a low level during FY82.

ii.M CONCLUSIONS

The tandem mirror magnetic confinement approach to fusion is a good candidate for a fissile material producer because its linear geometry and steady-state operation make it especially attractive. The power balance of the tandem mirror is good because of the thermal barrier mode of operation results in high Q (15), even higher than is required for economically competitive fissile fuel. The Tandem Mirror Research and Development Program is aiming to demonstrate the technology in two to three decades. This is the time frame for which a uranium shortfall is predicted, and a new source of fissile material may be required to sustain a vigorous growth of nuclear power.

If fusion neutrons are to produce this new source of fissile material, blankets and fuel cycles unique to the fusion breeder must be developed. To this end the main effort in this study was the conceptual design of blankets and fuel reprocessing. We emphasize the fission-suppressed type because previous studies show strong safety and deployment advantages over fissioning-blanket-type having similar economies. The objective was to develop design concepts that are technologically less demanding than the FY79 beryllium/molten salt (Be/MS) design. Two referenced blanket designs resulted from this FY81 study: the Li/molten salt (MS) and the helium-cooled Be/LiPb+ThO$_2$ designs, both turned out less demanding than the FY79 design. Both design concepts have attractive performance and safety characteristics, but several design and technological questions must be answered before their feasibility can be assured. Design improvements can also be made. For example, the Li/MS suffers economically because of its large molten-salt (MS) inventory, which in turn results in relatively large fissile-product inventories and Th-228 and U-232 concentration. The MS inventory can likely be reduced 5 to 10 times by adding graphite to and thinning the MS zone.

It should be stressed that development of the fission-suppressed blanket concept is in an early and evolutionary phase and more study is needed before the optimum design is obtained.

Our plan for FY82 is to concentrate on a more detailed conceptual design on a liquid metal-cooled (Be) blanket whose technology base is largely from the LMFBR program. This design we call "low technology" and is shown in Fig. ii L-1.

We also plan to spend a smaller effort on a search for ways in which beryllium and molten salt can be mutually compatible. The Be/MS blanket concept is our leading contender for a high performance, "high technology" blanket.

After more study of both the low technology and high technology based blanket concepts, we should lay out development programs and do a cost/benefit analysis to determine if the higher performance, high technology option is worth persuing. Based on the favorable outcome of the study of fission-suppressed fusion breeders in FY81, we are beginning an experimental program to check features common to these designs such as integral neutronic experiments, corrosion/compatibility experiments, and beryllium fabrication experiments and pebble transport experiments.

CHAPTER I

INTRODUCTION

The Tandem-Mirror Hybrid-Reactor (TMHR) Study was performed during FY81 with the intent of developing one or more fission-suppressed reactor blanket concepts for the production of fissile fuel to be used in conventional fission power reactors (e.g., LWR). In this report we discuss our results relating to the design and analysis of two such blankets.

When combined with conventional fission reactors TMHR represents an independent and inexhaustible energy generation technology which could be economically deployed during the first decades of the next century to satisfy future demand requirements and meet projected shortfalls.

For the purpose of clarification, several generic terms require early definition. To begin, the terms "fusion breeder," "fusion-fission hybrid," "hybrid," and TMHR are equivalent unless otherwise stated. The term "blanket" refers to the region surrounding the fusion plasma in which neutrons interact to produce fissile fuel and heat. In particular, 14.1 MeV fusion neutrons are produced in the D-T fusion reaction:

$$D + T \rightarrow n(14.1 \text{ MeV}) + \alpha(3.5 \text{ MeV}).$$

These energetic fusion neutrons interact in the blanket by multiplication reactions [e.g., ^{6}Li(n, n'T) or Be(n, 2n)] and, to some extent, fission. Some neutrons are ultimately absorbed to produce tritium from lithium,

$$n + {}^6\text{Li} \rightarrow T + \alpha(4.8 \text{ MeV}),$$
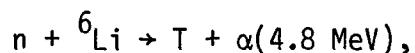
and fissile fuel from thorium,

$$n + {}^{232}\text{Th} \rightarrow {}^{233}\text{Th} \xrightarrow[23n]{\overline{B}} {}^{233}\text{Pa} \xrightarrow[27d]{\overline{B}} {}^{233}\text{U}$$
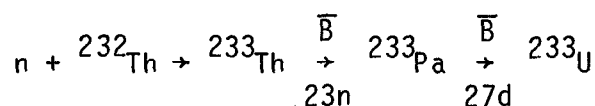
Plutonium can be produced by substituting ^{238}U for ^{232}Th above and the amount of power generation per unit of fissile fuel product can be varied by design.

The fission-suppressed blanket uses non-fission reactions [mainly (n,2n) or (n,n'T)] to generate excess neutrons for the production of net fuel, in contrast to the fast fission class of blankets which use (n,fiss) reactions to generate excess neutrons. Fusion reactors with fast fission blankets combine fusion and fission in the same device and emphasize power as well as fuel production. Those with fission-suppressed blankets produce less power per unit of fuel production and, consequently, support a larger number of LWRs. The latter type is expected to result in improved safety and institutional characteristics because its principle product is fissile fuel, like the current mining and fissile enrichment plants.

II-A. Fusion Breeder Motivation

The motivation for the fusion breeder is basically the same as the fission breeder--to tap the enormous energy potential of the world's abundant U-238 and Th-232 resources in a safe and economically competitive way. There are important differences that make the fusion breeder concept uniquely attractive. For example:

● The fusion breeder requires no fissile inventory and the doubling time for the fusile inventory (T) is measured in weeks, not years.

● The fusion breeder can produce many times (up to $\sim$ 30) more net fissile product per unit of energy.*

● Power densities are 10 to 100 times less.

_____

*Typically for suppressed fission:

$$\frac{BR-1}{E_{fusion}} \div \frac{BR-1}{E_{fission}} = \frac{1.8-1}{27} \div \frac{1.2-1}{200} = 30$$

- The fusion breeder adds flexibility to the long-term fission energy option. All sorts of fission reactors can be considered (not just fast breeders) by virtue of an inexhaustible source of fissile material from fusion breeders. For example, an attractive route to high-temperature, gas-cooled reactor (HTGR) synfuel production can be easily defined.

- The fuel production and energy production roles are performed in separate devices.

Another motivation for the fusion breeder is the potential for an early competitive application of fusion that in turn would advance fusion technology towards its goal of a stand-alone energy source. For example, consider a future scenario in which the following conditions exist:

- One or more fusion-driver concepts have had successful engineering demonstrations, but pure fusion electricity costs are expected to be in the range of 2 x LWR electricity costs.

- LWR capacity has expanded, but available uranium reserves are committed. Reprocessing, recycle, permanent waste disposal, and advanced isotope separation have already been commercially introduced.

- The fission fast breeder (LMFBR) has been developed but not yet commercially deployed, because it could not compete with the LWR.

- The energy cost ranking, in ascending order, of the major options for additional and replacement capacity is: conventional LWRs fueled by fusion breeders, LMFBRs, coal, and fusion.

With this scenario, economic considerations would suggest that LWRs plus fusion breeder reactors should be deployed. If fusion breeder specific technology were not developed, the fission breeder and/or coal would be the logical choice and then fusion would not benefit from early deployment. Also, the economic and environmental costs for power would be higher.

The above scenario, while only an example, does point to several conditions that must exist for fusion breeder deployment:

1. The fusion physics program must succeed and an engineering demonstration of fusion must be carried out.

2. Fission, with reprocessing, recycle, and waste disposal, must be commercially deployed.

3. Fusion breeder specific technology (blankets and fuel cycles) must be developed and demonstrated.

If such conditions existed, the fusion breeder could quickly become an important element in the energy system. This is possible because the first fusion breeder could support the makeup fuel needs of 10 or more fission reactors of similar nuclear power. The potential impact is magnified further, because a demonstration of fusion-breeder technology provides an assurance that new LWRs can be fueled throughout their 30-year operating lifetimes. In addition to quick introduction, another advantage of high support ratios is that the fusion-fission electricity generation cost is quite insensitive to performance and cost uncertainties of the fusion breeder.

The timely development of the fusion breeder could be considered an insurance policy to protect against a uranium resource shortfall, uranium cartels, or environmental limitations on coal usage. Preliminary economic analysis suggests the fusion breeder could be competitive with mined uranium when U_3O_8 reaches about 100$/lb, about twice the cost that uranium reached during the 1970s. The mere existence of a demonstrated fusion breeder technology might put a cap of about 100$/lb on uranium prices.

Considering the development of such a device, scientific feasibility (Q_p = 1) should be achieved in the early 1980s. Engineering feasibility (Q_p = 3 to 5) is predicted to be achievable in the early to mid 1990s with all components necessary to make net electrical power demonstrated. A successful demonstration of fusion coupled with development of fusion breeder specific technology would then allow a fusion breeder demonstration in the year 2000 to 2010 time frame. This is fortunate because this is about the time when a uranium shortfall could begin to curtail commitment to further conventional nuclear construction.

We believe that the fusion breeder can play an important role in our energy future and that its economic benefits will far outweigh its overall additional development cost relative to the main line magnetic fusion development program.

II-B. Historical Background

The idea of marrying fusion and fission was first considered at Livermore by Imhoff[1] in the early 1950s at the beginning of the fusion program. But the idea was not pursued because large uranium deposits were discovered and fusion was found to be far more difficult to achieve than first perceived. In the early 1960s Weale[2] performed integral experiments with a natural uranium pile and a DT neutron source and measured nuclear reaction rates of 14 MeV neutrons in uranium. In the late 1960s Lidsky at MIT did some studies on fusion-fission and presented the concept of fusion-fission "symbiosis."[3].

At about the same time Lee at Livermore started looking at fusion neutron-induced fission of U-238 as a way to improve the power balance of low Q fusion systems.[4] This work culminated with Livermore collaborating with General Atomic in the conceptual design of a "standard mirror" hybrid reactor.[5] This reactor used a minimum |B| mirror fusion neutron source with a fast fission U-238 blanket. The fusion reactor operated at 400 MW fusion, resulting in a blanket power of 3400 MW. Net output from this reactor was 600 MWe and 2000 kg Pu-239 per year (at a capacity factor of 0.74).

At this point in Livermore's fusion-fission program, emphasis switched from standard mirrors to higher performance tandem mirror fusion reactors[6] and we also began investigating the fission-suppressed class of fissile-breeding blankets.[7,8] In FY79 Livermore, Bechtel, General Atomic, and General Electric worked together on a conceptual design study of tandem mirror hybrids. This was the first year of a proposed, two-year study. The first year of this study had two principal purposes. One was to examine the applicability of a low technology (Q ∿ 2) tandem mirror as the driver for fusion-fission; the second was to develop and compare conceptual designs of U-233-producing blankets. The result was two conceptual designs, one based on fast fission of thorium, the other on the fission suppression concept.[9]

Conclusions reached were that the tandem mirror should make a good driver and that both blanket types resulted in attractive and similar economics but had grossly different operating characteristics and feasibility issues. The fission-suppressed blanket case produced 3 times more fissile fuel (U-233) per unit of nuclear power and its peak fission power density and fission product after-heat was $\sim$ 100 times less for a given fusion neutron current. The high specific fissile production, low fission power density, and low fission product inventory made the fission-suppressed blanket the preferred device.

While the performance of fission-suppressed blankets is attractive, feasible designs remained to be worked out. The specific blanket concept examined in the 1979 study used beryllium for neutron multiplication, and a molten salt ($LiF-BeF_2-ThF_4$) as a mobile fuel and heat transfer fluid (hence designated Be/MS) from which the U-233 (as well as T) could be removed economically at low concentrations. The feasibility issues of concern are how to protect the Be from the molten salt, how to deal with Be swelling, and what structural material(s) to use to contain the salt. The structural material must also stand up to the fusion neutron environment and not overly reduce breeding. In this design graphite was used to contain Be powder and TZM was chosen for the structure. Graphite is known to be compatible with MS but its radiation resistance is of concern. TZM is known to be compatible with MS and is expected to be reasonably resistant to radiation damage, but there are feasbility issues with TZM fabrication.

Performance parameters from our FY79 study of fusion-fission systems employing fast fission and fission-suppressed thorium blankets are summarized and compared in Table I-1. Another concern is molten-salt reprocessing technology. It is thought to be feasible but a development effort will be required for commercialization. The tandem mirror reactors and the fission-suppressed blanket were also found to compare favorably to other drivers and blanket types in an EPRI-sponsored feasibility assessment of fusion-fission.[10]

The history described above is intended to summarize how the Livermore fusion-fission concept evolved up to the start of this (FY81) study. For a more general review of fusion-fission, Ref. 11 is recommended.

Table I-1. Tandem mirror fusion-fission system parameters from FY79 study.

Blanket type	Thorium fast fission	Fission suppressed (base)	Fission suppressed (improved)
Blanket parameters			
Fissile breeding ratio	0.83	0.62	0.81
M (ave)	5.2	1.43	1.58
Hybrid nuclear power level, peak (MW)	4000	4000	4000
Driver parameters			
Fusion power (MW)	813	2976	2733
Wall loading (MW/m^2)	1.5	2.0	2.0
Wall radius (m)	2.0	2.1	2.1
Central-cell length (m)	35	90	82
Plasma Q	2.0	2.2	2.2
Fissile production rate, hybrid (kg/y)	2915	8023	9554
Electric power (MW)			
Hybrid net	892	270	362
LWRs (supported by hybrid)	9,634	26,510	31,194
Power support ratio (P_{LWR}/P_{HYB})			
Nuclear	8.5	20.7	24.6
Electric	10.8	98	87.0
Hybrid direct cost (M$)	1993	4585	4126
System direct cost ratio ($/kWe system/$/kWe-burner)	1.23	1.28	1.20
Hybrid fissile cost ($/g)			
Capital	97.1	81.1	61.3
Fuel cycle	14.6	(included in cap. cost)	
Blanket replacement	6.0	3.5	1.4
O&M	8.0	3.3	2.8
Power	-55.1	-6.2	-6.645
Total	70.6	81.7	58.9
LWR electricity cost (mills/kWh)			
Capital	9.9	9.9	9.9
O&M	2.5	2.5	2.5
Fuel cycle (less fissile makeup)	4.1	4.1	4.1
Fissile makeup (from hybrid)	4.0	4.6	3.3
Total	20.5	21.1	19.8

Capital charge rate is 6.74% based on constant dollars; capacity factor is 75%.

II-C. Study Objectives for the FY 1981 Study

The attractive performance of the FY79 fission-suppressed case, tempered by its feasibility concerns, set the stage for our FY81 work described in this report. The principle objective of this work was to develop fission-suppressed blanket design concepts that performed about as well as the FY79 case but that did not have its feasibility and development concerns. A secondary objective was to look at higher performance tandem mirrors as drivers, since with the development of a new tandem concept (thermal barriers), higher performance could be achieved without pushing fusion technology to extremes.

REFERENCES

I-1 D. H. Imhoff, et al., "A Driven Thermonuclear Power Breeder," CR-6, California Research and Development Corporation (1954).

I-2 J. W. Weale, H. Goodfellow, M. H. McDaggart, and M. L. Mullender, J. Nucl. Energy A/B, 14, 91 (1961).

I-3 L. M. Lidsky, "Fission Fusion Symbiosis: General Considerations and a Specific Example," Proc. Br. Nucl. Energy Soc. Nucl. Fusion Reactor Conf. (Culham Lab. 1969), pp. 41-53, Culham Laboratory Report CLM-MFE 1969.

I-4 J. D. Lee, "Neutronics of Sub-Critical Fast Fission Blankets for D-T Fusion Reactors," Proc. 7th Intersociety Energy Conversion Engineering Conf., San Diego, CA, 1972, p. 1294, American Chemical Society (1972); see also UCRL-73952, Lawrence Livermore National Laboratory (1972).

I-5 D. J. Bender, Ed., "Reference Design for the Standard Mirror Hybrid Reactor," UCRL-52478, GA-A14796, a joint report by Lawrence Livermore National Laboratory and General Atomic Company (1978).

I-6 T. K. Fowler and B. G. Logan, "The Tandem Mirror Reactor," Comments on Plasma Physics and Controlled Fusion Research, 2, 167 (1977).

I-7 J. D. Lee, "The Beryllium/Molten Salt Blanket," Lawrence Livermore National Laboratory Report UCRL-82663 (1979); also published in Proceedings of the 3rd US/USSR Symposium on Fusion-Fission, Princeton, NJ (1979).

I-8 J. D. Lee and R. W. Moir, "Fission-Suppressed Blankets for Fissile Fuel Breeding Fusion Reactors," Journal of Fusion Energy, 1,3 (1981).

I-9 R. W. Moir, et al., "Tandem Mirror Hybrid Reactor Design Study Annual Report," Lawrence Livermore National Laboratory Report UCRL-18808 (1980).

I-10 D. L. Chapin, Ed., "Preliminary Feasibility Assessment of Fusion-Fission Hybrids, EPRI Project RP-1463, WFPS:TME-81-003 (1980).

I-11 J. A. Maniscalco, et al., "Recent Progress in Fusion-Fission Hybrid Reactor Design Studies," Nuclear Technology/Fusion, 1, 4 (1981).

CHAPTER II

PLASMA PHYSICS AND PLASMA ENGINEERING

Chapter II describes, in broad terms, the important physics and engineering issues related directly to the tandem mirror driver selected for this study. Since the thrust of the report is on blanket design, and the majority of the readers will not have a strong plasma physics background, the descriptions will be of a qualitative nature, with the number of equations kept to a minimum.

Section A gives a short review of the history of tandem mirrors, Section B discusses the operation of thermal barriers, the different end-plug configurations under study, and describes briefly the physics model used to generate the physics cases. Section C mentions some of the problems which need to be considered when starting up or shutting down a tandem mirror reactor. Section D describes the base case tandem driver, and examines the sensitivity of plasma gain, Q, and wall load, Γ, on changes in plasma physics operating modes and physics assumptions. Section E examines the possible ways of producing the halo plasma, controlling impurities, and removing α particle ash from the plasma. Section F looks at the various sources of heat load on the first wall, and assesses the importance of each. Section G reviews the recent progress in the experimental and theoretical tandem mirror plasma physics programs. Section H discusses the possible scenarios for a plasma disruption, and describes the results of such events. Section I presents results of an analysis which determines the amount of fusion power generated in the end cells of a tandem mirror. Finally, Section J addresses the question of what is the amount of magnetic field ripple tolerable in the central cell before it appreciably affects MHD interchange stability.

II.A. BACKGROUND OF TANDEM MIRROR PHYSICS

The tandem mirror concept was invented in 1976 simultaneously by Dimov in the USSR (II.A.1) and Fowler and Logan (II.A.2) in the U.S. It was invented because a single cell mirror, a "standard mirror", made a poor reactor for pure fusion (II.A.3), with the ratio of fusion power to injected power, Q, about unity. The simplest form of the tandem mirror consists of two average minimum-$|\underline{B}|$ mirror cells at the ends of an array of circular coils termed the "central cell". Figure II.A.1 shows a simplified drawing of a tandem mirror. The good curvature in the ends weighted with high pressure there gives MHD stability to global modes of the entire system. Stability of localized modes (ballooning) at high central-cell pressure are presently assumed to be stabilized by finite ion gyroradius effects. In a tandem configuration such as TMX, potential peaks are produced by intense neutral-beam injection in the end cells and in principle confine ions in the central cell for a time long compared to an ion-ion collision time. A description of the on-going and planned tandem mirror experiments will be discussed in section II.G.1. Because the power is being supplied to only the end cells, if the ratio of central cell to end cell volumes is large, the corresponding reactor Q is large. The upper bound on Q is set by the maximum reasonable fusion power output, or by the length of the central cell.

The reactor embodiment of the tandem mirror without thermal barriers (II.A.4) described above gave considerably better performance than the simple mirror reactor, but it needed 17 T yin-yang magnets and beam energies of 1.2 MeV, to obtain a Q value of about 5 at a reasonable net electric power of 1000 MW. The cost of electricity from this pure fusion machine was about 4 times that of LWR costs.

It was next discovered that some of the demanding beam technology could be relaxed by applying electron heating to the end cells. The form of electron heating chosen was ECRH. This reduced the beam energies from 1.2 MeV to about 400 keV at the same Q value. Because the electrons which were heated in the end plug had good thermal contact with those in the central cell, only a comparatively modest increase in plug electron temperature could be achieved at a reasonable ECRH power, thereby limiting the benefits of the trade off of end cell density for temperature. A way was needed to isolate the electrons in the end cell from those in the central cell. This requirement has given birth to the idea of the thermal barrier.
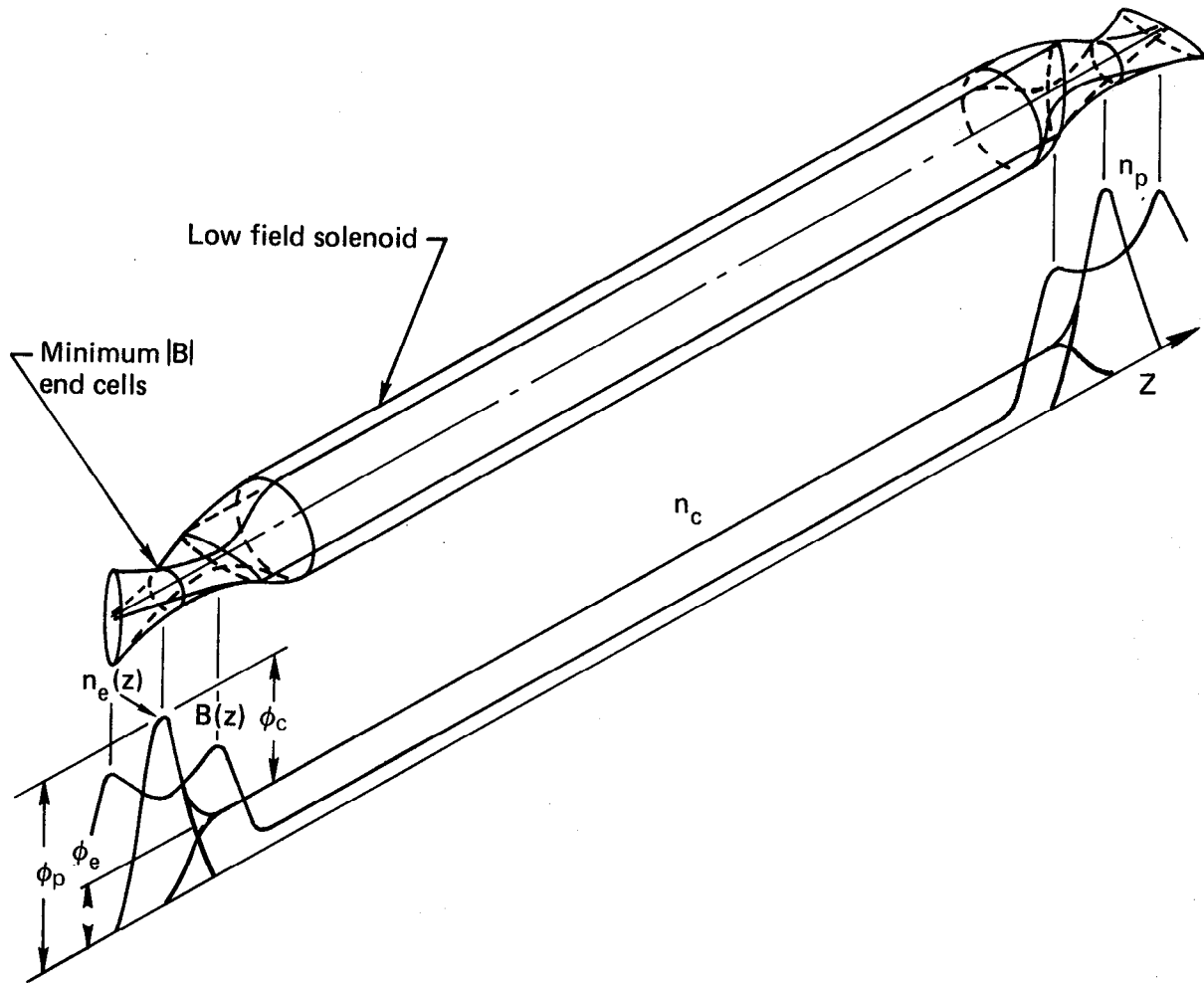
FIG. II.A.1 Simplified drawing of a tandem mirror.

II.B. TANDEM MIRROR PHYSICS

II.B.1 Thermal Barrier Mode of Operation

The thermal barrier idea was invented by Baldwin and Logan (II.B.1) at
LLNL in 1978. The basic idea behind the concept is to depress the ambipolar
potential between the central cell and the potential peak in the plug. This
creates a potential hill for electrons coming from the central cell, thereby
reducing their density at the potential peak. This allows the electrons at
the peak to be heated to higher temperatures than that in the central cell.
Figure II.B.1 shows the potential profile of an ideal end plug with a thermal
barrier. Standard tandems (barrierless) require the plug density to be greater
than that in the central cell. With a non-zero barrier potential dip, ϕ_b,
the plug density can actually be less than the central-cell density thereby
reducing the power to sustain the potential peak.

Some means for producing this potential dip is necessary. This may be
done by reducing the density of plasma in the barrier region, compared to that
in the central cell. The ion density there consists of two components, one
passing from the central cell, the other trapped due to the presence of the
potential dip. To reduce the density of plasma passing into the barrier from
the central cell, a peak in the magnetic field must be placed between the
central cell and barrier. This peak should be large compared to the magnetic
field at the barrier midplane. This field can be produced by a single coil, as
is the case for the early "inside" thermal barrier designs (II.B.2), by a yin-
yang magnet as in the MFTF-B "A-cell" thermal barrier (II.B.3) configuration,
or by two circular coils which are used in the recent axicell and modified cusp
end cell concepts. A description of these end-plug configurations is given in
section II.B.2. The reduction of the density of ions which become trapped in
the potential well is more difficult. There are presently two means proposed
to achieve this barrier "pumping".

The first, and most widely studied to date, is that of charge-exchange
pumping (II.B.4). In this concept, an ion which is trapped in the barrier
potential well receives an electron from an injected neutral atom beam. This
beam has a sufficient energy and is directed in such a way that the ion pro-
duced escapes the potential well and joins the central-cell passing ion
density distribution. For a reactor, this method of barrier pumping requires
a neutral
beam of high power. In some cases, up to half the power injected into the end
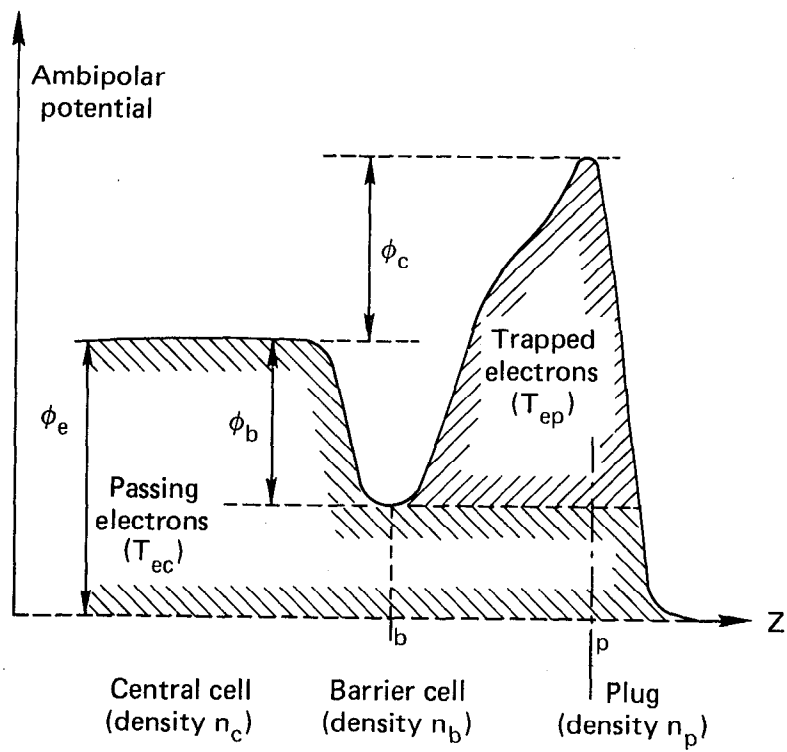
Fig. II.B.1   Ideal end plug with a thermal barrier.

cells is due to the charge-exchange pumping beam. There is considerable incentive to find another method to remove barrier ions.

A more recently proposed scheme called "gradient B pumping" (II.B.5, II.B.6) uses almost no power. The idea here is to break certain invariants of particle motion by putting perturbing coils at appropriate places in the barrier. Initial studies of this method of pumping have shown encouraging results, but more analysis is needed. Plasma Q values will increase by about a factor of 2 if this means of pumping appears feasible, and is adopted in the reactor studies.

Since the advent of the simplest form of the thermal barrier, there has been a method developed to further help depress the barrier potential. The introduction of hot, mirror-trapped electrons at the bottom of the potential well in Fig. II.B.2 tends to depress the potential further in order to maintain an equal number of ions and electrons at that point. These electrons will be sustained by ECRH applied near the barrier midplane. These electrons are produced at a position where the magnetic field and ambipolar potential are such that increasing their velocity perpendicular to the field (with ECRH) increases their confinement, as is the case which is analogous to that seen by hot ions in a simple mirror cell. Figure II.B.3a shows a picture of the confined and unconfined regions of velocity space for these hot electrons. Having expended power at the barrier minimum to make the dip deeper will reduce the density, and hence the power required to produce the outer potential peak which confines the central-cell ions. The reduction of power at the potential peak is
more than the power needed to deepen the barrier.

The presence of the electron thermal barrier helps minimize the ECRH power used to produce the ion confining potential peak. This power is applied in a region where both the potential and magnetic field increase axially. The diffusion of these electrons in perpendicular velocity from the ECRH at this location transports them from a confined region in velocity space to an unconfined region. This makes the ambipolar potential rise in order to maintain quasi-neutrality. Figure II.B.3b shows the confined and unconfined region in velocity space for electrons trapped in a so-called "ellipsoidal well". If the electrons exit through the top of the ellipsoidal well, they become part of the mirror trapped population at the barrier minimum; otherwise, they become part of the electron population in the central cell. Notice that this is a situation opposite to that for the hot mirror trapped electrons located at the
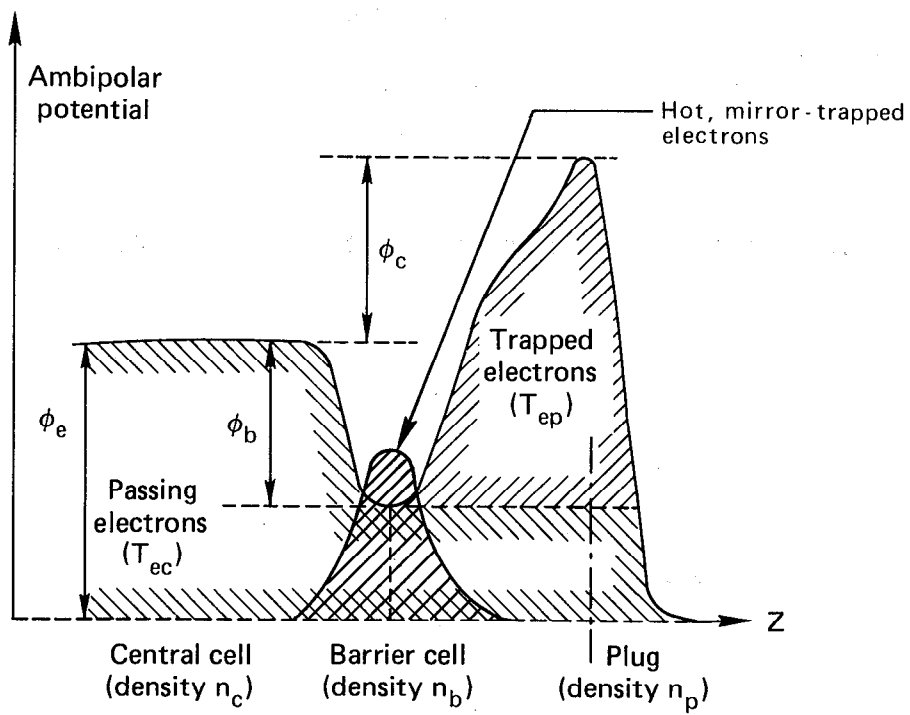
Fig. II.B.2 Thermal barrier with hot electrons.
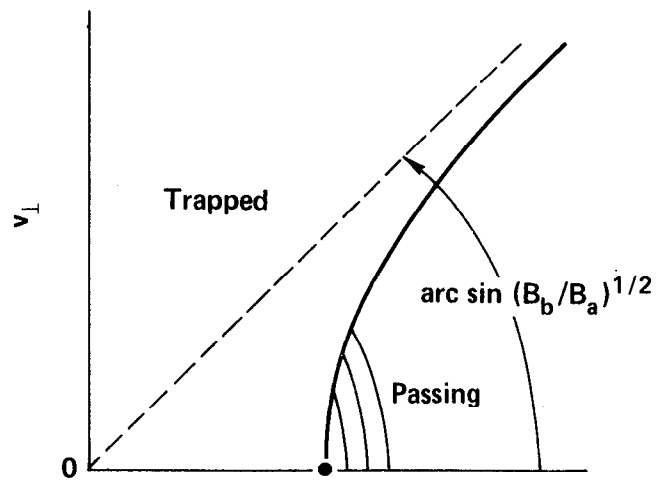
Fig. II.B.3a Velocity space boundaries for hot electrons in a thermal barrier.
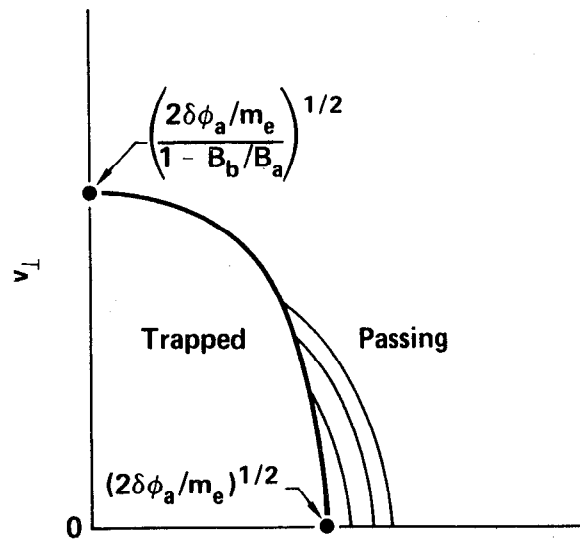
Fig. II.B.3b Velocity space boundaries for warm electrons at the potential peak.

barrier minimum, in which case increasing their perpendicular velocity improves confinement.

There is no operating experiment which has demonstrated the existence of thermal barriers. The soon-to-operate TMX upgrade (TMX-U) experiment has as one of its primary objectives the creation of thermal barriers in just the way described here. The experiment is scheduled to begin operation early in 1982.

II.B.2 Tandem Mirror End Plug Configurations

As part of the ongoing pure fusion and hybrid efforts at LLNL, numerous end-plug designs are being considered. The "ideal" design would be cheap, compact, rely on a simple magnetics design, confine plasma which is stable to both macro- and micro-instabilities, and require low power to sustain the proper potential and density profiles. Unfortunately, no plug conceived of to date possesses all of these desirable characteristics. The search, of course, will continue, but for the purposes of this hybrid study, the baseline end cell design will only reflect the progress made up until mid-June 1981. At this point in time, there are three possible candidates. These are the MFTF-B quadrupole stabilized A-cell thermal barrier type, the axicell type, and the so-called "modified cusp" type. Each will be described briefly in the following paragraphs, although the axicell end plug has been chosen as the baseline fusion driver configuration for this study. If more were known about the modified cusp, and the physics appears sound, there are advantages for going to this design as the baseline end cell.

Most of the tandem mirror analysis to date has concentrated on the end-plug design which stabilizes the entire configuration with a minimum-B yin yang, as in TMX, TMX-U, and MFTF-B. Such a standard configuration, along with plasma profiles expected for thermal barrier operation is shown in Fig. II.B.4.

This is the configuration which was considered in the TMNS study, the first iteration completed in 1980. Several of the problems associated with this end-plug design centered around the yin-yang magnet, which requires a magnetic field at the conductor of 12 T. The high field was required to reduce the passing density in the barrier, as well as confine the hot beam injected
ions in the yin yang itself. The 12-T yin yang is a difficult engineering task,
both in the areas of coil winding, and the design of a conductor cross section which can withstand the twisting and crushing loads. The final coil cost was
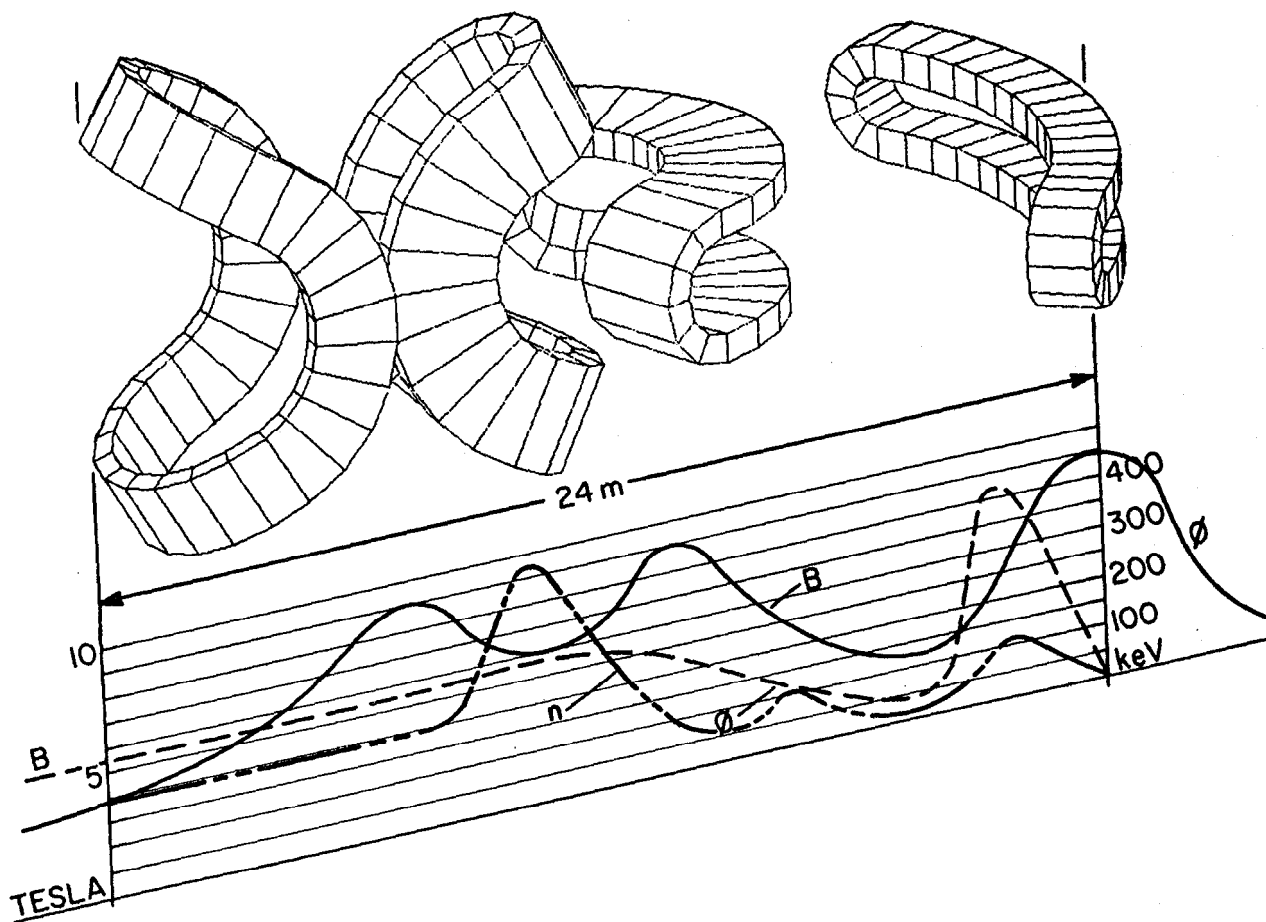
Fig. II.B.4   MFTF-B A-cell-type end-cell configuration.

large, around $450M for the complete set. A second examination (II.B.7) of the yin-yang coil showed that the original conductor cross section design was inadequate to carry the internal loads; conductor bundles near the steel casing were found to be crushed from the loads. Load carrying structure was added to the cross section, which solved the structural difficulty, but required the cross section to be about 50% steel. In order to produce the same magnetic field, the current density must be increased, thereby increasing the cooling requirements of the coil. By the use of superfluid helium, the required heat transfer can be provided, but the technology of this form of cooling is not well developed. There is no development program underway to consider this type of conductor configuration. Moreover, the use of superfluid helium increases the size of the cryoplant by a significant amount. These problems with the A-cell quadrupole stabilized end cell seem to point to the fact that the technology required for this case is not particularly near term, and is therefore not appropriate for the baseline TMHR end cell.

Two other concepts have been recently proposed (II.B.8, II.B.9) which could make a hybrid or pure fusion reactor more attractive from a performance and a simplicity of design point of view. The major feature of these two alternate end cell designs is that they are essentially axisymmetric. This means that the magnetic and plasma configuration have no dependence on the angle variable measured around the centerline of the machine. Among the currently perceived advantages of such axisymmetric configurations are:

(a) Radial transport of plasma particles caused by non-axisymmetry is eliminated.

(b) Higher magnetic field strengths are possible in a set of coils of axisymmetric design, due to a more favorable coil loading distribution.

(c) Simpler, and perhaps less costly, end cell designs are possible.

The "axicell" concept (II.B.8) has been adopted as the baseline driver for the fusion breeder described in this study. Figure II.B.5 gives a basic idea of the end-plug configuration. The stabilization of interchange modes in this case comes from the yin yang attached to the end of the device. The basic idea is to isolate solenoid ions from the yin yang where they would experience the non-symmetric fields, yet have enough communication between the yin yang and axicell so that the bad curvature in the axicell and solenoid is counteracted by good curvature in the yin yang. Note that the high field coil immediately after the solenoid is circular, simplifying considerably the
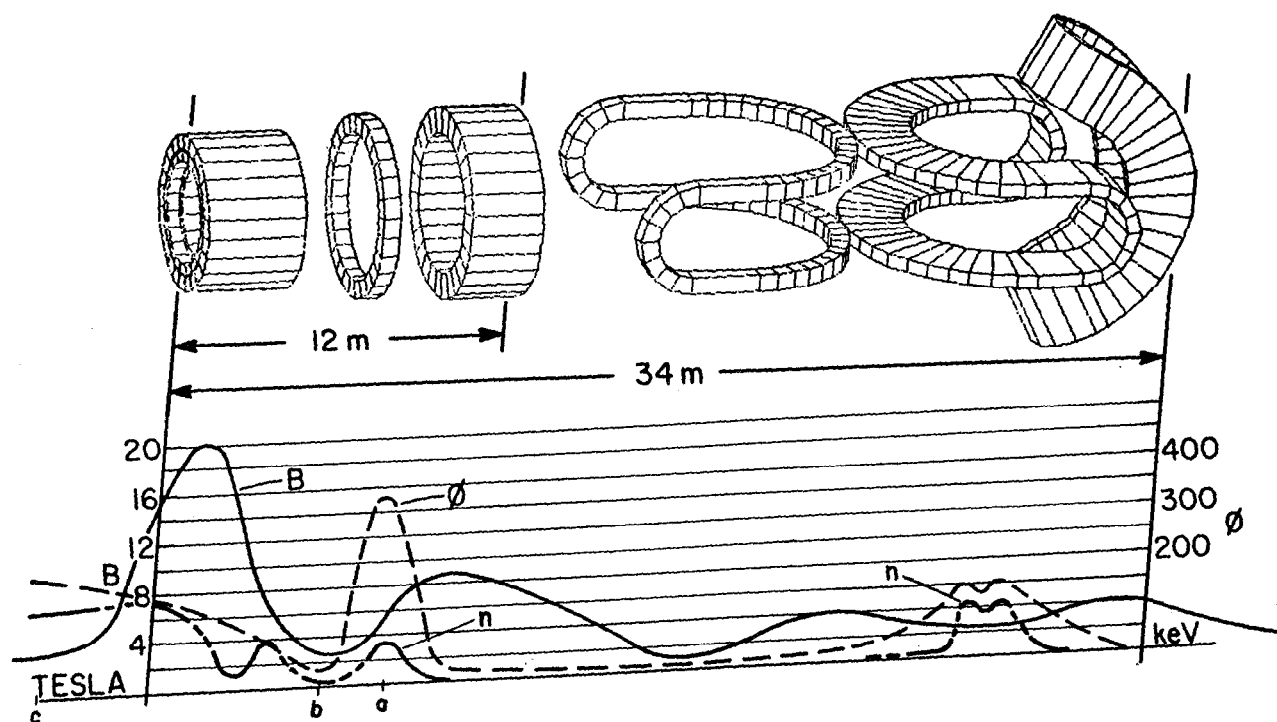
Fig. II.B.5 Axicell-type end-cell configuration.

design, and alleviating the stress problems compared to a yin yang. The yin yang in this configuration is on the outside where low field is adequate; the current design will work with NbTi superconductor and MFTF-B technology, although the size of the yin yang is a good bit larger. There are several means of producing the plasma pressure in the yin yang, however the preferred approach is to inject neutral beams in a special way to produce a double peaked "sloshing" ion distribution. These distributions are predicted to have good microstability properties, and are to be demonstrated on TMX-U, MFTF-B, and used in both the end cell designs in Figs. II.B.4 and II.B.6 as well. An alternate method to produce the plasma pressure is by creating hot electrons in the anchor. This method has difficulties in a small experiment (II.B.8) but has interesting possibilities for a reactor. Work is presently underway at LLNL to assess this means of producing plasma pressure.

A schematic of the "modified cusp" reactor end plug is shown on Fig. II.B.6 (II.B.9). The term "modified" refers to the fact that it is a modification of another axisymmetric cusp reactor considered at LLNL. The original concept possessed problems which prevented it from making a good reactor (II.B.10).

The magnetics configuration affords simplicity. A high field, circular, "hybrid" coil follows the central-cell solenoid magnets. The hybrid coil is followed by two coils, one inside the other, which forms the cusp geometry. The current flowing in the inside coil is in a direction opposite to that of the outside coil. This inside coil is cantilever-supported.

This end-plug configuration has the advantage of short length, simplicity of construction, and an expected lower cost compared to the axicell and MFTF-B type end cells. The problem of non-adiabaticity of fusion alpha particles near the magnetic field null which plagued the original form of the cusp reactor does not exist in this modified design. This is because the high energy alphas are magnetically confined to the central cell by the high field barrier coil, and the null now occurs in the barrier region, but on field lines devoid of plasma. Gone also is the extra power requirement to sustain a barrier plasma flowing through the inner coil bore which was present in the old cusp idea. In the new configuration, adiabaticity is an issue for the sloshing ions in the barrier. The innermost flux tube on which there exist adiabatic sloshing ions will define the minimum radial position in the barrier which contains plasma. Tubes closer to the null presumably will have lost their plasma because of microturbulence generated in the absence of sloshing ions.
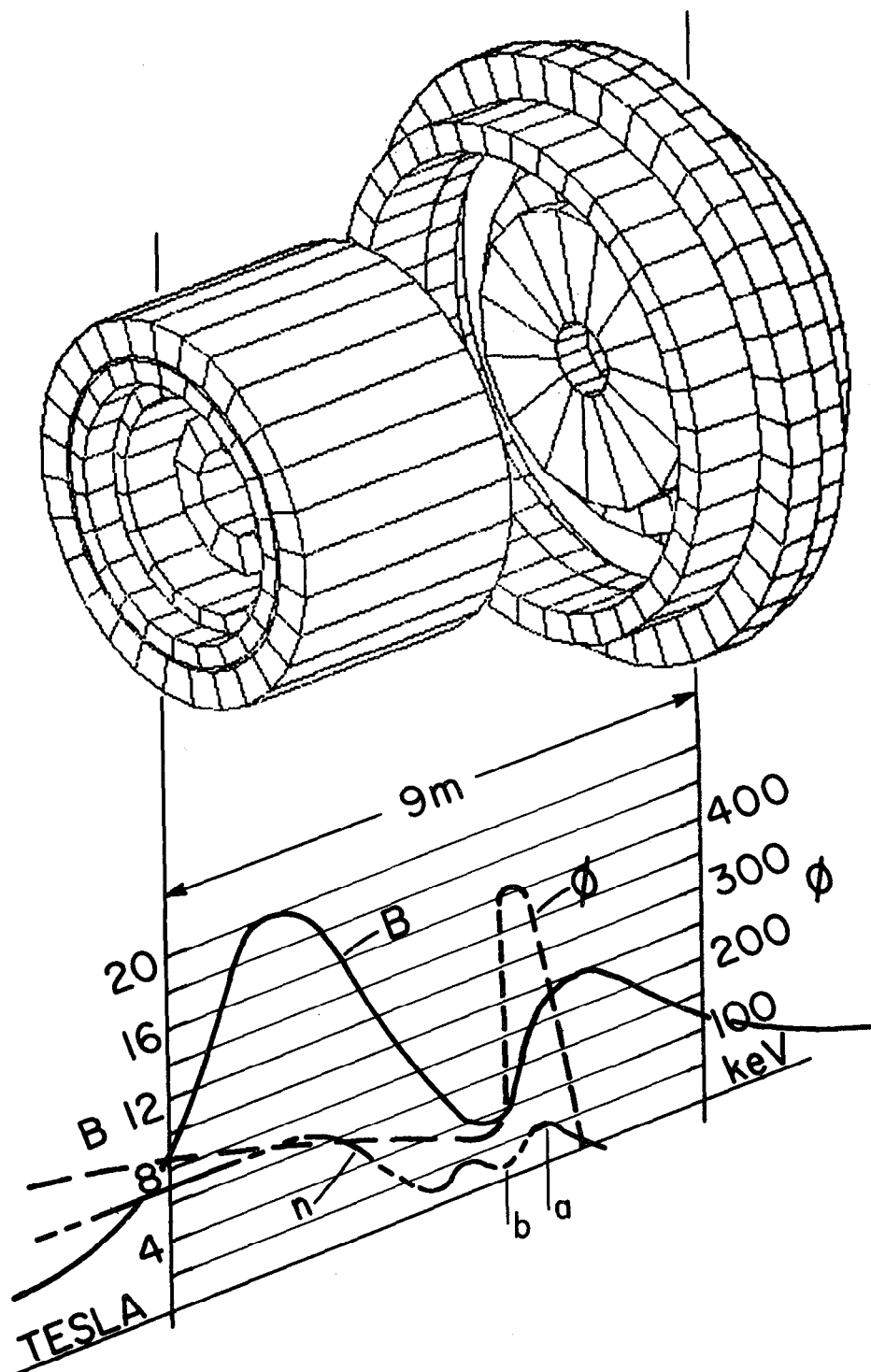
Fig. II.B.6 Modified cusp-type end-cell configuration.

This flux tube mapped into the central cell defines the inner radius of the annular plasma formed there. The outside radius of the central cell is determined in the usual ways by a combination of the fusion power per unit length required for a given central-cell plasma pressure and magnetic field strength; and also by the outermost field line which has interchange stability.

The principles behind the MHD stabilization of such a configuration are quite involved. The field lines on the outside of the plug annulus exhibit good curvature. The high pressure there due to hot electrons produced by ECRH allows for the line averaged curvature in plug and central cell to be good. This is in fact the opposite condition which exists in the MFTF-B and axicell end cells, where in these cases hot electron pressure weights bad curvature. The field lines on the inside of the plug annulus have bad curvature, and must be stabilized by means other than those described by "ideal MHD" theory. Some ideas (II.B.9) for stabilization of these field lines are by plasma rotation, by finite Larmor radius effects, and by the creation of a hot, rapidly drifting electron population to reverse the local radial gradient of the magnetic field. These hot electrons would be produced by ECRH. Both these approaches are currently under study at LLNL. The same principle of producing these hot electron rings has been used with success on the EBT device at ORNL (II.B.11).

One potential disadvantage of the modified cusp configuration is that the central-cell plasma is hollow. The ratio of inner radius to outer radius determined from sloshing ion adiabaticity appears to be about 1/2. This means that for the same power per unit length, plasma pressure, and magnetic field, the central-cell plasma radius needs to be larger. One would be able to compensate for this by increasing the central-cell magnetic field, or if MHD stability calculations permit, increasing central-cell β.

Another disadvantage of the modified cusp idea at the present time (July 1981) is that we really don't know as much about the physics of this end plug as we do about the MFTF-B or axicell end plug. Consistent with the conservative physics philosophy adopted for the hybrid, the much better defined axicell configuration is adopted. Indeed, the baseline case for the 1979 hybrid study (II.B.12) was an axicell-like design, without thermal barriers. For the modified cusp, questions which must still be answered are those regarding the adiabaticity of the sloshing ions and the MHD stability issues of the inner field lines.

The fusion reactor development program underway at LLNL has a direct impact on the hybrid program. This program is called the Advanced Mirror Systems (AMS) program. The objective of the AMS program is to propose tandem mirror end plugs which are simple, cheap, and provide good plasma performance. This effort, particularly at the present time, is producing end-plug concepts which are evolving at a very rapid rate. To define a baseline end-cell configuration, whether it be for a pure fusion or fusion breeder application, is premature at this time. The performance of the axicell base-line case is adequate to produce a system which makes economically competitive fissile fuel (the equivalent of $100/lb of uranium), and therefore meets the goals of the present hybrid study. However, since a pure fusion reactor is a stand-alone power producer, the demands on driver performance and cost are more stringent to produce an economical product. The search continues by the AMS program to find an end-plug concept which satisfies these demands. We show in this study that for a hybrid this further search is, although desirable, not absolutely necessary. Improvements for pure fusion will make improvements for the hybrid application, probably lowering equivalent cost to well under $100/lb of uranium.

This illustrates the long perceived notion that a hybrid requires a lower level of performance and allows a higher driver cost than does pure fusion. The baseline fusion breeder axicell case achieves the performance needed for the application by using a level of technology currently assumed in both the hybrid and pure fusion programs. For a pure fusion reactor, this technology and presently conceived end-plug concepts do not achieve the required performance to make its electricity economical. Pure fusion needs an improvement, which may be obtained in one of two ways: (1) demand a higher level of technology than is presently assumed, or (2) discover a better plug which will use technological capabilities more efficiently. It is the second path that the LLNL AMS program is pursuing.

Note that whatever new concepts the AMS program develops, the hybrid/LWR electricity cost reported on in this study will be affected in a small but important way due to the large LWR thermal support ratio of the suppressed fission blankets. Moreover, the baseline axicell parameters chosen here are on the conservative side, since present indications show that some of the end-cell configurations currently being considered by AMS have somewhat better performance and design characteristics.

II.B.3 Tandem Mirror Hybrid Physics Models

This section describes qualitatively some of the design characteristics of
the tandem mirror driver developed at LLNL used in this study. An additional
description of the tandem mirror driver may be found in the section on plasma
physics assessment and also in the recent article by Carlson (II.B.13). Here,
physics issues which will impact hybrid design and costing are described. The
physics basis for the evolution of the standard and tandem mirrors will be
reviewed. A brief description of the plasma physics model, emphasizing
explanations rather than cumbersome equations, will be given. In Section
II.D.2, results will be presented illustrating the sensitivities of plasma
gain, Q, and 14 MeV neutron wall loading, Γ, to changes in the physics and
technology assumptions in the model.

For the purposes of obtaining design and costing information of proposed
hybrid designs, the plasma driver is characterized by (1) the output fusion
power, P_{fus}, (2) the ratio of this power to the power injected to sustain
the plasma, P_{inj}, called the plasma gain, Q, and (3) the energy current of
fusion neutrons incident on the first wall of the solenoid, called the neutron
wall loading, Γ, measured in units of power/area. For a commercial hybrid
of the fission suppressed type, values of P_{fus} should lie between 2000 MW
and 3000 MW. Traditionally for adequate hybrid performance, Q should be at
least 4, and Γ should be at least 2 MW/m^2. We will show in this study,
however, that the high assumed cost for supplementary heating favors drivers
which have a Q value of at least 10. Pure fusion reactors require P_{fus}
around 3500 MW, with much higher values of Q and Γ to be economical.

The two performance characteristics Q and Γ are functions of many
variables. The assumption regarding the maximum magnetic field strength,
B_{max}, attainable in the end plug turns out to be quite important for
determining performance. Equally important is the ratio of plasma pressure to
magnetic field "pressure", β, allowable. The upper limits on the solenoid
β are established by investigating the stability of the plasma to various
classes of perturbations. The performance is also a function of the energy of
the injected neutral beams, E_{inj}. If a simple scaling relation which would
allow us to write $Q = f(\Gamma, P_{fus}, \beta, B_{max}, E_{inj})$, then the coupling of
the physics to the hybrid systems analysis and fissile material cycle analysis
would be straightforward. Unfortunately, at this writing we have been unable

to formulate a relationship general enough to examine all the sensitivities. We are therefore forced to couple the complete physics model directly to the other analysis codes. The complete process will be given in the parametric analysis sections of this report.

Plasma physics considerations establish design parameters important for the hybrid reactor blanket designer. Along these parameters are the neutron wall loading just discussed, the minimum first wall radius in the solenoid, the fraction of the reacting plasma which is surrounded by breeding blanket (either for fissile material or tritium), and the magnetic field strength and shape in the blanket. The minimum first wall radius is determined by the criterion that a 3.5 MeV fusion alpha particle born at the plasma edge in the solenoid does not intercept the first wall on its first orbit. For design purposes, a minimum of three hot alpha gyroradii are assumed between the plasma and the first wall.

Depending upon the end-plug configuration and the species of injected particle in this end plug, the fusion power generated and tritium consumed in the end cell may be appreciable. If the geometry is unfavorable for surrounding this region with blanket, the neutrons produced there cannot breed fissile material, and the replacement of any tritium consumed will have to be accomplished by increasing the tritium breeding ratio in the main blanket. This problem has in fact arisen in the yin-yang stabilized tandem mirror configuration, where an appreciable number of fusion reactions occur in the transition region between the solenoid and the yin yangs, and the yin yangs. Both of these regions are difficult to effectively cover with blanket. The latest end-plug designs of the axisymmetric variety (see Section II.B.2) alleviates this blanket coverage problem, for two reasons. First is that the magnetic field and potential profiles in the axisymmetric end cell are such that the density of the reacting tritium component is much smaller than in the non-axisymmetric yin-yang end cell. Another reason is that the geometry of the end-cell region where reactions would occur is very much like that in the solenoid, where simple, effective blankets may be used. Another solution to the blanket coverage problem is to suppress fusions in the end cell by injecting energetic hydrogen rather than deuterium.

The magnetic field magnitude and direction in the blanket is important in the designs which use an electrically conducting fluid as coolant. In these cases, these is a pressure drop associated with the coolant crossing the field lines. The way to minimize this loss is to run coolant lines along the

magnetic field as much as possible, and only cross the field when the coolant velocity is low, or the field is weak. Coating the coolant pipes with ceramic insulator when they cross field lines helps to reduce the MHD induced pressure drop, although radiation damage to ceramics by a high neutron fluence will limit the blanket life, as discussed in Section IV.C.2.

The tandem configuration which was chosen as the baseline in the study is the axicell configuration and is shown on figure II.B.7. Figure II.B.5 in Section II.B.2 shows axial profiles of magnetic field, density, and electric potential. References to points "c", "b", or "a" in this Section correspond to the subscripts used in this figure. This design incorporates thermal barriers for electrons produced by ECRH at points b and a, and sloshing ion injection at point a. The potential barrier for ions is also produced by the sloshing ions and the warm electrons at point a heated by ECRH. The sloshing ions' density peaks at the potential peak, and the ECRH applied nearest the outer circular magnet heats the electrons there to make the peak higher. A yin-yang magnet at the end of the device is provided to make a region of good magnetic curvature and high plasma pressure in order to stabilize MHD interchange and ballooning instabilities. This is one of the "axisymmetric" designs, which were described in the end-plug configuration Section II.B.2. The MFTF-B type A-cell thermal barrier end plug will be considered in the parametric analysis section to serve as a point of comparison. This end-cell design was that used in the first study of TMNS (II.B.14).

Notice that the end cell is far more complex than the central cell, containing all the high technology components which have programs underway or planned in order to develop them. The section on fusion technology assessment discusses these programs in detail. This points to one of the advantages of tandem mirrors over other magnetic confinement schemes in that the power producing regions are confined in a simple configuration which relies on comparatively low technological requirements. All of the complicated plasma physics occurs in the end cells, and all of the power required to sustain the entire machine is injected there as well. This suggests that the plasma Q can be affected considerably by what goes on at the ends of the machine.

There are four different kinds of neutral-beam injection in this reactor, and each serves a different purpose. The low, medium and high energy pump beams shown in Fig. II.B.7 remove low energy ions trapped in the potential dip of the thermal barrier (point b). A certain amount of these low energy ions is beneficial, for they help produce microstability of the sloshing ions

ECRH GYROTRON
(30 TOTAL)

ECRH WAVEGUIDE

VACUUM VESSEL

ANCHOR SLOSHING
ION BEAMS

DIRECT
CONVERTER

SLOSHING ION
BEAM APERATURE/SHIELD

AXICELL
SLOSHING ION
BEAMS

SLOSHING ION
BEAM DUMP
(TYPICAL)

CENTRAL CELL
FUSION PLASMA

YIN-YANG
ANCHOR COILS

TRANSITION COIL

MIRROR COIL

BARRIER COIL

SOLENOIDAL COILS

FOUNDATION/SUPPORT
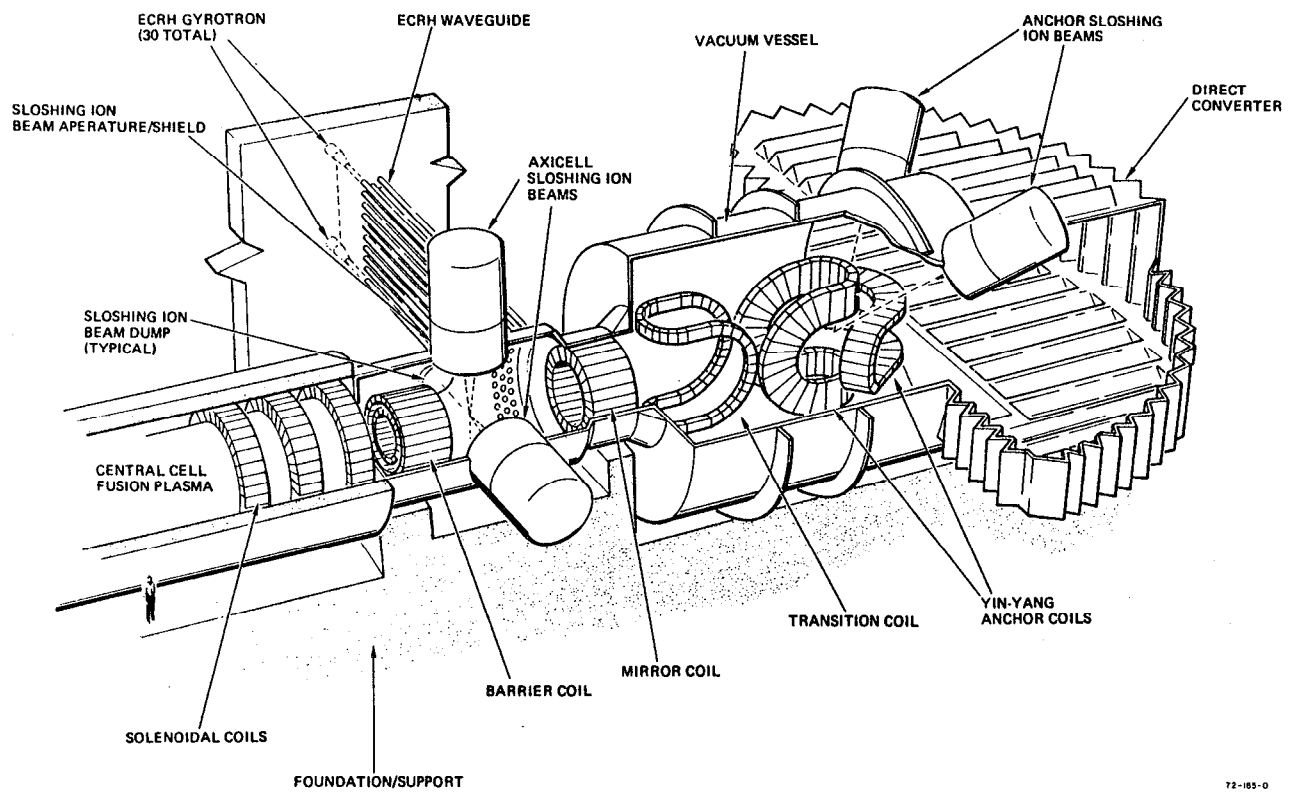
72-165-0

Fig. II.B.7 Axicell fusion driver.

II-20

in the barrier cell, but if too many accumulate, they tend to fill up the potential dip which is needed for the electron thermal barrier. The neutral-beam particles injected almost parallel to the machine axis exchange an electron with the cold ion, thereby replacing an electrostatically trapped ion with one which has an appreciable velocity component parallel to the magnetic field. This is called "charge exchange pumping".

Three energies and injection locations for these pump beams are used, because it was found (II.B.15) that the total beam power required could be reduced compared to using only one beam. The energy of the high energy pump beam in a reactor (> 150 keV), and the requirement that the pump beams be monoenergetic, strongly suggests that neutral beams produced by negative ions should be used. In the case of the medium energy pump beam, a conflict arises, because it requires the energy purity that negative ions give, but demands current densities which only positive ions at the present time can satisfy (II.B.15). This points to an important reason why the negative ion neutral-beam program should be accelerated in support of the immediate needs of tandem mirror reactors.

The parametric analyses, presented in Sections II.D and IX.E, will examine a 'low technology' case where positive ion beams are used in conjunction with magnetic extraction of the half and third energy components. This effectively reduces the beam generation efficiency by a factor of 2. We find that the hybrid may be able to tolerate the use of positive ion beam technology. Charge exchange pumping is fairly inefficient, since a beam particle may become a plasma particle by either ionization or charge exchange, the former not contributing to pumping. The pumping usually comprises the largest power requirement, which suggests that a more efficient means for selectively removing trapped ions would improve plasma performance considerably. Such alternative methods are being pursued at LLNL, and two schemes have emerged as possible candidates (II.B.5, II.B.6). Both rely on the modification of the guiding center drifts of the ions due to an axially localized perturbation in the magnetic field. One scheme (II.B.5) uses a static magnetic field perturbation near the turning points of the species of ions which are to be pumped. The other scheme (II.B.6) uses a time varying magnetic perturbation. For these schemes to work, the pumping must remove the cold trapped ions, without disturbing the sloshing or passing ions, or the hot electrons in the barrier. At first examination, both schemes seem to have good selectivity, even having

the potential to pump thermalized alpha particles and impurities trapped in the barrier. Further work is needed to determine which scheme will work best.

In addition to the charge exchange pump beams, high energy beams are needed to produce the double-peaked sloshing ion distribution in both the barrier cell and the "anchor" yin-yang cell. Work performed to date on the axicell design suggests that a lower energy can be used in the yin-yang anchor compared to that for the axicell sloshing ion beam. In fact, it may be possible to use positive ion neutral beams for the anchor sloshing injection.

To further complicate the end-cell design, ECRH must be applied at two distinct locations, at point "b" and point "a" in Fig. II.B.5 of the end-cell section. The required frequency of the radiation for a reactor will be between 60 and 120 GHz. The lower frequency is applied at the location closer to the high field barrier coil in Fig. II.B.7 at the bottom of the thermal barrier. The confined region of velocity space for electrons there is shaped such that increasing the electron's perpendicular energy due to the cyclotron acceleration by the ECRH will improve their confinement. This produces a hot electron distribution which is peaked at the barrier midplane and makes the electron barrier potential well deeper. The higher frequency (because it is required to heat electrons at a higher magnetic field) is applied at the location (point "a") close to the A-cell magnet. This location corresponds to the potential peak which confines ions. The velocity space boundary which separates trapped and passing space in this case is quite different. Increasing the perpendicular energy by ECRH <u>degrades</u> the confinement of the electrons residing there, producing passing electrons from the trapped ones, thereby <u>increasing</u> the potential peak. The presence of the thermal barrier allows the heating of the electrons at point "a" to be more economical than the barrierless case. In fact, the power saved in heating these isolated electrons is more than the power required to produce the electron thermal barrier. This is the reason why thermal barrier tandems appear so attractive compared to the standard (barrierless) tandem.

The physics model used for the hybrid study is the same which is being used for the pure fusion reactor development effort at LLNL (II.B.13). The code is a profile averaged, zero dimensional model of particle and energy balance in the solenoid, yin yang (in MFTF-B type end cell), barrier, and anchor (in Axicell end cell) region. The balances of three electron species and three ion species are solved in the steady state. Solenoid electrons and ions, hot plug ions, sloshing ions, "hot" electrons at the thermal barrier

minimum, and "warm" electrons* at the potential peak are considered in detail, using equations which are an extension of those used to predict the performance of MFTF-B (II.B.16).

In the code, the axial dependence of the density of the six species is accounted for by the use of density mapping equations. The particle and energy balance relations in the central cell establish, for a given ion temperature, the temperature of the electrons, the floating potential of the solenoid relative to ground, ϕ_e, and the confining potential of ions relative to this floating potential, ϕ_c.

The power balances for ions in the yin-yang, barrier and anchor regions determine the beam powers and currents required to sustain the yin yang (or anchor) hot ions, the barrier sloshing ions, and to accomplish charge exchange pumping of barrier trapped cold ions. The model used in the code to compute pumping power combines the low, medium, and high energy pump beams into a single beam with energy approximately equal to the barrier potential depression relative to the yin-yang potential, ϕ_b. The pump beam power is computed by computing the trapping rate of cold ions in the thermal barrier. This rate is obtained by fits to numerical solutions of the Fokker-Planck kinetic equation. The yin-yang (or anchor) hot ions are described by the so-called Logan-Rensink plug model (II.B.16) which is an analytic confinement model which agrees well with calculations which solve the Fokker-Planck equation numerically. The confinement time, average energy, loss energy and density of hot ions are all outputs from this simplified model, from which the sustaining power in the yin-yang is computed. The sloshing ion power in the axicell is obtained by fitting results obtained by the solution to the Fokker-Planck equation (II.B.16). The power is assumed to scale inversely with the time for a sloshing ion to scatter in pitch angle across its loss boundary in velocity space.

The ECRH power required to heat the electrons in the end cell consists of two parts. The power required to sustain the hot electrons at point "b", the thermal barrier minimum, is that which makes up for pitch angle scattering due to classical collisions into the electron loss cone, minus that power which is carried by the warm electrons produced at point "a" which become trapped at "b". Since these electrons are quite hot, syncrotron radiation losses are also

---

*the modifiers "hot" and "warm" refer to the degree to which the velocity space distributions deviate from Maxwellian. Hot electrons have anisotropic, highly non-Maxwellian distributions. Warm electrons are kept close to Maxwellian.

included, assuming no reabsorption. There is presently no allowance for anomalous pitch angle scattering of hot electrons due to turbulence produced by microinstabilities caused by non-Maxwellian distributions. Whether this is a problem or not is currently a subject of theoretical debate which will only be resolved by experimentation. The power applied to sustain the warm electrons at point "a" must make up for the energy loss when a warm electron is lost out of trapped velocity space and a cold passing one takes its place, as well as the energy loss which arises from exchange of energy due to binary collisions between cold and warm electrons.

The physics model also has the capability of investigating the impact of scaling laws which relate the maximum stable solenoid plasma β to magnetic field strengths and scale lengths throughout the device. The two criteria which have been used are that of ballooning and interchange, discussed in the plasma physics assessment Section II.G. of this report. It was discovered (II.B.13) that for the MFTF-B A-cell plug the maximum stable β_c (solenoid β) and solenoid magnetic field, B_c, are related by $\beta_c B_c^{1.6}$ = constant for both ballooning and interchange. These calculations were performed at a fixed yin-yang mirror ratio and magnetic field.

The ballooning criterion is much more restrictive, because the constant of proportionality is smaller, and because it depends on the length of the solenoid. As the length of the solenoid becomes longer, the maximum β for ballooning stability decreases. This length scaling is very important for determining the dependence of plasma Q on fusion power when using the ballooning criterion. Without it, Q is roughly proportional to P_{fus}, whereas when the unfavorable length scaling is included, Q is virtually independent of P_{fus}. The use of the ballooning criterion results in machines with low plasma Q values at low wall loading, and very large solenoid, barrier, and yin-yang plasma radii. This is discussed further by Carlson (II.B.13) using the pure fusion case as an example.

There has been no work done to date on the scaling of stable central-cell beta for the axicell configuration, and hence we rely primarily on an MHD interchange stability calculation in which the central-cell beta is 0.7.

The ballooning criterion discussed above is based on an ideal theory ignoring finite Larmor radius (FLR) effects. To include these effects in the analysis is an ongoing effort at LLNL. These FLR effects tend to make the maximum β value from ballooning mode theory larger. There is currently much optimism at LLNL that FLR effects will increase the ballooning β limit

almost to that of the interchange limit. The majority of the analyses performed thus far for the hybrid study incorporates the interchange beta limit, and will continue to do so until a scaling is developed for the ballooning criterion including FLR effects.

Another constraint dictated by MHD stability is the plasma beta value in the barrier region for a given central-cell beta value. The barrier beta value is the sum of the parallel and perpendicular beta values,* the perpendicular beta being produced primarily by hot barrier electrons, the parallel beta is due to the passing density of ions and electrons from the central cell. In order to produce an appreciable perpendicular beta value, which is important to barrier power balance, the parallel beta value needs to be controlled. There are several ways to control it, for a given maximum mirror field in the thermal barrier. Parallel beta may be reduced by lowering central-cell magnetic field or beta, or by increasing the minimum field in the barrier. The a combination of these methods seems to be the best option.

It is important to determine the sensitivity of plasma Q to changes in variables which may reflect the physics and technological demands to be met. The changes in the performance of the fusion driver by changing injection energies and magnetic field strengths could conceivably help planners determine where the most aggressive development efforts are required. Sections II.D and IX.E examine the performance of the tandem mirror driver and the rest of the system as assumptions are changed regarding the level of plasma physics performance which can be attained, the current level of technology available at the time of construction, and the point on the characteristic (Q,Γ) curve which one should operate.

II.C STARTUP AND SHUTDOWN

Some consideration must be given to the means by which the tandem mirror reactor plasma is initiated at the beginning of reactor operation and extinguished during a reactor shutdown. Because of the steady state nature of the tandem mirror, these procedures are to be performed infrequently. The TMR design study of 1977 (II.C.1) addressed the problem of startup of a tandem

---

*β can be a tensor quantity, having different values along and across the magnetic field.

mirror reactor without thermal barriers. A possible scenario was outlined, and an estimate of power drain from the grid or an energy storage system was made.

The sequence of events involves first the heating up of the blanket, then the energizing of the normal conducting magnets, and finally the firing of neutral beams in a cold, low density end-plug plasma produced beforehand by a means which is assumed not to consume much power. This latter phase takes a very short time, about 0.1 s. During this short time period, the reactor will demand from the energy storage system about 80% of its rated electric output.

The thermal conversion system can not be subjected to such rapid transients in fusion power. Therefore, during the initial phase of startup, the central cell is fueled with only deuterium. The fusion power density and neutron wall loading produced by the D-D reactions is acceptably low as an initial condition for the blanket heat load. At a rate determined by the maximum load swing allowable by the thermal power system (about 5%/minute for conventional power plants), the pure deuterium mixture is slowly replaced with more tritium until half of the plasma ions are tritium and the rated output is achieved.

The basic startup concepts advanced in the 1977 study remain unchanged when a more complex end-plug configuration, utilizing thermal barriers, is considered. However, we need to transiently create and maintain axial profiles of hot, warm, and cold electrons, cold and sloshing ions, as well as the selfconsistent ambipolar potential in these new designs. This will probably require a more complicated startup scenario, in which beam currents and energies, as well as ECRH powers will have to be tailored in a very special way. A qualitative discussion of startup of a thermal barrier equipped tandem mirror is given in the TMX Upgrade proposal (II.C.2). A brief description of the proposed scenario for TMX-U will now be presented. It is assumed at the present time startup in a reactor will be similar.

● The central cell is initially filled with plasma by use of stream guns or e-beam ionization of gas from the central-cell gas feed. The plasma is sustained by a programmed gas feed with neutral beams and/or ICRH. The efflux of plasma from the central cell should be low density and suitable for startup of the hot electron population. Trapping of electrons from escaping plasma, by scattering and diffusion in perpendicular energy, feeds the increase in hot electron density.

● After reaching the steady-state density and temperature for the hot electrons, the sloshing ion neutral beams are turned on with the hot electron population as a target. Trapping of hot ions occurs by both ionization and charge exchange on the cold ions required for charge neutrality of the hot electrons. As the sloshing-ion density builds up, the thermal-barrier pump beams are turned on to maintain the double-peaked ion distribution.

● Simultaneous with the startup of the sloshing-ion distribution, ECRH microwave power is applied to the electrons in the outer ion peak of the sloshing ions. With the thermal isolation provided by the thermal barrier at the bottom of the plug, the electrons are heated to their equilibrium value to create the confining potential peak.

● As plasma and potential buildup proceeds in the plug, the central-cell gas feed and heating power are increased so that center-cell density and temperature can be brought to their equilibrium values.

The shutdown procedure is easier to define. One would like to allow the fusion power to decrease at roughly the same rate as it was allowed to build up during startup. The same methods of modifying the composition of the D-T mixture can be used here as well. The stored thermal energy of the reference case plasma is around 1.5 GJ, which must not be lost instantaneously. If the refueling current in the central cell is turned off, the plasma density there will decay with a time constant of roughly the particle confinement time which is initially 10 s for the reference case. At this rate, the thermal energy content in the plasma after about 2 minutes will have decayed virtually to zero. The neutral beams have to be ramped down in current as the density, temperature and potential peak drop in order not to overfuel the end cells. The beam energy must be reduced as density drops so as to maintain a constant beam trapping fraction. This keeps the beam dumps from overheating. Once the plasma is gone, the blanket can be cooled. The magnets can then be deenergized and warmed up if necessary.

II.D PHYSICS PARAMETRIC ANALYSIS

This section presents the baseline fusion driver and the sensitivity of this fusion driver performance on changes in driver components and plasma physics assumptions.

It is important to see how much the requirements on technology can be reduced, and how much physics conservatism can be exercised before the

performance of the fusion driver degrades and the cost of fuel/electricity of the breeder/burner system becomes prohibitively high.

The baseline Axicell physics case around which the parametric analysis is performed is described in Section II.D.1. Section II.D.2 shows how the performance curves (Q vs. Γ) change when maximum magnetic field strength, neutral-beam injection energy, central-cell beta value, fraction of cold plasma at the thermal barrier, and fusion power are changed. Two "low technology/conservative physics" axicell cases are examined, each using a modest β value in the central cell. One uses positive ion neutral-beam technology, the other also uses positive ion injection along with lower magnetic field strength. This section also presents performance curves for the MFTF-B/TMNS A-cell thermal barrier end-cell configuration, which is then compared to the performance of the axicell driver.

The results presented in this Section serves as input to the parametric analyses performed in Section IX.E. There, the impact of changing these same physics and technology assumptions are reflected in changes of the breeder capital cost, equivalent cost of U_3O_8, and ultimately the levelized cost of symbiotic electricity produced by the fusion breeder/LWR burner system.

II.D.1 Baseline Physics Case

The baseline fusion driver for the fusion breeder uses the Axicell end-cell configuration as described in Section II.B and shown in Fig. II.B.7. The maximum magnetic field strength is 20T and is produced with a circular coil made of layers of superconductor and room temperature copper. The other end-cell coils can be made with just superconductor, the lower field circular coil requires both NbTi and Nb_3Sn, but the yin-yang coil set demands only NbTi. The magnetic field strength on the axis of the central cell is 3T, and the central-cell coils require NbTi conductor.

The design chosen as baseline produces 3000 MW of fusion power in a central cell which is 129 meters in length, and supports an interchange stable beta of 70%. The neutron wall loading is 2 MW/m^2 at a first wall radius of 1.5 meters. The end cell requires 30 MW of ECRH power incident at 38 GHz (fundamental) at the barrier minimum (point b), 29 MW of ECRH power incident at 84 GHz (fundamental) at the potential peak (point a). A 90% absorption efficiency is assumed for ECRH. The end cell requires 120 MW of charge exchange pumping power to be deposited in the plasma, 170 MW incident on the

plasma surface. To sustain the sloshing ion distribution in the axicell requires 17 MW deposited in 250 keV neutral beams, and about 74 MW incident, since the trapping fraction is relatively poor for these beams. The sloshing ions in the anchor need 6 MW of 150 keV neutral-beam power deposited; 19 MW incident. These powers translate to a Q value, = fusion power/(deposited power), of 15.3. Multiplying this by the average trapping fraction, n_t, gives a Qn_{tr} product of about 9. Table II.D.1 shows some of the key physics parameters of the baseline case. Section II.B.3 provides background for understanding these parameters.

It is of interest to determine the impact of lowering the maximum magnetic field strength from 20T. By removing the copper insert from the high field layered coil, about 14T can be produced on axis. Table II.D.2 shows the important parameters for this driver design, using a 14T high field magnet in place of the 20T magnet. The Q value has dropped from about 15 to 6.7, the Qn_{tr} product has dropped by a smaller factor, from 10 to 5. The reason Qn_t drops by a smaller factor than Q is because the central-cell ion density which reaches the barrier increases with decreasing B_{max}, thereby improving the beam trapping fractions there, although the increased density increases the deposited power required. A driver of this kind might be used if there develops any unforeseen problems with producing the 20T magnet with the copper insert.

II.D.2 <u>Physics Sensitivities</u>

There is a tradeoff between plasma Q value and wall loading, Γ. Simply stated, if we wish to operate the central-cell plasma at high fusion power density, then it will take more power in the end cells to keep this high grade plasma properly contained.

Figure II.D.1 shows the tradeoff between Q and Γ for the 20T Axicell case, at a fusion power of 3000 MW and β_{cc} of 70%. The baseline case is shown on this figure to have a Γ of 2.3 MW/m^2, rather than the baseline value of 2 MW/m^2. This is because for all the parametric analyses the first wall radius is assumed to be the minimum in order to allow for fusion alpha particle confinement, instead of the larger fixed value of 1.5 meters assumed for the baseline. The tradeoffs are also performed with a physics case which exhibits slightly better plasma performance (Q ≃ 16.3) than the baseline shown in Table II.D.1.

TABLE II.D.1. Physics Parameters for the Baseline Axicell Case

Parameter	Value
Central Cell	
Density, n_c (cm^{-3})	1.6×10^{14}
Ion Temperature, T_c (keV)	40
Electron Temperature, T_{ec} (keV)	32
Plasma Radius, r_{cc} (cm)	104
Vacuum Magnetic Field, $B_{c,vac}$ (T)	3
Beta, β_c	0.7
Floating Potential, ϕ_e (keV)	234
Cold Fueling Current, I_c (kamps)	1.6
Ion Confinement Parameter, $(n\tau)_i$ (s cm^{-3})	1.3×10^{15}
Electron Confinement Parameter, $(n\tau)_i$ (s cm^{-3})	1×10^{15}
First Wall Radius (cm)	150
Central Cell Length (m)	129
Axicell/Barrier	
Maximum Hybrid Coil Field B_{max} (T)	20
Sloshing Ion Injection Energy, $E_{inj,a}$ (keV)	250
Vacuum Magnetic Field at Barrier Minimum (point b) (T)	1.69
Total Barrier Beta (β + β)	1.2
Perpendicular Barrier Beta, β	0.56
Passing Ion Density at Point "b", $n_{pass,b}$ (cm^{-3})	2.84×10^{12}
Hot Electron Energy at Point "b", E_{eh} (keV)	361
Warm Electron Energy at Point "a", T_{ew} (keV)	93
Barrier Length, L_B (m)	12
Cold Electron Density Fraction, F_{ec} (%)	2.54
Sloshing Beam Trapping Fraction (%)	23
Pump Beam Trapping Fraction (%)	70
Beta at Point "a", β_a	0.35
Barrier Potential Dip, ϕ_b (keV)	192
Ion Confining Potential, ϕ_c (keV)	137

TABLE II.D.1 (Continued.)

Parameter	Value
Anchor	
Anchor Plasma Radius, r_{anch} (cm)	122
Anchor Effective Length, L_{eff} (cm)	168
Sloshing Beam Trapping Fraction (%)	33
Sloshing Ion Energy, $E_{slosh,anch}$ (keV)	150
Hot Ion Density, $n_{slosh,anch}$ (cm^{-3})	1.5×10^{13}
Anchor Ion Confinement Parameter, $(n\tau)i,anch$ (s cm-3)	5.95×10^{12}
Anchor Floating Potential, ϕ_{anch} (keV)	158

Power Balance	Trapped	Incident
Axicell Sloshing Beam Power (MW)	17	74
Anchor Sloshing Beam Power (MW)	6.4	19.4
Axicell Charge Exchange Pumping Power (MW)	120	170
ECRH Power Applied to Barrier Minimum (point b) (MW)	27	30
ECRH Power Applied to Potential Peak (point a) (MW)	25.7	28.5
Fusion Power (MW)	3000	
Neutron Wall Loading (MW/m^2)	2	
Plasma Q (P_{fus}/P_{inj})	15.3	9.25

TABLE II.D.2. Physics Parameters for the 14T Axicell Case

Parameter	Value
Central Cell	
Density, n_c (cm^{-3})	1.6×10^{14}
Ion Temperature, T_c (keV)	40
Electron Temperature, T_{ec} (keV)	32
Plasma Radius, r_{cc} (cm)	104
Vacuum Magnetic Field, $B_{c,vac}$ (T)	3
Beta, β_c	0.7
Floating Potential, ϕ_e (keV)	229
Cold Fueling Current, I_c (kamps)	1.8
Ion Confinement Parameter, $(n\tau)_i$ (s cm^{-3})	$1. \times 10^{15}$
Electron Confinement Parameter, $(n\tau)_i$ (s cm^{-3})	8.5×10^{15}
First Wall Radius (cm)	150
Central Cell Length (m)	129
Axicell/Barrier	
Maximum Hybrid Coil Field B_{max} (T)	14
Sloshing Ion Injection Energy, $E_{inj,a}$ (keV)	250
Vacuum Magnetic Field at Barrier Minimum (point b) (T)	2.3
Total Barrier Beta $(\beta + \beta_{\parallel})$	1.2
Perpendicular Barrier Beta, β	0.6
Passing Ion Density at Point "b", $n_{pass,b}$ (cm^{-3})	5.75×10^{12}
Hot Electron Energy at Point "b", E_{eh} (keV)	327
Warm Electron Energy at Point "a", T_{ew} (keV)	105
Barrier Length, L_B (m)	12
Cold Electron Density Fraction, F_{ec} (%)	2.94
Sloshing Beam Trapping Fraction (%)	31
Pump Beam Trapping Fraction (%)	93
Beta at Point "a", β_a	0.46
Barrier Potential Dip, ϕ_b (keV)	169
Ion Confining Potential, ϕ_c (keV)	128

TABLE II.D.2 (Continued.)

Parameter	Value
Anchor	
Anchor Plasma Radius, r_{anch} (cm)	122
Anchor Effective Length, L_{eff} (cm)	211
Sloshing Beam Trapping Fraction (%)	33
Sloshing Ion Energy, $E_{slosh,anch}$ (keV)	150
Hot Ion Density, $n_{slosh,anch}$ (cm^{-3})	1.5×10^{13}
Anchor Ion Confinement Parameter, $(n\tau)_{i,anch}$ (s cm^{-3})	$6. \times 10^{12}$
Anchor Floating Potential, ϕ_{anch} (keV)	152

Power Balance	Trapped	Incident
Axicell Sloshing Beam Power (MW)	48.6	156
Anchor Sloshing Beam Power (MW)	8	24.2
Axicell Charge Exchange Pumping Power (MW)	212	228
ECRH Power Applied to Barrier Minimum (point b) (MW)	97	108
ECRH Power Applied to Potential Peak (point a) (MW)	82	91
Fusion Power (MW)	3000	
Neutron Wall Loading (MW/m^2)	2	
Plasma Q (P_{fus}/P_{inj})	6.7	5.0
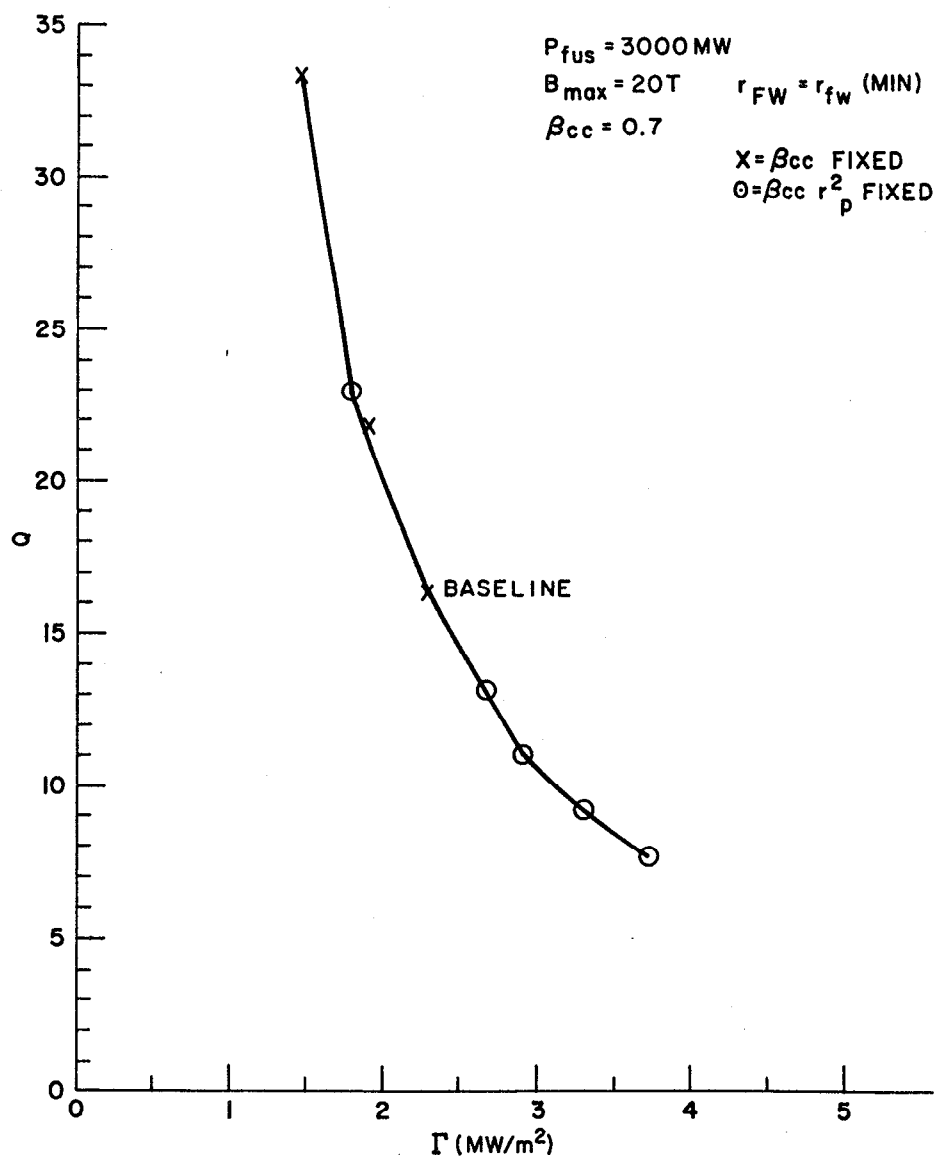
Fig. II.D.1 Q versus Γ for the 20-T axicell driver.

There are several means by which the (Q,Γ) curve can be swept out, the easiest is to change the central-cell plasma radius keeping central-cell magnetic field, fusion power, and central-cell beta value fixed. This method is acceptable for wall loadings below the baseline, for it means the end-cell plasma gets smaller, allowing it to fit inside the given coil set. However, if the baseline end-cell plasma size is the largest it can be for a given coil set, this method is unacceptable to achieve higher wall loadings. For the higher wall loadings, the amount of magnetic flux which is mapped into the end cell is conserved. This is done by varying central-cell plasma radius and central-cell magnetic field in such a way that $B_{cc}r_{cc}^2$ is preserved. Both methods are shown on Fig. II.D.1, the former shown as "X"s, the latter as "O"s. It appears that they follow the same curve fairly closely. Other methods are possible, such as varying central-cell beta value while keeping fusion power and magnetic field fixed, or increasing fusion power at a fixed central-cell length and field, but these will not be pursued here.

Figure II.D.2 shows the (Q,Γ) curve for the 14T Axicell Case, at 3000 MW fusion and 70% for β_{cc}. The degradation in plasma Q by going to lower field is quite evident at all wall loadings.

An important parameter for determining the performance of a tandem mirror driver is the plasma pressure sustainable for a given magnetic field in the central cell. The physics code was run varying β_{cc} from 0.7 to 0.2. This variation is important because it can show the sensitivity of system cost and performance on the prediction of different models for MHD stability, i.e., interchange versus ballooning (Section II.G.2). In these runs, the plasma pressure was held constant ($\simeq \beta_{cc}B_c^2$ fixed), and the product $r_{cc}^2 B_{cc}$ is held fixed (plug size fixed). Keeping pressure fixed essentially fixes density. This fact, along with the fact that mirror ratios and potentials in the barrier remain almost constant, the passing density in the barrier remains the same. Since this density and the plug volume are fixed, so is the injected power, which fixes Q. From a systems analysis point of view, however, there will be a cost penalty associated with the higher central-cell field ($B_{cc} \sim 1/\sqrt{\beta_c}$) and longer central-cell length, ($L_{cc} \sim B_{cc}$). The result of this penalty will be examined in Section IX.E.

The sensitivity of plasma Q on the sloshing beam injection energy is shown in Fig. II.D.3. For sloshing beams which are well confined, the sensitivity of Q on $E_{inj,a}$ is weak. However, as one reduces the injection energy to the point at which the confinement is poor ($\sim$ 125 keV), Q is a very strong function
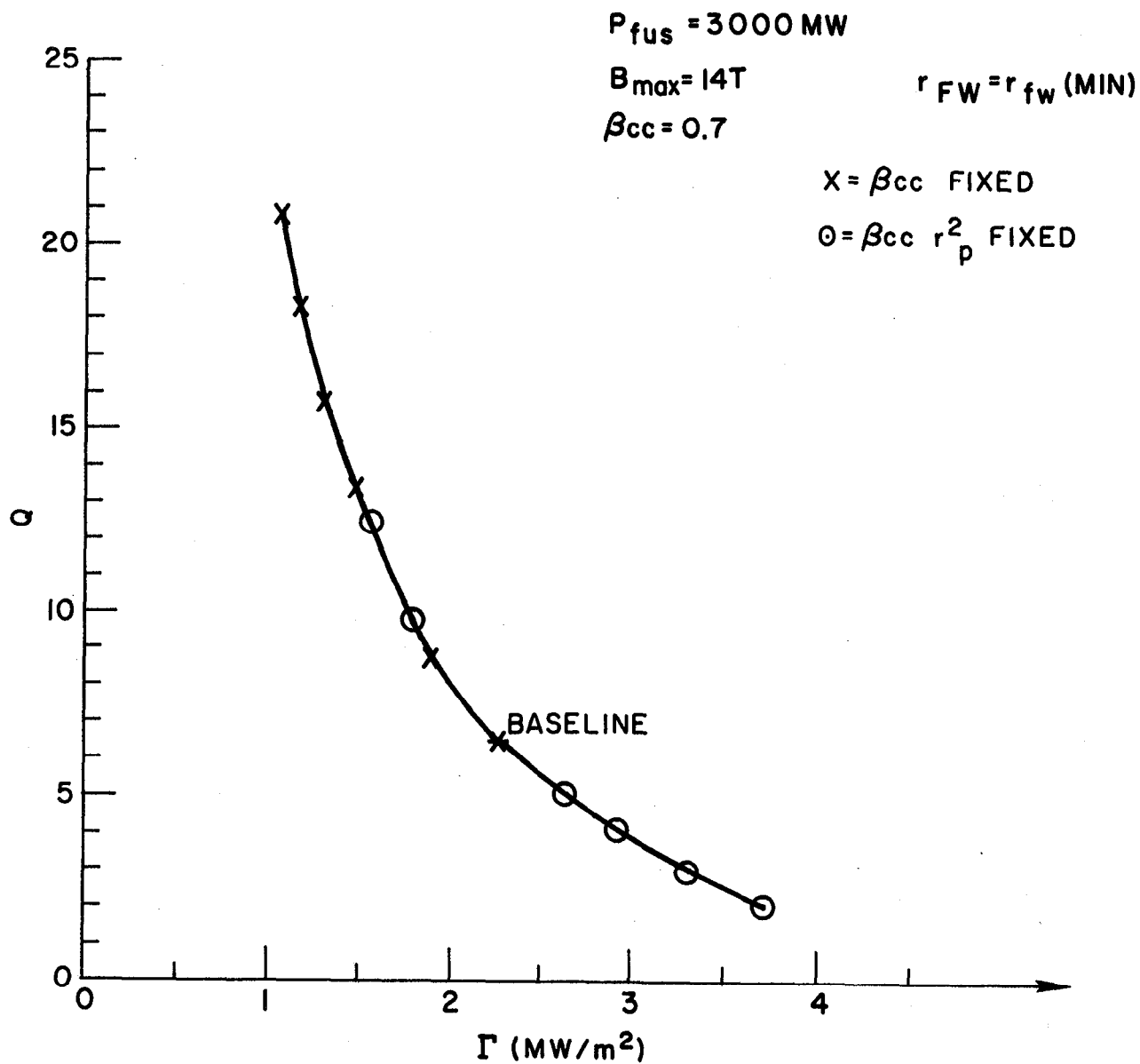
Fig. II.D.2 Q versus Γ for the 14-T axicell driver.
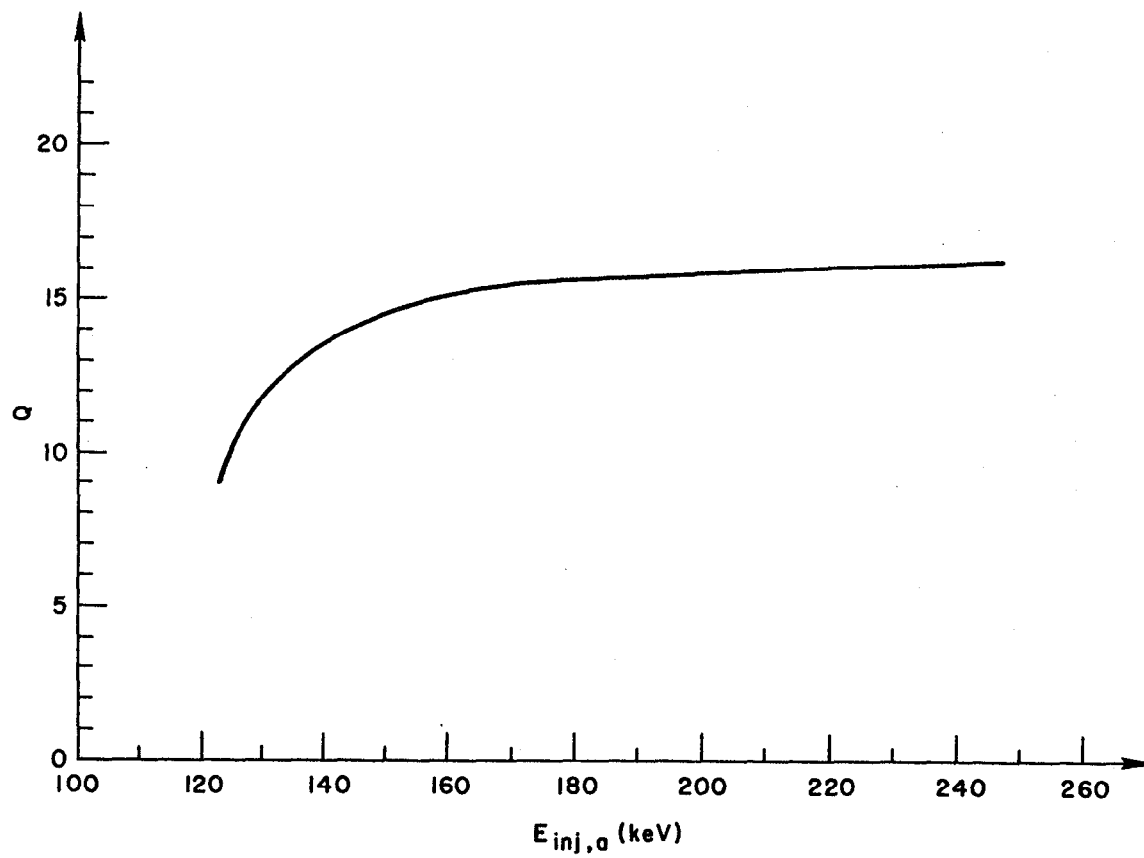
Fig. II.D.3   Sensitivity of plasma Q on sloshing-ion injection
energy, Einj,a.

of $E_{inj,a}$. Even for the lowest sloshing beam injection energies, the high energy pump beam will require about 200 keV energy, so this sensitivity curve does not suggest that positive ion injection can be used at higher efficiency than the 35% characteristic of the 200 keV system.

A parameter which is a measure of the effectiveness of the thermal barrier is the ratio of the cold electron density at the barrier minimum, to the total (cold plus hot) electron density there, called F_{ec}. The smaller the value of F_{ec}, the better the performance of the machine. There are lower bounds on F_{ec} which cannot be violated. One consideration is the minimum value at which the hot electrons do not have a sufficient fueling source of cold electrons to establish their density. Another constraint which must be observed is to have enough cold electron plasma to avoid microinstabilities driven by the aniso-tropic hot electrons. It is presently not known what the minimum F_{ec} is, so it is important to determine the sensitivity of plasma and hybrid system performance on varying F_{ec}. Figure II.D.4 shows plasma Q versus F_{ec}, with the baseline case also shown.

As described in Section III.C.1, the negative ion beam program is at present modest. It is, therefore, of interest to determine the hybrid cost penalty associated with a reduction of beam injection energy to a value which can be produced using positive ions. A 200 keV positive ion beam can be converted to neutrals at a 35% efficiency (II.D.1), which includes magnetic separation to achieve the energy purity of negative ion beams.

Considering a case with sloshing beams and high energy pump beams at 200 keV, the reduction in plasma performance is actually quite modest, Q drops only ∿ 2%. Whether this system has comparable cost results (with lower beam efficiency) is another question, which will be addressed in detail in the parametric analysis Section IX.E. It turns out that the positive ion case is quite close to the baseline, the capital cost of the breeder increases by ∿ 2%, cost of U_3O_8 increases by ∿ 10% and symbiotic electricity cost increases by ∿ 2%.

The performance of a "low technology" axicell case is next considered; the important parameters are presented in Table II.D.3. This case considers a 12T circular coil, 200 keV neutral-beam injection (positive ions at 35% efficiency), and a conservative physics assumption of a central-cell beta of 40%. The performance of this machine is rather poor, having a plasma Q value of only 3.3, at a wall loading 1.4 MW/m^2. There are large supplementary
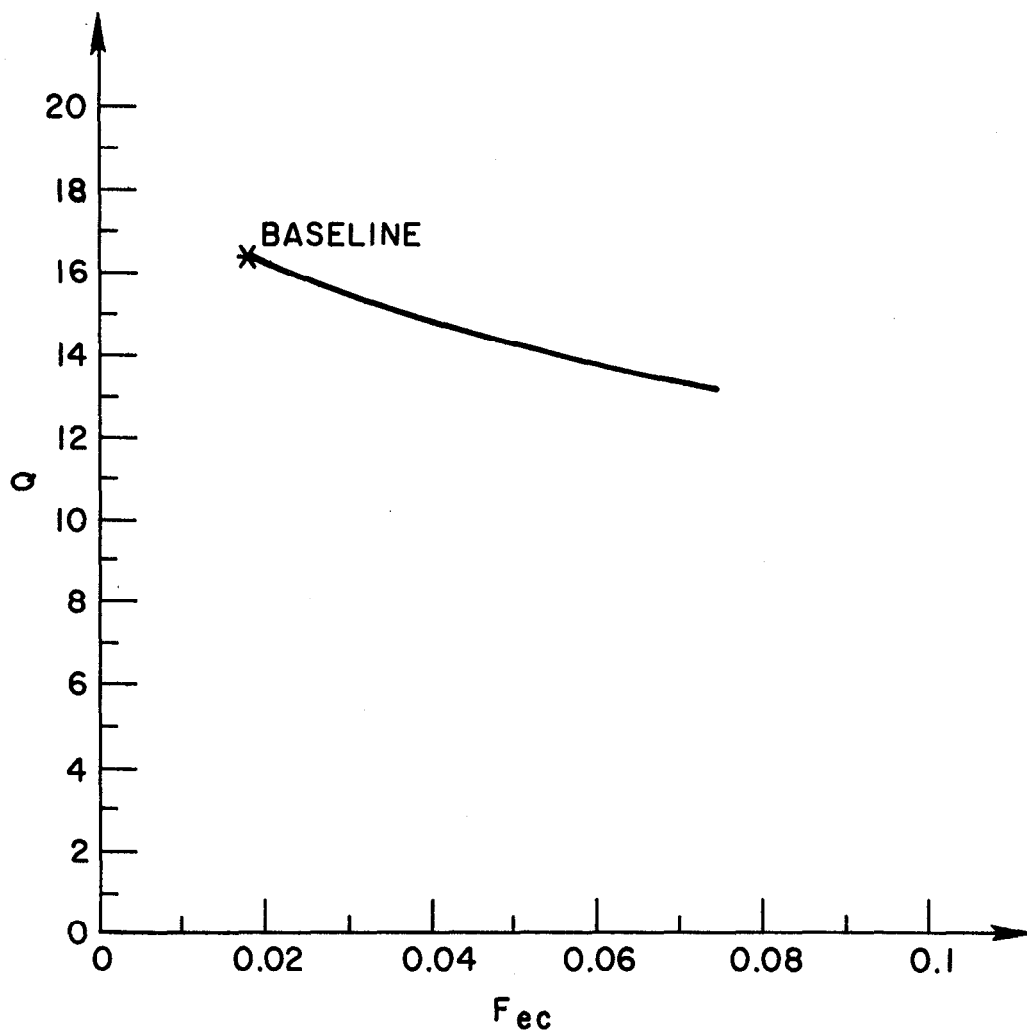
Fig. II.D.4 Q versus F_{ec}, the fraction of cold electrons at the barrier midplane.

TABLE II.D.3. Physics Parameters for the "Low Technology" Axicell Case

Parameter	Value
Central Cell	
Density, n_c (cm^{-3})	9.6×10^{13}
Ion Temperature, T_c (keV)	40
Electron Temperature, T_{ec} (keV)	31
Plasma Radius, r_{cc} (cm)	179
Vacuum Magnetic Field, $B_{c,vac}$ (T)	3
Beta, β_c	0.4
Floating Potential, ϕ_e (keV)	219
Cold Fueling Current, I_c (kamps)	2.2
Ion Confinement Parameter, $(n\tau)_i$ (s cm^{-3})	7.9×10^{14}
Electron Confinement Parameter, $(n\tau)_i$ (s cm^{-3})	6.9×10^{14}
First Wall Radius (cm)	206
Central Cell Length (m)	129
Axicell/Barrier	
Maximum Hybrid Coil Field B_{max} (T)	12
Sloshing Ion Injection Energy, $E_{inj,a}$ (keV)	200
Vacuum Magnetic Field at Barrier Minimum (point b) (T)	2.7
Total Barrier Beta $(\beta + \beta_{||})$	1.2
Perpendicular Barrier Beta, β	0.77
Passing Ion Density at Point "b", $n_{pass,b}$ (cm^{-3})	3.9×10^{12}
Hot Electron Energy at Point "b", E_{eh} (keV)	1034
Warm Electron Energy at Point "a", T_{ew} (keV)	63
Barrier Length, L_B (m)	12
Cold Electron Density Fraction, F_{ec} (%)	0.52
Sloshing Beam Trapping Fraction (%)	51
Pump Beam Trapping Fraction (%)	79
Beta at Point "a", β_a	0.525
Barrier Potential Dip, ϕ_b (keV)	198
Ion Confining Potential, ϕ_c (keV)	122

TABLE II.D.3 (Continued.)

Parameter	Value
Anchor	
Anchor Plasma Radius, r_{anch} (cm)	225
Anchor Effective Length, L_{eff} (cm)	138
Sloshing Beam Trapping Fraction (%)	52
Sloshing Ion Energy, $E_{slosh,anch}$ (keV)	150
Hot Ion Density, $n_{slosh,anch}$ (cm^{-3})	1.5×10^{13}
Anchor Ion Confinement Parameter, $(n\tau)_{i,anch}$ (s cm^{-3})	5.87×10^{12}
Anchor Floating Potential, ϕ_{anch} (keV)	162

Power Balance	Trapped	Incident
Axicell Sloshing Beam Power (MW)	207	405
Anchor Sloshing Beam Power (MW)	18.3	35
Axicell Charge Exchange Pumping Power (MW)	317	400
ECRH Power Applied to Barrier Minimum (point b) (MW)	339	377
ECRH Power Applied to Potential Peak (point a) (MW)	26.5	30.
Fusion Power (MW)	3000	
Neutron Wall Loading (MW/m^2)	2	
Plasma Q (P_{fus}/P_{inj})	3.3	2.4

heating powers required, particularly critical is the ECRH power applied at the barrier potential minimum, since it has a large cost per unit power. The results of Section IX.E shows that the equivalent cost of U_3O_8 for this system is larger than the baseline 20T case by about 370%, taking the lithium/ molten-salt blanket as an example. Comparing this case with the high field but low beam technology case, we see that the impact thjat a low peak magnetic field and low beta have on performance is much greater than any effect that positive ion technology has.

It appears that the requirement that Q > 4 for acceptable hybrid performance claimed in our previous tandem mirror hybrid study (1979) is overly optimistic. The minimum Q for good hybrid performance is an increasing function of the cost of supplementary heating. In the previous study, supplementary heating was costed at just above $0.50/watt delivered, whereas for the present study neutral beams are assumed to cost $1.50 and ECRH $3.00 for each watt of delivered power. If we were to propose a relationship between the minimum Q value needed, Q_{min}, and the average cost per unit power of supplementary heating, S_{avg}, it would look roughly like $Q_{min} \simeq 8 S_{avg}$. The variable S_{avg} is the sum of the beam and ECRH costs weighted by the fraction of the total power each comprises. Using this prescription, $Q_{min} \simeq 14$ for the baseline 20T hybrid case presented in Table II.D.1; suggesting that the baseline Q of 15.3 places the device within the acceptable regime.

All the previous point cases and parametrics have considered only the driver using the axicell endplug design. We now present some Q versus Γ results for the MFTF-B A-cell endplug design, shown in Fig. II.B.4. Figure II.D.5 shows the characteristic Q versus Γ curve for a TMHR which is scaled analytically from the A-cell version of TMNS (II.B.14). In this curve, the plug plasma size remains approximately fixed by keeping $B_{cc}r_{cc}^2$ constant. The results shown in this figure will be used to generate cost versus wall loading for the A-cell end cell case to be compared to the axicell results.

The message to carry away from this section is that as far as plasma performance is concerned, high neutral-beam injection energies are not nearly as critical as high magnetic field strengths. This conclusion leads one to suggest that the axicell fusion driver might be able perform satisfactorily with positive ion beam technology. If energy purity is obtained with magnetic separation, and direct conversion is applied to the unneutralized beam, 35% efficiency can be obtained for pure 200 keV positive ion beams. Analysis
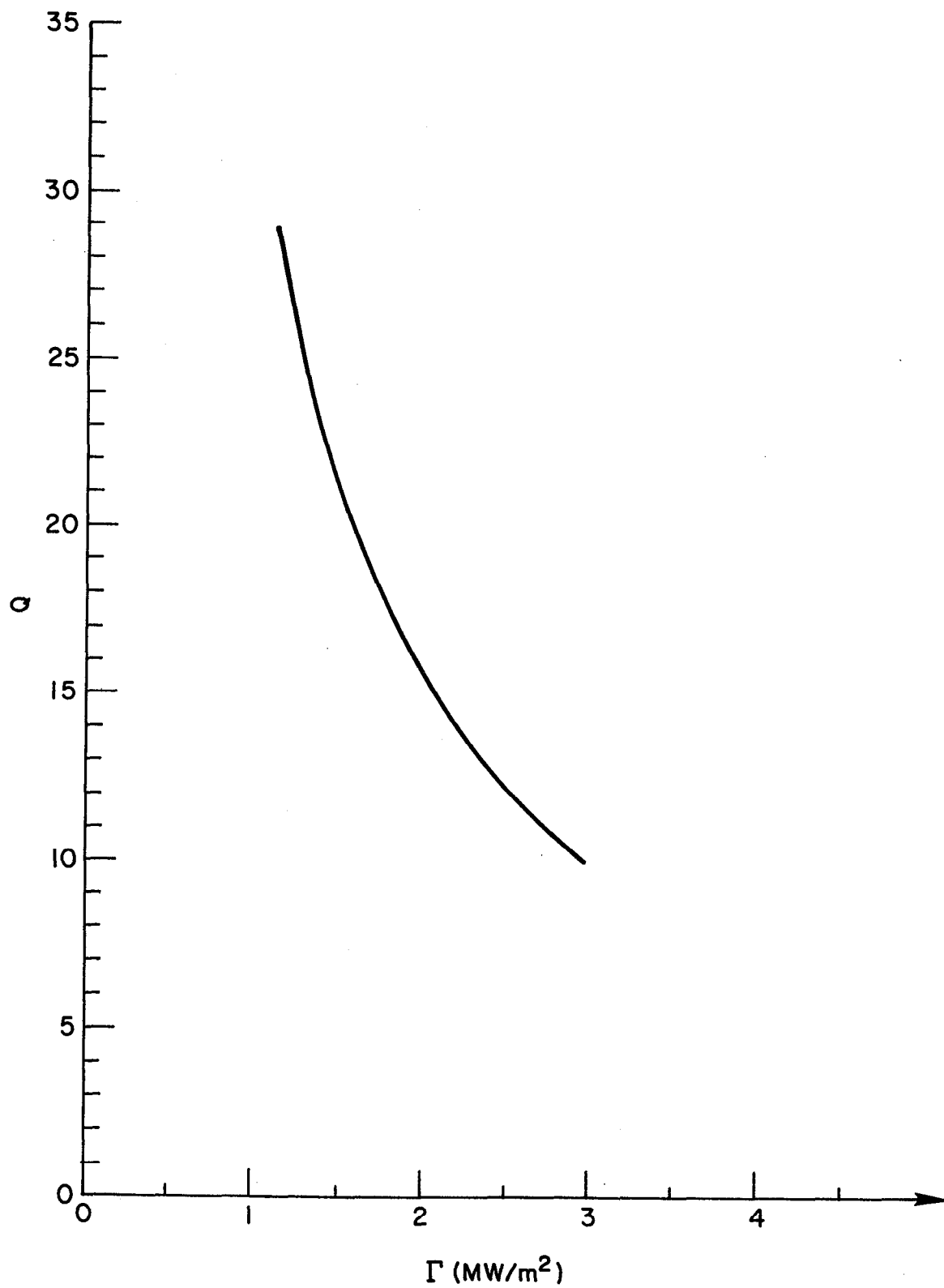
Fig. II.D.5 Q versus Γ for the MFTF-B A-cell end-cell configuration.

presented in Section IX.E will show that the penalty paid to use positive ion beam technology is not severe. This is not to say that negative ion neutral beams should not be developed, since a more desirable end-plug configuration conceptualized sometime in the future may need them.

II.E. HALO PLASMA

A cool halo plasma is needed to protect the hot, reacting plasma from gas and sputtered metal atoms released at the wall. Without a halo plasma, impurity ions would accumulate because their greater charge would cause them to be much better confined axially than fuel ions. Also, each high-Z ion would contribute Z cold electrons. The exchange of cold electrons for hot ones causes a loss of power.

The thickness of the halo in the central cell is 0.2 m, and this thickness must equal several mean free paths for the ionization of incoming molecules. Since the probability of ionization of a D_2 molecule by 200 eV electrons is about $<\sigma v_e> = 5 \times 10^{-14}$ m^3/s, this condition requires an electron density of about $n_e \simeq 10^{18}$ m^{-3}.

II.E.1 Electrical Potential of the Halo

Because the electrical conductivity of the halo plasma along the field lines is high, the potential of the halo is only on the order of a few kT_e, relative to the end wall of the halo plasma. The electrical resistance from one end of the halo to the other is $R = \eta L/2\pi rw$, where η is the resistivity, L is the length, r is the mean radius, and w is the thickness of the halo. At $n_e = 1 \times 10^{18}$ m^{-3} and $T_e = 200$ eV, $\eta = 3 \times 10^{-7}$ ohm-m and $R < 10^{-4}$ ohm. Therefore, the expected current, $I < 10^3$A, in the halo produces a drop in potential along the halo that is negligible. An additional drop exists across the sheath where the halo contacts the end walls.

II.E.2 α-Particles in the Halo

We assume that the α-particles are pumped out radially from the barrier cell plasma and into the halo. The α-particles are produced by fusion reactions in the central cell. Those αs that are not born in the loss cone for the magnetic mirrors initially are magnetically confined in the central

cell. As they cool on the electrons, their cross section for scattering on ions increases. At an average of about 100 keV they are scattered into the loss cone and become passing ions, passing through the barrier cell and reflecting from the positive potential ϕ_c. Only a very small amount of additional scattering while inside the barrier cell can leave an α particle trapped there. This is the ultimate fate of nearly all central-cell α's. These trapped α's must be removed from the barrier in order to keep the density and potential low there. We assume that either grad-B pumping or resonant magnetic pumping selectively removes these α's radially out to the halo. Since there is no confining potential in the halo, the α's stream freely along the field lines in the halo to the dump in the end tanks. They all go out the nearest end because they are reflected by the stronger magnetic mirror on the central-cell side of the barrier.

Each α particle spends about 20μs in the halo before reaching the end. In that time, each α gives up about 100 eV to the halo electrons, for a power input to the halo of about 8 kW in each end.

A much greater heating of the halo is produced by those hot α's in the central cell whose guiding centers are close enough to allow them to pass through the halo. As an α slows down, its energy decreases at a constant rate. On the average, then, the α energy is half of 3.5 MeV, and the perpendicular energy is $\frac{2}{3}$ of that. The average orbit size is, therefore, 0.05 m, and about 1.6×10^{-3} of the central-cell α's exist within that distance from the halo. (This assumes a cubic density profile, and an α density proportional to the square of that.)

The 95% of the α's that are born outside the loss cone give up most of their 570 MW of power to central-cell electrons. About 1.6×10^{-3} of the α's spend about $\frac{1}{4}$ of their time in the halo. Since the rate of cooling by electrons varies approximately as $n_e T_e^{-3/2}$, the cooling rate in the halo is about $(10^{18}/10^{20})(32/0.2)^{3/2} = 20$ times faster than in the hot plasma. Therefore, most of the 0.9 MW of α power generated in the outer layer is transferred to the halo electrons.

II.E.3 Fueling the halo

The halo plasma must be externally fueled because the natural input of gas and metal vapor is too low. To avoid contaminating the hot plasma, the halo is

fed only D_2 gas, which is ionized by electrons, and then heated by the hotter electrons. The rate of gain of energy by the ions is:

$$\frac{dU}{dt} = \frac{Z^2 e^4 nm \ln \Lambda}{2\pi \epsilon_0^2 M \sqrt{2\pi mkT_e}} \quad ,$$

where U is the ion energy, Z is the charge number, M is the ion mass, and n, m and T_e are the electron density, mass and temperature. We use mks units where $\epsilon_0 = 8.85 \times 10^{-12}$ f/m, and take $\ln \Lambda \simeq 15$. For D^+ ions in a halo where $n = 1 \times 10^{18}$ m^{-3} and $kT_e/e = 200$ eV,

$$\frac{dU}{dt} = 2.5 \text{ keV/s}$$

per ion.

The flow of ions out each end of the halo is:

$$I = nvA_m e/4,$$

where v is the average ion velocity, and A_m is the minimum cross-sectional area of the halo at the magnetic mirrors. Or, in terms of the life time τ of the halo ions, the flow out both ends is:

$$2I = nA_c Le/\tau,$$

where the product $A_c L$ is the volume of the halo between the strong mirrors. Therefore, $v\tau = 2A_c L/A_m$. Also, the mean ion energy U is $U = (\frac{dU}{dt})\tau$, and $Mv^2/2 \simeq U$. Solving for v, we obtain:

$$v^3 = (2RL/M)(\frac{dU}{dt}),$$

where we have set $R = A_c/A_m = B_m/B_c$, the mirror ratio from the central cell.

In the present case, $R = 20T/3T$, $L = 130$ m, $M = M_D$, and $\frac{dU}{dt} = 2.5$ eV/s. Therefore, $v = 5.9 \times 10^4$ m/s, $U = 37$ eV, $\tau = 0.029$ s, and $I = 570$ A of ions per end.

II.E.4 Power flow in the halo

The input of power to the halo is 0.9 MW from central-cell α's, and 15 kW from the α's after they are expelled from the barrier cells. About 15 eV per ion (30 eV per molecule) is required to ionize the halo fuel. Each fuel ion is then heated to about 2U = 75 eV before it reaches the dump. For each ion that leaves the halo, a 200 eV electron must also leave. The power required to maintain the halo is, therefore, only:

$$P_{halo} = 2 \times 570 \text{ A} \times (90 \text{ V} + 200 \text{ V}) = 330 \text{ kW,}$$

and most of the 0.9 MW of heating by α's must be conducted away by the recycling of cold, secondary electrons.

For comparison, the power that was calculated (II.E.1) to be needed for a halo plasma in the single-ended Fusion Engineering Research Facility (FERF) was 120-360 kW. There, an array of hollow cathode discharges surrounded the plasma. We have assumed here that the losses from the halo are due mostly to streaming out the ends, and that the greater length here requires no additional power. Charge neutrality in steady state requires that the net electron current out of the halo must equal the ion current. The excess of hot electron current over ion current leaving the halo is balanced by a current of cold secondary electrons back in. The electron temperature, and therefore the sheath potential at the halo ends, will adjust until the currents and the power input and output balance. Detailed calculations are required to tell whether the T_e = 200 eV assumed here is correct. Calculations of the self-consistent halo are in progress.

II.E.5 Pumping the halo gas

In addition to the halo fuel ions, also streaming out each end of the halo is one half of the α's that result from the fusion reactions and that are not created within the magnetic loss cone. The α-current out each end is, therefore:

$$I_\alpha = 0.95 \times (2P_F/E_F) \times \frac{1}{2} = 160 \text{ A.}$$

At the halo dumps in the end tanks (see Fig. III.A.4,3), the halo ions become gas molecules and must be pumped to maintain the vacuum. These dumps are enclosed as much as possible to allow more efficient pumping of the halo gas and we call these structures "skimmers". The skimmers are located in the end tanks where the magnetic field strength has fallen to about 0.3T, allowing the halo thickness to increase to about 0.6 m, and the cross sectional area to 15 m^2. The conductance for the gas to leave through the annular entrance channel is:

$$C = C_0(1 + 3\ell/8w)$$

where the length of the channel is ℓ = 1.2 m, and the width is w = 0.6 m. C_0 is the conductance of an aperture of the same area A through a thin wall:

$$C_0 = Av_0/4,$$

where v_0 is the average velocity of the molecules:

$$v_0 = \sqrt{8kT_0/\pi M_0} \ .$$

For the gas temperature T_0 we assume a value $T_0 \simeq$ 300 K as an approximate average of the 77 K of the chevrons, the $\sim$ 300 K of the enclosure, and the hotter surface of the dump. This gives C_0 = 4.5 x 10^3 m^3/s and C = 2.6 x 10^3 m^3/s for the conductance back out of the enclosure.

The pumping speed S of the cryopump inside the enclosure must be comparable to or greater than C to prevent the halo gas from adding significantly to the gas load in the end tanks. A cryopanel with two sets of chevrons has a specific pumping speed of about S_0 = 40 m^3/s-m^2 for a mixture of D_2 and He at 300 K, if the cryopanel is equipped with argon jets to cryotrap the helium (II.E.2).

We set S = C by making the cryopanel area A_{cry} = C/S_0 = 65 m^2. Then, if p is the pressure inside the enclosure and p_0 = 2 x 10^{-5} Torr is the pressure in the end tank, the total flow rate out of an enclosure is:

$$Q = (p - p_0) C + pS.$$

In steady state, Q must also equal the rate of input which is Q = 730 A = 64 Torr - ℓ/s. This gives p = 2.2 x 10^{-5} Torr and a flow out through C into the end tank of only 6 Torr-ℓ/s, less than 10% of the halo gas, and only a very small additional load on the end tank vacuum system.

Since the halo gas is kept rather well isolated from the the end-tank gas, the halo cryopumps receive very little tritium and all except about 15% of the helium. These are important facts because it is more complicated to periodically degas a helium-pumping cryopump than a more conventional one. This is because of the much higher temperature required to remove the argon than hydrogen isotopes.

Cost of the halo skimmers is discussed in Sec. III.A.4,8.

II.F. WALL BOMBARDMENT

The heat load on the inside surface of the first wall is due almost entirely to three effects other than that of the 14 MeV neutrons. Bremsstrahlung dominates, cyclotron and line radiation are small, radially diffusing α particles are probably unimportant, while charge-exchange neutrals and radially diffusing plasma are negligible. A convenient reference value is the ∿10W/cm^3 of heating in stainless steel in transmitting 1MW/m^2 of 14MeV neutrons.

The plasma radiates like a black body at a temperature T_e in the frequency range below the plasma frequency ω_p, where it is optically thick. For frequencies $\omega \gg \omega_p$, the plasma is transparent and the radiation per unit frequency is small compared to that of a black body. However, the range of frequency is infinite and the total radiation in this range is significant. Typically, the electron cyclotron frequency ω_{ce} is comparable to ω_p, and radiation at the higher harmonics of ω_{ce} is only partially reabsorbed. The total cyclotron power produced per unit volume of plasma is (II.F.1,2,3):

$$W_c = \frac{\omega_{ce}^2 \omega_p^2 kT_e}{3\pi c^3}$$

if the electrons are not strongly relativistic. Here T_e is the electron temperature and c is the velocity of light. We assume a cylindrical plasma of length L and a radial density profile that decreases as -r^3 to zero at r = r_c. We use the "long, thin" approximation and integrate $n_e B^2$ over the plasma volume to obtain:

$$w_c dV = (67 \text{kW/m}^3) \, \frac{4-3\beta}{\beta} \left(\frac{n_{eo}}{10^{20} \text{m}^{-3}}\right)^2 \left(\frac{T_e}{30 \text{ keV}}\right)^2 (\pi r_c^2 L),$$

where $\beta = 2\mu_0(n_{io}kT_i + n_{eo}kT_e)B_0^{-2}$ and we set $n_{io}T_i = n_{eo}T_e$ here.

Most of this power is reabsorbed in the plasma. The fraction K_L that actually leaves the plasma has been calculated in Ref. II.F.2 as a function of the dimensionless plasma size $L = r_c \omega_p^2/c\omega_{ce}$, and is plotted in Fig. II.F.1. Wall reflections can be taken into account by increasing L by a factor $(1-R)^{-1}$, where R is the reflection coefficient. Since K_L is nonlinear in L, setting R = 0.9 only reduces the power absorbed at the wall by 1/4. The power absorbed at the wall is:

$$S_c = (67 \text{kW/m}^3)(K_L)\left(\frac{4-3\beta}{\beta}\right)\left(\frac{n_{eo}}{10^{20} \text{m}^{-3}}\right)^2 \left(\frac{T_e}{30 \text{ keV}}\right)^2 \left(\frac{r_c^2}{2r_w}\right)$$

where K_L is typically < 0.01 (see Fig. II.F.1).

Bremsstrahlung produces a spectrum (W/Hz) that is roughly constant for photon energies up to the electron energy, and then drops rapidly to zero above that. Most of the radiation is therefore in the x-ray range where the plasma is completely transparent, and where reflection by the walls is negligible. The total power radiated as bremsstrahlung per unit of volume of plasma is (II.F.3):

$$w_x = 4.8 \times 10^{-37} Z^2 n_i n_e T_e^{1/2} \text{ Watts/m}^3$$

where T_e is in keV, n_i and n_e are in m^{-3}. When integrated over the plasma volume, again assuming a cubic radial density profile, this results in a power density at the wall of:

$$S_x = 2.2 \times 10^{-37} Z^2 n_{io} n_{eo} T_e^{1/2} r_c^2/2r_w.$$

We assume that Z = 1 and $n_{io} = n_{eo}$. Then,

$$S_x = (12 \text{kW/m}^2)\left(\frac{n_{eo}}{10^{20} \text{m}^{-3}}\right)^2 \left(\frac{T_e}{30 \text{ keV}}\right)^{1/2} (r_c^2/2r_w).$$

The heat load due to the bombardment of the wall by alpha particles is difficult to estimate because it depends critically on the rate that energetic (> 1 MeV) alphas diffuse radially out of the plasma. Only the most energetic
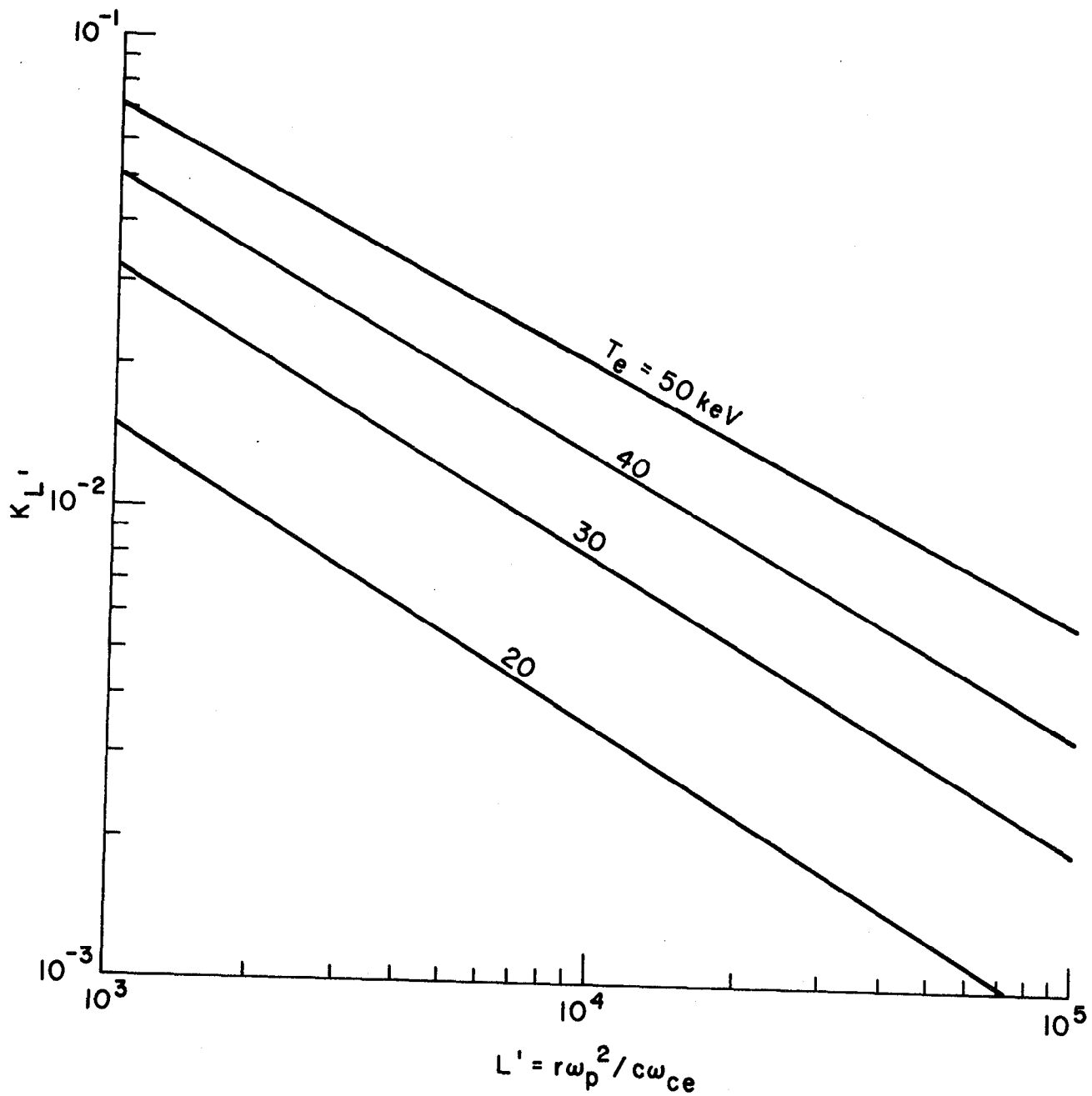
Fig. II.F.1   Transparency coefficient K_L for cyclotron radiation in a plasma slab.   After B. A. Trubnikov and V. S. Kudrayavtsev.

alphas have any significant probability of diffusing across the halo plasma and striking the wall before they scatter in angle into the loss cone and go out the ends. Most of the alphas enter the halo plasma only after losing most of their energy to plasma electrons. Since there is no strong electric field in the halo, an alpha particle will move radially about one gyroradius in one 90 scattering time. Therefore, the probability P that an alpha will move radially a distance d in one scattering time is about:

$$P \simeq \exp(1-d^2/a^2)$$

where a is the gyroradius. Or, if d is equal to two gyroradii for 3.5 MeV alphas,

$$P \simeq \exp(-14 \text{ MeV}/w_\alpha),$$

where w_α is the energy of the alpha particle as it enters the halo.

An estimate of the heating of the wall by alphas requires an analysis of the diffusion of energetic alphas in the hot plasma. However, we can easily determine the maximum possible heating. If all of the alphas that are produced were to strike the wall with their full initial energy of 3.52 MeV, the power density at the wall would be:

$$S_{\alpha,max} = \Gamma/4$$

where $\Gamma \simeq 2 \text{MW/m}^2$ is the neutron wall load. Typically then $S_{\alpha,max} \simeq 500 \text{ kW/m}^2$. The actual value of S_α will be much less than this amount because most of the alpha power must be transferred to the plasma. Since the probability P drops so fast with decreasing α-energy, we expect $S_\alpha \simeq 0$.

Similarly, wall heating by plasma ions and electrons is negligible because of the small orbit sizes. Heating by line radiation from impurity ions in the halo is also negligible (mainly because the photon energies are small) even though the frequency of excitation and the density of impurity ions are significant. We estimate $n_{F_\ell} \simeq 10^{15}$-to-$10^{16}$ m^{-3}, $\nu_{ex} \simeq 5 \times 10^4$ s^{-1} in the halo giving $S_{line} \simeq 0.5 \text{ kW/m}^2$. Also, heating by charge-exchange neutrals is insignificant in the steady state except near regions of deliberate gas input. Therefore, bremsstrahlung is the main heating mechanism, and it results in only about $S_x \simeq 10 \text{ kW/m}^2$.

In summary, the heating of the first wall by processes other than neutron heating is approximately:

Bremsstrahlung	10 kW/m^2
Cyclotron	1 kw/m^2
Radially diffusing α's	0
Radially diffusing plasma	0
Impurity line radiation	0.5 kW/m^2

II.G PLASMA PHYSICS ASSESSMENT

This section briefly reviews: (1) the very recent progress made in mirror experiments, and expectations of planned experiments; (2) issues facing the mirror theory effort; and (3) the current direction tandem mirror reactor physics seems to be taking, and how these new developments will effect the reference design point of the TMHR chosen in this study. The timely introduction of both hybrid and pure fusion reactors depends upon the scheduling of major experiments and the solution of pressing problems in tandem mirror plasma physics.

II.G.1 Tandem Mirror Experiments

Within the last five years in the mirror program, considerable progress has been made in both the development of new mirror concepts, and in obtaining encouraging results in present experiments and anticipated encouraging results in planned experimental devices. We shall concentrate on the progress regarding tandem mirrors, the remainder of the mirror experimental program is reviewed in the recent article by Simonen (II.G.1).

The Tandem Mirror Experiment (TMX) at LLNL began operation in FY 1979 and has demonstrated the basic operation of a tandem mirror. The machine is shown in Fig. II.G.1 and consists of an axial array of solenoid magnets with a "plug" attached to each end. The plugs consist of minimum $|\underline{B}|$ high magnetic field "yin-yang" magnets. Intense neutral-beam injection at a few tens of kilovolts in these plugs sustains the density there above that in the solenoid by a factor of 2 to 4. This density difference is necessary in order to produce the potential peak which in principle confines solenoid ions for many ion-
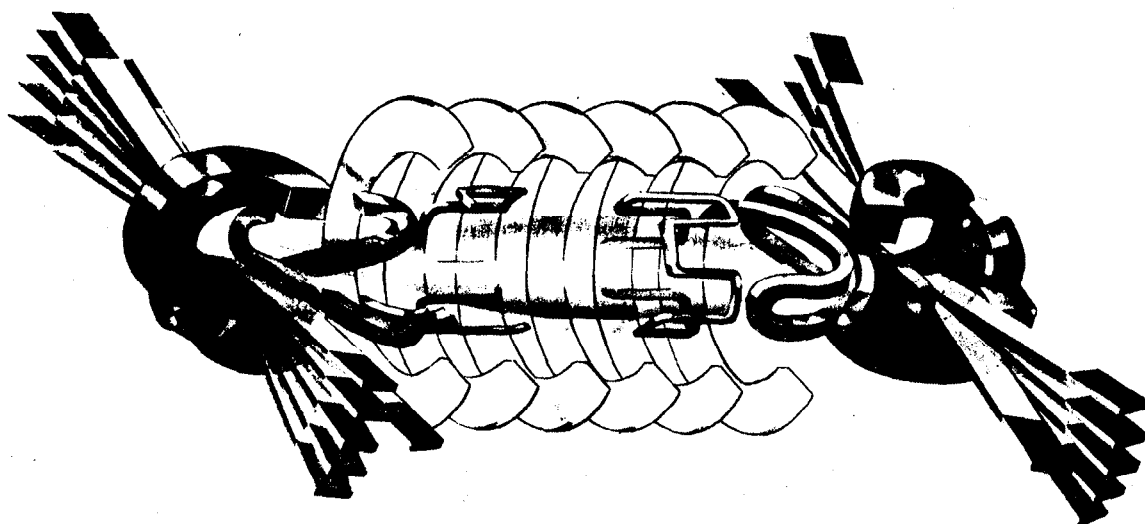
Fig. II.G.1 Tandem Mirror Experiment (TMX).

ion collision times. Figure II.G.2 shows the profiles of density, n, potential, ϕ, and magnetic field strength, $|\underline{B}|$, in a tandem mirror such as TMX.

Table II.G.1 shows some typical experimentally obtained parameters (II.G.1, II.G.2) from TMX. Note that the potential barrier for ions is from 1 to 3 times the ion temperature. For a hybrid or pure fusion reactor, this number should be from 2.5 to 3.5. Note also that the ratio of plasma pressure to magnetic field pressure (β) in the solenoid is 0.2, and a value twice this locally was attained in the presence of neutral-beam injection. Practical hybrid reactors need at least $\beta \sim 0.4$ in the solenoid.

There are two other tandem mirror experiments in operation at the present time. They are GAMMA6 at the Tsukuba University in Japan, and the Phaedrus device at the University of Wisconsin. There is another tandem known as AMBAL-1 nearing completion at Novosibirsk in the Soviet Union. Reference II.G.1 discusses these other devices in more detail. A proposal for a new tandem mirror device (II.B.8) known as TARA, was recently submitted to the Department of Energy by a group at MIT. This experiment will test an advanced end-plug design called an "Axicell", which will replace the yin yang used on TMX. This configuration has attractive features, and has been adopted as the end-plug design for the baseline TMHR fusion driver. The basic concept was described in Section II.B.2.

TMX has, in its short lifetime, accomplished all the goals it was designed to achieve. These goals are:

● Demonstration of the establishment and maintenance of an electrostatic potential well for ions between two mirrors.

● Development of a scalable magnetic geometry while maintaining macrostability at high beta.

● Investigation of the microstability of the end-cell and solenoid combination to maximize the density to power ratio in the end cell.

The investigation of microstability dealt with the issue of whether a sufficient cold plasma component streaming from the solenoid could stabilize modes associated with the non-Maxwellian "loss cone" nature of the ion distributions in the yin yangs. The streaming component was found insufficient to thoroughly eliminate RF activity (due to microinstabilities) and has motivated a search for other means to stabilize microinstabilities.

TMX has now been dismantled, and is currently being converted to an upgraded version, TMX-U (II.C.2). Figure II.G.3 shows a schematic of the new machine's magnet configuration. The end plugs have been re-designed
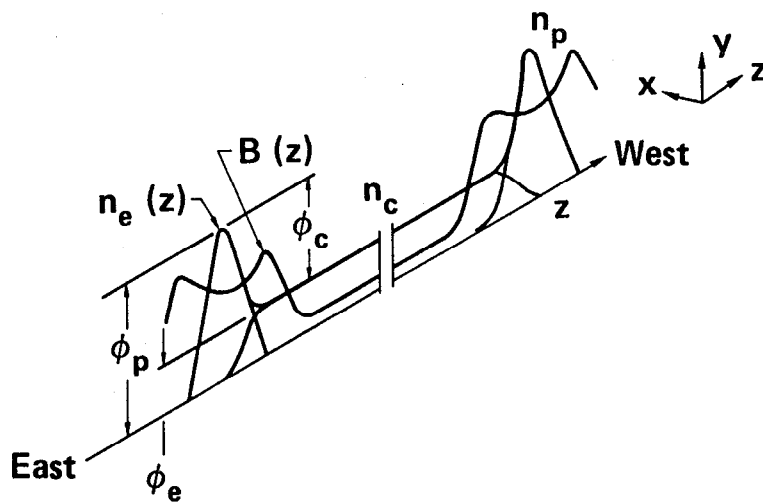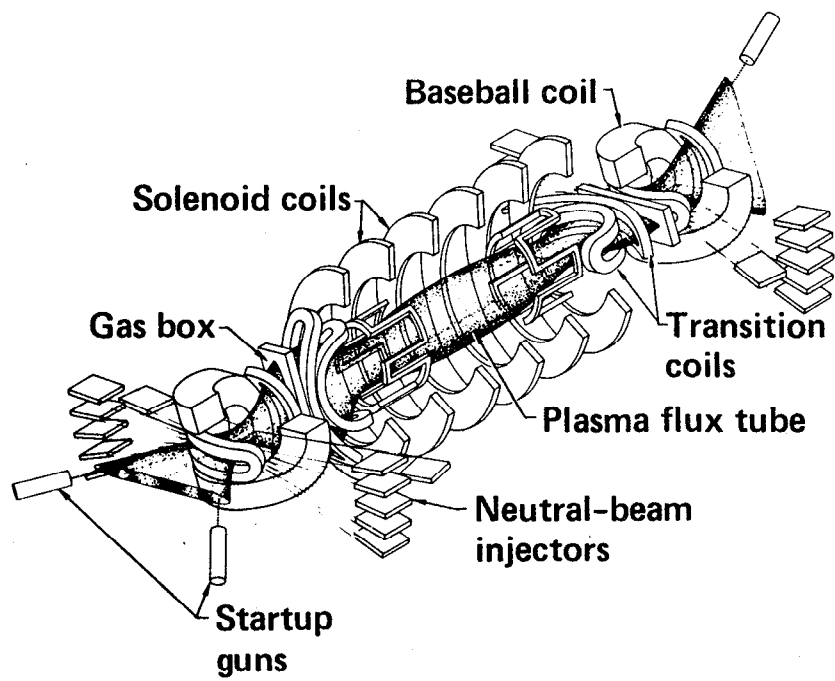
Fig. II.G.2 Profiles of density, potential, and magnetic field
strength in TMX.
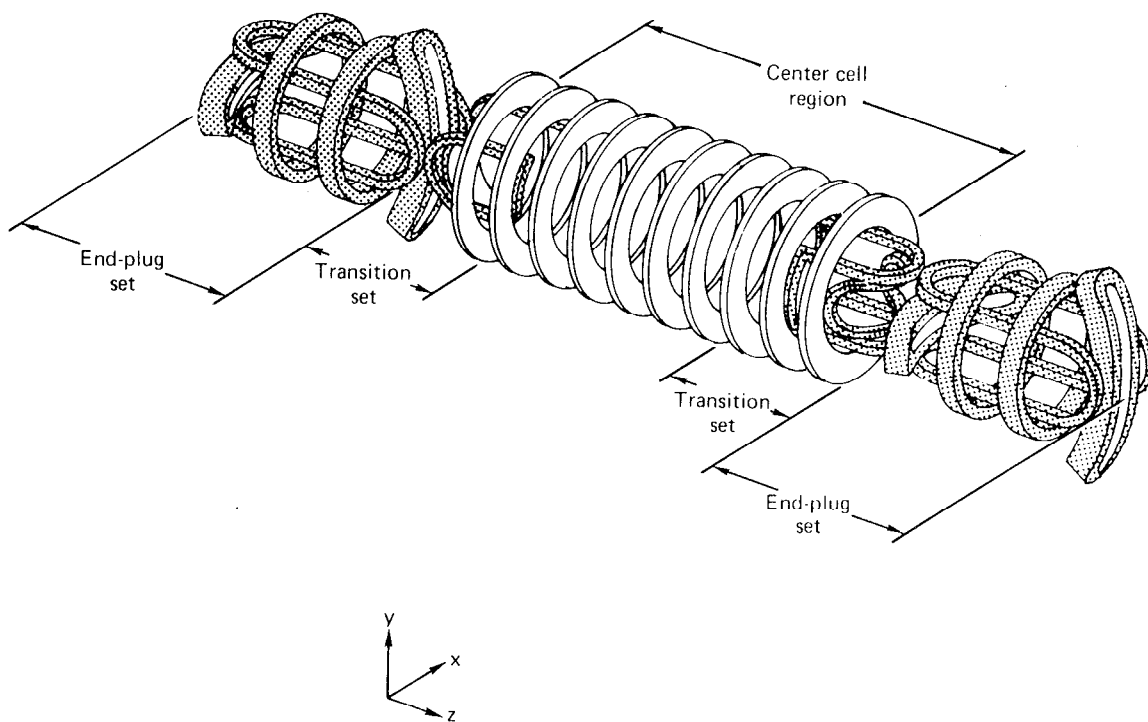
Fig. II.G.3 Magnet system configuration of the upgraded TMX (TMX-U).

TABLE II.G.1. Experimentally obtained parameters from TMX.

Parameter	Value
Energy of neutral beams injected into the end cells	20 and 40 keV
Magnetic field at the center of the end plugs	1.0 T
End-cell mirror ratio	2
End cell-to-end cell (center-to-center) length	6.4 m
Magnetic field in the central cell	0.1 to 0.2 T
Ion density in the end cells	2 to 5 x 10^{13} cm^{-3}
Electron temperature	0.2 keV
Ion density in the central cell	0.5 to 1 x 10^{13} cm^{-3}
Typical ion temperature in the central cell	0.1 keV
Potential barrier for central-cell ions	0.1 to 0.3 kV
Potential barrier for electrons	1 kV
Maximum ratio of plasma pressure to magnetic field pressure in the central cell	0.2

TABLE II.G.2. Physical features and expected parameters for MFTF-B.

Parameter	Two-component mode	High Q with thermal barriers
Machine performance requirements		
End-cell mirror field	4.3 T	4.3 T
End-cell midplane field	2 T	2 T
End cell neutral beams		
Extraction voltage	80 kV	80 kV
Duration	0.5 s	30 s
Central-cell axial field	0.5 T	1.0 T
Central-cell length	32 m	32 m
Central-cell neutral beams		
Extraction voltage	80 kV	80 kV
Duration	0.5 s	0.5 s
A-cell peak axial field	--	--
ECRH power	--	1 MW
Approximate plasma parameters:		
Yin-yang cell particle density	$8 \times 10^{13} \text{ cm}^{-3}$	$5 \times 10^{13} \text{ cm}^{-3}$
End-cell plasma radius	20 cm	30 cm
Central-cell particle density	$5 \times 10^{13} \text{ cm}^{-3}$	$2 \times 10^{13} \text{ cm}^{-3}$
Central-cell ion temperature	0.73 keV	9 keV
Confinement product	$8 \times 10^{11} \text{ cm}^{-3} \cdot \text{s}$	$5 \times 10^{13} \text{ cm}^{-3} \cdot \text{s}$
Equivalent power gain[a]	0.02	0.5

(lengthened) in order to place additional neutral beams and electron cyclotron resonance heating (ECRH) there. These additions will be needed to test the means of suppressing microinstabilities in which cold ions are trapped in a local potential well created by ions injected at an angle from the normal. These injected ions are called "sloshing" ions. These additions are also needed to test the idea of thermal barriers proposed by Baldwin and Logan (II.B.1) in 1979. The thermal barrier was invented in order to reduce the technological requirements from that of a barrierless tandem mirror (II.A.4) which required magnetic fields in a yin-yang configuration of 17T and neutral-beam injection energies of over 1 MeV.

The basic idea of a thermal barrier is to insulate the electrons in the plug from those in the solenoid by means of an electrostatic potential depression produced between the solenoid and the end cell. Electron thermal (heat) conductivity is reduced, hence the name thermal barrier. This thermal insulation allows the plug electrons to be heated independently of those in the solenoid, allowing the ion confining potential to be established with greatly reduced requirement on reactor technology compared to a standard tandem mirror. Figure II.B.1 shows a schematic of the magnetic field, potential, and density profiles which characterizes a type of thermal barrier. Note that beam injection occurs in three distinct spots, and the electrons are to be heated at two different locations.

It is the purpose of TMX-U to answer the questions which would be critical for the operation of a tandem mirror reactor. The objectives of the TMX-U experiment are, in broad terms (II.C.2):

1)   Demonstrate microstable plugs via sloshing ions and warm plasma filling of the loss cone.

2)   Create thermal barriers via high mirror ratio, charge exchange pumping and hot electrons.

Questions arise regarding the microstability of the barrier and end-plug plasma, magnetohydrodynamic (MHD) stability of the solenoid/plug configuration (and the limit on plasma pressure in the solenoid it implies), the nature of the electron heating and the amount required in the plug and thermal barrier, the control of the electron temperature gradient across the thermal barrier, and the removal of cold, trapped ions within the thermal barrier. All must be answered in order to realize these objectives, and provide an experimental physics basis from which to build a reactor, either hybrid or pure fusion. The TMX-U experiment is scheduled to begin operation in early 1982.

To supplement the results obtained with TMX and TMX-U, a scaled up demonstration of the thermal barrier tandem will be accomplished with MFTF-B (II.B.16), scheduled for operation at the end of 1984. This device will use as end plugs yin-yangs, one set of which was originally intended for the standard mirror experiment, MFTF. MFTF-B will provide the same kind of information that TMX-U will, but it will be obtained in a hotter, denser plasma contained in a geometry which will be more like a reactor.

The objectives of MFTF-B are to:

● Demonstrate an equivalent* $Q \sim 1$;

● Demonstrate the operation of thermal barriers;

● Provide scaling data on tandem-mirror confinement; and

● Provide the necessary data base to design and construct a Tandem Mirror Next Step (TMNS) D-T-burning tandem-mirror facility.

An artist's conception of what MFTF-B will look like is shown in Fig. II.G.4. Table II.G.2 shows some physical features of MFTF-B and parameters which should be attainable by MFTF-B operating in a thermal barrier and non-barrier "two component" mode. The two-component mode is characterized by injection of 80 keV beams in the central cell for the duration of the discharge. By comparing this table with Table II.G.1, it can be seen that MFTF-B represents an impressive improvement from those physical parameters of TMX.

II.G.2 <u>Tandem Mirror Theory</u>

There are several physics issues (II.B.16, II.G.3) which are undergoing careful theoretical analysis, which will have great impact on a hybrid tandem mirror reactor, and ultimately a pure fusion reactor. The conclusions drawn from these theoretical studies will be corroborated on the soon to operate TMX-U and MFTF-B devices described above.

One of the most important of these topics is the question of MHD stability of a high β solenoid plasma. It is important from an economic point of view to sustain a high plasma pressure for a given magnetic field, since the fusion power density scales in this case as β^2. Much theoretical work is being done at LLNL to determine just how large β can be. From the

_____

*MFTF-B experiments will be carried out using a pure deuterium plasma. Equivalent Q is calculated as if a D-T plasma were at the conditions achieved in the experiment.
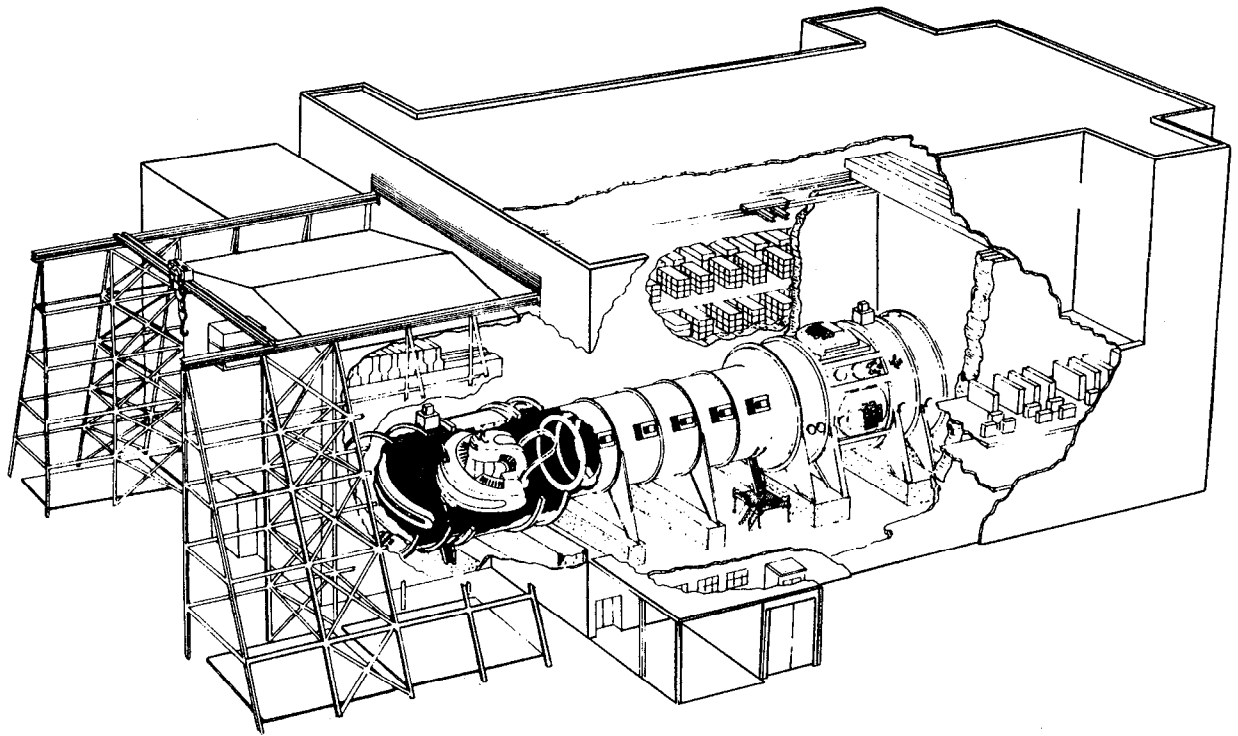
Fig. II.G.4 Artist's concept of MFTF-B.

work performed thus far, two criteria have emerged. These place a limit on β based on the stability of "interchange" or "ballooning" perturbations of the plasma configuration. The pressure weighted interchange criterion (II.B.16) is the least restrictive, and corresponds to assuring that the plasma be stable to global displacements which move entire tubes of magnetic flux radially without any bending of the field lines. The ideal ballooning criterion (II.B.16, II.G.3) on β is by far the most restrictive, and pertains to the situation when β is large enough so that the plasma can bend field lines. The ability of the plasma to distort the magnetic field locally in regions of bad curvature makes it quite difficult to stabilize the perturbations by regions of good curvature (i.e., minimum-$|B|$ yin-yangs). The beta limit scales roughly as $B_{cc}^{1.6}\beta$ = constant, where B_{cc} is the central-cell magnetic field. The constant of proportionality for ballooning is about a factor of 7 smaller than that for interchange. Since fusion power density scales as β^2, this factor results in a large penalty. The ballooning criterion is based on a model which assumes the plasma to be a conducting fluid. However, there is reason to believe (II.G.4) that the criterion derived from this theory is overly pessimistic because it neglects the effect of the helical motion of the plasma ions around the magnetic field lines, and neglects the physical size of the perturbation compared to the physical dimensions of the plasma. These so-called finite-Larmor-radius (FLR) effects are thought to stabilize the short wavelength ballooning modes treated in the ideal theory. The question which as yet has not been answered is to what degree does FLR stabilize the ballooning modes which have long but finite wavelength. Until this question is answered through analysis, the philosophy (II.G.5) at LLNL is to adopt the interchange criterion for the bulk of the reactor studies.

There are other physics issues which must be addressed theoretically, including detailed microstability calculations of the sloshing ion distributions, the stability of the hot electron distributions produced in the thermal barrier, as well as improvement in the techniques for removing ("pumping") cold trapped ions from the thermal barrier. The latter topic was discussed in Section II.B.3 on the plasma models of the fusion driver; for the discussion of the other topics the reader is referred to references II.B.16 and II.G.3 and references therein.

II.H PLASMA DISRUPTION SCENARIO

The failure of any of several components could result in the loss of plasma confinement. For example, a loss of input power to one of the end plugs would drop the potential there and allow plasma to escape out that end. Or, a coolant leak into the plasma chamber could cause a sudden cooling of the plasma and an axial plasma dump. The momentary increase in current to the direct converter should cause no problem, but the change in magnetic field due to the change in plasma β would induce currents and therefore forces in the wall and blanket of the central cell.

Another possibility is that an instability could develop that would move the plasma radially to the wall. The most probable instability is the flute mode, which has a growth rate of $(gk)^{1/2}$, where g is the net outward acceleration due to curvature of the field lines, and k is the wave number. If a flute should develop it would probably be driven by the bad curvature at the ends of the solenoid where $g \simeq v^2/R_c$, and $R_c \sim 10$ m is the radius of curvature of the field lines there. The growth rate for the lowest mode would, therefore, be about 2×10^5 s^{-1}. A typical ion would move about 8 m along a field line in one e-folding time for the instability. Wall protectors may have to be spaced as close as every 8 m along the wall. However, since this is a rather extreme disruption mode, we assume here that wall protecting limiters need only be located in the end cells.

II.H.1 Plasma Energy

The total kinetic energy E of the confined ions and electrons is:

$$E = \int(n_i eT_i + n_e eT_e)dV \simeq 5 \times 10^8 \text{ J}$$

We assume here a cubic radial density profile with $n_i = n_e = 1.6 \times 10^{20}$ m^{-3} on axis, a length of 129 m, and temperatures $T_i = 40$ keV and $T_e = 32$ keV. This amount of energy is capable of vaporizing one square meter of tungsten to a depth of 5 mm (or of raising a small automobile to a height of 50 km). Although there may be no mechanism for concentrating all of this energy, the first wall must be protected. Limiters designed to protect the first wall are discussed in Sect. III.A.5.

II.H.2 Magnetic Effects

Any disruption that changes β in the central cell will induce currents and, therefore, exert forces on the first wall and blanket. If B_0 is the vacuum magnetic field in the central cell, the field with plasma present is $B_\beta = B_0 \sqrt{1-\beta}$. The magnetic flux ψ through the plasma volume is therefore reduced by the amount:

$$\Delta\psi = \pi \, r_p^2 \, B_0 \, (1 - f_\beta),$$

where r_p is the plasma radius and

$$f_\beta = 2 \int_0^1 \sqrt{1 - \beta(1 - x^3)} \; x dx$$

if we assume a cubic pressure profile. When $\beta = 0.7$, $f_{.7} = 0.75$. In the present design $B_0 = 3.0T$ and $r_p = 1.05$ m, giving $\Delta\psi = 2.6$ Wb. The plasma could be lost and β go to zero in a transit time for the ions to go out the ends, about 50 μs. The change in flux would induce electrical currents in the first wall and blanket. Most of the current would flow in the liquid lithium because of its large volume and, therefore, low electrical resistance. A change in magnetic field penetrates a material whose conductivity is σ at a rate

$$x^2 = \frac{4t}{\mu\sigma}$$

where μ is the magnetic permeability of the material. For liquid lithium $\sigma = 2.8 \times 10^6$ mhos/m, $\mu = \mu_0 = 4\rho \times 10^{-7}$ H/m, and

$$x^2 = t/0.88 \text{ m}^2/s$$

Therefore, t = 0.2s is required to penetrate the roughly 0.5 m of Li in the inner part of the blanket. The pressure pulse in the Li can be calculated from the induced current, but more simply from the difference in magnetic field strength supported by the current.

Immediately after the plasma is removed, the field strength inside the first wall drops to:

$$B = B_{in} = B_0[1 - (1 - f_\beta)(r_p/r_w)^2],$$

where r_w is the wall radius; $r_w = 1.3$ m here. At $\beta = 0.7$, $B_{in} = 0.84$ x $B_0 = 2.53T$, and the force per unit area, Δp, is

$$\Delta p = (B_0^2 - B_{in}^2)/2\mu_0 = 1 \times 10^6 \text{ Pa.}$$

The inner wall must withstand a 1×10^6 Pa (150 psi) inwardly directed pulse that decays with a time constant of about 0.2 s. This does not appear to be a serious problem. It is interesting that the ohmic heating due to the induced current is insignificant, amounting to less than 1.0 J/cm^3 of conducting lithium.

Another type of disruption could result from the failure of one of the solenoidal field coils. With one coil turned off the vacuum field would drop from 3.0T to 2.0T at that axial position, and the field line at the outer edge of the plasma (1.05 m) would bulge out to 1.30 m and just miss contacting the wall. However, the failure of a coil should be detected in the power supply circuit, and the plasma could be dumped out the ends before the magnetic field could change significantly.

II.I FUSION REACTIONS GENERATED IN END CELLS

In this section, we briefly address the issue of how much fusion power is generated in the end plugs of a tandem mirror reactor. The end cell is defined here as the part of the tandem mirror beyond the last central cell solenoid magnet. The end cell for the baseline axicell case is the sum of the region between the last central solenoid coil and the high field circular coil, the barrier region, the transition region between the circular coil set and yin-yang anchor, and the yin-yang anchor itself. A picture of the end-cell configuration is shown on Fig. II.B.5. This power is not included in the baseline 3000 MW fusion power, because it is assumed that there is no blanket to thermally convert this energy. It is nevertheless important to know what this power is, because it determines the shielding in the end region, as well as the extra tritium which must be bred in the blanket to make up for that consumed in the end cells by D-T fusion.

There are a number of ion species in the end cell, and each will have a fusion reaction rate associated with it and another species. The fusion power density is given by:

$$P = n_1 n_2 \langle \sigma v \rangle_{1,2}^f E_f \tag{1}$$

where n_1 and n_2 are the densities of the two species of ions undergoing a fusion reaction, $\langle\sigma v\rangle^f_{1,2}$ is the fusion reaction rate parameter, which is a function of the energies of the two reacting species, and E_f is the energy released per reaction. The ion species which exist in the end cell are ions which leak from the central cell into the end cell, and any hot ions which are injected at various positions along the axis of the cell. For all cases considered thus far, the hot species has been deuterium. For the MFTF-B type end cell, the hot species are ions injected in the yin-yang plug, and sloshing ions injected in the A-cell barrier region. For the axicell, the hot ions are the sloshing ions injected in the barrier region, and the sloshing ions injected in the yin-yang anchor. For the modified cusp, the only hot ion species are those that slosh in the barrier region.

The densities and energies of both the cooler central-cell ions and the hot ions are complicated functions of axial position. This is because the magnetic field and amibpolar potential are functions of axial position. Since a particle's total energy and magnetic moment are conserved, the magnetic field and potential can accelerate, decelerate, or even stop particles axially. This fact, along with the fact that magnetic flux is conserved axially, results in variation of plasma density. This is manifested in the z variation of $n_1 n_2$. The aforementioned acceleration of a particle also changes the energy used to evaluate the reaction rate parameter, $\langle\sigma v\rangle^f_{1,2}$. Both the $n_1 n_2$ and $\langle\sigma v\rangle^f_{1,2}$ terms contribute to the axial dependence of the fusion power density.

The model we have assumed here ignores D-D fusion reactions. These reactions were investigated and found not to be of importance, compared to D-T reactions between the cold passing deuterium and tritium and between the hot deuterium beams and the cold passing tritium. Improvements to the model are necessary to assess shielding requirements in the regions devoid of tritium. The reactions which we do include depend upon the end-cell configuration. All configurations include the reactions between the passing central-cell deuterium and tritium, and between the passing tritium and the sloshing deuterium beam. For the MFTF-B A-cell type end cell, the passing tritium/hot yin-yang ion fusions are included. The axicell anchor sloshing ions do not see any of the central-cell tritium, and hence the fusion power density in the anchor is small.
There seems to be plenty of room in the anchor to install shielding from neutrons produced by D-D reactions.

The models used for the axial density distributions are those derived by B. M. Boghosian at LLNL (II.I.1). The expressions are lengthy, and will not

be reproduced here in the interest of saving space. The profiles of beam energies and central-cell temperatures are obtained crudely in the plug fusion model by conserving the total energy of a particle which has the average energy of the distribution. More work needs to be done in order to determine the proper energy mappings.

Some sample cases of fusion power per unit length, P_{fus}/L versus axial position are shown on Figs. II.I.1a and II.I.1b. The baseline axicell case is shown in Fig. II.I.1a, and a representative MFTF-B A-cell case is shown in Fig. II.I.1b. Note that the axicell case has a P_{fus}/L which drops much more rapidly than the MFTF-B A-cell case. This is because of two reasons. First, the high field hybrid coil blocks out more of the passing ion density and does it in shorter axial distance than does the lower field MFTF-B yin-yang. Also, the MFTF-B type design injects hot deuterium beams in the yin-yang where the passing ion density has not appreciably attenuated. Both of these profiles of P_{fus}/L have some structure, due to the double peaked nature of the sloshing ions in the barrier, and in the case of the MFTF-B type cell, the peaking of the plug trapped cold ions and the hot mirror trapped ions. For the baseline axicell case, the fusion power is 60 MW per end, whereas for the MFTF-B end cell, for the same central-cell P_{fus}/L, each end cell generates about 200 MW of D-T power. The total breeding, T+F, will be decreased in the latter case by approximately 10%, which is another reason the axicell was chosen for the baseline case.

II.J EFFECT OF CENTRAL-CELL FIELD
RIPPLE ON INTERCHANGE STABILITY

Important for reactor designs is the size of tolerable magnetic field ripple in the central cell since it determines coil spacing which affects access for plumbing, etc. For the TMR with an axisymmetric plug, the chief limitation on ripple appears to be MHD stability (in the MFTF-B style reactor, ripple-diffusion effects near the transition coil could be the decisive factor). At present the MHD limits are evaluated with the long-thin, low-β version of the classic interchange criterion,

$$\int_0^L \frac{(\hat{p}_\perp + \hat{p}_{\parallel}) \, (x^{\parallel} x + y^{\parallel} y) dz}{B} \geq 0$$
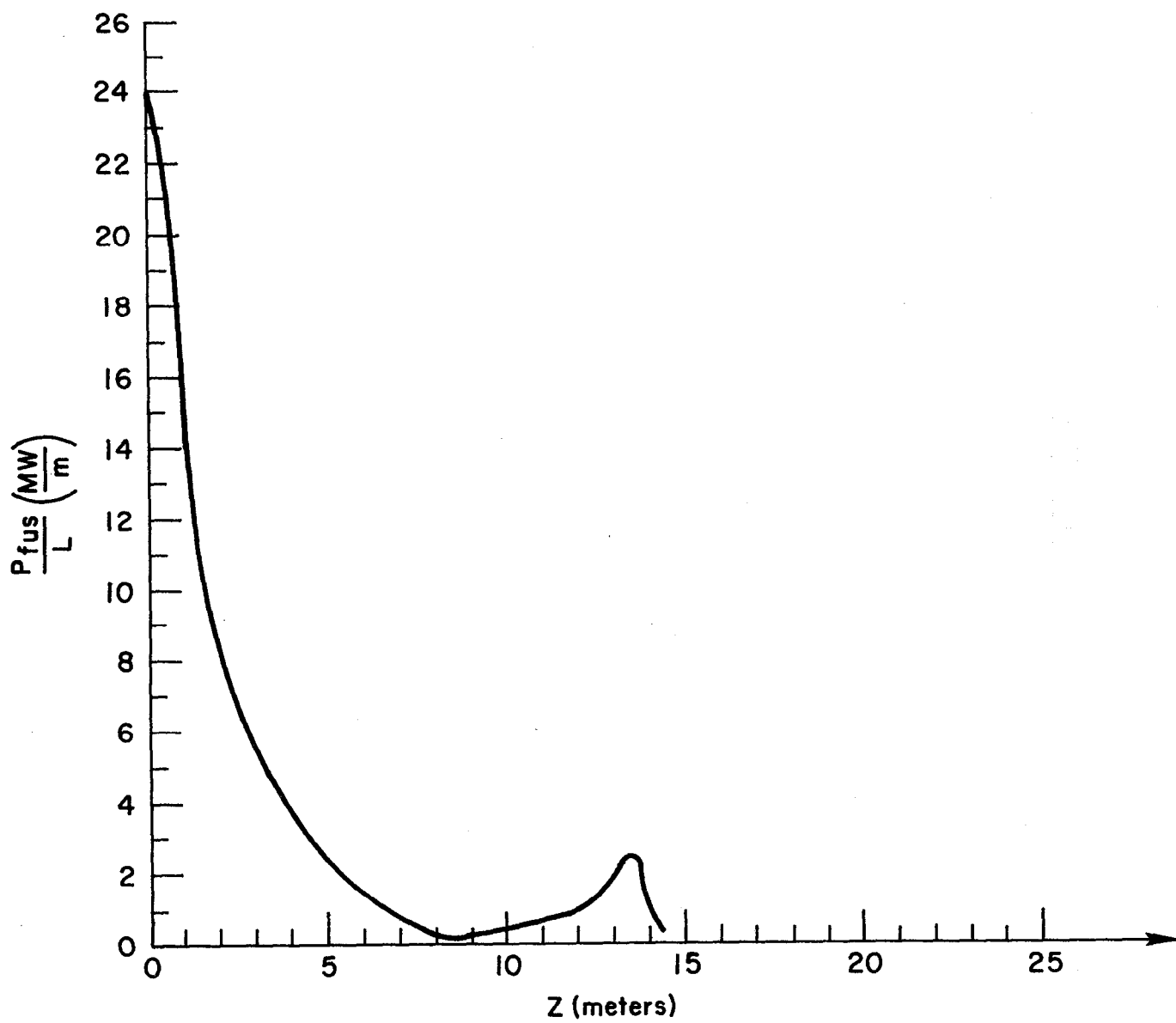
Fig. I.I.1a Fusion power per unit length for axicell end plug.
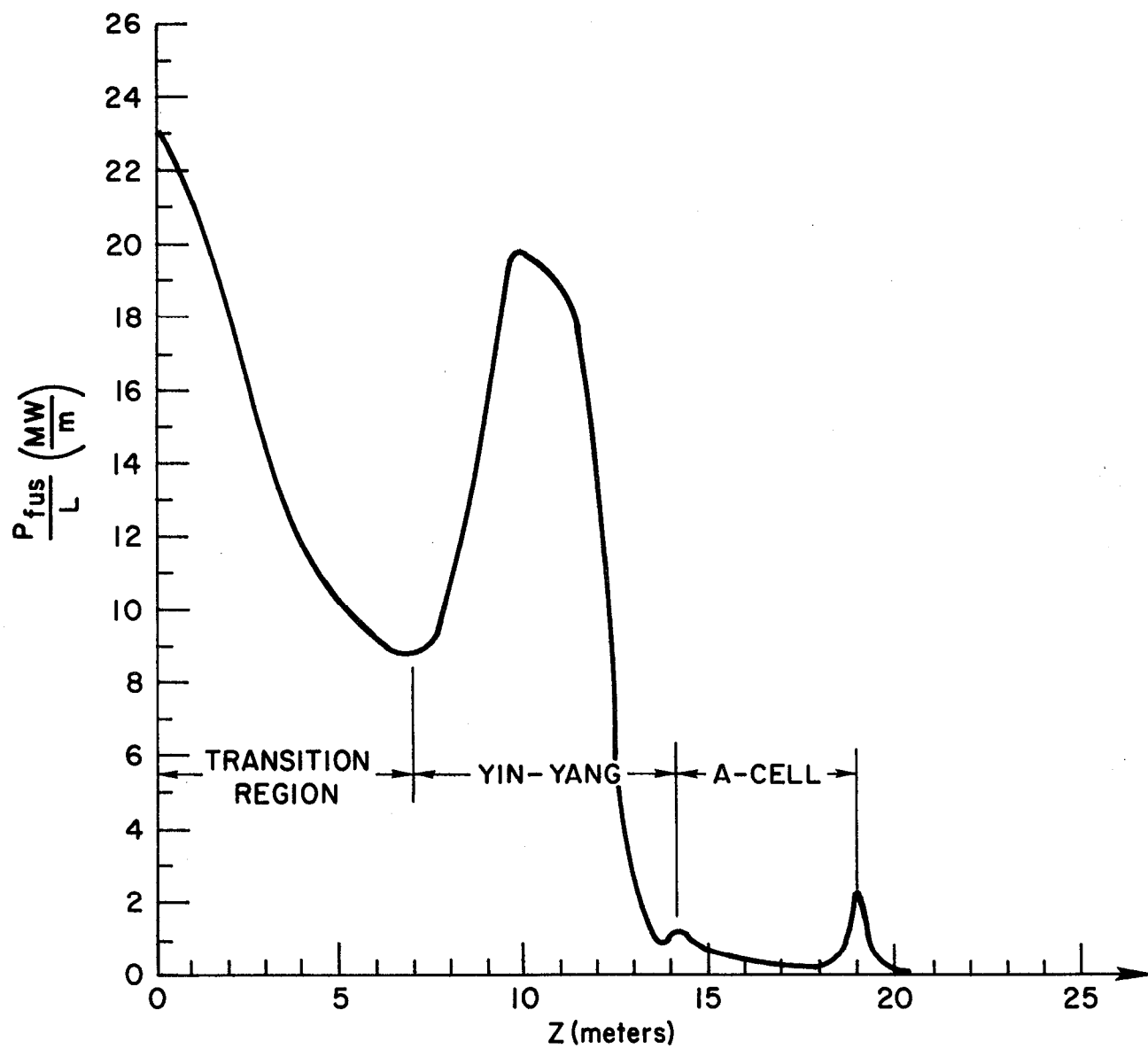
Fig. II.I.1b Fusion power per unit length for MFTF-B A-cell end plug.

The integral is evaluated from the machine center to the outer anchor along a 45° field line close to the axis ($x=y = 10^{-2}$ m).

For this case an axicell TMR was chosen and number of coils in the 150 m central cell was varied with current adjusted to give approximately constant B on axis. The results for β_c/β_a vs. $\Delta B/\bar{B}$ are shown in Fig. II.E.1. The definitions for ΔB and B are

$$\Delta B = \frac{B_{max} - B_{min}}{2}$$

and

$$\bar{B} = \frac{B_{max} + B_{min}}{2}$$

on the field line used in the stability integral, i.e., essentially on axis. B_{max} and B_{min} are taken directly under the coil and half way between coils. ΔB and $\bar{B}$ increase slightly outward from the machine center, but the variation in $\Delta B/B$ would not show on the figure. For these calculations pressure in the central cell is constant, β_p (axiplug)/β_c = 1 and β_t (transition section)/β_c = 0.08.

The typical design rule for TMR's have been $\Delta B/\bar{B}$ < 5%. We see that this magnet configuration would suffer a reduction in β_c/β_a of about 5% over the "ideal" magnet. In other words, for a desired central-cell β of 70%, the anchor β must be 35% instead of 26%. It seems that the 5% ripple rule should be adequate for future designs.
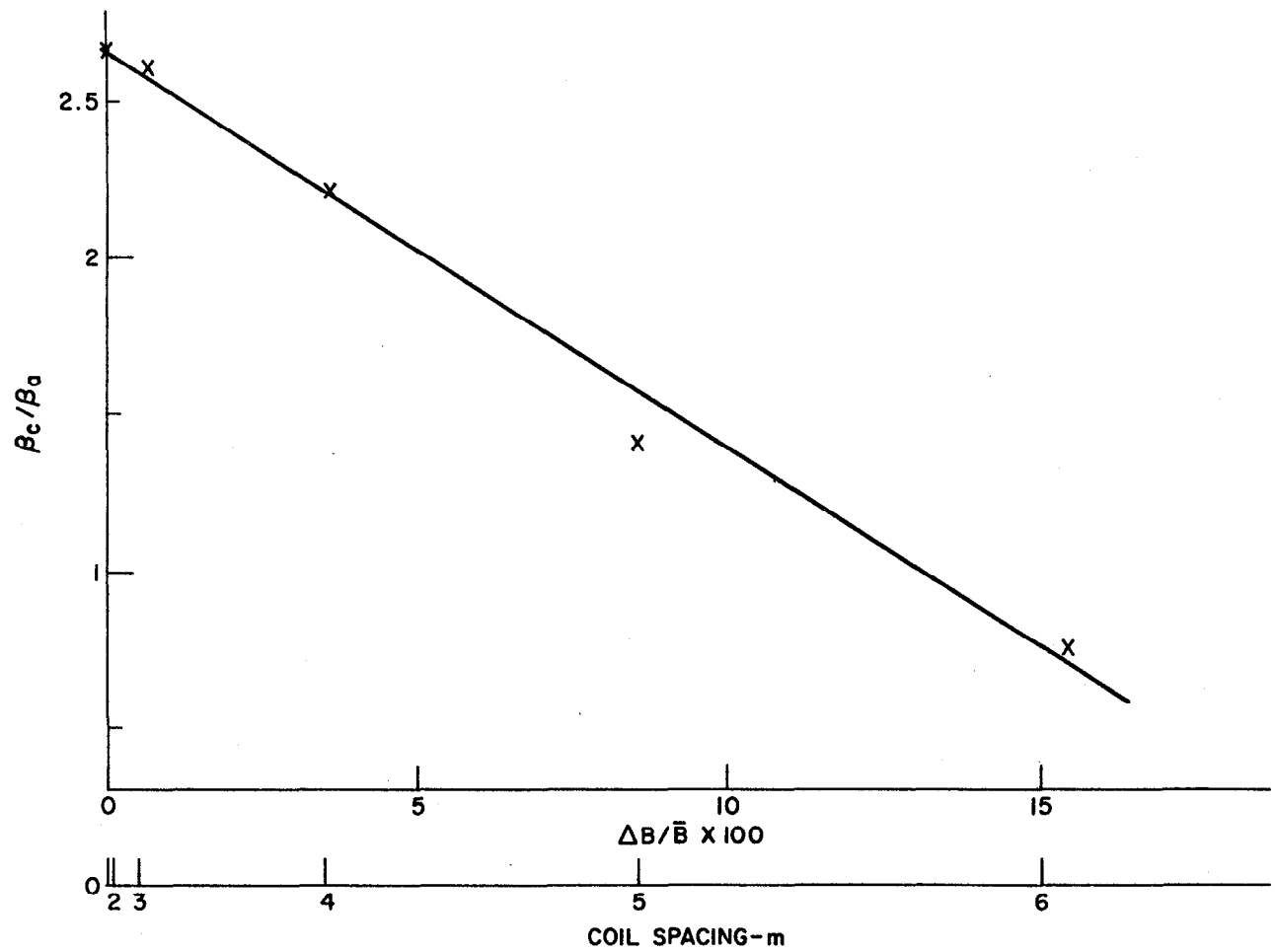
Fig. II.J.1 Central cell to anchor beta ratio versus percent field ripple.

CHAPTER II REFERENCES

References, Section II.A

II.A.1. G. I. Domov, V. V. Zakaidakov, M. E. Kishinevskii, Sixth
International Conference Plasma Phys. and Controlled Nuclear Fusion
Research, Berchtesgaden, Fed. Rep. of Germany, 1976, Paper C4 (IAEA).

II.A.2. T. K. Fowler, B. G. Logan, Comments on Plasma Phys. and Controlled
Fusion 2, 167 (1977).

II.A.3. R. W. Moir, Ed., Standard Mirror Fusion Reactor Design Study,
Lawrence Livermore National Laboratory, Rept. UCID-17644 (1978).

II.A.4. R. W. Moir, et al., Preliminary Design Study of the Tandem Mirror
Reactor (TMR), Lawrence Livermore National Laboratory, Rept.
UCRL-52302 (1977).

References, Section II.B

II.B.1. D. E. Baldwin, B. G. Logan, "An Improved Tandem Mirror Reactor,"
Physical Review Letters 43 (1979), p. 1318.

II.B.2. G. A. Carlson, et al., Tandem Mirror Reactor with Thermal Barriers,
Lawrence Livermore National Laboratory, Rept. UCRL-52836 (1979).

II.B.3. B. G. Logan, et al., "Tandem Mirror Reactors with Thermal Barriers,"
presented at 8th Intl. Conf. on Plas. Phys. and Cont. Nucl. Fusion
Research, Brussels 1-10 July 1980. See also Lawrence Livermore
National Laboratory, Rept. UCRL-83505.

II.B.4. Reference II.B.2, Chapter 5.

II.B.5. G. W. Hamilton, "Grad-B Pumping of TMR Thermal Barriers,"
Proceedings of the Engineering Problems of Fusion Research, Chicago,
Ill., Oct. 26-29, 1981.

II.B.6. D. E. Baldwin, "Pumping of Thermal Barriers in Tandem Mirrors by
Induced Radial Transport," Sherwood Controlled Fusion Theory
Conference, paper 1C48, Austin, Texas, April 8-10, 1981.

II.B.7. B. G. Logan, D. Cornish, Lawrence Livermore National Laboratory,
private communication, July 1981.

II.B.8. R. S. Post, J. Kesner, "Construction of TARA Tandem Mirror Facility
with an Ion Anchor," MIT proposal, Nov. 1980, revised March 1981.

II.B.9.   B. G. Logan, "Improved Axisymmetric-Cusp Plugs for Tandem Mirror Reactors," Lawrence Livermore National Laboratory, Rept. UCRL-86085 (1981). To be published in Comments on Plasma Physics and Controlled Fusion.

II.B.10. G. A. Carlson, W. L. Barr, "The Effects of Non-Adiabaticity of Alpha Particles in the Axisymmetric Cusp TMR," Lawrence Livermore National Laboratory, Rept. UCID-19150 (1981).

II.B.11. C. L. Hedrick, R. A. Dandl, J. A. Cobble, R. A. Dory, H. O. Eason, E. G. Harris, G. R. Haste, H. Ikegami, E. F. Jaeger, N. H. Lazar, D. H. McNeill, D. G. McAlees, D. B. Nelson, L. W. Owen, D. A. Spong, and N. A. Uckan, "Transport and Scaling in the Elmo Bumpy Torus (EBT)," in Proc. 6th Conf. Plasma Physics and Controlled Nuclear Fusion Research (IAEA, Vienna), Vol. 2, p. 145 (1977).

II.B.12. R. W. Moir, Ed., "Tandem Mirror Hybrid Reactor Design Study," Lawrence Livermore National Laboratory, Rept. UCID-18808 (1980).

II.B.13. G. A. Carlson, "Mirror Reactor Concepts," section in "Trends and Developments in Magnetic Confinement Fusion Reactor Concepts," Nucl. Tech./Fusion, 1, p. 5 (1981).

II.B.14. C. C. Damm, et al., Preliminary Design of a Tandem-Mirror-Next-Step Facility, Lawrence Livermore National Laboratory, Rept. UCRL-53060 (1980).

II.B.15. G. W. Hamilton, "Negative Deuterium Ions for Tandem Mirror Next Step and Tandem Mirror Reactors," in Proceedings of the Second Intl. Symposium of the Production and Neutralization of Negative Ions and Beams, Brookhaven National Laboratory, Rept. BNL-51304 (1980).

II.B.16. D. E. Baldwin, B. G. Logan, T. C. Simonen, Eds., "Physics Basis for MFTF-B," Lawrence Livermore National Laboratory, Rept. UCID-18496 (1980).

References, Section II.C

II.C.1.   Same as Ref. II.A.4.

II.C.2.   F. H. Coensgen, et al., TMX Upgrade Major Project Proposal, Lawrence Livermore National Laboratory, Rept. LLL-PROP-172, April 30, 1980.

References, Section II.D

II.D.1. J. Fink, "Neutral Beam Injectors for 1990 and 2005," Lawrence
         Livermore National Laboratory, Rept. UCRL-53112 (19??).

References, Section II.E

II.E.1. J. T. Woo, "Shielding of Mirror FERF Plasma by Arc Discharges,"
         LNRL, Rept. UCRL-52181 (1976).
II.E.2. T. H. Batzer, R. E. Patrick, and W. R. Call, "A Neutral Beam Line
         Pump with Helium Cryotrapping Capability," Livermore National
         Laboratory, Rept. UCRL-81196 (1978).

References, Section II.F

II.F.1. G. Bekefi, "Radiation Processes in Plasmas," (John Wiley and Sons,
         Inc., New York, 1966), p. 201ff.
II.F.2. B. A. Trubnikov and V. S. Kudryavtsev, in Proc. 2nd U.N. Conf. on
         Peaceful Uses of Atomic Energy, Vol. 31, United Nations, Geneva
         (1958), p. 93.
II.F.3. D. J. Rose and M. Clark, Jr., "Plasma and Controlled Fusion," (The
         MIT Press and John Wiley and Sons, Inc., New York, 1961).

References, Section II.G

II.G.1. T. C. Simonen, "Experimental Progress in Magnetic Mirror Fusion
         Research," to be published in the Proc. Institute of Electrical and
         Electronics Engineers (1981).
II.G.2. T. C. Simonen, et al., the 8th Conference on Plasma Physics and
         Controlled Thermonuclear Research, Brussels, 1980, paper CN/38/F1.
II.G.3. B. G. Logan, "Improved Axisymmetric-Cusp Plugs for Tandem Mirror
         Reactors," Lawrence Livermore National Laboratory, Rept. UCRL-86085
         (1981). To be published in Comments on Plasma Physics and
         Controlled Fusion.
II.G.4. F. H. Coensgen, et al., TMX Upgrade Major Project Proposal, Lawrence
         Livermore National Laboratory, Rept. LLL-PROP-172, April 30, 1980.

II.G.5.   D. E. Baldwin, B. G. Logan, "An Improved Tandem Mirror Reactor," Physical Review Letters 43 (1979), p. 1318.

II.G.6.   R. W. Moir, et al., Preliminary Design Study of the Tandem Mirror Reactor (TMR), Lawrence Livermore National Laboratory, Rept. UCRL-52302 (1977).

II.G.7.   Same as Ref. II.B.21.

References, Section II.I

II.I.1.   B. M. Boghosian, Lawrence Livermore National Laboratory, in preparation.

References, Section II.J

II.J.1.   R. S. Devoto, "Tandem Mirror Hybrid Reactor Design Study Final Report," edited by R. W. Moir, Lawrence Livermore National Laboratory, Rept. UCRL-18808 (1980), pp. 3-8.

CHAPTER III

FUSION COMPONENT TECHNOLOGIES

This chapter describes the various technologies which need to be developed in order for the construction of a fusion breeder to proceed.

The most basic technologies required to produce the plasma are neutral-beam injectors, superconducting magnets, and microwave tubes. The description of these components and the requirements for the current design of the breeder are given in Sections III.A.1 through III.A.3.

In order to collect the energy lost out the ends of a tandem mirror, direct converters are beneficial and should be developed. Section III.A.4 describes the characteristics of the direct converter required for the TMHR.

The first wall needs to be protected from plasma disruptions. A disruption could deposit 5×10^8 joules of energy onto the walls if there was not some means to prevent this. Section III.A.5 describes a method by which a possible disruption would dump the plasma energy locally on a sacrificial tungsten liner inside the high field coil.

Section III.B discusses the important end-plug issues. Subsection B.1 gives an overview of the design and describes the mechanical layout, and subsection B.2 addresses the question of how the fusion power generated (e.g., tritium consumed) in the end cells affect the fissile breeding capacity of the central cell.

Finally, in Section III.C, an overview of the present level of development and planned development of the different fusion component technologies is presented. To end this Chapter, subsection C.2 discusses the technological requirements of the hybrid as they compare with that of pure fusion.

III.A DESCRIPTION AND MODELS FOR FUSION COMPONENT TECHNOLOGIES

III.A.1 <u>Neutral Beam Injectors</u>

Neutral Beams are required for the Axicell TMHR for injection of high-energy sloshing ions into the anchor and into the thermal barrier, and for charge-exchange pumping of the thermal barrier. These topics have been discussed in previous reports (III.A.1,2,3,4). In this section we concentrate on some developments because of new requirements and newly available technology.

Neutral Beam Requirements are shown in Table III.A.1, in which the absorbed neutral-beam powers, energies, and trapping fractions have been computed after an optimization procedure. From these data we compute the injected power and the total input power, assuming reasonable efficiencies of the ion sources, acceleration, and neutralization. Not shown in Table III.A.1 are certain losses such as collimation and power supply losses, which have been adequately discussed in other reports. The total input power should be increased by about 10% to allow for such additional losses. However, several options are available to reduce these power requirements.

Beam energy requirements for the axicell TMHR are rather high because of the need for high-energy sloshing ions and high-energy charge-exchange neutrals. The sloshing ion energy must be high to avoid rapid diffusion in pitch angle. Ions derived from the charge-exchange beams must have sufficient energy to escape from the barrier potential well (ϕ_b = 200 kV) and enter the TMHR central cell. Because of the high energy requirements and the need for high-purity charge exchange beams almost all of the injected neutrals will be derived from negative ions (D^- or T^-) rather than from positive ions. These requirements require some discussion of the technology of D^- sources, accelerators, and neutralizers; however, we will avoid repetition of such work described elsewhere.

III.A.1.a <u>D^- Injector Modules</u>. The ion source and accelerator will be similar to those designed for the Field Reversed Mirror Reactor (III.A.2) or Tandem Mirror Next Step (TMNS) (III.A.4) as shown by Fig. III.A.1. Each module may contain three or four beams, each of which has a cross-section of 2 cm in thickness and 100 cm in width. We assume a beam intensity of 0.1 A/cm^2,

Ion-source chamber

10⁻⁴ Torr

Ground

−120 kV

−190 kV

Sector magnet

D⁻ source
at −200 kV

Cryopump

|———0.5M———|

Stripping cell

10⁻⁴ Torr

Energy recovery chamber

Electrostatic
deflectors

Ground

Ground

−40 kV

Ground

10⁻⁶ Torr

D−

D°

D+

4° beam envelope

Helium-cooled
beam dump
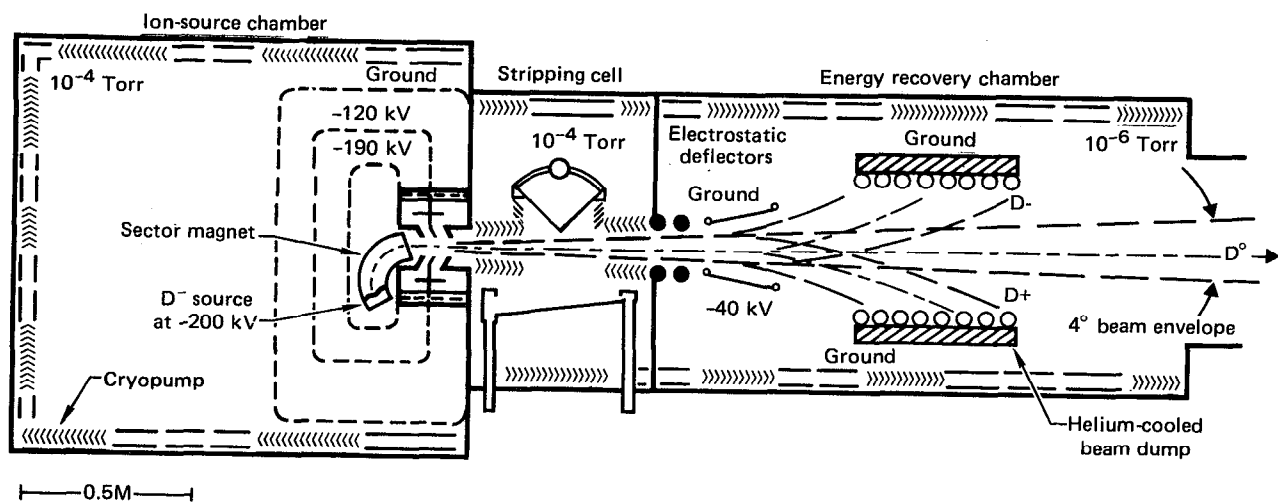
Fig. III.A.1   Beamline schematic of an 11-A, 200-keV D-injector (ion
source chamber dimensions: roughly 1 by 1 by 2 m).

TABLE III.A.1. Axicell TMHR neutral-beam power requirements based on D^- and T^- neutralized by photodetachment.

	Axicell slosh	Axicell pump	Anchor slosh	Total
W (keV)	250	200	150	
P absorbed (MW)	9	121	6	136
Trapping fraction = f_t	.25	0.7	0.32	
$P^0 = P/f_t$ injected (MW)	36	173	19	228

Neutralization fraction, f_n (photodetachment optimized for total power)

	Axicell slosh	Axicell pump	Anchor slosh	Total
	0.9	0.9	0.9	
Accel efficiency f_a	0.95	0.95	0.95	
$P^- = p_i/f_n f_a$ (MW)	42	200	22	264
$I^- = P^-/W$ (A)	168	1000	147	1315
Ion source power = I x 2.5 kW/A (MW)	0.42	2.5	0.37	3.29
Laser input power = P^- x 0.1 (MW)	4.2	20	2.2	26.4
Total input power	46.6	222	24.6	293
Number of D^- modules required				
= I^-/60 A/module (both ends)	4	18	4	26
(each end)	2	9	2	13

which is larger than available from large-area D⁻ sources now under development, but is modest in comparison with the intensities of positive ion sources now in operation. Consequently, each D⁻ beam consists of 20 A; each module produces 60 A.

III.A.1.b Photodetachment Neutralizer. Neutralization of the D⁻ after acceleration could be accomplished either by collisional electron detachment in a gas or vapor cell (as shown by Fig. III.A.1) or by photodetachment in an optical cavity illuminated by a powerful laser (III.A.5,6). Photodetachment has potential advantages of a higher neutralization fraction and higher overall efficiency, including the power required to operate the laser.

The ribbon-shaped beam specified above is well-suited for the optical cavity shown by Fig. III.A.2. In this geometry the D⁻ beam passes through the laser optical cavity, which consists of an assembly of mirrors reflecting the light through the D⁻ beam many times. After many reflections the light is reflected back into the laser to be amplified by another cycle of stimulated laser emission.

In principle, the neutralization fraction in a photodetachment cell can be made to approach unity if the photon density is high enough. However, in practice the photon density will be adjusted to optimize the overall efficiency, defined as follows:

$$\text{Overall Efficiency} = \frac{\text{Neutral Beam Power}}{\text{Charged Beam Power + Laser Input Power}}$$

We will design for an overall efficiency of about 80% and for a neutralization fraction of 90%. If the beam energy is 250 keV the charged beam power will be 5 MW for a 20-A D⁻ beam. Therefore the laser input power P_{in} must be no greater than about 500 kW. These requirements provide the basis for the requirements of laser efficiency and mirror reflectivity.

The neutralization fraction is

$$f_n = 1 - e^{-\alpha} \qquad\qquad\qquad \text{(III.A.1)}$$

where in the terminology of reference III.A.2:

$$\alpha = (\sigma/h\nu) \, \phi L_s/v \qquad\qquad\qquad \text{(III.A.2)}$$

$$= 1.7 \times 10^{-4} \, \phi L_s v^{-1/2}$$
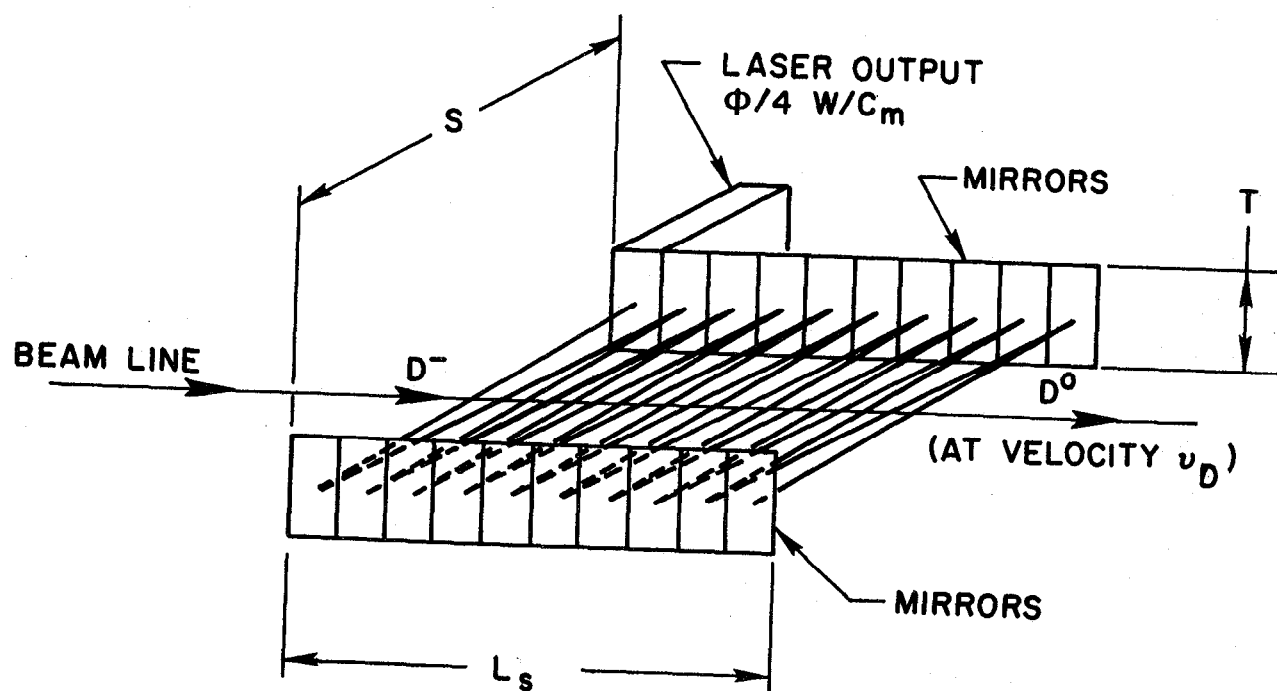
Fig. III.A.2 Laser-activated photodetachment cell.

72-167-0

The light intensity ϕ depends upon the circulating laser power P_{circ} and the area of the laser beam $2TL_s/N$. Since there are four light beams at any point in the optical cavity,

$$\phi = 4 \, P_{circ} N/2TL_s \qquad\qquad\qquad (III.A.3)$$

The light reflects two times from each of the N mirrors in the cavity. Therefore the power loss to the mirrors is

$$P_{loss} = P_{circ} \, 2N \, (1-R) \qquad\qquad\qquad (III.A.4)$$

where R is the reflectivity. This loss will be more important than other light losses and must be balanced by P_{stim}, the stimulated laser emission

15   P_{stim} = laser input power x laser efficiency

$$= P_{in} \times n_L$$

$$\geq P_{loss} \qquad\qquad\qquad (III.A.5)$$

By combining equations (2), (3), (4), and (5) we find the requirement for laser efficiency and mirror reflectivity.

$$\frac{n_L}{(1-R)} \geq \frac{\alpha T V^{1/2}}{1.7 \times 10^{-4} P_{in}} = 40 \qquad\qquad\qquad (III.A.6)$$

where we have used $\alpha = 2.3$ to obtain $f_n = 0.9$. The thickness T of the optical cavity must be about 3-cm to allow for the angular spread of the 2-cm D^- beam. We use $V = 250$ kV and $P_{in} = 500$ kW.

At a wavelength of about 1 micron, the reflectivity R of a mirror consisting of alternating layers of dielectrics of one-half wavelength thickness can be 0.999. Therefore under these requirements the laser efficiency must be at least 4%, which is probably possible with development effort. The mirrors can be shielded against neutrons and other radiation. The power damage threshold of the mirror surfaces is at least 20 kW/cm^2; this leads to the conclusion that the length of the assembly L_s need be no greater than 80-cm.

Other geometries have been proposed for photodetachment neutralizers. The requirements for laser efficiency can be reduced by focusing the ion beam and thereby intensifying the beam density. However, such a focus geometry may be incompatible with TMR requirements.

III.A.1.c <u>Pumping of Thermal Barriers.</u> To maintain the low density and low plasma potential of the thermal barriers, the trapped ions must be pumped out as fast as they diffuse into the barrier. Two techniques are available for this--charge-exchange and/or grad-B pumping. Charge exchange pumping is predictable since it relies only on classical processes, but is rather expensive in terms of input power and capital cost.

A neutral beam injected into the thermal barrier will undergo some attenuation by charge exchange and by ionization. Charge exchange with a trapped ion will cause the neutral product to go to the wall. If the neutral beam is injected with sufficient energy E_B and small pitch angle θ the ionized products will go into the central cell and not be trapped in the barrier. The requirement for this is

$$E_B > \Delta\phi/(1 - R \sin^2\theta) \qquad\qquad (III.A.7)$$

where the potential difference $\Delta\phi$ and the mirror ratio R are defined at the point of ionization, relative to the potential and magnetic field at the entrance of the central cell. Within the thermal barrier the maximum value of $\Delta\phi = \phi_b = 200$ keV, while the maximum value of R may be 13. Therefore the charge exchange beam must be injected almost parallel to the magnetic field (θ less than 10°) to satisfy equation (7) and to minimize the required E_B.

In our previous designs (III.A.1,3,4) we have explained correction factors to take into account the competition between charge exchange and ionization and beam attenuation. These corrections are now built into the code, and provide the data for Table III.A.1. The Axicell Pump Beam of Table III.A.1 is actually a composite of three pump beams injected at high energy (HEPB), medium energy (MEPB), and low energy (LEPB). In our previous reports we showed that a large economy is possible by injecting three pump beams into the thermal barrier at three different potentials. We find that the absorbed powers predicted by the composite model are very close to those computed using a model which considers the beams separately, however the composite energy is too high and the average trapping fraction therefore conservative. Most of the trapped ions are pumped while they are at a relatively high plasma potential, such $\Delta\phi$ for the MEPB and LEPB may be much less than ϕ_b, or may even be negative.

In Fig. III.A.3(a) we show injection paths for these three pump beams, aimed at the appropriate parts of the thermal barrier. The injection paths
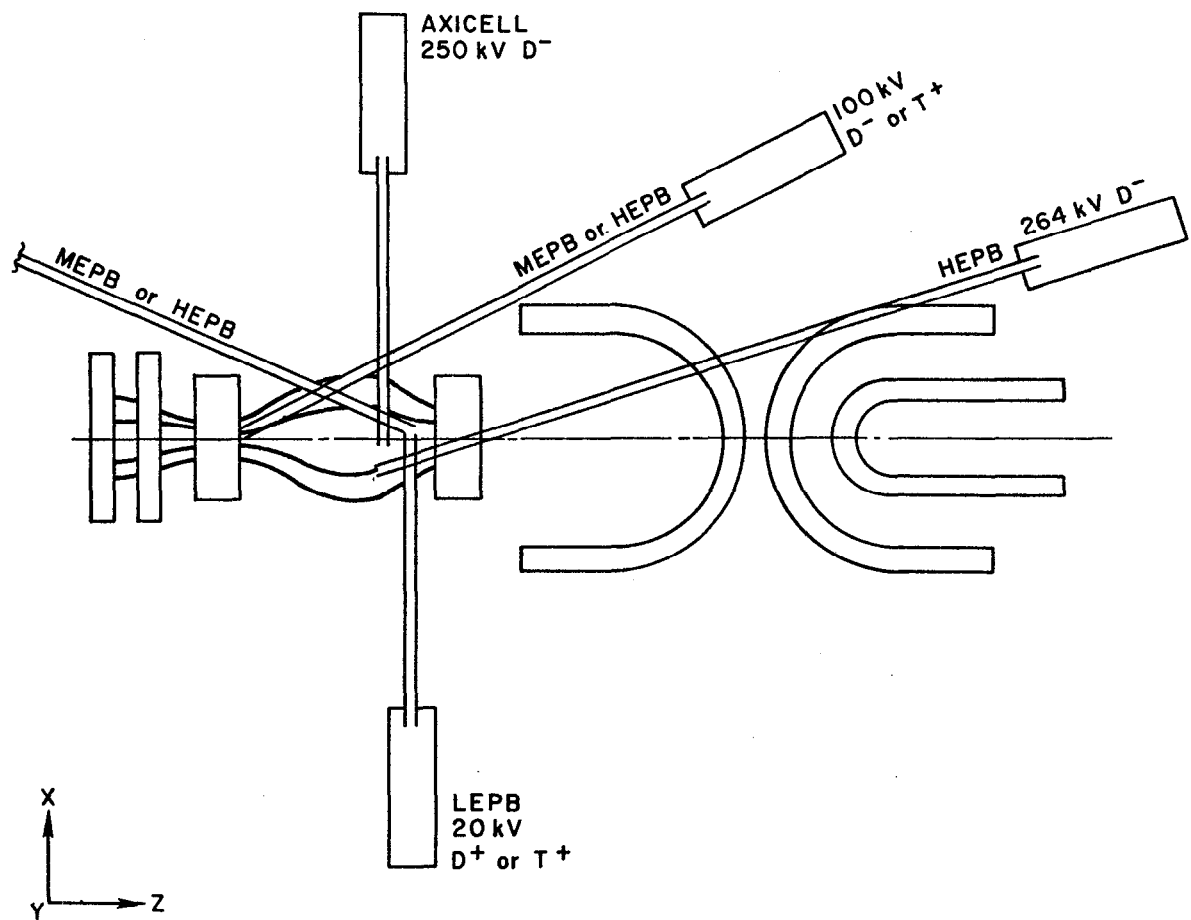
Fig. III.A.3a Injection paths for high-, medium-, and low-energy pump
beams in the thermal barrier region.

for the MEPB and HEPB are selected such that the pitch angle θ is small in the region of ion production. In the axicell TMR the injector modules can be located symmetrically around the z-axis, as shown in Fig. III.A.3(a).

Also shown in Fig. III.A.3(a) and III.A.3(b) are the injection paths for the sloshing ions injected into the barrier and anchor. One available option (not shown by Fig. III.A.3 or Table III.A.1) is to increase the pitch angle θ for the HEPB so the injected HEPB ions become trapped as sloshing ions. This option would eliminate the first column of Table I and save 104 MWe of input power. To illustrate the available possibilities we have selected this option in the anchor but not in the barrier.

Yet another option is to use T^0 as pump beam neutrals rather than D^0. This option takes advantage of the fact that the charge-exchange cross-section for T^0 is larger than the cross-section for D^0 at equal energies. This option also fulfills the requirement for reactor fueling.

Figure III.A.3(a) indicates that the HEPB and MEPB can be injected into the barrier either from left to right or right to left. In either case the injected ions escape into the central cell after reflection from the ambipolar plug. Injection from left to right (away from the central cell) has the advantage of charge-exchange pumping of thermalized alphas passing through the barrier (III.A.7).

Potentially, a great power saving can be made by pumping the thermal barrier by grad-B perturbations rather than by charge-exchange. Two versions have been proposed--either by AC (III.A.8) or DC (III.A.9) coils mounted close to the plasma to increase the rate of grad-B drift transversely out of the plasma.

Most of the grad-B drift occurs near the turning point of the trapped ions. Therefore, conditions can be arranged such that trapped thermalized ions can be made to drift out of the plasma, while high-energy trapped ions and hot electrons are retained in the plasma. This type of selectivity has been proven both by guiding center computations and by a simplified theory using DC perturbation coils.

The theory of DC perturbation coils requires some type of non-uniform azimuthal drift, as illustrated by Fig. III.A.4 in the case of a quadrupole TMHR. With each bounce there is a displacement δ(x) of a few millimeters, which may be either positive or negative, depending upon which side of the perturbation the bounce occurs on. Because of the non-uniform azimuthal drift the trapped ion bounces more frequently on one side than on the other side.

ANCHOR
SLOSHING IONS
150 kV D⁻
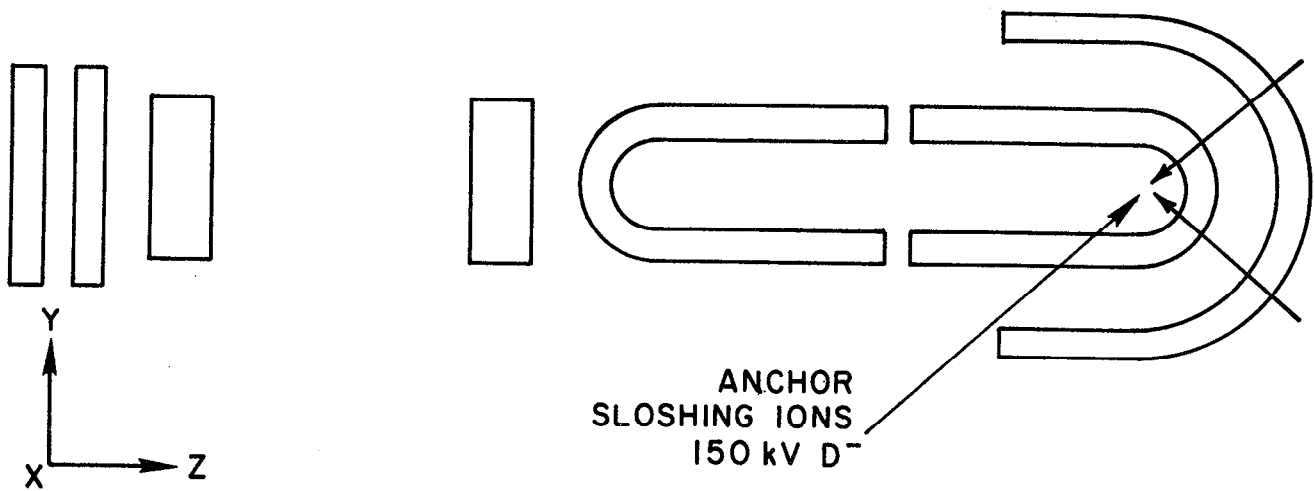
72-233-0

Fig. III.A.3b Injection paths for anchor sloshing/pump beams.
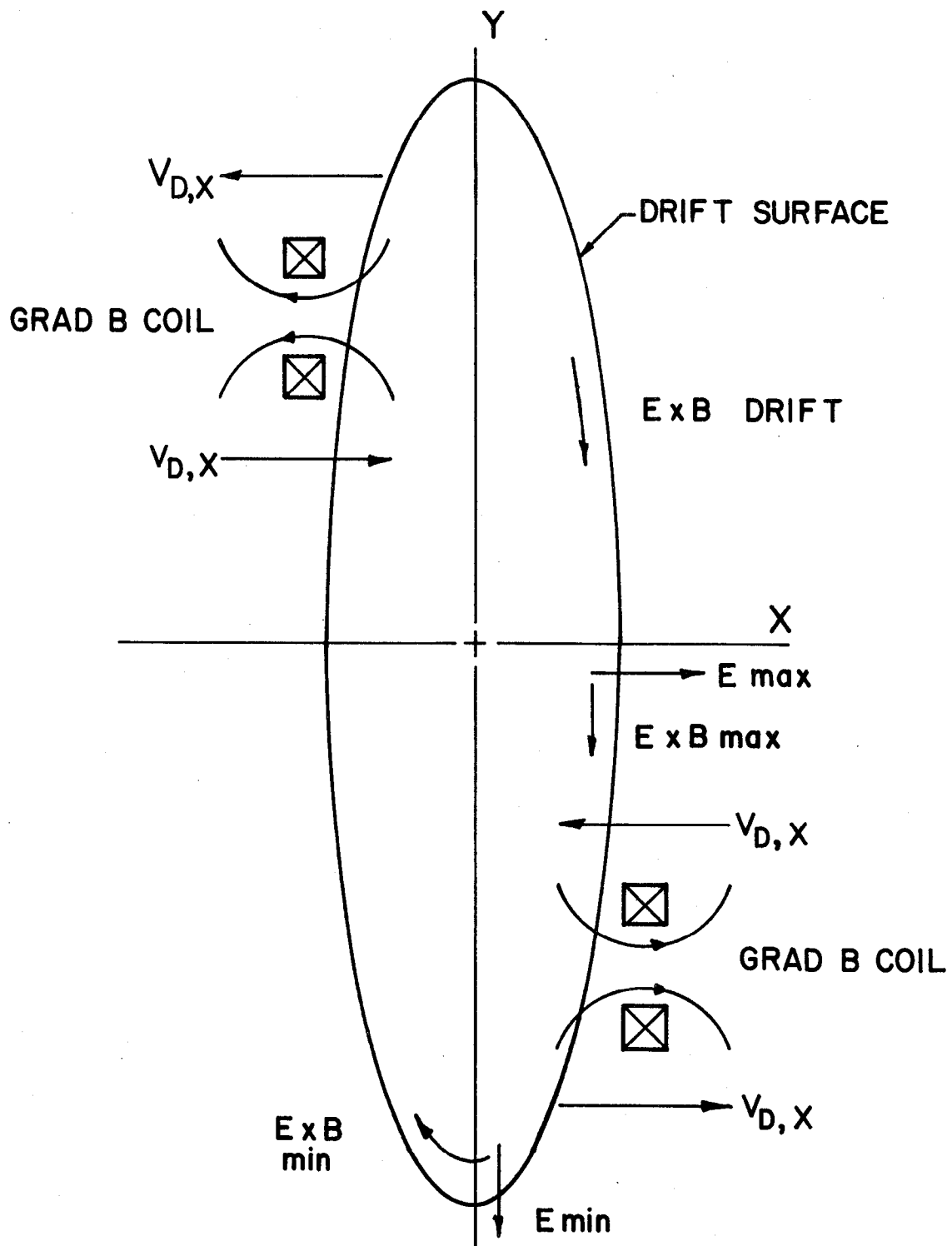
Fig. III.A.4 Schematic of grad-B pumping.

Consequently it is possible to arrange conditions such that the cumulative drift $\Sigma\delta(x)$ is non-zero.

Figure III.A.5 shows guiding-center trajectories in the y-z plane of two trapped ions under conditions identical except for the longitudinal kinetic energy $W_{\parallel}$. The ExB drift speed in the y direction is changed because of a change in the E_x field due to the plasma potential. Conditions are adjusted such that the turning point of the trapped thermal ion is to the right of the perturbation coil while the turning point of the sloshing ion is to the left, where grad-B is of the opposite sign.

Figure III.A.6(b) shows that the trapped ion suffers an outward displacement each time it passes one of the four perturbation coils. After several drift periods it has been pumped out of the plasma. On the other hand, the sloshing ions of Fig. III.A.6(a) is retained by the net inward drifts. The results are similar if we eliminate the electric fields and use the non-uniform azimuthal drift caused by the quadrupole component of the Yin Yang.

The ExB drifts of ions and electrons are in the same direction, but their grad-B drifts are in opposite directions. Therefore the same fields that pump the ions outward will retain the electrons.

In order to apply this model to the Axicell TMR some type of non-uniform azimuthal drift is necessary. There are several ways to accomplish this.

1. The transition coil between the thermal barrier and the anchor has a large quadrupole component, which will cause non-uniform azimuthal grad-B drifts.

2. The plasma potential of the yin-yang anchor is not axially symmetric. Since the barrier plasma is electrically in contact with the higher-density anchor, the azimuthal ExB drift will be non-uniform.

3. If necessary, one of the circular barrier coils (9-T or 20-T) can be deformed. If these coils were square or hexagonal the barrier plasma would have azimuthal gradients of plasma potential and also of B.

In addition to pumping of trapped D-T ions, the grad-B perturbations will pump thermalized alphas and impurities after they diffuse into the region of velocity space accessible to grad-B pumping. By considering the rates of alpha production and diffusion, we estimate that the density alpha in the central cell will be about 7% of the D-T density.

Engineering of the perturbation coils is straightforward, using water-cooled copper conductors and silicon carbide insulation. Neutron shielding

(a) SLOSHING IONS. $W_\perp = 37.5\,KeV$ $W_{II} = 100\,KeV$

(b) TRAPPED IONS $W_\perp = 37.5\,KeV$ $W_{II} = 50\,KeV$

SLOSHING ION TURNING POINT IS BEYOND PERTURBATION COIL. NOTE CHANGE IN RATE OF Y DIRECTION DRIFT DUE TO CHANGE IN E FIELD STRENGTH

TRAPPED ION TURNING POINT IS COINCIDENT WITH PERTURBATION COIL.
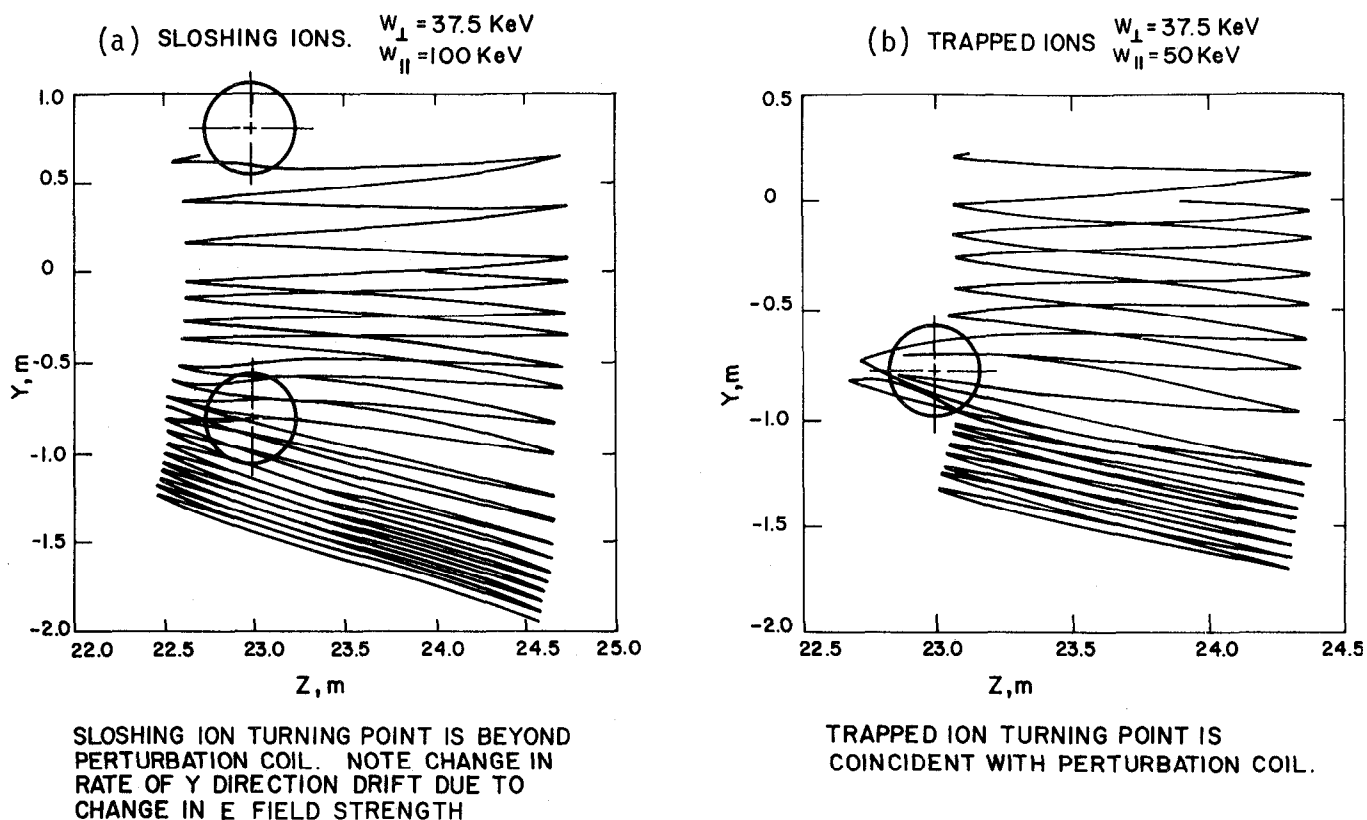
Fig. III.A.5 Grad-B pumping trajectories, y-z plane. Guiding-center trajectories in the y-z plane computed by MAFCO-II for two ions under conditions identical except for the initial value of W : (a) 100 keV; W = 37.5 keV, simulating a thermal ion deeply-trapped in the potential well. The turning points of sloshing ions (a) are beyond the perturbation coil ($\Delta z < 0$), while the turning points of deeply-trapped ions (b) are near the perturbation coil ($\Delta z \sim 0$). Note the change in v_{Dy} at y = -1 m, which is due to the change in E_x.

(a) SLOSHING IONS. $W_\perp = 37.5$ KeV
$W_{||} = 100$ KeV

(b) TRAPPED IONS $W_\perp = 37.5$ KeV
$W_{||} = 50$ KeV
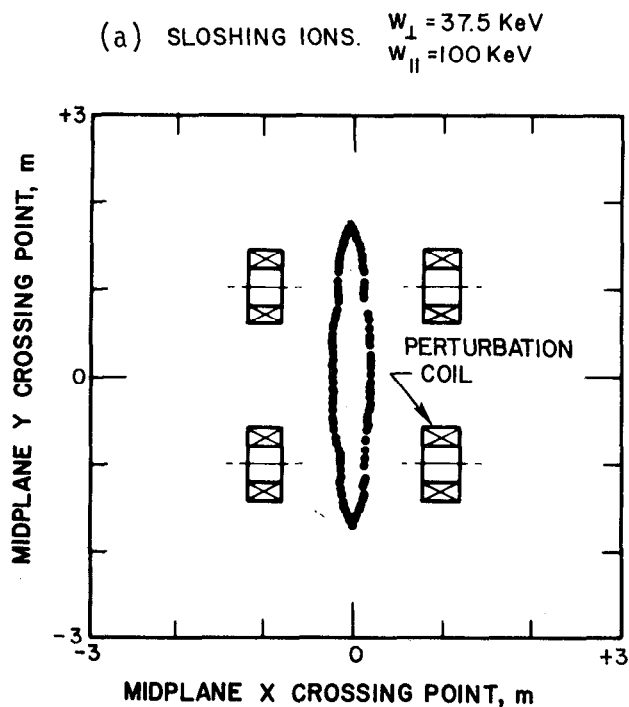
SLOSHING IONS ARE NOT PUMPED OUT OF THE BARRIER.
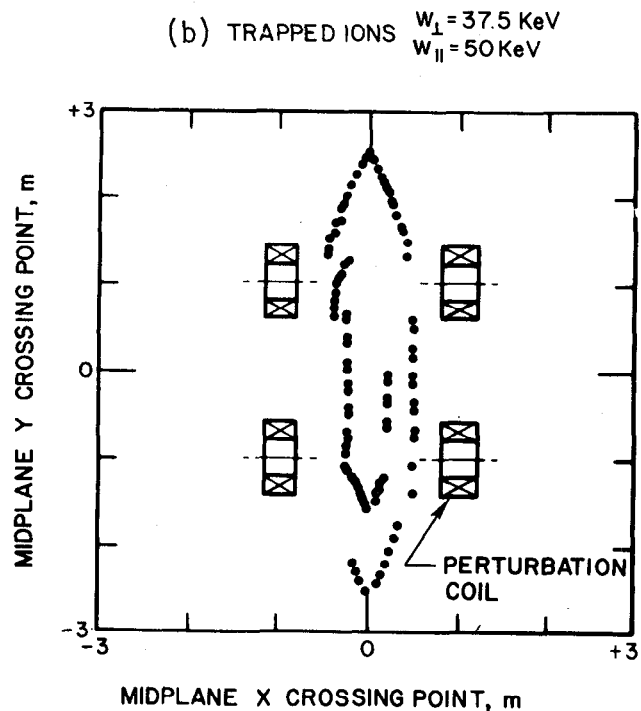
TRAPPED IONS ARE PUMPED OUT OF THE BARRIER.

72-206-1

Fig. III.A.6 Grad-B pumping trajectories, x-y plane. The traject-
ories of dirfting ions indicated by crossing points at the
barrier midplane, z = 23.9 m. The conditions are the same
as in Figure III.A.5. The sloshing ions are retained
while the trapped thermal ions are selectively pumped out
of the plasma after a few drift cycles.

III-15

cannot be used because the coils must be mounted as close as possible to the plasma. The ohmic power consumed by the copper coils will be in the range from 1 to 10 MWe, depending upon the ampere-turns and the number of coils decided upon.

III.A.2 Axicell End Plug Magnets - General

In the axicell end plug a 20-T solenoid using a copper insert in the high magnetic field zone is closest to the central cell. It is followed by a super-conducting solenoid creating 9-T field on axis. The region between the two solenoids forms the thermal barrier. A "C"-shaped transition coil assists the field lines in entering the outermost "anchor" coil-pair which is a yin yang with 4 T mirrors. This latter quadrupole provides the MHD stability required to avoid plasma disruptions. Figures III.B.1 and III.B.2 show the end-plug configuration.

III.A.2.a High Field Barrier Solenoid.
A water-cooled copper insert combined with both Nb-Ti and Nb_3Sn layers of superconductor to make a 20-T solenoid is the first coil seen by the plasma as it attempts to leave the central cell. Figure III.A.7 shows the cross section of that magnet. Note that three separate layers of superconductor are needed--two with Nb_3Sn and one with Nb-Ti. Each superconductor region requires some steel in the conductor space to help transmit conductor force to the outer case without overstressing outer layers of conductor. The case and shield are integrated to a single heavy housing. Also note that the copper insert itself serves as part of the shielding required by the superconductors.

The question of resistivity changes and material property changes resulting from 14 MeV neutron damage are being examined. Both lattice damage and transmutations occur, and both affect resistivity and ductility. B. G. Logan (LLNL) has calculated that neutron radiation of 6 MW-yrs $\cdot$ m^{-2} can be withstood before a coil change is required. The resistivity change, hence power consumption increase, is the determining factor on replacement time.

III.A.2.b The 9-T Solenoid.
The 9-T solenoid can not be made of only Nb-Ti superconductor. The inner 20% of the coil's cross section must be made of Nb_3Sn to allow conductor fields in excess of 9-T. Our calculations for field do not differentiate the two zones from the standpoint of current
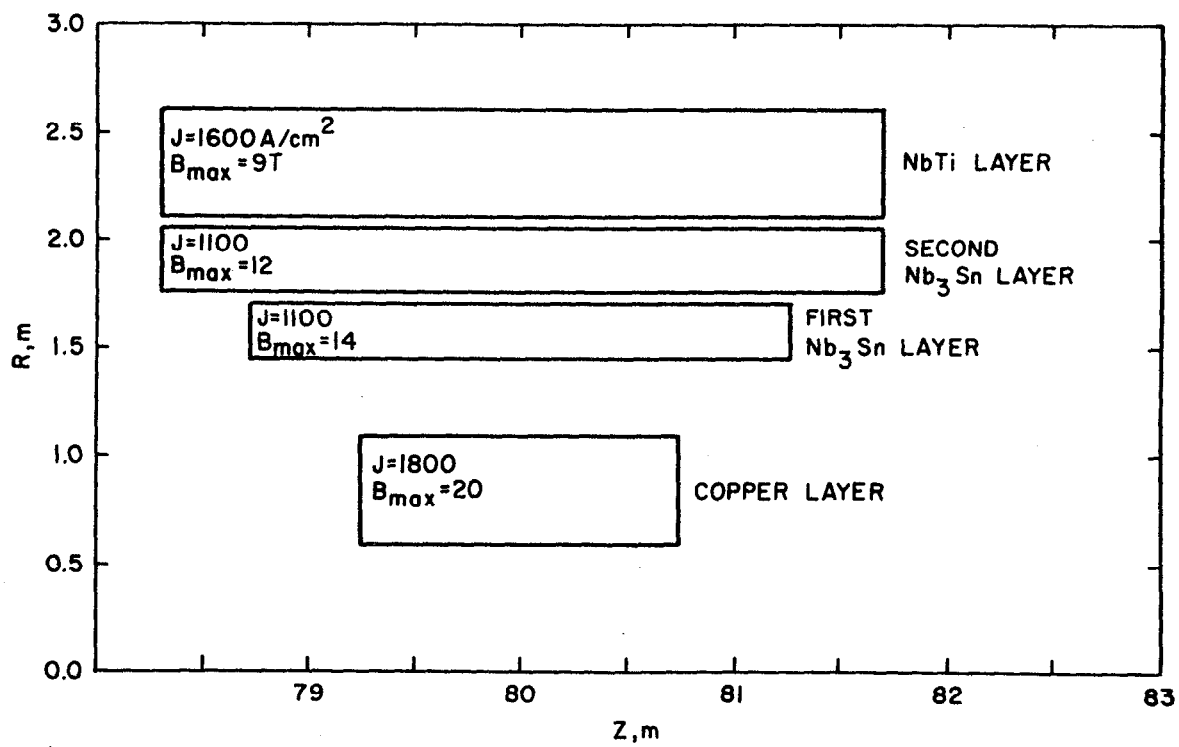
Fig. III.A.7 20-Tesla solenoid.

density. We assumed 2000 A · cm^{-2} for both zones. This is conservative compared to MFTF-B solenoids which use 2900 A · cm^{-2} in Nb-Ti conductor. However, it may be a bit optimistic for the Nb_3Sn region. Since the latter is only 16% of the conductor mass, we do not anticipate a significant change in size or cost after design optimization calling for more structural steel in this Nb_3Sn zone.

III.A.2.c <u>The Transition and Yin-Yang Anchor Magnets.</u> The yin-yang anchor and its associated transition magnet are all constructed of Nb-Ti superconductor operating at conductor fields well under 8 T. The current density is 2000 to 2200 A · cm^{-2} which is conservative when compared to about 2682 A · cm^{-2} in similar MFTF-B yin-yang coils.

The conductor for all three magnets could be identical to that used in MFTF-B. Their shape is similar. Both the transition and yin coil have sweep angles of 90°. The yang coil has a sweep angle of 53.5^o. The size of the magnets far exceeds the MFTF-B magnets. Coil forces and structure are discussed later in this section.

III.A.2.d <u>Solenoid Magnets in the Central Cell.</u> The central-cell solenoids could use the same superconductor (Nb-Ti) as is planned for use in the MFTF-B solenoids. It is in cross section a 10 mm-by-4 mm rectangle of copper with a superconducting square (copper plus Nb-Ti filaments) inset at the middle of one of the 10 mm-wide surfaces. This is a less expensive design than the yin-yang superconductor with its milled copper stabilizer jacket. The lower conductor field strength in the solenoid permits the simpler conductor design.

The solenoids are of rectangular cross section with very simple case structure. It will be necessary to insert thrust spacers at several locations around the coil annulus to maintain coil separation during reactor operation. A system of self-locking hydraulically adjusted wedges can accomplish this bracing. It is necessary to unlock and/or remove all thrust spacers prior to repositioning a magnet or removing a cell module.

III.A.2.e <u>Field Ripple.</u> The spacing between magnet coils in the solenoid must be small enough relative to the diameter of the coils so that the resulting ripple in the field is small enough. If the ripple is too large, the plasma becomes unstable to the interchange mode. Fig. III.A.8 shows a plot of the field ripple (defined as the peak-to-peak variation in B divided by the

(a)

(b)
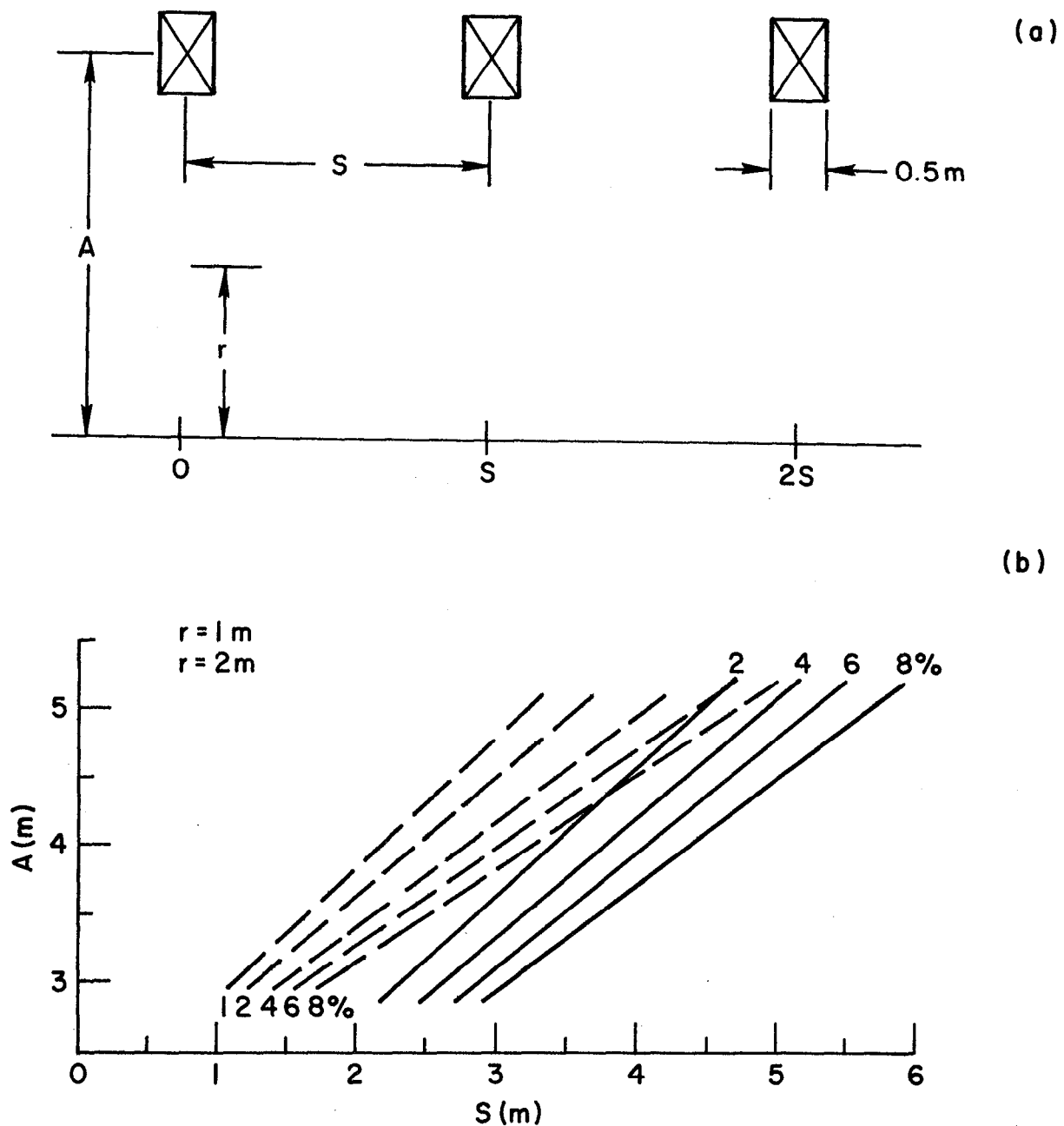
Fig. III.A.8 Ripple in magnetic field versus coil parameters.
The geometry and notation shown in (a) is used to
calculate the ripple in magnetic field,
$[B(0) - B(S/2)]/B(S/2)$, at different radii $r = 1$ m
and 2 m. Current density and mean-axial field
$(2.5 \times 10^7$ A/m^2, 4.0 T) were fixed as S and A
were varied, causing the radial thickness of the
coils to vary also.

smaller value of B) at a radius of 1 m and at 2 m as a function of mean coil radius A and center-to-center spacing S for coils of 0.5 m length. In calculating the ripple, both current density (2.5×10^7 A/m^2) and average axial field (4.0T) were held constant. Therefore, the coil thickness in the radial direction varied as S was changed. Shorter but thicker coils give slightly larger ripple, while longer, thinner coils give smaller ripple. The 5 m radius coils with 3.2 m spacings shown in Fig. III.B.2 produce less than 1% ripple at the 2 m radius, and even less at 1.5 m or 1 m.

III.A.3 Electron Cyclotron Resonant Heating (ECRH)

It has been explained how the performance of tandem mirrors can be improved by two types of electron heating. The most obvious improvement is the increase in the peak plasma potential in the thermal-barrier cell, where the warm electrons are electrostatically contained by the positive ambipolar potential. Also, the potential well in the thermal barrier can be deepended by heating the electrons enough that they become collisionless and are therefore confined magnetically rather than electrostatically. To meet these two purposes, two heating systems are required. Of the various possible techniques for heating electrons, we prefer ECRH, because this technique heats the electrons directly, without ion interactions, and because a large body of experimental evidence is available to prove its effectiveness.

The ECRH power requirements for the reference case of the Axicell TMHR have been computed by the second-generation code as 18.7 MW into the potential-peak region of the barrier cell and 29 MW into the thermal barriers [points (a) and (b), respectively, in Fig. II.B.5]. The frequency requirements are determined by the magnetic field and electron densities at these two points. The condition for resonance and for accessibility is

$$f = f_{ce} > f_{pe},$$

where f is the microwave frequency, $f_{ce} = eB/2 \pi m_e$ is the electron cyclotron frequency, and $f_{pe} = (ne^2/m_e \epsilon_0)^{1/2}/2\pi$ is the electron plasma frequency.

Table III.A.2 shows how these requirements are used to specify the ECRH power absorbed by the plasma and the microwave frequency required. By making further assumptions of overall efficiency, power density, and power per unit, we obtain the performance requirements of the gyrotrons, waveguides, and

Table III.A.2   ECRH requirements for the reference case of the
Axicell TMHR   [Points (a) and (b) may be found on Fig. II.B.5]

	Potential Peak [Point (a)]	Center of Barrier [Point (b)]	Total
Power absorbed by plasma, both ends (MW)	19	30	49
B_{vac} (T)	2.7	1.8	
$f = f_{ce} = 28\ B_{vac} \sqrt{1-\beta}$ (GHz)	64	40	
$f_{pe} = 8.97 \times 10^{-6} n_e^{1/2}$ (GHz)	36	30	

windows. The condition for accessibility of the resonance is satisfied, since f_{ce} is larger than f_{pe} in both cases.

Recent ray-tracing computations (III.A.10) have improved the expectations that the accessibility and absorption of ECRH microwaves by tandem mirror plasmas will be excellent, especially as the electron temperatures, densities, and dimensions are increased above the conditions of the present generation of experiments. Mirror plasmas, with minimum-B configurations, are natural candidates for ECRH, because the magnetic field is decreasing radially inward so that there is good accessibility for both the O-mode and the X-mode of propagation. Single-pass absorption of both modes will be essentially 100% for both modes under conditions of the TMHR. The questions regarding the absorption of the ordinary mode in the plasma during startup, when the conditions are not ideal for absorption of this mode need to be addressed.

The performance requirements indicated in Table III.A.2 are believed to be within the reach of near-term technology. In our TMR design of 1979 (Ref. 4, Ch. 6), we discussed a similar set of ECRH requirements and showed how they can be fulfilled by extensions of technology already under development. During the past few months, these expectations have been strengthened in the following ways:

● Improved rf windows have recently made possible the steady-state operation of commercially available, 28-GHz gyrotrons at power levels up to 212 kW. The improved windows consist of two slabs of dielectric (alumina or beryllia) cooled by a liquid dielectric flowing between them. Since the window losses are proportional to frequency, it is possible to design for average power densities of K/f, where K has been experimentally proven to be at least 187 kW· GHz/cm^2, and where new designs are based upon values of K = 400 kW·GHz/cm^2.

● Development of gyrotrons with steady-state outputs of 1 MW each is a reasonable expectation during the next few years, according to the opinions of several scientists working in this field (III.A.11). Pulsed gyrotrons have already been reported at 1-MW operation (III.A.12). This implies a window diameter of 18 cm for a frequency of 100 GHz. The 0.3-cm microwaves must be transmitted at high mode numbers in the 18-cm waveguide.

● Gyrotron efficiencies can theoretically be improved either by tapering the magnetic field in the resonant cavity or by tapering the cavity itself (III.A.13). The Naval Research Laboratory is predicting an enhanced efficiency of 60%; a gyrotron with an output of 147 kW at 47% efficiency has already been commercially tested. We believe that the other losses (waveguide, windows, plasma absorption, etc.) will be small under TMNS conditions, and we are therefore assuming an overall efficiency of 50%.

A recent experiment in the ISX-B Tokamak (III.A.14) is noteworthy because a high-power gyrotron (80-kW, 35-GHz) has injected microwaves into a plasma under conditions such that significant ECRH absorption occurred for a single transit. The electron temperature increased from 850 eV to 1250 eV, in agreement with calculations. For the first time, it was demonstrated that the electron temperature in a tokamak scales linearly with ECRH power.

Four ECRH assemblies are required to heat each of the two thermal barriers and the two potential-peak regions. Each assembly will consist of 10 gyrotrons at each end at the potential peak and 15 gyrotrons at each end at the barrier minimum. Each gyrotron will have an input power of 2-MWe, which is the power of an 80-keV, 25-A electron beam. The total input power is 100-MWe for the 50 gyrotrons.

ECRH requirements for the Axicell TMHR will require improvements in power, efficiency, and cost, in comparison to systems now in operation. However, these improvements are already programmed for other large fusion projects and will be available well in advance for the TMHR. The draft of the Engineering

Development Plan for Fusion Power Systems indicates that development of steady-state 110-GHz, 1-MW gyrotrons and transmission systems will be completed by September 1989. There is every reason to expect that the improvement in efficiency and cost reductions because of economics of scale and experience will occur on the same time scale.

Figure III.A.9 shows how the waveguides are brought in a large experiment, MFTF-B, for heating of a tandem mirror by ECRH. A similar system would be suitable for the Axicell TMR. Recent experience indicates that the long-radius bends are more efficient than the mitre bends. An rf window is normally installed so that most of the waveguides can be pressurized with an inert gas. This prevents breakdowns in the fringing-field region where $f = f_{ce}$ locally within the waveguide.

III.A.4. Plasma Direct Converter

A single stage plasma direct converter (PDC) on only one end of the reactor recovers 390(450) MW of electricity from the total 745(985) MW of end loss power. The first values given here are for the reactor design with 20T peak mirror field, while the values in parentheses are for the 14T case which has more recirculating power. The net efficiency of the PDC is therefore 52(46)%. A simple thermal dump at the other end of the reactor receives 85(156) MW of electron power plus smaller amounts of α- and ECRH-heated electron power. About half of the end loss power that is not directly recovered is available for thermal recovery.

The PDC has a single collector stage and two water-cooled grids. Experimental tests of PDCs at up to 100 kV and 6 kW are reported in Ref. III.A.15. Because only a small amount of electron power has to be handled by the PDC, it needs only 265(340) m^2 of collector surface. About an equal area of cryopanels is required to maintain the pressure at 2×10^{-5} Torr in the end tanks. The halo plasma and its additional cryopumps are discussed in Sec. II.E.

One novel feature of the TMR concept is that the end-loss ions can be preferentially lost out one end and the center-cell electrons preferentially lost out the other end. This condition is accomplished by lowering the potential in one plug slightly so that, as the ions that are confined in the central-cell scatter in phase space, they escape over the lower potential barrier before they can gain enough energy to pass over the higher one. The
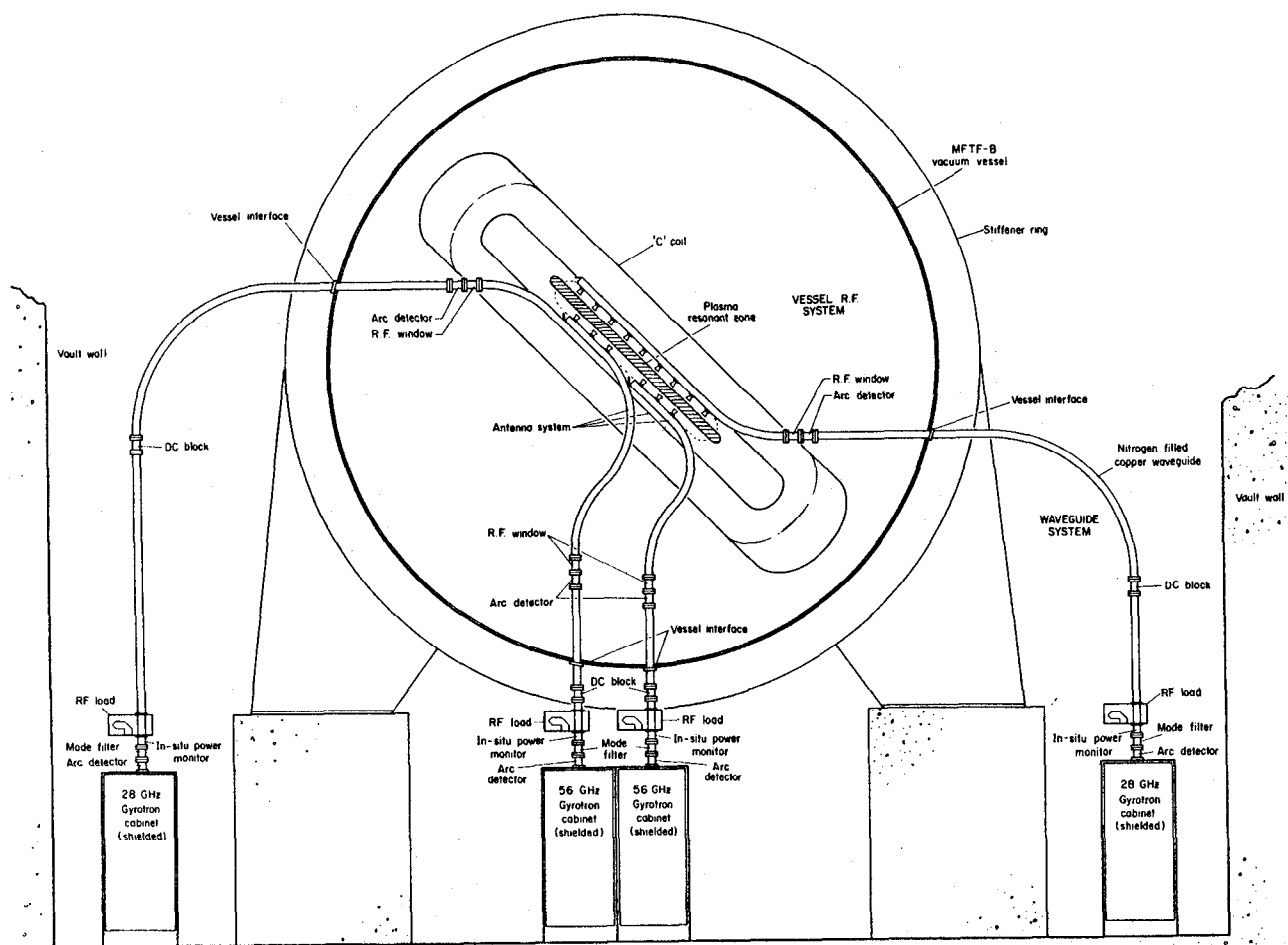
Fig. III.A.9 Typical MFTF-B ECRH rf system.

electrons are unaffected by the change in plug potential since they are confined by the combination of the positive potential, ϕ_e, and the magnetic mirror. By holding the entrance grid to the ion collector at a small negative potential and by decreasing the magnetic mirror on the electron end, the central-cell electrons can be allowed to leak out one end before they scatter into the loss cone for the ion end.

The great advantage in separating the end-loss electrons from the ions is gained at the ion end. At the PDC, which recovers most of the ion power electrically, an electron repeller grid (see Fig. III.A.10) prevents electrons from reaching the ion collector. Most of the electrons flowing out of or produced in the ion end are reflected by the repeller grid and are eventually collected on the entrance grid, which immediately precedes the repeller. The entrance grid, therefore, has to handle the heat generated not only by the small fraction of the ions that are intercepted but also by most of the electrons that go out that end. By causing most of the end-loss electrons to go out the other end, the heat load on the entrance grid is greatly reduced - in these cases from 95(115) MW to essentially only the intercepted 35(45) MW of ions and barrier cell electrons. About 25(90) MW of electrons go out each end from the barrier cell. These electrons are too energetic to be selectively leaked to only one end, or even to be stopped by the repeller grid of the PDC.

The separation of most of the electrons allows a relatively compact PDC for the ion power. The small size of the PDC allows the use of convectively cooled grids, which in turn allows a higher power density than radiatively cooled grids. In the present design, the longest of the grid elements is about 7 m long. Their outside diameter is 10 mm, making each grid 5% opaque to the beam. A tube wall thickness of 1 mm allows sufficient water flow with 50 atm of pressure difference to handle an average heat load of 3.5 MW/m^2 along the length on one side. The exit pressure must be 20 atm to prevent bulk boiling in the tubes at 3.5 MW/m^2. Both TZM and Ta-10W have sufficient strength and thermal conductivity to give a safety factor of at least 5 for the hoop stress and at least 2 for the thermal stress. Thermal stress improves with times as the tube walls become thinner due to sputtering.

III.A.4.a <u>Energies and Currents of End-Loss Particles.</u> Eighty percent of the fusion power, P_F, is carried out by neutrons. A fraction of the alphas $f = 1 - \sqrt{1 - 1/R} \simeq 0.05$, where R is the mirror ratio, is born in the loss cone and lost immediately out the ends, each with its original 3.5 MeV of

ENTRANCE GRID   REPELLER GRID   ION COLLECTOR

$V_1 = -1\,kV$ $V_2 = -35\,kV$ $V_C = +365\,kV$

ION FLUX

20 cm

1.0 cm o.d.

0.5 m

d = 1.0 m
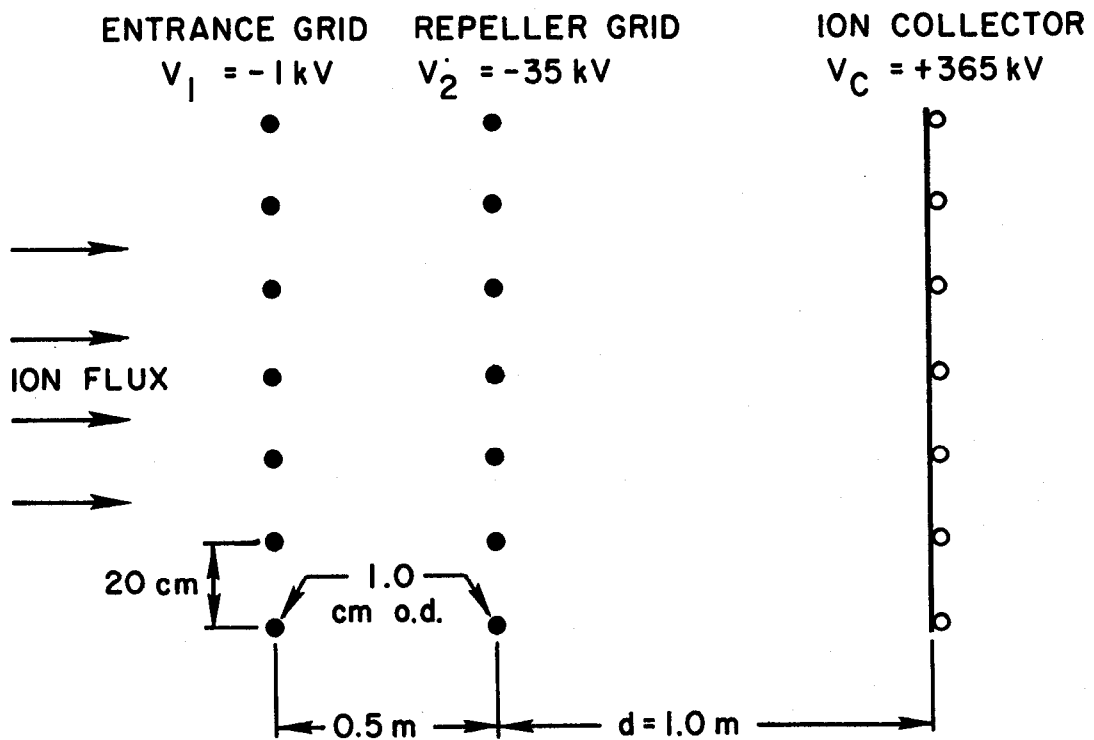
72-206-0

Fig. III.A.10   Grids and collector in plasma direct converter.

energy. We assume that the confined alpha particles escape radially after giving up all but $E_\alpha \simeq 100$ keV of their original 3.5 MeV to the confined plasma. Nearly all of the remaining alpha power plus most of the injected power finally escapes out the ends. In Sect. II.F it is shown that only $P_{rad} \simeq 10$ MW is radiated to the walls, mostly by bremsstrahlung. Therefore, the total power carried out both ends by charged particles is:

$$P_{end} = P_F(\frac{1}{Q} + 0.2 - E_\alpha/E_F) - P_{rad},$$

where the fusion energy is $E_F = 17.6$ MeV.

The preservation of charge neutrality requires that the currents of electrons, I_e, and of escaping fuel ions, I_i, out the ends be related by:

$$I_e = I_i + 2P_F/E_F,$$

where the last term represents the alphas, which go out radially to the halo plasma (see Sect. II.E). On the average each escaping center-cell ion has an energy of $T_{ic} = 40$ keV (i.e., thermal energy in two degrees of freedom), and is then accelerated by the potential difference $\phi_c + \phi_e = 370(360)$ kV before reaching the entrance grid at the PDC. The average energy is, therefore, 410(400) keV, and the minimum is 370(360) keV. Some fraction of the energetic sloshing ions escape out the near end with average kinetic energy $T_{s\ell} = 250$ keV plus 370(360) keV from the potential difference. The power carried by these ions is, therefore, about half of $P_{s\ell}$, the sloshing ion beam power, and half of that goes to each end. The total power, P_i, carried out the ends by ions is, therefore:

$$P_i = I_i(\phi_e + \phi_c + T_{ic}) + \frac{1}{2} P_{s\ell}\left(1 - \frac{T_{ic}}{T_{s\ell}}\right) .$$

Only the high-energy tail of the central-cell electrons can escape from the confining potential ϕ_e. If the energy distribution of the confined electrons is Maxwellian, the escaping electrons arrive at ground potential with a mean energy of T_{ec}. We assume the escaping barrier-cell electrons arrive with a mean energy of T_{eb}. Therefore, the power, P_e, carried out by electrons is:

$$P_e = I_e T_{ec} + \frac{1}{2} P_{ECRH}\left(1 - \frac{T_{ec}}{T_{eb}}\right) ,$$

where we have assumed that half of the ECRH power is lost in the form of high energy electrons, and half of that goes to each end. (Calculations (III.A.16) have shown that 45% of P_{ECRH} is lost this way, while the remainder goes into heating center-cell electrons.)

By equating $P_{end} = P_i + P_e$, we can solve for I_e and obtain I_i, P_i, P_e, and the fractions of each of these at the PDC and at the electron dump. The power deposited on the entrance grid consists of the intercepted fraction of the ion power and of the energetic, barrier cell electrons, plus all of any lower energy electrons. To cover the general case where the central-cell electrons may, or may not, be selectively leaked out one end, we write the power to the entrance grid as:

$$P_g = (1 - T_g) \left\{ \left(I_e - \frac{2P_F}{E_F} \right) (\phi_e + \phi_c + T_{ic}) + \left(\frac{1 + \delta}{4} \right) \left[P_{s\ell} \left(1 - \frac{T_{ic}}{T_{is\ell}} \right) \right. \right.$$

$$\left. \left. + P_{ECRH} \left(1 - \frac{T_{ec}}{T_{eb}} \right) \right] \right\} + \delta I_e T_{ec}$$

The selective leakage parameter δ is defined by: $\delta = 0$ if the central-cell electrons are selectively leaked out one end, and $\delta = 1$ if they are not selectively leaked but are present at the PDC. The transparency of the grid is T_g. In the present design $\delta = 0$ and $T_g = 0.95$. The other PDC parameters are tabulated at the end of this section.

We define an effective power density $(P/A)_{eff}$ which, if made up entirely of ion power, would give the same heating at the grid as P_g. That is,

$$(1 - T_g) (P/A)_{eff} = P_g/A_{PDC} \quad ,$$

where A_{PDC} is the surface area of the PDC. Typically $(P/A)_{eff} = 1$ MW/m^2 is allowed by grids of tungsten wires that are cooled only by radiation, while $(P/A)_{eff} \simeq 2.5$ MW/m^2 is allowed by water cooled grids. The limit for water cooled grids depends on the size, length, material, and on the reliability that is required. In the present design where the tubes are 7 m long, we use 1 cm diameter tubes of TZM or Ta-10W and an initial safety factor of about 2 to allow 2.5 MW/m^2 average over the length of a tube. The area is $A_{PDC} \simeq 265(340)$ m^2. Without selective leakage the area would be about 765(970) m^2.

III.A.4.b Spacings in the Plasma Direct Converter. The grid parameters are
determined by the spacing d between the collector surface and the surface of
the negative grid (see Fig. III.A.10). Element-to-element spacing in a grid
must be small compared to d to give reasonably smooth surfaces of
equipotential near the grid so that the ions are not deflected more than about
10°. The spacing
d is determined by the space charge of the ions. The mean ion current density
j_i at the PDC is about $j_i \sim 6$ A/m^2, and the space charge limited
spacing, d_{max}, is

$$d_{max}^2 = \left(\frac{4\varepsilon_0}{9}\right)\left(\frac{2q}{M}\frac{V^{3/2}}{j_i}\right),$$

where $\varepsilon_0 = 8.85 \times 10^{-12}$ F/m, q is the charge, M is the mass of an ion,
and V is the voltage difference across the space d_{max}. In this expression
it is assumed that the ions all have zero energy at the anode. In the PDC the
collector voltage is about 365(350) kV and only some of the ions are decelerer-
ated to near zero energy. The average ion arrives with 40 keV of kinetic
energy remaining. For this reason, the above expression gives a slightly
smaller value for d_{max} than the true value. Actually, in a PDC the main
consequence of exceeding d_{max} is to increase the loss due to charge exchange.
If the spacing is greater than d_{max}, a virtual anode tends to form near the
collector. If the potential at the virtual anode were to rise above the
collector voltage, some ions would be reflected before reaching the collector.

But, the emission of secondary electrons from the collector prevents the
space charge potential from rising more than a few volts above that of the
collector. The result is a region near the collector where the potential is
high and nearly constant. Here, the ions move with low velocity and therefore
with large cross sections for charge exchange. It is therefore prudent to
design for $d < d_{max}$.

The voltage difference across the spacing d is approximately the
difference between the 365 kV collector voltage and the -35 kV grid voltage
(see below), or 400 kV. The above equation gives $d_{max} = 1.2$ m for an equal
mixture of 400-keV tritons and deuterons making up the current density $j_i =$
6 A/m^2. We choose d = 1.0 m and set the spacing between the negative grid
and the grounded grid equal to 0.5 m.

The spacing, a, between tubes in each grid plane must be small as
compared to d in order to produce smooth equipotential surfaces near the
grid. A ratio of the spacings a/d < 0.3 is required to reduce the mean

scattering angle for ions passing through the grid to less than 0.1 radius. Therefore, a < 0.3 m is required. But, since the grid tubes have a 1 cm diameter, a >> 1 cm is required to reduce the interception on the grid. We choose a = 0.2 m, giving an opacity of 5% to the grid.

III.A.4.c <u>Capacitively Stored Energy</u>. In designing the support structure, the total capacitively stored electrical energy must be considered. The stored energy that can be released in a spark must be kept below about 10 J to prevent damage to the electrodes. To limit the stored energy available, the PDC must be electrically divided into sections. The total stored energy E_{st} in the PDC is:

$$E_{st} = \frac{1}{2} CV^2 \quad,$$

where

$$C = \frac{\varepsilon_0 A_{PDC}}{d}$$

$$\varepsilon_0 = 8.85 \times 10^{-12} \text{ F/m} \quad.$$

$A_{PDC} = 265(340) \text{ m}^2$ is the surface area of the PDC, d = 1.0 m is the grid-to-collector spacing, and V = 400 kV is the potential difference between grid and collector. The above gives E_{st} = 200 J, indicating that the PDC must be divided into at least 20 electrically isolated sections.

III.A.4.d <u>Grid Voltage</u>. Each section of the PDC is similar to a plane, triode vacuum tube. We must operate it beyond the cutoff condition to prevent cold electrons at the entrance grid (cathode) from reaching the collector (plate). The analysis described by Spangenberg (III.A.17) for the grid voltage required for cutoff in triodes shows that the grid voltage, V_g, must satisfy:

$$V_g \leq -V_p/16$$

for our geometry ratios. Here, V_p = 365(350) kV is the collector voltage. Since the center-cell electrons are dumped at the other end and the barrier-cell electrons are too energetic to stop, it is only the cold electrons from ionizedgas that the grid must repel. If center-cell electrons

were incident on the grid, V_g would have to be increased by 3 or 4 times T_{ec} (i.e. about 100 kV more).

Spangenburg's analysis does not include the space charge of the ions. The effect of space charge can be approximately allowed for by observing that in a space-charge limited diode (considering only the negative grid and the collector now), the electric field at the cathode is just 4/3 times the vacuum field. We can include this effect in the analysis by using 3/4 of the actual d value. This gives $V_g \leq -V_p/13 = -28$ kV. We set $V_g = -35$ kV.

III.A.4.e <u>Vacuum Requirement</u>. The vacuum in the region between the plug and the PDC must be good enough so that only an allowable fraction of the escaping ions undergo charge exchange. Any ion that does capture an electron from a gas molecule will arrive at the PDC as a fast neutral. It will impact the collector with its full energy and generate heat but no direct electric power. The cold ion that is produced is trapped by the combination of the magnetic field and the high positive potentials of the plug on one side and the PDC on the other. It will finally diffuse to a magnetic flux tube that intercepts a grid element and will be collected there. Since its energy is low, very little heat is generated, but electrical power is consumed at the negative grid.

It is more serious if the ion suffers charge exchange inside the PDC near the collector where the potential is positive. Then the resulting ion is accelerated and can deposit a significant amount of heat on the grid that collects it.

The cross section for charge exchange of fast D^+ with D_2 molecules is 4×10^{-18} cm^{-2} at 400 keV and has a broad maximum value of 8.6×10^{-16} cm^{-2} between about 4 and 20 keV. Those ions that reach the PDC with only slightly more than the minimum energy are decelerated into that 4- to 20-keV range where the cross section is large. Higher energy ions see a much smaller average cross section. We can, therefore, estimate the vacuum requirement (see Ref. 1 for a more detailed calculation of the vacuum requirement) by calculating the pressure at which about 1% of those worst-case ions undergo charge exchange inside the PDS (see Ref. III.A.15). The fraction, $F_{0,L}$ of those ions that capture an electron in a charge-exchange collision in going the distance L from the plug to the collector surface is:

$$F_{0,L} = 1 - \exp\left(-\int_0^L n_0 \sigma_{10} \, dx\right),$$

or approximately

$$F_{0,L} \simeq \int_0^L n_0 \, \sigma_{10} \, dx \quad .$$

Here, n_0 is the neutral gas density, σ_{10} is the cross section for electron capture, and both n_0 and σ_{10} may vary with the distance x along the ion path. For those worst-case ions, the last 10 cm before collection dominates the integral so that:

$$F_{0.L} \sim n_0 \, \sigma_{10}(max)(10 \text{ cm}) \quad .$$

For $F_{0,L} \leq 0.01$, we must have $n_0 \leq 1 \times 10^{12}$ cm^{-3} giving a pressure $p \leq 3 \times 10^{-5}$ Torr. This is a rough estimate of the vacuum requirement. A more detailed determination of the allowed neutral density involves the economic trade off between increased vacuum pumping and increased PDC performance.

The allowed pressure, p, and the gas throughput, Q, then determine the pumping speed, S, that is required. The 1900(2400)A input of atomic ions becomes Q = 170(210) Torr-litres/s of molecular gas. Then:

$$S = \frac{Q}{p} = 8 \times 10^6 \ (1 \times 10^7) \text{ litres/s}$$

is the required pumping speed for the fuel ions. A cryopump with two sets of chevrons has a specific pumping speed of 4.4 litres/s-cm^2 for a mixture of D_2 and T_2 gas at 300 K. Therefore, about 210(260) m^2 of cryopanels is needed to pump the escaping fuel ions at the PDC end of the reactor.

Skimmers encircling the beam at each end remove the cold plasma, including the fusion alphas, that streams out along magnetic field lines leading from the outer boundary of the central-cell plasma. These skimmers direct their gas onto enclosed cryopanels which are equipped with argon jets for cryotrapping helium (III.A.18). See Sect. II.E for a discussion of the halo plasma and the skimmers.

III.A.4.f Shape of the Direct Converter. The shape of the PDC is determined by the magnetic field lines. From the conservation of magnetic flux and the known area of the PDC we can determine the location of the PDC along the flux tube from the central-cell plasma. We assume a cubic radial variation of β in the central cell, and find that the magnetic flux within the plasma radius is reduced by a factor of 0.75 if $\beta = 0.7$ on axis. Therefore, we can map the boundary of the end-loss plasma by calculating the field lines starting

from a radius of $\sqrt{0.75}$ times plasma radius in the vacuum central-cell field. The entrance grid of the PDC is formed into a cylindrical surface with an area of 265(340) m^2 that intercepts the field lines at nearly 90^0 everywhere.

Since the vacuum magnetic field in the central cell is B_c = 3.0 T, the flux ψ through the plasma is ψ = 0.75 x π(1.05 m)^2 x (3.0 T) = 7.79 Wb. Therefore, the average field strength at the PDC is B_{PDC} = 7.79 Wb/265 m^2 = 0.029(0.023) T. The constant-B surface at B = B_{pdc} T locates the entrance grid.

Figure III.A.11 shows the intersection of the B = 0.028 T surface with the field lines started at uniformly spaced intervals around the central-cell plasma. The end view, shown in Fig. III.A.11(a) as the projection onto the X-Y plane, shows a shoulder where those field lines that started at 45^0 from vertical in the central cell intersect the surface. These field lines make large X-excursions in the anchor and large Y-excursions in the end tank. However, the power density in the shoulder is low. Half of the end loss power is within the field lines from r = 0.5 m in the central cell, and 88% is from within r = 0.75 m. The PDC therefore can have a rectangular shape when projected onto the X-Y plane, with a width of about 7 m. The skimmer that receives the halo plasma (see Sect. II.E) can intercept any beam that would be outside of the 7 m wide PDC.

In Fig. III.A.11(b) it can be seen that the projection onto the Y-Z plane rather accurately forms the arc of a circle of radius 20 m, and centered at Z = 112 m. The PDC therefore has the shape of a section of a circular cylinder, as shown in Fig. III.A.12.

Figure III.A.12 shows the PDC and the outer boundary of the end-loss plasma as it leaves the last magnet and passes through the annular skimmer for the halo plasma. The division of the PDC into 20 electrically isolated sections is indicated in the figure. Not shown in Fig. III.A.12 is the neutron shielding around the magnet which also shields the cryopanels and the electrical insulators from fusion neutrons.

III.A.4.g <u>Summary of the Direct Converter Performance.</u> Table III.A.3 lists the values of the parameters used to analyze the performance of the PDC. In Table III.A.3, $P_{e\ell}$ is the electrical power output from the PDC, and P_{end} is the total end-loss power--including electron power dumped at the other
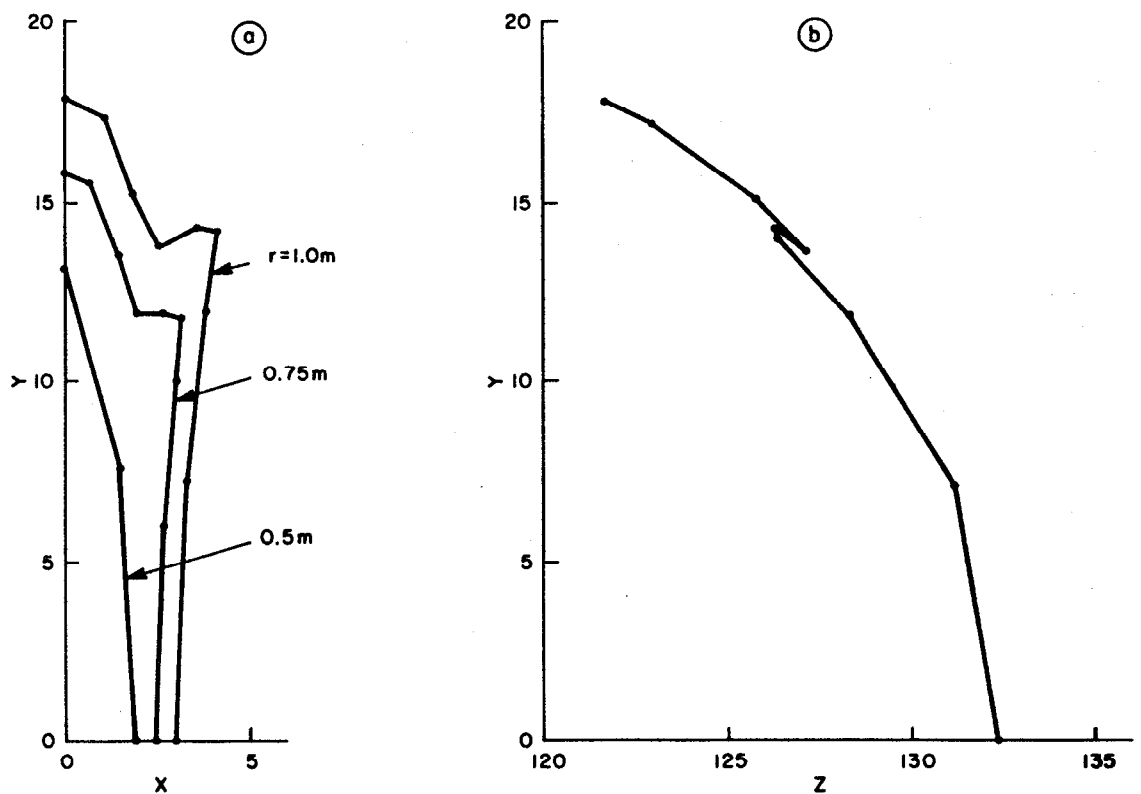
Fig. III.A.11 Geometrical shape of the end-loss plasma. The shape
of the direct converter on the axicell as indicated
by the intersection of field lines from the outer
boundary of the central-cell plasma with the surface
of constant B = 0.028 T. (a) shows the end view and
includes field lines from radii of 0.5 to 0.75 m in the
central cell. (b) shows the top view.

III-34

TABLE III.A.3. The Parameters Used to Analyze the PDC Performance for the Two Cases (20 T and 14 T) Studied.

		20 T case	14 T case
Q		15.3	6.7
P_F	(MW)	3000	3000
T_{ic}	(keV)	40	40
T_{ec}	(keV)	32.0	32
$T_{i,s\ell}$	(keV)	250	250
T_{eb}	(keV)	361	327
ϕ_e	(kV)	234	229
ϕ_c	(kV)	137	128
$P_{s\ell}$	(MW)	27.4	61.9
P_{ECRH}	(MW)	52.7	179
P_{end}	(MW)	745	985
P_i	(MW)	659	829
P_e	(MW)	85	156
I_e	(A)	1915	2360
p	(Torr)	2×10^{-5}	2×10^{-5}
A_{PDC}	(m^2)	265	340
A_{cry}	(m^2)	210	260
$P_{e\ell}$	(MW)	390	450
Net efficiency	(%)	52	46

end. Therefore the net efficiency is $\eta_{net} = P_{e\ell}/P_{end} = 52\%$ in the 20 T case and $\eta_{net} = 46\%$ in the 14 T case.

The table also lists the area A_{PDC} of the direct converter that results in an average effective power density of 2.5 MW/m^2. For the 20 T case, $A_{PDC} = 265$ m^2, while the 14 T case with its lower Q and higher end loss requires $A_{PDC} = 340$ m^2. To maintain a pressure of 2×10^{-5} Torr requires a cryopanel area of $A_{cry} = 210$ m^2 in the 20 T case, and 260 m^2 in the 14 T case. Notice that $A_{PDC} \simeq A_{cry}$ here. To halve the pressure (to 1×10^{-5} Torr) would require doubling A_{cry}. Since the pressure must be maintained at about this value to control the flow of cold electrons back into the plasma, the size of the end tanks cannot be significantly reduced by

eliminating the PDC. Skimmers for the halo plasma are also located in the end tanks and contain additional cryopumps (see Fig. III.A.12).

Table III.A.4 gives a summary of the effects on the PDC performance of the distribution of power flowing out the ends of the reactor. The indicated increments of power represent the change in the output electrical power $P_{e\ell}$ when that effect is suppressed. Therefore, these increments do not necessarily represent the total power carried by that species. Interception on the grids is the mechanism that gives the largest loss to the PDC. This large loss is due to the use of water cooled grids, each of which is 5% opaque to the beam. Power lost as heat to the grids is not useful in a thermal cycle because of the rather low temperature. However, most of the other losses result in heating of either the ion collector or the electron dump. These rugged structures can run hot and provide useful heat for thermal recovery.

In the 20 T case, 390 MW of electricity is produced from a total 745 MW of end loss power. The net efficiency of the PDC is therefore 52%. Mostly because of the difference in the energy of the barrier cell electrons, the net efficiency of the PDC in the 14 T case is slightly lower; 46%.

III.A.4.h Costs for the End Plasma Dump Components. The end plasma dump components consist of the end vacuum vessels, the direct converter in one end and the electron dump in the other, the cryopump systems (including the refrigerators) for both ends, and the halo plasma dumps in both ends. Estimates of the costs of these components are summarized in Table III.A.5. These cost estimates are based on the scaling laws for costs given in Ref. III.A.19 in 1975 dollars and repeated in Ref. III.A.20 in 1979 dollars.

For the vacuum vessel we take $13/kg (stainless steel III.A.230), and estimate the weight W_T by (III.A.19)

$$W_T = 200 \, R_T^3 \left[\left(\frac{H_T}{R_T} \right)^{1.4} \left(\frac{\theta_T}{360^0} + 0.32 \right) + 0.21 \, \frac{\theta_T}{360^0} \right] \quad .$$

Here, R_T is the radius, H_T is the height, and θ_T is the angle of the fan-shaped tank. To enclose the PDC shown in Fig. III.A.11, the vacuum vessel must have $R_T \simeq 24$ m, $H_T \simeq 10$ m, and $\theta_T \simeq 130^0$. Therefore, $W_T \simeq 7.6 \times 10^5$ kg, and the cost of the vessel containing the PDC is $C_T = \$9.9 \times 10^6$. The electron dump vacuum vessel at the other end has a similar shape but is about half as large. Its cost is therefore one eighth as much. The cost of both vacuum vessels is therefore about 11×10^6.
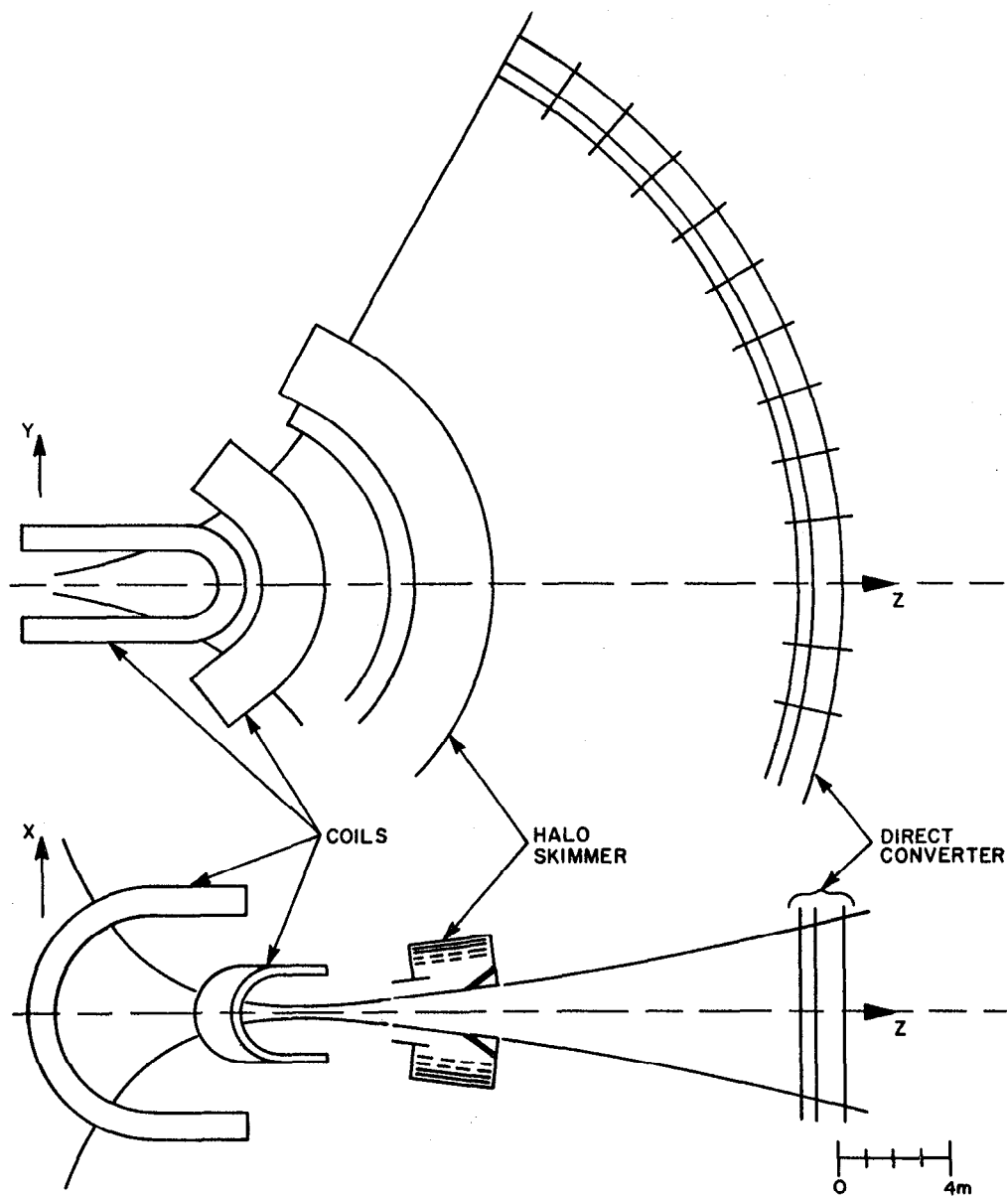
Fig. III.A.12 Location of the direct converter and the skimmer for
the halo plasma. Top and side views of the direct
converter on the axicell. The skimmer for the halo
plasma and the outermost coil are also shown. Neutron
shileding around the coil will also shield the skimmer
and the insulators in the direct converter.

TABLE III.A.4. The Distribution of End Loss Power (MW) in the Two Cases Studied, and the Power $P_{e\ell}$ Directly Recovered.

		20 T case		14 T case	
P_{end}	(total end loss power)	745		985	
P_e	(central-cell electrons)	85		156	
			660		829
P_α	(carried out by alphas)	42		52	
			618		777
P_{be}	(barrier cell electrons)	13		47	
			605		729
T_g	(grid interception)	109		144	
			496		585
p	(ionize and ch. ex.)	30		37	
			466		548
ΔE_i	(ion energy spread)	59		74	
			407		474
$\Delta\theta_i$	(ion angular spread)	18		22	
$P_{e\ell}$	(electrical output)	389		452	
Net Efficiency	$(P_{e\ell}/P_{end})$	52%		46%	

TABLE III.A.5. Costs of the End Plasma Dump Components.

	Cost ($M)
Vacuum vessels	11.1
Direct converter	2.1
Electron dump	0.02
Power conditioning	28.
Vacuum pumping	11.2
Halo plasma skimmers	11.0
Total	63.4

A single stage PDC with water cooled grids costs about $7500 m^{-2} in 1979-1980 dollars. The 280 m^2 PDC here costs, therefore, 2.1×10^6. The electron dump at the other end of the machine has an area of about 20 m^2 and, if made of water cooled copper, costs about $10/kg for a total cost of the dump of only 2×10^4.

Electric power conditioning (i.e. the conversion from d.c. to a.c. power at a different voltage) costs $70/kW. Since the electric power output from the PDC is about 400 MW, the cost of conditioning is 28×10^6.

Cryopanels cost $9600 m^{-2} and the refrigeration system costs $3.75 \times 10^5 \times A_{cry}^{.605}$, where A_{cry} is the cryopanel area. Since A_{cry} 200 m^2, the cost of the cryopump system for the gas generated in the PDC is 11.2×10^6. In addition, a small amount of gas is produced at the electron dump. We ignore the small cost of the additional pumping.

Also in the end tanks are the skimmers for the halo plasma discussed in Section II.E. Each halo dump contains a 65 m^2 cryopanel and a 65 m^2 plasma dump. The costs are 5.3×10^6 per cryopump, including the refrigeration system, and 6.5×10^4 per plasma dump. The total cost per skimmer is therefore about 5.4×10^6, or 11×10^6 for both skimmers.

The estimated costs of the end-tank components are summarized in Table III.A.5. These costs differ from those given elsewhere in this report due mainly to the reduced size of the PDC here that resulted from the use of water cooled grids. Also, we include here an estimate of the cost of the skimmers for the halo plasma.

III.A.5 First Wall Protection

A plasma disruption could deposit the 5×10^8 J of plasma energy on the first wall if it is not protected. We assume that any radial motion of the plasma is slow relative to the speed of the particles along the field lines, so that a single limiter at each end can protect the entire wall. Other limiters could be spaced along the wall in the solenoid, but the effect of the increased gas production that would result must be analyzed. The gas from limiters in the ends can be pumped by cryopanels in the end chambers.

High density neutron shielding is required at the mirror coils where the field is between 14T and 20T. This shielding also serves as the limiters. Water cooled tungsten bushings inserted in the inner, copper part of the high-field coils serves both purposes. Additional shielding is required at the end faces of the coils.

The outer diameter of the tungsten bushings is, therefore, nearly equal to the inner diameter of the copper, and the volume of each tungsten limiter is at least 0.5 m^3. The inside diameter of the limiter is 1.0 m, the thickness is 0.1 m, and the width is 1.5 m. Since the heat capacity of the 0.5 m^3 of tungsten is 1.3 x 10^6 J/^{0}C, all 5 x 10^8 J of plasma energy would only rasie the temperature of the tungsten by 400^{0}C if the heat were uniformaly distributed in the metal. The plasma energy 5 x 10^8 J is enough toevaporate 5000 cm^3 of tungstem. In a worst case scenario where the plasma energy is all dumped onto a small area of one limiter, much less than 5000 cm^3 of tungsten would be evaporated. The reason is that the metal vapor would protect the solid metal under it. Thermalization time for 0.1-m-thick tungstem is about 40 s. Most of the plasma energy would go into ionizing and heating the vapor, which would then stream along the magnetic field lines and deposit the enrgy on the plasma dump designed for the halo plasma.

III.B END PLUG ISSUES

III.B.1 Design Overview

III.B.1.a Magnets. All end-plug magnets, with one exception, were designed and costed with present state-of-the-art technology in mind. No inventions are required to design, construct and operate the coils with the same probability of success accorded the MFTF-B end-plug and solenoid coil set.

The one exception is the copper-insert portion of the high field barrier coil. Such coils have been operated above 20 T but only in very small sizes. At the National Magnet Laboratory at MIT, Bitter type coils 3.6 centimeters in bore have been tested to 30 T and 5.4 centimeter bore coils to 25 T. Our design requires a 120 centimeter bore solenoid with on-axis field of 20 T. The cooling system for such a magnet is beyond current achievements but is regarded as feasible.

Conductor current densities were kept within those to be employed in the MFTF-B experiment using Nb-Ti superconductor. In those cases where Nb$_3$Sn superconductor was required to meet higher field requirements, current density recommendations from the LLNL superconductor design group were followed.

Winding and insulation techniques employed in the MFTF-B fabrication are planned for all the superconducting magnets in this study. However, the insulating material would hjave to be a ceramic instead of organic G10 to

increase tolerance to neutron damage. Yttrium oxide, aluminum oxide, and magnesium oxide are candidate materials.

The enclosing cases for the various coils were individually considered. No detailed structural analysis could be performed but comparisons were made to the MFTF-B yin-yang magnets. Simple burst pressure calculations led to case thickness selection for simple solenoids. In many of the solenoids practical considerations for handling large metal plates led to thickness choices beyond operating strength requirements.

The opening forces were calculated on the major radii of all the "C"-shaped coils, both transition and yin yang. A box girder was designed to span each side of the coil's major arcs with two tensile members connecting the ends of each box girder. Bending stress of 50,000 psi (345 MPa) was permitted in each box girder and tensile stress of 40,000 psi (276 MPa) was allowed in the end tie-bars. (The latter allows 25% additional stress due to the bending associated with girder end rotation. This is a rough estimate.)

The structure design was not optimized to minimum weight for this first-cut cost estimate. More complete analysis of these huge structures should result in cost reductions. Our purpose here was to get within about 30% of an optimum design's cost.

In estimates for shielding the superconductors, very simple geometrics were assumed and nominal shield thickness of 50 cm of steel was assumed. Due to complex coil geometries, it is possible that some areas of the "C" magnets are too well protected. Neutronics analysis will probably lead to some economics in thickness of material; but some regions may employ more exotic shield materials at higher unit cost. The assumption of very simple and uniform shield thickness will probably lead to cost estimates accurate to ±25%.

Figures III.B.1 and III.B.2 show a plan and elevation view of the end plug for this reactor. Discussion of individual components can be found in Section A of this chapter.

III.B.1.b Coil Structure Supports. The 20 T and 9-T solenoids are encased in steel hoops which resist the magnetic field burst-pressure. The 20 T coil consists of several layers, each of which has an outer jacket to carry the outward force generated on the enclosed conductors. Each region of superconductor has sufficient steel distributed within the region to transmit body forces to this outer shell. No layer of conductor is loaded beyond its yield point.

NOTE : SEE ELEV. VIEW FOR
COMPONENT IDENTIFICATION

CYCLING CRYOPUMP
PANEL (TYPICAL)

ELECTRON GRID

DIRECT CONVERTER ELEMENT

PLAN VIEW

0   5   10m

72-212-011
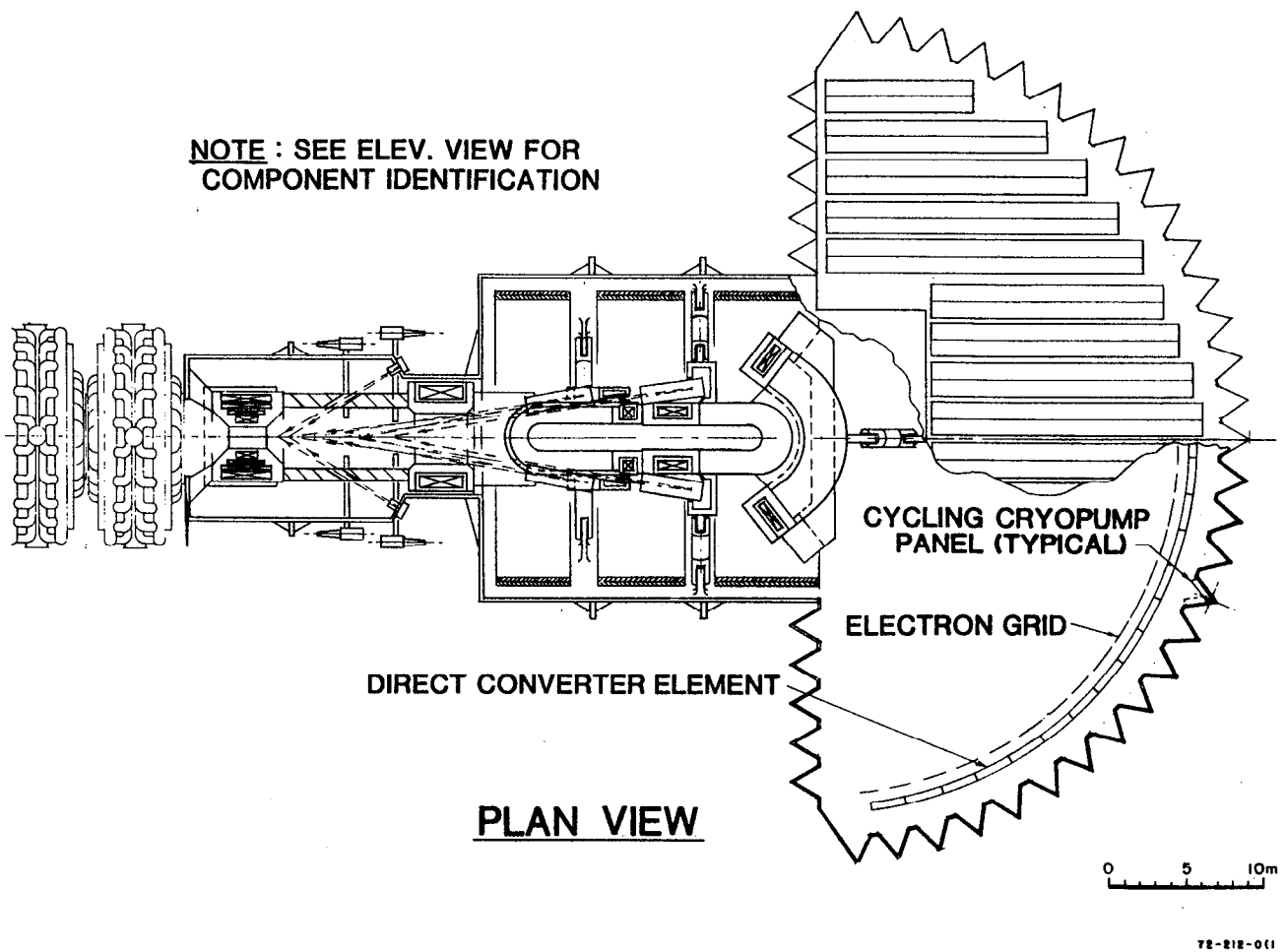
Fig. III.B.1 Plan view of axicell end plug.

III-42

CENTRAL CELL   BARRIER   TRANSITION   QUAD.Y-Y

E.C.R.H.
GYROTRON

CRYOPUMP PANELS

LOW ENERGY
PUMP BEAMS
(P.B.)

MEDIUM
ENERGY P. B.

HIGH
ENERGY P.B.

STRUCTURAL BOX GIRDERS

0   5   10m

D.C. SERVICE
DOORS

DIRECT CONVERTER
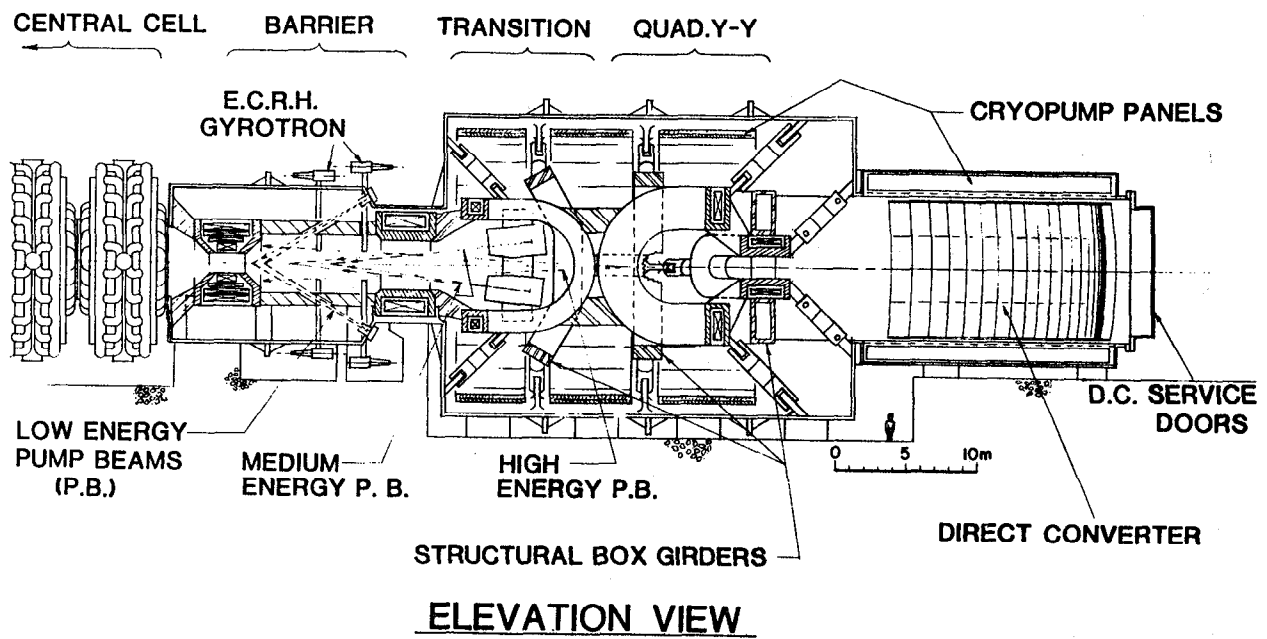
ELEVATION VIEW

Fig. III.B.2 Elevation view of axicell end plug.

The three C-shaped coils (transition and yin yang) have very high lobe-opening forces and so require box-girder support structures to resist them. The two girders backing each magnet are tied together at their ends by large tension bars. The yin-yang anchor can be partially self-supporting. (The smaller MFTF-B yin-yang pair is entirely self-supporting.) We did not take credit for the coil case's supportive strength in estimating the box-girders' size and cost. Neither did we allow for the added weight and special load tie-pieces needed to integrate the separate coil cases. These two omissions will tend to cancel, so for a first estimate the simpler (girder-only) approach was deemed sufficiently accurate. For all three beams an allowable stress of 50,000 psi (345 MPa) was used. The girders will be refrigerated to 4.5 K as will the magnet cases. Table III.B.1 compares the lobe-opening forces and the box-girder span for each of the three coils.

TABLE III.B.1 Comparison of Lobe-Opening Forces and the Box-Girder Span for the Three Coils.

	Separating Force Newtons	Span Meters
Transition	$4.77(10)^7$	9
Yin coil	$2.34(10)^8$	10
Yang coil	$2.26(10)^8$	10

III.B.1.c Axicell Beam Lines. The barrier region between the 20 T and 9-T solenoids requires injection of pumping beams. High, medium and low energy beams are necessary to efficiently remove all the ion species desired. Unfortunately, the apparently ample access to this barrier from the side is useless. The angles relative to the flux lines must be lower than 15° in the high and medium energy case. This limits beam access to the clear aperture within the 9-T barrier solenoid. Beam angles relative to the reactor center-line are less than 10°. Table III.B.2 lists the energy and amperage of the pump beams.

TABLE III.B.2. Energy and Amperage of the Three Pump Beams.

	Energy keV	Equiv. current into both ends Amperes
HEPB	192	41
MEPB	77	469
LEPB	40	1380

Refer to Figs. III.B.1 and III.B.2, which show plan and elevation views of an axicell end-plug, during the following discussion of beam location.

The high energy beams are located on the horizontal plane through the reactor. The source boxes mount directly on the yin magnet case with the back of the box intruding on the box-girder which restrains that magnet's lobe-opening force. Appropriate alternate load paths must be included in the girder design to allow this 2-m-by-2-m square clearance hole in one side of the beam. Each end of the reactor requires two such beam sources.

Another interference must be avoided. In the HEPB path is the box-girder which restrains the transition coil lobe-opening forces. The pump beam must be provided a reinforced notch between the transition coil conductor case and the box-girder. The HEPB will then have clearance between those members.

The MEPB requirements are satisfied by four source boxes at each end of the reactor. Those boxes mount to the transition coil case, above and below the centerline of the reactor and on both sides as well (i.e., a view looking down the reactor axis would show one beam source box in each quadrant, at each end plug). It will be noted that they lie inside the "horseshoe" outline of the transition coil, occupying some space between the two planes defining the outer surface of the lobes. This box position does not encroach on the plasma boundary as the plasma transforms from a circular cross section in the 9 T solenoid to its highly elliptical shape between the transition coil and the yin-yang coil set.

To provide beam path clearance it may be necessary to notch the shield a small amount at the end of the 9 T solenoid nearest the MEPB source.

The low energy pump beams can be directed outside the 9-T coil case. This allows a ring of MFTF-B-type neutral-beam sources--15 at each end of the reactor--to be mounted on the vacuum case surrounding the barrier region. They aim in a direction 30^0 off the reactor centerline. Beam apertures must be provided in the thrust cylinder which maintains separation of the barrier cell solenoids.

III.B.1.d. Electron Cyclotron Resonance Heating (ECRH). All of the microwave power needed by this reactor concept must be injected into the barrier regions, one at each end of the reactor. In each barrier there are two regions which are focal points of the ECRH power. One is the barrier field minimum. The other is the barrier potential peak. They require 30 MW and 19 MW, respectively (total for both ends).

Present plans are for 1 MW gyrotron tubes. We can arrange two rings of 15 gyrotrons each interposed between the 15 low energy pump beam lines. One ring of gyrotrons directs energy at the field minimum, the other aims at the potential peak. The waveguides from such tubes can probably be straight lines as shown in Figs. III.B.1 and III.B.2. This would be desirable from an efficiency argument (i.e., no elbows). However, neutron damage to a microwave "window" would be prohibitive. Windowless designs are possible but are not expected to be used on the first reactors. We can still imagine straight radial waveguides from the plasma edge to the vacuum chamber wall. A bend (perhaps as little as 30^0) beyond that wall would be followed by the "window" and then a short run of waveguide to the gyrotron. In this way the window can be shadow-shielded and good transmission efficiency is still achievable.

III.B.2 End Plug Effects on Breeding

The neutronics analysis of the blankets was done in cylindrical geometry. The end effects were not included because infinite cylinders were modeled with the 1-d ANISN calculation of the Be blanket and reflecting boundaries were used at the module ends with the 3-d TARTNP calculations of the Li blanket.

To account for end effects the tritium breeding ratio calculated with the blanket geometry discussed above, (T-local) must be greater than 1.0 to account for T "burned" in both the central cell (blanket region) and the end cells, for T lost by decay, T lost in the process loops, and for neutron leakage out

blanket ends. Remember only the central cell has a breeding blanket, therefore, T-local is:

$$T_\ell = T \cdot \frac{P_{f,tot}}{P_{f,cc}} \cdot NL_T^{-1} \qquad (1)$$

where: T = tritium production per DT fusion needed to make up for loss by fusion plus decay and other losses ($T \sim 1.02$).

$$P_{f,tot} = P_{f,cc} + P_{f,end\ plugs} \quad .$$

For an example case: $P_{f,cc} = 3000$ MW

$P_{f,end\ plugs} = 94$ MW

NL_T = non-leakage factor, ratio of T breeding in a finite, open-ended blanket to a blanket with reflecting ends. For a 95 m long blanket with a 2 m radius first wall and modeled with radial zones approximating the blankets, NL_T for the 2 blankets are:

for Be case, $NL_T = \frac{1.262}{1.328} = 0.947$

for Li case, $NL_T = \frac{1.225}{1.232} = 0.994$

For our cases then, the local T breeding (T_i) requirements are:

Be case: $T_\ell = 1.02 \left(\frac{3000 + 94}{3000}\right) 0.947^{-1} = 1.11$

Li case: $T_\ell = 1.06$

The next step is to determine the local value of blanket fissile breeding (F_ℓ) by one of two ways:

a.   Using the local value for total breeding $(T + F)_\ell$:

$$F_\ell = (T + F)_\ell - T_\ell \qquad (2)$$

Implicit in this method is the assumption that there is a 1 to 1 trade off in T_ℓ and F_ℓ.

b.   Iterate blanket design until T_ℓ is achieved, thus giving F_ℓ directly.

The next step is to account for blanket end effects to determine blanket F (F_b) by weighting F_ℓ values by the ratio of F unreflected to F reflected calculated with the 2-d blanket model:

$$F_{ur}/F_r \text{ (Be case)} = \frac{.593}{.618} = 0.96$$

$$F_{ur}/F_r \text{ (Li case)} = 0.93$$

Therefore, using equation 2:

$$F_b = [(T + F)_\ell - T_\ell] \, F_{ur}/F_r \qquad\qquad (3)$$

Example:

$$F_b \text{ (Li case)} = [1.57 - 1.06] \, 0.93 = 0.47$$

A simpler but somewhat less rigorous approach to find F_b is to use only the sum of T + F to scale from:

$$F_b = (T + F)_\ell \cdot NL_{(T+F)} - T(P_{f,tot}/P_{f,cc}) \qquad\qquad (4)$$

where again NL accounts for blanket end leakage. For the 95 m blanket cases:

$$NL_{(T+F)} = \frac{1.86}{1.95} = .9564 \text{ (for Be case)}$$

$$NL_{(T+F)} = \frac{1.50}{1.53} = .980 \text{ (for Li case)}$$

Examples: F_b (Be case) = 1.87 $\cdot$ .954 - 1.02 $\cdot \frac{3094}{3000}$ = .73

$$F_b \text{ (Li case)} = 1.57 \cdot .980 - 1.02 \cdot \frac{3094}{3000} = .49$$

For blankets with different lengths (L), $F_b(L)$ can be estimated by assuming absolute end leakage is length dependent.

$$F_b = (T + F)_\ell \left[1.0 - 1.0 - NL_{(T+F)re} \, \frac{L_{re}}{L} \right] - T\left(\frac{P_{f,tot}}{P_{f,cc}} \right) \qquad\qquad (5)$$

where re ≡ reference case.

For Li case: $F_b = 1.57\left[1.0 - (1.0 - .980)\,\dfrac{95}{L}\right] - 1.02\left(1 + \dfrac{P_{ends}}{P_{cc}}\right)$

For Be case: $F_b = 1.87\left[1.0 - (1.0 - .954)\,\dfrac{95}{L}\right] - 1.02\left(1 + \dfrac{P_{ends}}{P_{cc}}\right)$

The above methods of accounting for end effects on breeding are considered conservative. They should underpedict F_b because no account is taken of neutrons born in the ends and getting into the blanket.

III.C FUSION TECHNOLOGY ASSESSMENT

III.C.1 Fusion Component Technologies

The timely introduction of both hybrid and pure fusion reactors depends upon the implementation of development and testing (D&T) programs of the needed technologies. The technology development programs (III.C.1) underway and planned at LLNL and elsewhere are intended to provide the necessary components for tandem mirrors with thermal barriers, both for hybrid and pure fusion applications. Development of neutral beams, superconducting magnets, microwave heating, and vacuum systems are necessary for the operation of such devices. Direct converters would be advantageous. Each will now be considered individually.

III.C.1.a Neutral Beams. Neutral beams both heat the plasma and modify particle distributions in a magnetic bottle. In a mirror, the energy of the beam particles must exceed a certain energy for them to be confined. Also, as the plasma becomes denser and larger in physical dimension, the beams must be more penetrating. This suggests that as the temperature, density, size, and plasma potential increase in planned mirror facilities, beam energies must also increase.

High power, neutral atom beams made from positive ions were a key to the success of the standard mirror equipment, 2XIIB, and the tandem mirror experiment, TMX. These beams were originally developed by a Lawrence Berkeley Laboratory/Lawrence Livermore National Laboratory cooperative program (III.C.2). A major neutral-beam program is also underway at the Oak Ridge National Laboratory (ORNL).

Neutral beams can be generated with reasonable efficiency by passing positive ions through a background gas, up to a maximum energy of about 150 keV for deuterium and 75 keV for hydrogen. Above this energy, the neutralization probability of positive ions has become too small for practical use, and therefore negative ions must be used for beams above this energy.

Current work in the positive ion based neutral-beam program is being pursued by both LBL and ORNL and devoted to developing an advanced positive ion source (APIS). The stated goals of this development program (III.C.3) are to provide a source which will have the capability of pulse lengths from 5 s to steady state, energies from 75-100 keV/nucleon, with a current of up to 100 A per source. Additional goals for these designs are that they exhibit high quality optics, source reliability greater than 95%, with an arc efficiency of about 1 kW per ampere of beam produced. Direct energy conversion (DEC) of the unneutralized component of the beam is also necessary for good efficiency. There is currently a program at ORNL intended to develop a working DEC system for neutral beams. A full size source operating at 80-keV and a 30-s pulse length will be available by the middle of FY 1983, with a 150 keV/30-s source coming on line during the first quarter of FY 1984. The 80 keV source will find its first application on MFTF-B.

Even though the thermal-barrier concept has led to reduced energy and power requirements for neutral beams, tandem-mirror reactors will most likely require beam energies above 150 keV. The principal option available is production of energetic negative ions that can be neutralized efficiently by stripping an electron in a background vapor. Aggressive development of negative-ion sources and suitable strippers is needed to meet the requirements of tandem-mirror facilities in the mid-1980's. Their first use will be an early upgrade to MFTF-B.

The development program for neutral beams produced by negative ions has been modest. The laboratories involved in negative ion neutral-beam development are LBL, ORNL, and Brookhaven National Laboratory (BNL). A short term development goal is to produce a 1 ampere source of negative ions of approximately 40 keV energy which can operate with a minimum pulse length of 5 seconds. A parallel effort is to be performed in which a conceptual design of a 10-ampere, 200-keV beamline would be defined. According to plan (III.C.3), these efforts should have been completed at the end of FY 1981. At the beginning of FY 1982, the best concept for the 10 A/200 keV source will be

chosen, and a proof-of-principle will be built, based on this chosen best design. This proof-of-principle stage should be completed at the end of FY 1983, with a MFTF-B prototype available in the FY 84-85 timeframe.

Testing of neutral-beam sources requires multimegawatt power supplies, high-power arc and filament supplies, high-speed pumping, and beam dumps capable of dissipating very high peak power. Such systems are major facilities in themselves; e.g., the High Voltage Test Stand (HVTS) at LLNL is designed to test 80-keV, 85-A and 120-keV, 65-A neutral-beam sources with pulse length up to 1.5 s and has the power supply capability for 30-s operation. The HVTS is currently being used to test sources for MFTF and for Doublet III at General Atomic (GA). In the future, it will be used to test the APIS. Major test facilities are also located at ORNL, and a 200 kV, 100 A system is planned at BNL.

If negative ion beams prove necessary for a tandem mirror hybrid reactor to operate, the early introduction of the hybrid could be hampered by the lack of an aggressive program to develop negative ion neutral beams. If some additional funding could be appropriated to set up parallel efforts in the development of sources, accelerator technology, and general facility layout, then the negative ion neutral-beam development program might be considerably accelerated (III.C.4).

III.C.1.b Magnets. The intense magnetic fields needed to contain plasmas of the density and temperature required for a fusion reactor can be produced with reasonable power consumption only through use of superconducting coils. Development of high-field superconductors and large superconducting magnet coils has long been important to the mirror program. The end-cell coils being constructed for MFTF-B are would with Nb-Ti superconductor and are among the largest yet produced.

Current planning in the D&T program for magnets involves the development and fabrication of large coils using Nb_3Sn superconductor, which is capable of higher fields than Nb-Ti. One of the facilities supporting steady-state magnets and conductor development in the D&T program is the High Field Test Facility (HFTF) at LLNL.

HFTF will generate a maximum field of 12 T in a solenoid of 40 cm bore. At the present time, the fields generated by Nb_3Sn appear necessary for both a pure fusion and a hybrid tandem mirror reactor. The HFTF facility is also used in the development of high field superconductors for a tokamak intended

as an engineering test facility (ETF). The present goal of the high field magnet group at LLNL is to demonstrate that a Nb_3Sn magnet can be produced for a tandem mirror with end cells the size of the Tandem Mirror Next Step (TMNS) (II.B.14) in the 1985-87 timeframe (III.C.5). Fiscal restrictions move the date probably closer to 1987. A hybrid reactor would have end cells about the size of an axicell based TMNS, which makes the goals of the high field magnet development program supportive for an early commercial introduction of the hybrid.

The baseline fusion driver for this study uses a high field circular coil between the central cell and the rest of the end cell. The baseline case requires a centerline field strength at this coil of about 20T for a Q value of 15 (the product of Q and trapping efficiency is 9), at a central-cell power per unit length of 23 MW/m. The coil, as presently envisioned, has three concentric regions. The outermost region is made from NbTi superconductor, the middle from Nb_3Sn, and the innermost ring, which sees fields of 22 T, is made from copper. The joule heating inside the copper is considerable, the reference design requires about 45 MW of cooling per coil. Magnets of 40 cm bore have been operated with fields in excess of 20T, but only for short times (several minutes) and they are reported to have lasted only several cycles. The pulse length is limited because of the limitations on energy storage systems and on the way in which the copper is cooled in these experiments and long life was not a design constraint for these coils. There appears to be no fundamental reason why a coil producing the required field strengths cannot be designed. A development plan is needed to make the hybrid coil a viable option for either the hybrid or pure fusion.

In the parametric analysis sections (II.D and IX.E), we present a "low technology" baseline case using the axicell endplug, but with a 14T centerline field strength at the high field coil. This coil might be just the hybrid coil with the copper insert removed. This driver design has the product of Q and trapping efficiency of about 5, at a power per unit length of 23 MW/m. For this low technology case, the ECRH power more than doubles. At an assumed cost of $3/watt of delivered power, the cost of the ECRH system is just over $590 M, unacceptable for pure fusion, but perhaps allowable for the hybrid, although not desirable.

III.C.1.c <u>Electron Cyclotron Heating</u>. Progress on the EBT concept at ORNL requires development of very high power, high frequency steady state sources

of microwaves for electron heating (III.C.6). The availability of these sources is now a critical factor in the mirror program as well, since electron heating is necessary to obtain the advantages of the thermal barrier. Currently available sources at 28 GHz will be used on TMX-U. MFTF-B will require 60 GHz sources, which are under development. These 60 GHz CW sources should be available by 1984. A tandem mirror reactor with thermal barriers will require microwave sources which have frequencies between 55 and 120 GHz, suggesting that additional tube development is required.

III.C.1.d Direct Conversion. Mirror containment devices offer the possibility of direct conversion of plasma exhaust energy to electricity (III.C.9). Direct conversion can also be used to increase the efficiency of the neutral-beam system. Efficiencies on the order of 60% or higher can be obtained. The principles involved in direct conversion have been demonstrated both for plasma streams (III.C.10) and for charged particle beams (III.C.11). The facility designed to demonstrate plasma direct conversion, described in reference III.C.10, operated for 70 hours, continuously converting the power contained in 100 keV particles at a power density of 70 W/cm^2. Encouragingly, there was no detectable degradation of the collector material.

A plasma direct conversion (PDC) test facility is planned for FY 1983, but at present there is no development work underway. It is designed to test the direct conversion of a plasma stream when the hardware is subjected to charged particle power densities similar to those anticipated in a reactor. For a hybrid reactor with a fusion power of 2500 MW and a plasma power gain (Q) of 4, 1125 MW of charged particle power must be directly converted. This is about the same load as a pure fusion reactor operating at 3500 MW fusion power and a Q of 10.

III.C.1.e Vacuum Pumping. Reacting plasmas require a high vacuum environment that must be maintained despite the very large gas throughput introduced by neutral-beam sources. As pulse lengths increase in future systems, substantial improvements in ability to pump will be needed.

For mirror reactors, which operate in the steady state, a cryogenic pumping system must be designed which can be outgassed during operation at a rate equal to the throughput. A facility (III.C.12) intended to test this rapid cycle pumping technique is now under construction, with experiments beginning in FY 1982.

In a fusion reactor the effective pumping of tritium is particularly important from a safety point of view. The inventory of tritium quite vulnerable in an accident situation is that which is frozen on cryopanels. This points to the requirement that the pumping system must be effective enough to keep this inventory below an acceptable level. Just what this level should be is not clear at present, but should be ideally on the order of several tens of grams. For example, in order to keep the inventory under 10 grams on the cryopanels, the panels must be warmed roughly every twenty minutes.

An additional problem which must be addressed in a reactor is that of helium pumping. Since helium by itself will not freeze on cryopanels, inter-molecular "sticking" forces must be used to collect it. An idea which is receiving attention is to freeze a layer of argon onto the cryopanel, and allow the helium to build up a fraction of a monoatomic layer, at which point the helium will no longer stick. Another layer of argon is then frozen over the helium and the process is repeated. This pumping concept has been tested in small sizes, and scale up poses no special problems.

III.C.2   Technological Requirements of the Hybrid

It is important to see how the hybrid compares with pure fusion reactors with respect to: (1) the requirements on technology, (2) the timetable on which an economically competitive hybrid could be introduced in the energy marketplace. The details of these comparisons and deployment considerations will be left to another section of this report, but some comments which are relevant to the physics and technology discussion seem approriate.

Before the advent of tandem mirrors with thermal barriers, the technology requirements of barrierless tandems producing pure fusion power (II.A.4) were quite severe, maximum yin-yang magnetic fields exceeded 17T and neutral beams were of energies greater than 1 MeV. If the same concept were used as a hybrid reactor (II.B.12) with a lower demand on plasma Q (about a factor of 5), the technology could be relaxed considerably. When thermal barriers were invented, the tandem mirror pure fusion could achieve Q values three or four times as large as before (II.B.2) at higher power densities, at the techno-logical level of Nb_3Sn superconductors ($\sim$ 12T) and lower beam energies ($\sim$ 300 keV), although negative ions may still be needed to produce these beams.

Further study of the plasma physics of tandem mirrors possessing an axial temperature gradient (III.C.13) has resulted in the derivation of a "modified" Boltzmann relation. Including this in the modeling forces us to apply more power at a given maximum magnetic field to maintain the electron temperature difference between the central cell and plug. To recover some of the performance, a larger maximum magnetic field is necessary (> 12T). The recent WITAMIR-I design (III.C.14) needs 14T to achieve its quoted pure fusion performance employing the modified Boltzmann relation. When radial density profiles are accounted for, along with additional effects to add more realism to the model, we find a pure fusion driver using an axicell end-plug design appears to need a circular coil with a maximum field in the neighborhood of 20T to achieve a Q of 20. A Q this large, with a Q times power trapping efficiency of around 12, helps pure fusion produce more economic electricity.

It is not absolutely necessary that the fusion driver for the hybrid have such high plasma Q. The parametric analysis section of this report presents a "lower technology" case with a maximum field strength of 14T with the required hybrid performance. The amount of ECRH power increases by more than a factor of two over the 20T case, and at an assumed cost of $3/watt (delivered) represents a large additional cost. This added cost would be prohibitive for a pure fusion driver, but perhaps acceptable for a hybrid.

In addition to the lower performance requirements for a hybrid, an important near-term advantage of a hybrid reactor over a pure fusion reactor is that the allowed cost of a given technology may be much larger in the case of a hybrid, and still produce an economical product. This is because the hybrid, particularly one using suppressed fission blanket technology, produces fissile material whose economic value is larger than the value of the heat alone. Simply stated, the revenues from the sale of fissile material are predicted to exceed the revenues from the sale of electricity. In fact, it will be shown in Chapter IX that the cost of the hybrid can be up to 3 times that of an LWR, and still have the system electricity cost increase only modestly ($\leq$ 15%) over that of the LWR cost of electricity. On economic grounds alone, pure fusion reactors can only cost more than LWRs by the amount of the LWRs' fuel cost which should only be at most around 20% of its annual cost of capital. This means that hybrids may be competitive much earlier than pure fusion in the energy marketplace when the cost of producing hardware based on a developing advanced technology is high. Estimates (III.C.15) indicate that the hybrid could produce fuel competitively and could be introduced as

soon as the technology is ready and the price of uranium rises sufficiently. The market entry point may be about $100 per pound of uranium for hybrids costing 3-4 times a LWR and this may occur as soon as the year 2000. This carries with it the caveat that the technology development and experimental programs remain aggressive and successful. This early introduction of the hybrid will allow experience to be gained with exactly those technologies which are needed for pure fusion. Through this experience, along with further technical developments, the cost of these technologies will be reduced, thus aiding the prospects of the commercialization of pure fusion.

The fusion reactor development program underway at LLNL has a direct impact on the hybrid program. This effort is called the Advanced Mirror Systems (AMS) program. The objective of the AMS program is to propose tandem mirror end plugs which are simple, cheap, and provide good plasma performance. These end plugs were briefly described in Section II.B.2. This effort, particularly at the present time, is producing end-plug concepts which are evolving at a very rapid rate. To define a baseline end-cell configuration, whether it be for a pure fusion or fusion breeder application, is premature at this time. The performance of the axicell baseline case is adequate to produce a system which makes economically competitive fissile fuel (the equivalent of $100/lb of uranium), and therefore meets the goals of the present hybrid study. However, since a pure fusion reactor is a stand alone power producer, the demands on driver performance and cost are more stringent to produce an economical product. The search continues by the AMS program to find an end-plug concept which satisfies these demands. We show in this study that for a hybrid this further search is, although desirable, not absolutely necessary. Improvements for pure fusion will make improvements for the hybrid application,
probably lowering equivalent cost to well under $100/lb of uranium.

This illustrates the long perceived notion that a hybrid requires a lower level of performance and allows a higher driver cost than does pure fusion. The baseline fusion breeder axicell case achieves the performance needed for the application by using a level of technology currently assumed in both the hybrid and pure fusion programs. For a pure fusion reactor, this technology and presently conceived end-plug concepts do not achieve the required performance to make its electricity economical. Pure fusion needs an improvement, which may be obtained in one of two ways: (1) demand a higher level of

technology than is presently assumed, or (2) discover a better plug which will use technological capabilities more efficiently. It is the second path that the LLNL AMS program is pursuing.

Note that whatever new concepts the AMS program develops, the hybrid/LWR electricity cost reported on in this study will be affected in a small but important way due to the large LWR thermal support ratio of the suppressed fission blankets. Moreover, the baseline axicell parameters chosen here are on the conservative side, since present indications show that the axicell performance can be improved by decreasing barrier length while increasing the magnetic field at the barrier minimum.

REFERENCES

Section III.A

III.A.1. G. A. Carlson, et al., "Tandem Mirror Reactor with Thermal Barriers," Lawrence Livermore National Laboratory, Rept. UCRL-52836 (1979).

III.A.2. G. A. Carlson, et al., "Field Reversed Mirror Fusion Reactor," Lawrence Livermore National Laboratory, Rept. UCID-18550 (1980).

III.A.3. D. E. Baldwin, et al., "Physics Basis for MFTF-B," Lawrence Livermore National Laboratory, Rept. UCID-18496 (1980).

III.A.4. C. C. Damm, et al., "Preliminary Design of a Tandem-Mirror-Next-Step Facility," Lawrence Livermore National Laboratory, Rept. UCRL-53060 (1980).

III.A.5. M. W. MacGeoch, "Laser Neutralization of Negative Ion Beams for Fusion," in Proc. of the Second International Symposium on the Production and Neutralization of Negative Hydrogen Ions and Beams, Brookhaven National Laboratory, Rept. BNL-51304 (1980), p. 304.

III.A.6. J. H. Fink, and G. W. Hamilton, "Another Look at Photodetachment of Negative Deuterium Ions in Neutral Beam Injectors," Livermore National Laboratory, Rept. UCID-18806 (1980).

III.A.7. G. W. Hamilton and B. G. Logan, "Charge-Exchange Pumping of Thermalized Alpha Particles in Steady-State Tandem-Mirror Reactors," Comments Plasma Phys. 6, 139 (1981).

III.A.8. D. E. Baldwin, "Pumping of Thermal Barriers by Induced Radial Transport," Mirror Theory Monthly, May 15, 1981.

III.A.9. G. W. Hamilton, "DC Grad-B Pumping of TMR Thermal Barriers," submitted to the 9th Symposium on Engineering Problems of Fusion Research, Chicago (1981).

III.A.10. M. Porkolab, L. Friedland, and I. Bernstein, "ECRH of Plasmas in Tandem Mirrors," submitted to Nuclear Fusion; Livermore National Laboratory, Rept. UCRL-84345 (1980).

III.A.11. M. E. Read, B. Arfin, J. M. Baird, K. R. Chu, D. Dialetis, A. T. Drobot, V. L. Granatstein, K. J. Kim, and A. Palevsky, "Prospects for Multimegawatt Gyrotrons," Bull. Am. Phys. Soc. 25, 911 (1980).

III.A.12. V. V. Alikaev, V. A. Flyagin, V. I. Khizhnyak, A. G. Luchinin, G. S. Nusinovich, V. G. Usov, and S. N. Vlasov, "Gyrotrons for the Electron-Cyclotron Plasma Heating in Large Tokamaks," in Proc. Joint Varenna-Grenoble Intern. Symp. on Heating in Toroidal Plasmas, Grenoble, France, 1978 (French Atomic Energy Agency, Grenoble, France, 1978), p. 339.

III.A.13. K. R. Chu, A. T. Drobot, H. H. Szu, and P. Sprangle, "Theory and Simulation of the Gyrotron Traveling Wave Amplifier Operating at Cyclotron Harmonics," IEEE Trans. Microwave Theory Tech. MTT-28, 313 (1980).

III.A.14. R. M. Gilgenback, M. E. Read, K. E. Hackett, R. Lucey, B. Hui, V. L. Granatstein, and K. R. Chu, "Heating at the Electron Cyclotron Frequency in the ISX-B Tokamak," Phys. Rev. Lett. 44, 647 (1980).

III.A.15. W. L. Barr and R. W. Moir, "Test Results on Plasma Direct Converters," submitted for publication in Nuclear Technology/Fusion.

III.A.16. G. W. Shuy, UCLA, private communication.

III.A.17. K. R. Spangenberg, "Vacuum Tubes," McGraw-Hill Book Company, New York, N.Y. (1948), p. 148.

III.A.18. T. H. Batzer, R. E. Patrick, and W. R. Call, "A Neutral Beam Line Pump with Helium Cryotrapping Capability," Lawrence Livermore National Laboratory, Rept. UCRL-81196 (1978).

III.A.19. M. A. Hoffman, "Electrostatic Direct Energy Converter Performance and Cost Scaling Laws," Lawrence Livermore National Laboratory, Rept. UCID-17560 (1977).

III.A.20. S. C. Schulte et al., "Fusion Reactor Design Studies--Standard Unit Costs and Cost Scaling Rules," Pacific Northwest Laboratory, Richland, WA, Rept. PNL-2987 (1979).

Section III.C

III.C.1. R. R. Borchers, C. M. Van Atta, eds., "The National Mirror Fusion
        Program Plan," Lawrence Livermore National Laboratory, Rept.
        UCAR-10042-80, January 1980.

III.C.2. W. R. Baker, K. H. Berkner, W. S. Cooper, K. W. Ehlers, W. B.
        Kunkel, R. V. Pyle, and J. W. Stearns, "Intense-Neutral-Beam
        Research and Development," in Proc. 5th Conf. Plasma Physics and
        Contreolled Nuclear Fusion Research (IAEA, Vienna), vvol. 1, pp.
        329-337 (1974).

III.C.3. "Neutral Beam Development Plan," U.S. Department of Energy, Office
        of Fusion Energy, Division of Development and Technology, Rept.
        DOE/ER-0075, August 1980.

III.C.4. J. Fink, private communication, May 1981.

III.C.5. D. Cornish, private communication, May 1981.

III.C.6. C. L. Hedrick, R. A. Dandl, J. A. Cobble, R. A. Dory, H. O. Eason,
        E. G. Harris, G. R. Haste, H. Ikegami, E. F. Jaeger, N. H. Lazar,
        D. H. McNeill, D. G. McAlees, D. B. Nelson, L. W. Owen, D. A. Spong,
    and N. A. Uckan, "Transport and Scaling in the Elmo Bumpy Torus (EBT),"
    in Proc. 6th Conf. Plasma Physics and Controlled Nuclear Fusion Research
    (IAEA, Vienna), vol. 2, p. 145 (1977).

III.C.7. S. C. Schulte, et al., Fusion Reactor Design Studies--Standard Unit
        Costs and Cost Scaling Rules, Pacific Northwest Laboratory, Rept.
        PNL-2987, September 1979.

III.C.8. Cost est. for MFTF-B?

III.C.9. R. F. Post, "Direct Conversion of Fusion Energy to Electricity,"
        Proc. Intersociety Energy Engineering Conf. "Energy 70" (Energy 70,
        Albuquerque, NM), vol. 1, pp. (1-19)(1-28), (1970).

III.C.10. W. L. Barr and R. W. Moir, "A Review of Direct Energy Conversion for
        Fusion Reactors," Proc. of the Second ANS Topical Meeting, The
        Technology of Controlled Thermonuclear Fusion, Sept. 21-23, 1976,
        Richland, WA, p. 1181. See also W. L. Barr and R. W. Moir, Lawrence
        Livermore National Laboratory, report in preparation.

III.C.11. W. L. Barr, R. W. Moir, G. W. Hamilton, and A. F. Lietzke, "Tests of
        High-Power Direct Conversion on Beams and on Plasma," Eighth
        Symposium on Engineering Problems of Fusion Research, San Francisco
        (1979).

III.C.12. T. Batzer, private communication.

III.C.13. R. H. Cohen, et al., "Particle and Energy Exchange Between Untrapped and Electrostatically Confined Populations in magnetic Mirrors," Lawrence Livermore National Laboratory, Rept. UCRL-84147, Rev. 1, August 5, 1980.

III.C.14. B. Badger, et al., WITAMIR-I, A University of Wisconsin Tandem Mirror Reactor Design, Report UWFDM-400, September 1980.

III.C.15. D. L. Chapin, et al., "Preliminary Feasibility Assessment of Fusion Fission Hybride," WFPS TME-81-003, Westinghouse Fusion Power Systems Department (1980).

CHAPTER IV
REFERENCE LIQUID METAL COOLED BLANKET DESIGN

IV.A DESIGN OVERVIEW

IV.A.1 Concept Description and Motivation

The Westinghouse molten salt suppressed-fission blanket is a two zone design which uses ^{6}Li-depleted liquid lithium as a coolant, neutron multiplier, and tritium breeding material in the front zone. A thorium bearing molten salt is used as a fertile fuel and coolant for the back breeding zone. Elevation and cross section views of the reference blanket module concept are shown in Figure IV.A-1. The advantages of suppressed fission blankets are a higher ratio of fissile production per unit of nuclear power, lower afterheat generation rates, and lower fission product hazard generation. These features lead to both operational and reactor safety advantages. In contrast with hybrid reactors employing high power density fissioning blankets, suppressed fission blanket fusion breeders are expected to be more easily designed and licensed, will support more fission reactors per unit of nuclear power generated in the breeder, and will be more suitable for siting in safeguarded fuel cycle centers.

In this blanket design, fast and thermal fissioning are suppressed by three methods:

● A 50 cm front region of lithium moderates the fission neutron flux to lower energies

● Fissile ^{233}U is discharged from the blanket at very low concentration (0.11% in thorium)

● The fertile thorium in the back of the blanket is diluted in the sense that only one atom of 22 in the molten salt is thorium.

These result in a blanket fission rate which is reduced 1-2 orders of magnitude relative to fast fission blankets considered in previous studies.

Both liquid lithium and molten salts are uniquely qualified for the suppressed fission environment. Concerning ^{6}Li-depleted lithium, it is the only single material that provides substantial neutron enhancement, in situ

MOLTEN
SALT

LITHIUM
OUTLET
MANIFOLD

LITHIUM
INLET
MANIFOLD

MOLTEN
SALT

FROZEN
SALT
LAYER

LITHIUM
IN →

LITHIUM
OUT

← 4.9 m →

← 6.4 m —

LITHIUM
INLET
MANIFOLD

MAGNET

MOLTEN
SALT
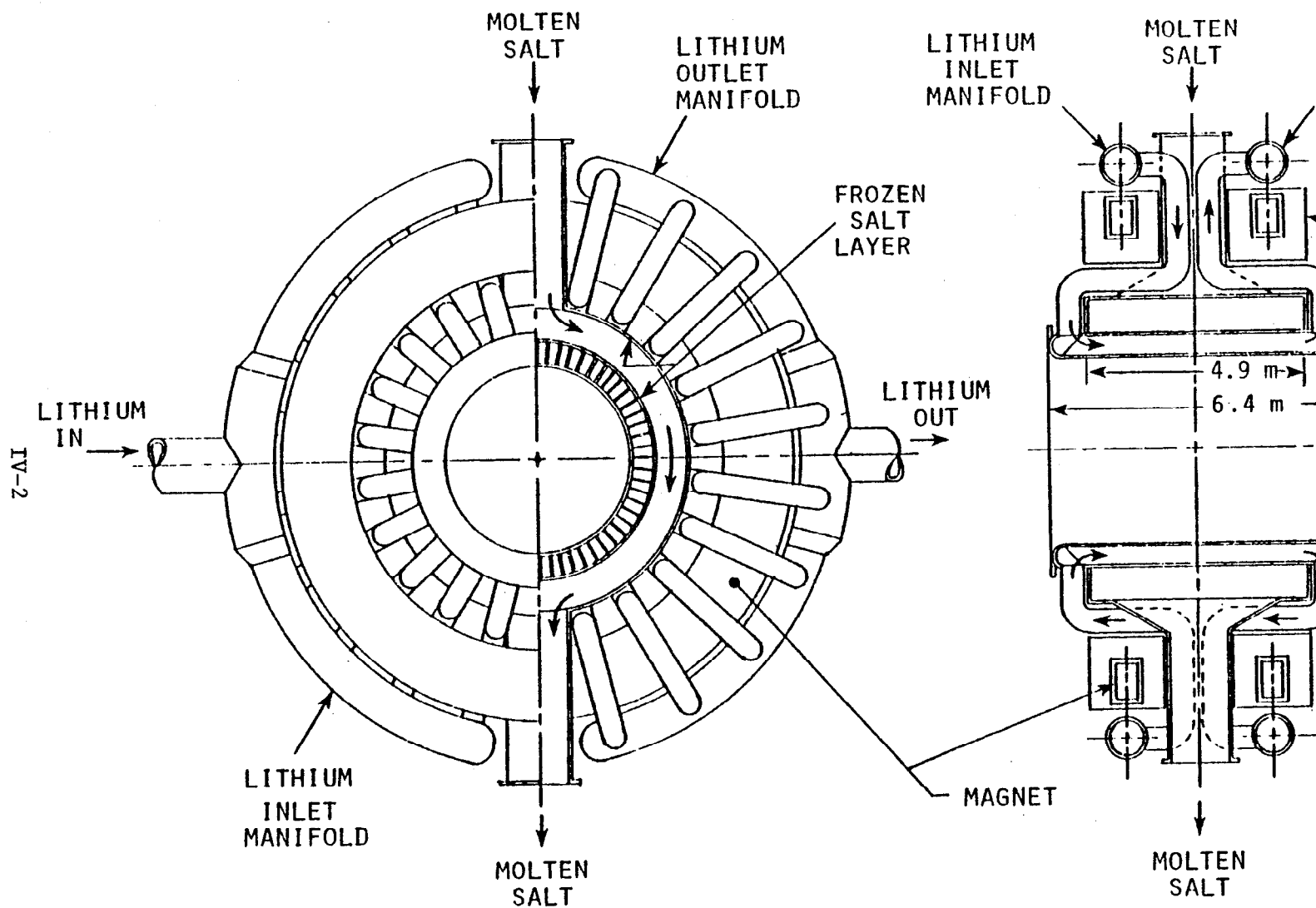
MOLTEN
SALT

FIG. IV.A-1.   Reference liquid metal cooled – molten salt blanket module concept for TMHR

tritium breeding, and has excellent coolant properties. Unfortunately, liquid lithium has two well-known drawbacks: it is chemically reactive with water and other materials and, because it is a liquid metal, MHD pressure drop effects must be considered.

Concerning the molten salt, the principal advantage is a potential for low cost reprocessing at low ^{233}U concentration in thorium—a necessary ingredient for good economic performance. Its principal drawbacks are its highly corrosive nature and the lack of commercially demonstrated molten salt reprocessing and primary loop technologies.

The idea of utilizing a thick (>50 cm) zone of liquid lithium followed by a molten salt breeding zone was first suggested by McGrath[1] as an alternate design option for the TRW HYLIFE Hybrid[2] design study for a laser fusion driver. In the alternate HYLIFE Hybrid design, MHD difficulties are not applicable, but radiation damage to the proposed Hastelloy structural materials (which are compatible with the molten salt) was considered to pose serious constraints on the design lifetime of the blanket. Similarly, for a recent one zone TMHR blanket design featuring a beryllium multiplier and molten salt coolant,[3] LLNL chose TZM as the best of a limited number of structural material candidates that are both chemically compatible with the salt as well as resistent to fusion neutron irradiation damage. In the final analysis, TZM was judged to be unacceptable due to poor fabricability (i.e., weldability) and somewhat unknown irradiation resistance. These and other issues associated with the previous one zone TMHR blanket design have motivated the present consideration of two zone blankets.

The present design concept introduces several novel design features which can mitigate concerns due to both MHD effects on liquid lithium and materials compatibility issues for the molten salt.

First as shown in Figure IV.A-1, the simple, two zone, design results in a less complex blanket that should result in high reliability. In this design, the inner zone is a thick (50 cm) annular region of axially flowing lithium. The outer zone consists of a flowing region of molten salt. Since the active volumes of both zones also serve as the coolant materials, internal piping is eliminated and structure is minimized.

Second, the design features minimal MHD-induced pressure drops ($\lesssim 220$ psi). This results because the liquid metal flow within the blanket is parallel to the central cell field. The liquid metal does flow perpendicular to the field in inlet/outlet ducts which direct the coolant into and out of the blanket. This flow component would normally produce large MHD pressure drops. However, by a combination of design features including electrically insulated duct walls and large cross sectional flow areas, the pressure drop can be greatly reduced. Westinghouse has proposed a novel pipe design incorporating low conductivity ceramic or refractory textile materials as an electrical insulator to accomplish the above purpose.

The method used to contain molten salts in this design is also novel. By freezing on a thin layer of the thorium bearing salt (typically 72 LiF-16 BeF_2-12ThF_4), the 316 stainless steel structure is expected to survive for many years with respect to corrosion. This approach eliminates the need to use Hastelloy or TZM in the blanket. The maximum lithium temperature ($\sim 400^\circ C$) is significantly lower than the salt melting point ($\sim 500^\circ C$). The liquid lithium essentially surrounds the salt (with the possible exception of some points on the back wall), and the salt thermal conductivity is low. Therefore, establishment of the protective frozen salt layer should be straightforward. A Hastelloy structural option has also been investigated as a backup and for use as a back wall containment material.

IV.A.2 Blanket Design and Performance Overview

Table IV.A-1 is an overview of several key design and performance parameters for the lithium/molten salt TMHR blanket. These parameters are discussed in more detail throughout this chapter. Additional data relating to a reference TMHR based upon the lithium/molten salt blanket is presented elsewhere in this report.

TABLE IV.A-1. Key design and performance parameters for the reference
lithium/molten salt blanket.

(Design basis: 3000 MW fusion power)

Mechanical Design	
Central cell length	96 m
First wall radius	2 m
Number of blanket modules	15
Fraction of module axial length used for molten salt zone[a]	77%
First wall thickness	0.5 cm (ave.)
Lithium zone thickness	50 cm
Molten salt zone thickness	80 cm
Total blanket thickness	130 cm
Shield thickness	50 cm
Magnet innor bore (diameter)	9.2 m
Magnet width	50 cm
Magnet pitch	3.2 m
Blanket structural material	316 stainless steel

Power Flow and Thermal Hydraulic Design	
Central cell fusion power	3000 MW
First wall surface heat load[b]	0.01 MW/m^2
First wall neutron loading	2.0 MW/m^2
Total thermal power removed by blanket coolants	3658 MW
Thermal power deposited in liquid lithium zone[c]	2233 MW
Lithium inlet/outlet temperatures	$220/390^\circ C$
Design liquid lithium coolant pressure at blanket inlet	200 psia
Number of liquid lithium inlet/outlet pipes per module	20/20
Thermal power deposited in molten salt zone	1425 MW
Molten salt inlet/outlet temperatures	$550/650^\circ C$
Molten salt coolant pressure	∿65 psia
Number of molten salt coolant inlet/outlet pipes per module	1/1

TABLE IV.A-1. (Continued.)

Nuclear Design and Performance[d]

^{6}Li enrichment in liquid lithium	0.2%
Tritium breeding ratio[e]	1.05
Lithium processing rate for tritium recovery	43 m^3/hr
Tritium inventory in liquid lithium	1.0 kg
^{233}U equilibrium concentration per atom of molten salt thorium	0.11%
^{233}Pa equilibrium concentration per atom of molten salt thorium	0.03%
Net fissile breeding ratio	0.49
Net fissile production rate[f]	6360 kg/yr
Molten salt processing rate for uranium recovery[g]	0.46 m^3/hr
Fissions in ^{232}Th per fusion	0.003
Fissions in ^{233}U per fusion	0.024
Fission power	786 MW
Blanket energy multiplication[h]	1.51

---

[a]Remainder of axial length used for lithium coolant piping.

[b]Dominated by Bremsstrahlung radiation.

[c]Includes first wall surface heat contribution.

[d]Includes 2-D leakage effects.

[e]Must breed at least 1.027 to make up for breeding losses due to 80 MW fusion in end plugs.

[f]At 100% plant capacity.

[g]"Fluorination only" process removes only uranium from molten salt.

[h]Defined as (energy per fusion deposited in blanket)/14.1.

IV.A.3 Overview of Blanket Design Issues

The molten salt blanket design which follows is much like a liquid
lithium blanket for a fusion electric plant, but features the addition of
a molten salt zone for fissile breeding. It combines the economic advantage
of on-line molten salt reprocessing technology with the mechanical design,
thermal hydraulic, and neutronic advantages of liquid lithium. Two novel
features, the active maintenance of a protective frozen salt layer and a
design concept for electrically insulated pipes for liquid lithium, enable
the blanket to be fabricated from modified 316 stainless steel and to operate
at relatively low pressure with minimal internal piping. The molten salt
balnket also preserves the perceived safety, reliability, fissile inventory,
and developmental advantages of low power density suppressed fission
blanket designs.

In this chapter, several design issues are explored in some detail,
but others will require further resolution. First is the issue of liquid
lithium. The development of electrically insulated pipes could result in
lower MHD pressure drops than have been assumed in our mechanical design.
Several concepts which offer wide flexibility in design and appear to be
suited to immediate development are proposed. The issue of electrically
insulated piping is also of importance for fusion electric blankets which
utilize a flowing lithium or lead-lithium coolant. Concerning liquid lithium
safety issues (more detailed discussion in Chapter VI), the lithium and
molten salt are not reactive and many of the same protection systems pro-
posed for the LMFBR (e.g., cover gas, steel liners for concrete) are
applicable to this system. Dump tanks for both the liquid lithium and
molten salt coolants are provided.

Two global issues relating to the molten salt features of this
blanket are of interest. The first relates to the state-of-the-art for
molten salt fuel processing and energy conversion technologies. The
required fuel processing technology is expected to be less demanding than
that required for the Molten Salt Breeder Reactor[4] (see Chapter VII), but
a technology development program is required. The second issue relates
to the selection of structural materials that are compatible with the

molten salt. The frozen salt protection concept is promising, but is difficult to model analytically. Although the scoping studies provide favorable indications, an experimental determination will be required.

In comparison with blankets utilizing a beryllium multiplier, the lithium multiplier blanket produces about 65% as much ^{233}U per fusion. This disadvantage is somewhat compensated by low cost fuel reprocessing, but several ideas for incorporating beryllium multipliers have been proposed. These are discussed in more detail in Section IV.D. A preliminary design concept featuring a one zone packed bed of thorium and beryllium pebbles is presented in Appendix A. A more conventional two zone design replacing the molten salt zone with a packed bed of thorium balls is also presented in Appendix A. It is believed that the liquid metal cooled blanket concept for the TMHR represents an acceptably low development risk because most design issues allow several possible design solutions within the same overall design framework.

THIS PAGE INTENTIONALLY LEFT BLANK

IV.B REFERENCE MECHANICAL DESIGN CONCEPT DESCRIPTION

IV.B.1. Design Guidelines

The blanket concept was developed in accordance with the design
guidelines presented in Table IV.B-1. In addition, other guidelines such as
designing for reliability, ease of remote maintenance/service consistent with
producing a blanket with attractive thermal and neutronic performance were
considered. Some of the key design characteristics of the concept are also
listed in the table.

IV.B.2. Design Configuration

The selection of liquid metal as the coolant was a major influence on the
design configuration, particularly as it affected the coolant pipe size
necessary to maintain low coolant velocities and thereby minimize MHD induced
pressure drops. The space provision necessary for piping the coolant into and
out of the blanket was the principal consideration instrumental in
establishing the 3.2 m pitch between magnets. This pitch provided adequate
space for incorporation of 0.5 m of shielding around the magnets and the
lithium piping into and out of the blanket. The central cell magnet geometry
is shown in Figure IV.B-1. A 6.4 m length module with two magnets was
selected to enhance fissile fuel production by providing a fertile fueled
region which is greater than 75% of the total module length. The remainder of
the module length is occupied by the liquid lithium coolant and is used to
breed tritium only.

IV.B.2.a General Arrangement. A more detailed layout of the TMHR blanket
module concept is shown in Figure IV.B-2. Lithium coolant enters the inlet
manifold, is directed between and under the magnets and flows radially into
the inner blanket region through 20 electrically insulated pipes of 0.5 m
diameter. The flow then traverses parallel to the axis of the reactor where
it acts as coolant to remove heat from the corrugated first wall. In addition
the lithium removes heat from the intermediate wall between the inner lithium
region and outer molten salt zone to provide the protective frozen salt layer
on the molten salt side of the wall. The coolant then flows radially out

TABLE IV.B-1. Key design guidelines and design parameters of the liquid metal cooled blanket.

Design and Performance Guidelines

First Wall Radius	2 m
Central Cell Length	96 m
First Wall Neutron Loading	2 MW/m^2
First Wall Surface Heat Load	0.01 MW/m^2
Peak Magnetic Field	3 Tesla
Tritium Breeding Ratio	1.1
Fuel Processing	On Line, Continuous or Batch
Coolant	Liquid Metal, Molten Salt
Availability	$\sim$ 0.7

Design Parameters

First Wall Radius	2 m
Outer Blanket Radius	3.3 m
Magnet Pitch	3.2 m
Number of Modules	15
Total Module Length (Lithium Zone)	6.4 m
Fertile Zone Length	4.9 m
Liquid Metal Coolant	Liquid Lithium
Tritium Breeding Ratio	1.05
Fuel Form	Molten Salt
Composition (Mole %)	72% LiF-16% BeF_2-12%ThF_4
Structural Material	316 SS (Modified)*
Lithium Coolant Pipes (20 each Inlet and Outlet)	
Material	316 SS, (Modified)*
	Electrically Insulated Ducts
Diameter	0.5 m
Molten Salt Pipes (1 each Inlet and Outlet)	
Material	316 SS
Diameter	1.4 m

*Prime Candidate Alloy (PCA), Ref. 5.
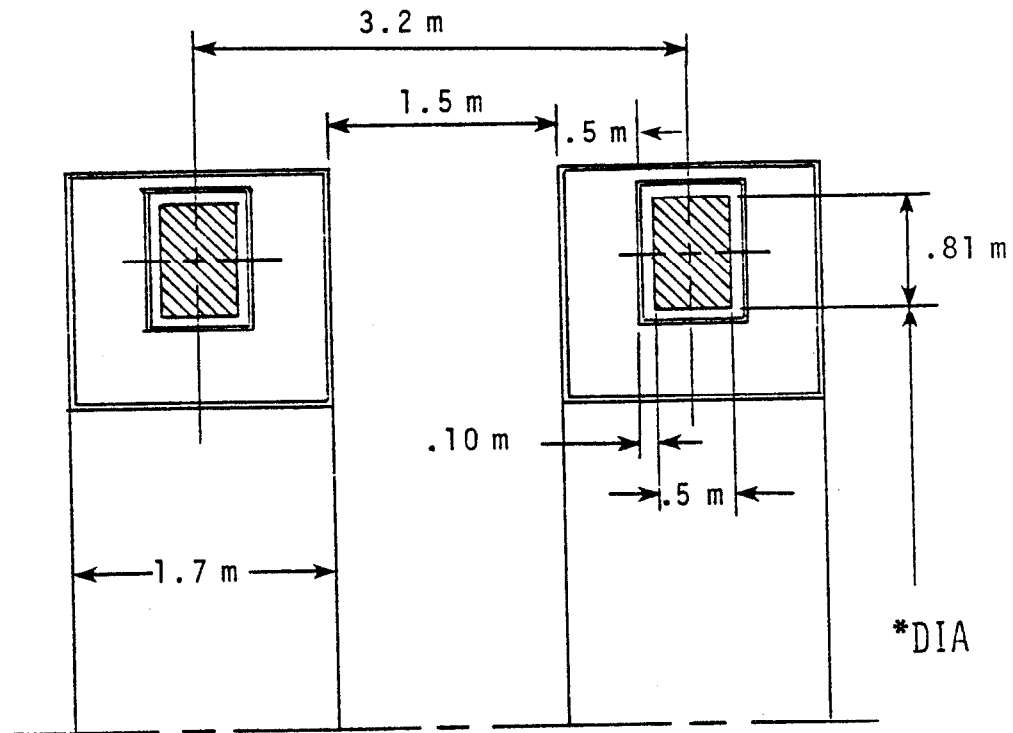
Magnet Width	0.5 m
Dewar Allowance	0.10 m
Shield Thickness	0.50 m
Magnet Pitch	3.2 m
Clearance Between Magnets (Incl. Shield)	1.5 m

*Magnet Inner Bore for Piping Concepts Considered

Reference Piping Concept	9.2 m
Alternate Piping Concept	8.0 m

FIG. IV.B-1. TMHR magnet geometry for reference liquid metal cooled blanket.
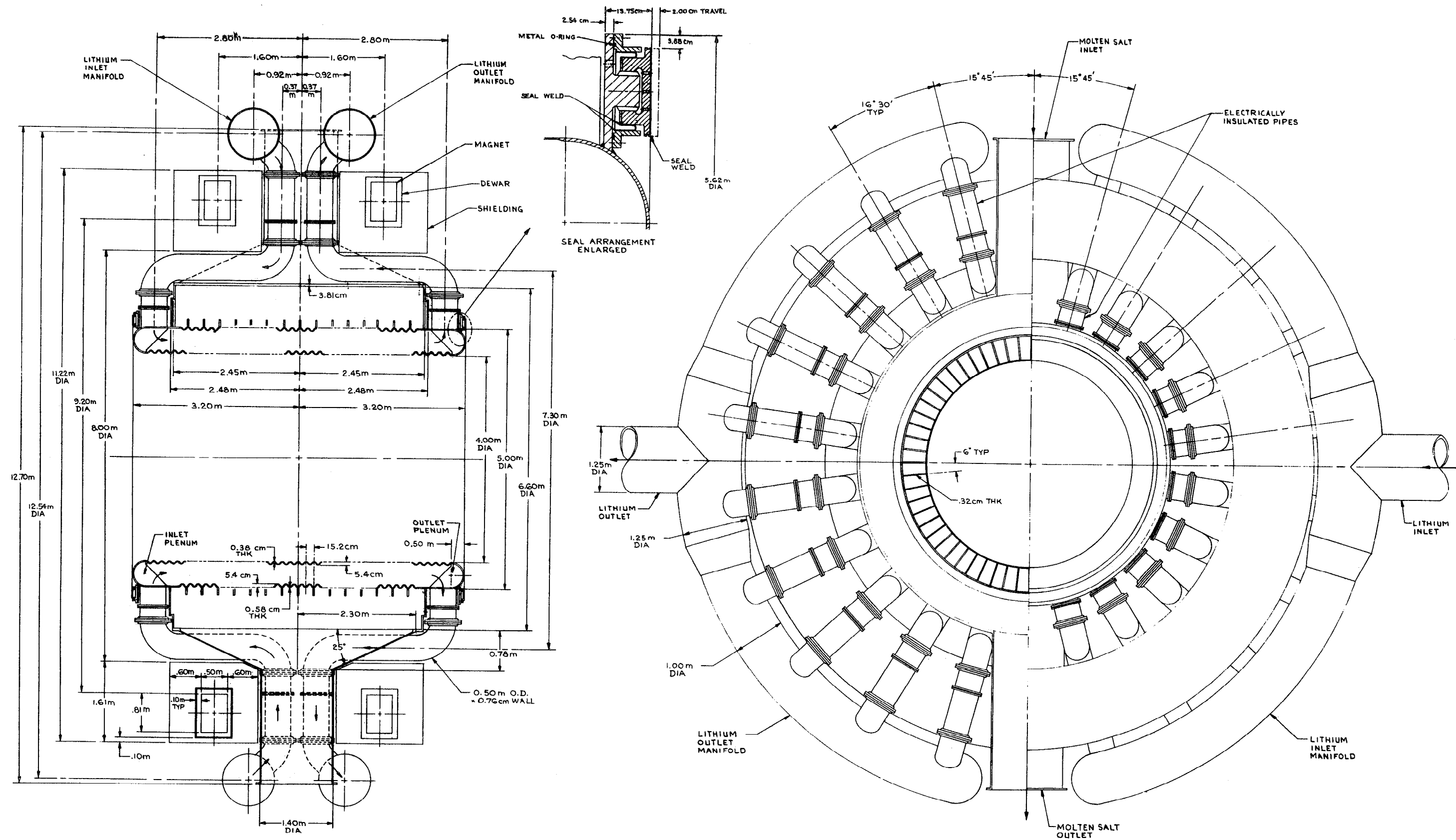
FIG. IV.B-2. Component arrangement and dimensions for the reference TMHR liquid Metal cooled blanket module assembly.

through the 20 exit pipes, turns under the magnets, and is directed outward between the magnets and to the lithium outlet manifold.

The molten salt enters the top of the module through a 1.4 m diameter pipe located between the magnets, flows circumferentially through the outer region of the blanket and exits through a single pipe located in the bottom center of the module.

The piping for both the lithium coolant and the molten salt are located to provide access for magnet removal (after a module is removed from the central cell assembly) without the cutting of the piping inboard of the manifolds.

IV.B.2.b. <u>First Wall Concept</u>. A structurally thin first wall is a prerequisite design requirement to attain satisfactory neutronic performance in the suppressed fusion fission hybrid blanket. Since the inner blanket zone is subjected to $\sim$110 psi lithium pressure, the first wall is connected to the intermediate wall which separates the inner blanket zone from the molten salt fertile zone to minimize first wall thickness. This connection between the two concentric shells consists of 60 radial ribs equally spaced around the perimeter of the inner blanket zone. By corrugating the first wall circumferentially, a wall thickness of 0.38 cm (0.15") was achieved without exceeding the permissible bending stress in the first wall sections which span the radial stiffeners. The intermediate shell between the inner and outer blanket zones is similarly corrugated, but circumferential stiffening ribs are used to provide additional protection against buckling due to molten salt pressure in the outer region which places the intermediate cylindrical shell in compression. The ends of the module in the inner zone are cylindrical and 1.0 cm (0.4") thick. (If flat ends were adopted, a thickness of the order of 5 cm would be required to adequately sustain the lithium pressures.) The entire blanket structure is fabricated from modified 316 SS[5]. The blanket structural dimensions, and first wall corrugation and end wall configurations are shown in Figures IV.B-3 and -4. Design features are summarized in Table IV.B-2.

3.8 cm WALL
(1.5")

15.2 cm STIFFENING
(6.0") RIB (TYP)

3.3 mR
(130")

2.5 mR
(98.4")

2.0 mR
(78.7")

CORRUGATED FIRST WALL .38 cm
(.15")

BAFFLES 6° APART

CORRUGATED WALL .58 cm
(.23")
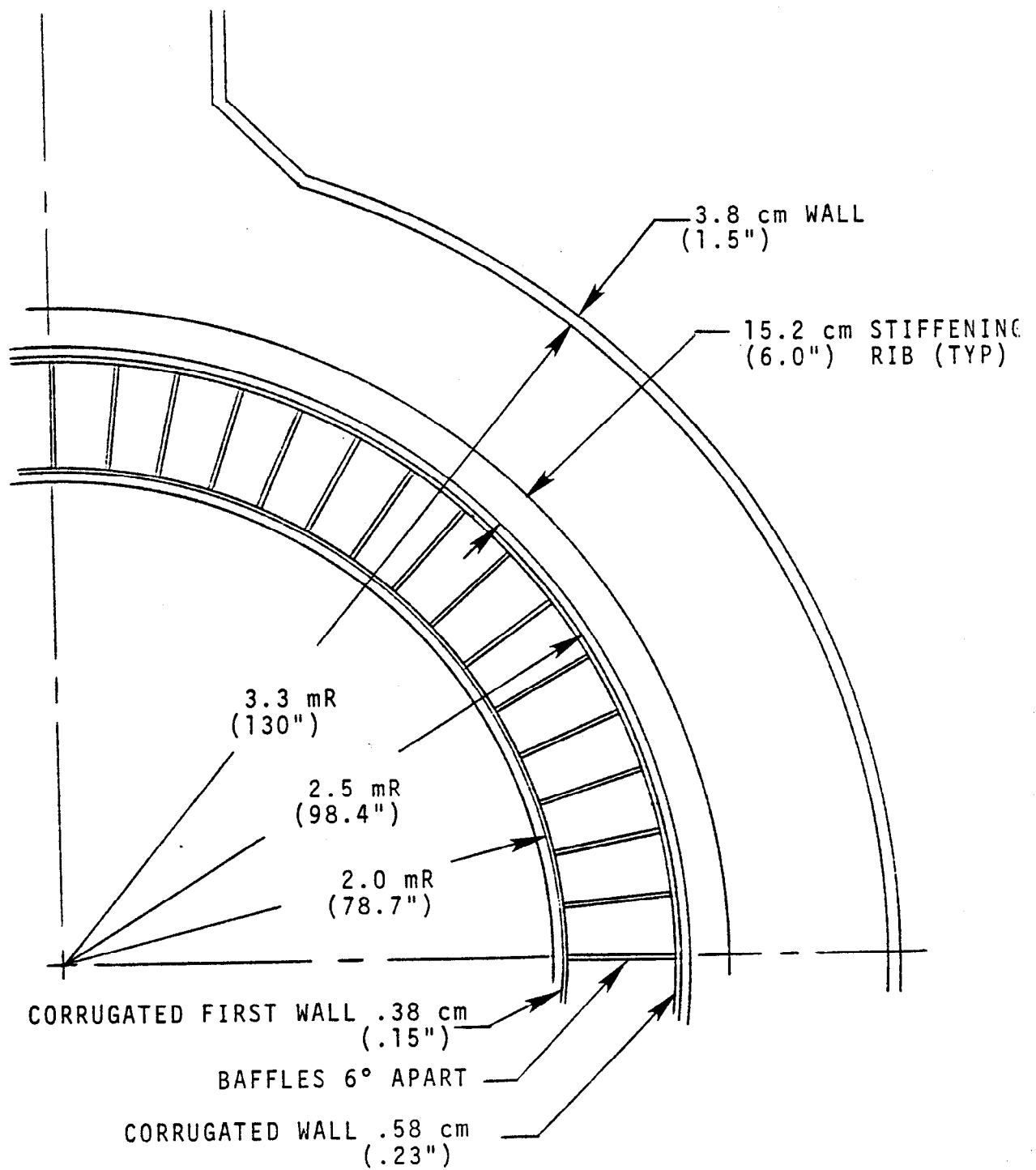
FIG. IV.B-3. Structural Dimensions for TMHR liquid metal cooled
reference blanket concept.

CORRUGATED
FIRST WALL

3.8 cm

1.5"   11.4 cm
        4.5"

5.4 cm
2.1"

0.38 cm
0.15"

1.5"
3.8 cm

1.3 cm
0.5"   STIFFENER
                             (TYP)

7.6 cm
3.0"

NOT TO SCALE   1.0 cm
                             0.4"
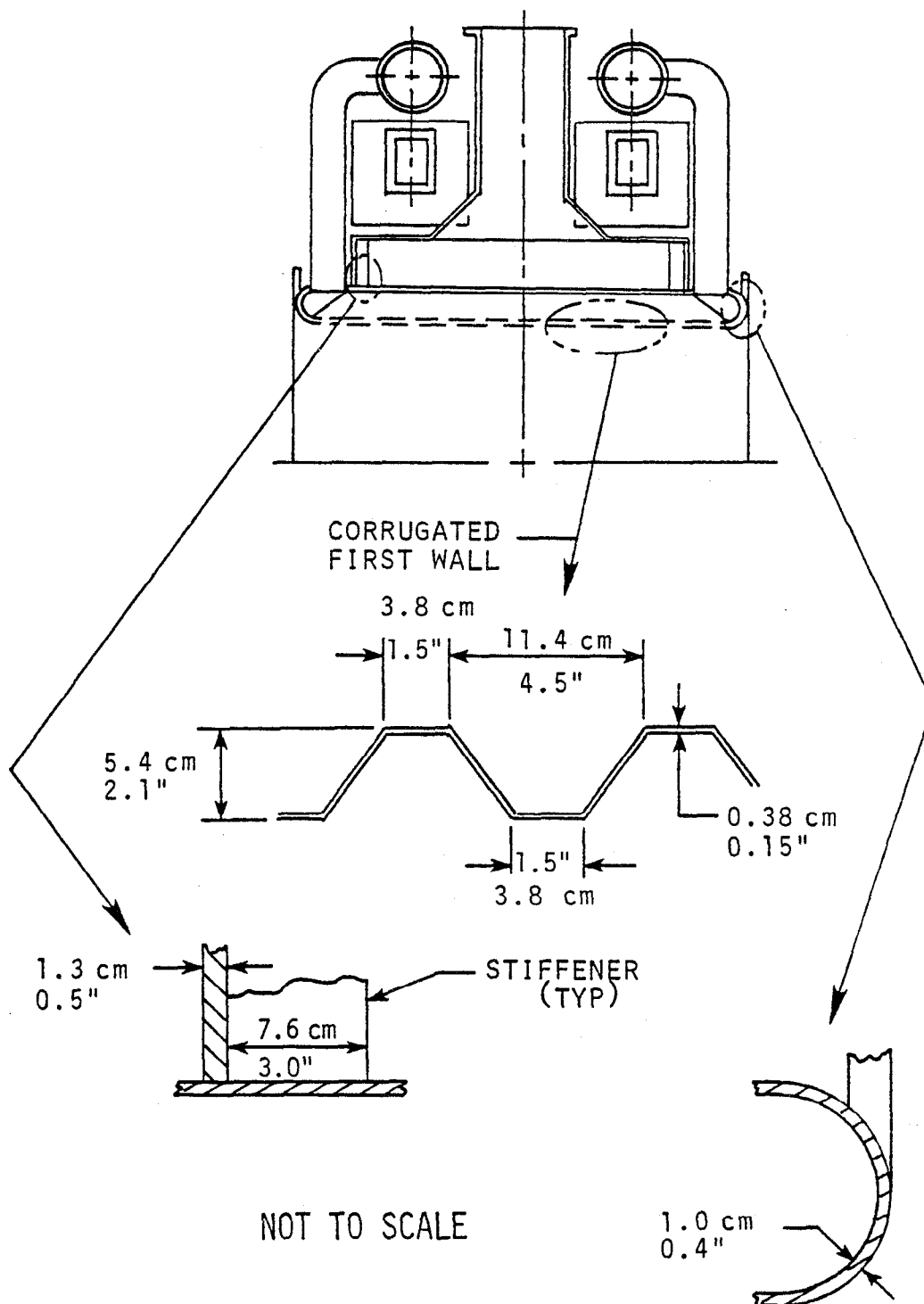
FIG. IV.B-4. Structural dimensions for TMHR reference liquid metal
cooled metal blanket module.

Table IV.B-2. Design features of the liquid metal cooled molten salt blanket concept.

Total Length of Module	6.4 m
Length of Fertile Region	∿ 5 m
First Wall Radius	2 m
Inner Lithium Breeding Zone Thickness	∿ 50 cm
Fertile Fuel Form	Molten Salt
Molten Salt Outer Zone Thickness	∿ 80 cm
Corrugated First Wall Thickness	0.38 cm (0.15 in)
Equivalent Thickness*	0.5 cm (0.2 in)
Lithium Zone Corrugated Outer Wall Thickness	0.58 cm (0.23 in)
Equivalent Thickness*	0.8 cm (0.3 in)
Equivalent Thickness of Stiffening Ribs	∿ 1.1 cm (0.45 in)
Outer Wall of Blanket	∿ 3.8 cm (1.5 in)
Number of Inlet/Outlet Coolant Pipes Required	20 Each
Coolant Pipe Diameter	∿ 0.5 m
Molten Salt Inlet and Outlet Pipe Diameter	1.4 m

*Actual thickness of a flat plate having the same volume and length as the corrugated section.

IV.B.2.c. <u>Outer Blanket Zone</u>. The outer zone of the blanket is relatively simple in design compared to the inner zone. Except for one inlet and one outlet pipe, no additional cooling pipes are necessary to cool the molten salt, since the molten salt is circulated slowly to remove the heat generated in the salt. Back wall cooling of module will have to be provided to assure that a frozen salt layer is established to protect the stainless steel containment structure as discussed in Section IV.E. An active or passive cooling system which is closely coupled with the shield coolant system (which can be of a lower temperature design) will have to be devised. The cooling system was not designed because it was beyond the scope of work during this phase of the study.

The molten salt pressure in this region is comparatively low - approximately one-half of that in the lithium inner zone, ($\sim$ 65 psi versus 110 psi) and is due primarily to the 12 m molten salt hydrostatic head at the bottom of the blanket. The pressure will tend to place the intermediate cylinder in compression, particularly when the pressure is reduced in the inner zone in the event that the lithium flow is stopped. As structural material outboard of the fertile zone is not crucial to neutronic performance, a thicker wall of the order of 3.8 cm (1.5") is provided.

IV.B.2.d. <u>Shield</u>. The magnet shielding interfaces with the blanket and associated support structures; therefore space requirements for the shield were considered. One-half meter of space was allocated for shielding to provide magnet protection from radiation from the outer surface of the blanket. The presence of the shield influenced the coolant pipe routing and was considered in establishing the magnet pitch and diameter and the maximum diameter of the module. The design of the shield and its cooling system were not an explicit part of this year's study. The shield design will have to be included in more detailed studies of the module assembly to assure proper interfacing with the blanket, first wall coolant piping, magnets and module external supporting structure.

IV.B.2.e. <u>Lithium Coolant Piping</u>. The coolant piping for the reference concept shown in Figure IV.B-2 was routed near the center of the module to provide access to the magnets without disconnecting the 20 inlet and 20 outlet pipes during remote disassembly. The 316 SS piping shown in the figure is provided with appropriate flanged spool pieces to connect the manifold and the axial and radial pipe runs. The radial pipe section for the lithium inlet and outlet contain electrically insulated pipe sections (described in Section IV.C) to reduce the MHD induced pressure losses. The axial runs of pipe are not insulated since the MHD effects are expected to be negligible because the flow is nominally parallel to the magnetic field. The piping insulation (necessary to prevent excessive heat losses to the surroundings) is not shown. The insulation thickness required was shown to be less than 1/2 inch (Section IV.E) for low conductivity Min-K® thermal insulation manufactured by Johns-Manville. Inclusion of insulation, therefore, would have minimum effect on the space requirements for routing the piping.

Other piping arrangements were investigated to further reduce the piping pressure loss and provide more access to the blanket for structural supports external to the blanket. An alternate concept that was developed is shown in Figure IV.B-5. In this concept, the piping from the manifolds has no pipe bends once the piping enters the magnetic field. Thus only a single insulated spool piece is required in each pipe. In addition, more access to the exterior of the blanket is available for handling, structural supports interfacing with shield coolant system for back wall cooling, etc. A comparison of some of the advantages and disadvantages (not necessarily of equal importantance) of both the reference and alternate piping concepts is shown in Table IV.B-3.

IV.B.3. Maintenance and Accessibility

IV.B.3.a. Module Interface Sealing. The method for sealing the vacuum boundary in the contact plane between the modules is a key design issue. A module installed at room temperature will grow due to thermal expansion by approximately 4.4 cm (1.7 inches), which requires that a seal must deflect this amount at operating temperature or one-half the amount if similar flexible seals are incorporated at each end of the module. Seals with appreciable flexibility have been proposed by LLNL for such applications[3,6]. In addition, LLNL is currently investigating a surface seal[7] design similar to that shown in Figure IV.B-6 which is the current proposed sealing arrangement for the reference design.

If an intermediate vacuum ($\sim 10^{-3} - 10^{-6}$ Torr) is maintained outside the vacuum vessel as has been proposed[8,9] in other reactor studies, then a perfect seal may not be required. With this arrangement, the impedance to flow at the module to module interface could be tolerable with the pumping capability of the high vacuum reactor vessel pumps. The sealing is accomplished by pressurizing the chamber to deflect until it contacts the mating surface, exerting uniform interface pressure (as opposed to bolting) on the adjacent module (which has an identical type seal).

MOLTEN
SALT

LITHIUM
OUTLET
MANIFOLD

FROZEN
SALT
LAYER

LITHIUM
IN

LITHIUM
OUT

LITHIUM
INLET
MANIFOLD

MAGNET
TYP

MOLTEN
SALT

LITHIUM
INLET
MANIFOLD

MOLTEN
SALT

LITHIUM
OUTLET
MANIFOLD

SHIELDING
TYP

4.9 m

6.4 m

4.0 m
DIA
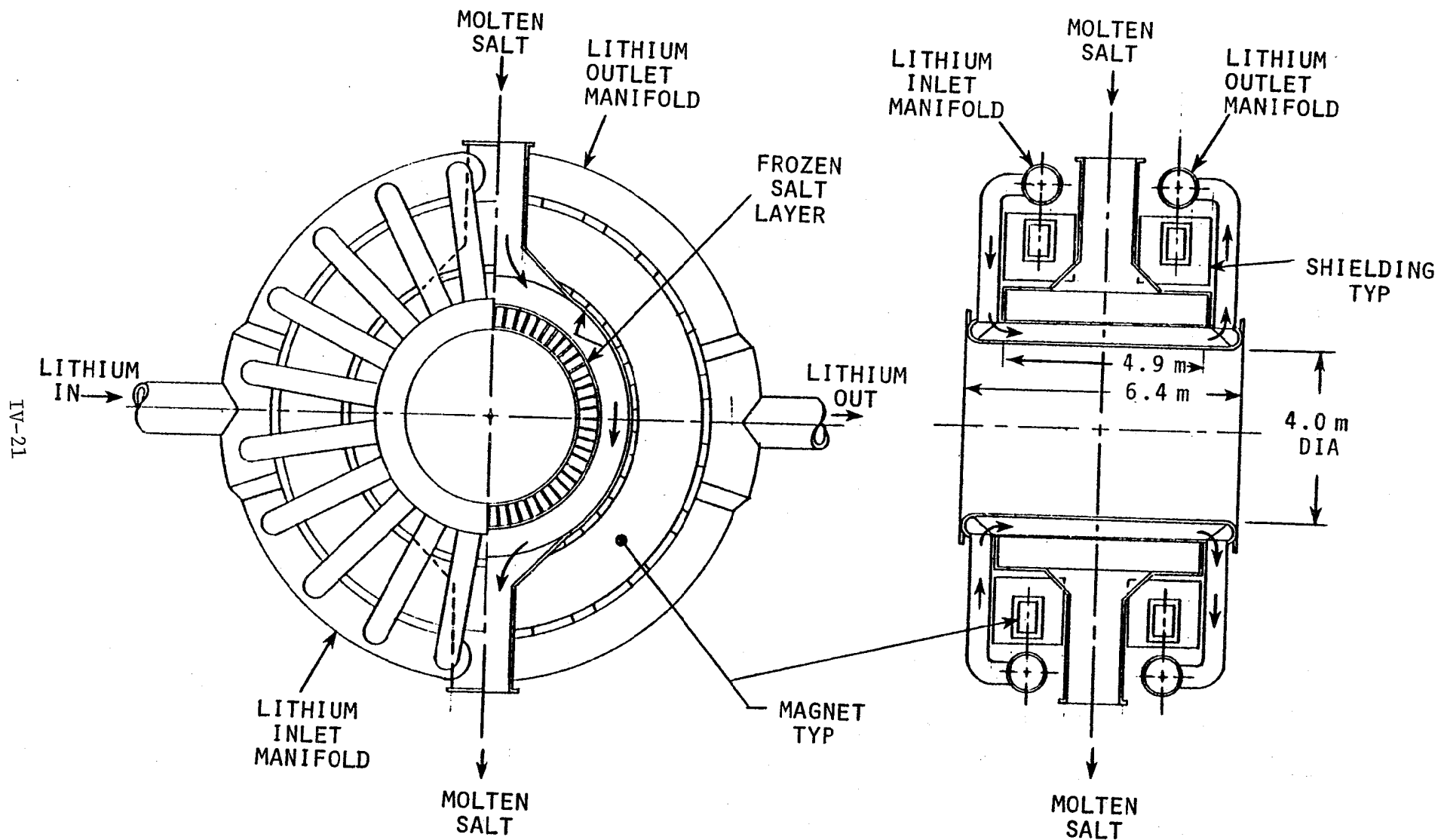
MOLTEN
SALT

FIG. IV.B-5. Alternate piping arrangement for the TMHR reference liquid metal cooled –
molten salt blanket module concept.
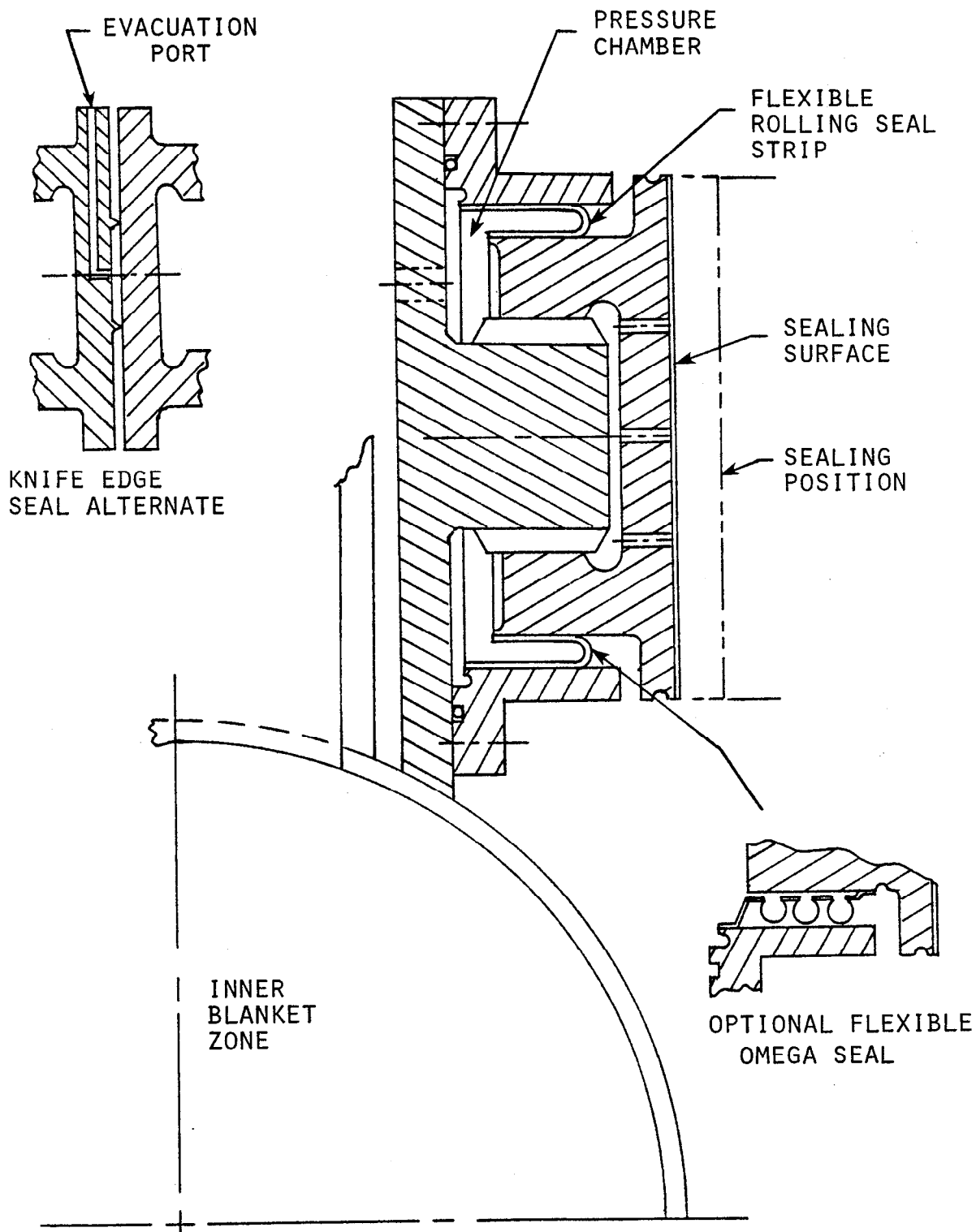
FIG. IV.B-6. Module interface sealing concept for TMHR liquid metal
cooled - molten salt blanket. (See enlarged inset in FIG. IV.B-2.)

Table IV.B-3. Comparison of piping configurations.

REFERENCE PIPING ARRANGEMENT	
ADVANTAGES	DISADVANTAGES
Magnet Access and Removal With Pipes Intact	Longer Pipes, Extra Bends Higher ΔP
	More Difficult to Incorporate Insulated Pipes with Bends
	Larger Magnet Bore Required
	Less Access for Structural Supports
	Back Wall May Require a Separate Active Cooling System

ALTERNATE PIPING ARRANGEMENT	
ADVANTAGES	DISADVANTAGES
Shorter Pipes, Fewer Bends -Lower ΔP	Magnet Access Requires Coolant Pipe Removal
More Amenable to Incorporate Electrically Insulated Pipes	
Fits Within Smaller Magnet Bore	
More Access for Blanket Structural Supports	
Possibility for Cooling Back Wall Via Shielding System	

To prevent leakage from the pressure chamber very thin, "U" type, annular flexible "rolling" seal strips are used. In applications such as this (steady operation with few shutdown cycles), it appears possible to maintain leak integrity even though the flexible seal strip may deform plastically. In principle, the annular seal strips could be replaced with the omega type flexible seals shown, since they have been commonly used to seal against components with relative motion. If more effective sealing is required because an external vacuum is not employed, the face of the seal could be fitted with raised knife edges which would embed in the surface of a soft material in the mating seal face. This alternate is also shown in the

figure. Further sealing effectiveness can be achieved by evacuating the volume between the knife edges. Finally, the mating surfaces could be seal-welded; however, this approach would entail a penalty in the time required for cutting and welding the seals. Future design efforts should focus on designing and testing concepts which have the potential for a practical seal design without welding.

IV.B.3.b. <u>Maintenance Considerations</u>. During the development of the blanket concept, remote maintenance was a key consideration which affected the module assembly configuration. This is evidenced in the reference piping concept which permits magnet access and removal without disassembly of all the inlet and outlet lithium coolant lines. In addition, the module interface sealing concepts without bolted connections and welded seals is an attempt to simplify and expedite removal of modules from the reactor. In general terms, the following sequence of events represents a removal/replacement scenario. First, the reactor is shut down, and the lithium and molten salt are drained from the blanket module to be removed. If an intermediate vacuum is maintained outside of the vacuum vessel, access to the central cell must then be provided by opening up the secondary vacuum containment boundary.

The intermodule seals in the affected modules are then depressurized and the modules cooled to provide clearance between the module and its neighbors. All service connections (instrumentation, etc.) are disconnected. The module is then backed out from the central cell, supported by either high capacity roller assemblies or air pads. The magnets and shielding are then removed from the module and the module transported to a remote maintenance area. A spare module would then be fitted with the magnets previously removed and the module assembly reinserted into the central cell in essentially the reverse order of the above outlined steps. Maintenance has been considered in an overview sense and the treatment is cursory compared to the type of detailed procedures which must ultimately be developed. More in depth design studies of the blanket system will be required to develop maintenance procedures to a reasonable degree of detail.

IV.B.4. Fuel Handling Systems

The molten salt is circulated slowly through the outer blanket and discharged through the pipe at the bottom of the blanket module. It flows through an intermediate heat exchanger where it transfers the power generated within it to the intermediate heat transport system coolant. After flowing through the intermediate heat exchanger (Section IV.E) a small fraction of the flow ($\sim$ 0.46 m^3/hr) is directed to the molten salt reprocessing plant for fuel removal. The main stream plus makeup salt is then returned to the molten salt inlet pipe at the top of the blanket to complete the cycle. Molten salt reprocessing and fuel recovery are discussed in detail in Chapter VII.

IV.B.5. Mechanical Design Overview and Comments

The reference blanket concept which has been proposed has several attractive mechanical design features. Most importantly, the concept is relatively simple and features low pressure operation. Also, the reference module can be fabricated from readily available and fabricable stainless steel and avoids the use of more exotic high nickel content alloys. Finally, the use of two fluid coolants allows for rapid discharge to dump tanks in the event of a loss of flow/loss of coolant accident, minimizing the consequence of such accidents.

Concerning the use of liquid lithium for cooling/tritium breeding/neutron multiplication, both advantages and disadvantages are apparent. Lithium is an excellent heat transfer fluid which provides for low intrinsic coolant pressures which should result in improved reliability. Tritium is easily recovered from lithium and our results suggest that total coolant tritium inventories less than one kilogram appear possible[10] (see Section IV.F.2). Although the neutron multiplication properties of lithium are inferior to those of beryllium, feasibility is less of an issue and substantial multiplication is achieved. Safety issues associated with the chemical reactivity of liquid lithium are a concern, but the combined use of dump tanks, inert atmospheres, and engineered safety systems similar to those proposed for LMFBR use should be adequate.

A demonstration of the feasibility of electrically insulated pipes (i.e., MHD pressure drop) is pre-requisite for operation at relatively low coolant

pressure. Therefore, insulated pipe concepts should be pursued, a design developed, and tested. The initial step would be the development of sprayed insulating coatings compatible with a metal substrate simulating the pipe material. Coated samples could be readily obtained and screening tests performed to determine candidate materials prior to fabricating actual insulated pipes. The behavior of the insulation and the concentric pipe assembly with its seal welds must be evaluated to assure structural integrity during pressure and thermal cycling tests to simulate start-up and shut-down operating conditions.

Concerning the molten salt region, a novel corrosion protection scheme has been proposed. It must be demonstrated that a solid molten salt layer that will offer protection to the stainless steel structure containing the salt can be maintained. Similarly, the dump tank strategy for the salt assumes that afterheat cooling in the dump tank will be more easily accomplished than in the blanket. It appears possible to design a natural circulation convective heat removal system for the dump tank, but the design of such a system must be developed. Finally, auxiliary/trace heating must be provided to assure that both the molten salt and liquid lithium are able to flow freely. However, it might be possible to eliminate the need for trace heating in the blanket itself by draining and pre-heating the lithium and molten salt after shutdown and prior to startup. The design of trace heating systems has been handled successfully in LMFBR's.

The large lithium and molten salt coolant inlet and outlet pipes complicate component interfacing by competing for space with structural supports, magnets, the shield, and access for maintenance and disassembly. Also, the effect of corrugated surfaces in the lithium flow path on MHD induced pressure losses is not known, but is not believed to be excessive. Finally, the intermodule sealing problem may be generic to many blanket designs and candidate seal concepts should be developed and tested.

In summary, the liquid metal cooled blanket has enough attractive attributes to warrant further design and development effort. It is important to consider the entire module system since the blanket is intimately related to other components including the shield, magnets, structural supports, and shield cooling system where this interrelationship has significant effect on availability and maintenance.

IV.C. MATERIALS ISSUES

IV.C.1. Electrically Insulated Duct Concept for Liquid Metal Coolant and
         Proposed Materials of Construction

This section discusses the possible material choices, particularly
insulating materials, for use in fabrication of insulated ducts or pipes.
Electrically insulated inlet pipes are necessary in order to minimize the
magnetohydrodynamic (MHD) pumping pressures. In addition, because of concern
for materials operating at elevated temperatures and in a severe radiation
environment, the rationale for selection of a variant type 316 SS for the
first wall and blanket structural material is presented.

IV.C.1.a. MHD Pressure Drop Problem. Liquid lithium is an attractive blanket
coolant since, in addition to being an effective coolant it can serve as the
tritium breeding material as well as the medium to transport the tritium to a
tritium recovery system. An inherent disadvantage of a liquid metal coolant
however are the magnetohydrodynamic (MHD) losses encountered when the liquid
metal is pumped through a magnetic field. The losses can result in high
coolant pressure drops. The amount of additional piping and module wall
structure required to contain the coolant pressure has an adverse effect on
neutronic performance. Analysis of the MHD induced pressure drops in the
lithium piping is discussed in detail in Section IV.E. The results indicate
that these pressure drops can be significantly reduced if electrically
insulated pipes are used where the coolant flows perpendicular to the magnetic
field. The following section discusses a pipe or duct concept and proposed
insulating materials to achieve an electrically insulated section in the
lithium coolant inlet and outlet pipes.

IV.C.1.b. Proposed Configuration and Materials. An electrically insulated
pipe, or spool piece, concept was developed to minimize the MHD losses in the
lithium coolant pipes which feed the inner blanket zone. Although some
uncertainties relative to selection of materials and design must ultimately be
resolved, the concept appears to be feasible. As shown in Figure IV.C-1, the
candidate concept consists of an electrical insulating material sandwiched
between a thin metal liner and a heavier outer metal structure. Radially

SEAL WELD

THIN METAL
(LOW ELECTRICAL
CONDUCTIVITY)
LINER

0.04 - 0.05 cm
0.015-0.020"

ELECTRICAL
INSULATING
SLEEVES (TYP)

METAL STRUCTURAL
COMPRESSIVE SLEEVE

ELECTRICAL
INSULATION

OUTER METAL STRUCTURAL
SECTION (TYP)

0.64 - 0.76 cm
0.250-0.300"

SEAL WELD

WASHER (TYP)
ELECTRICAL
INSULATING
SLEEVE (TYP)

INSULATING RING
(SEGMENTED)

~ 0.50 m D
19.7"

ALTERNATE BOLTING
ARRANGEMENT
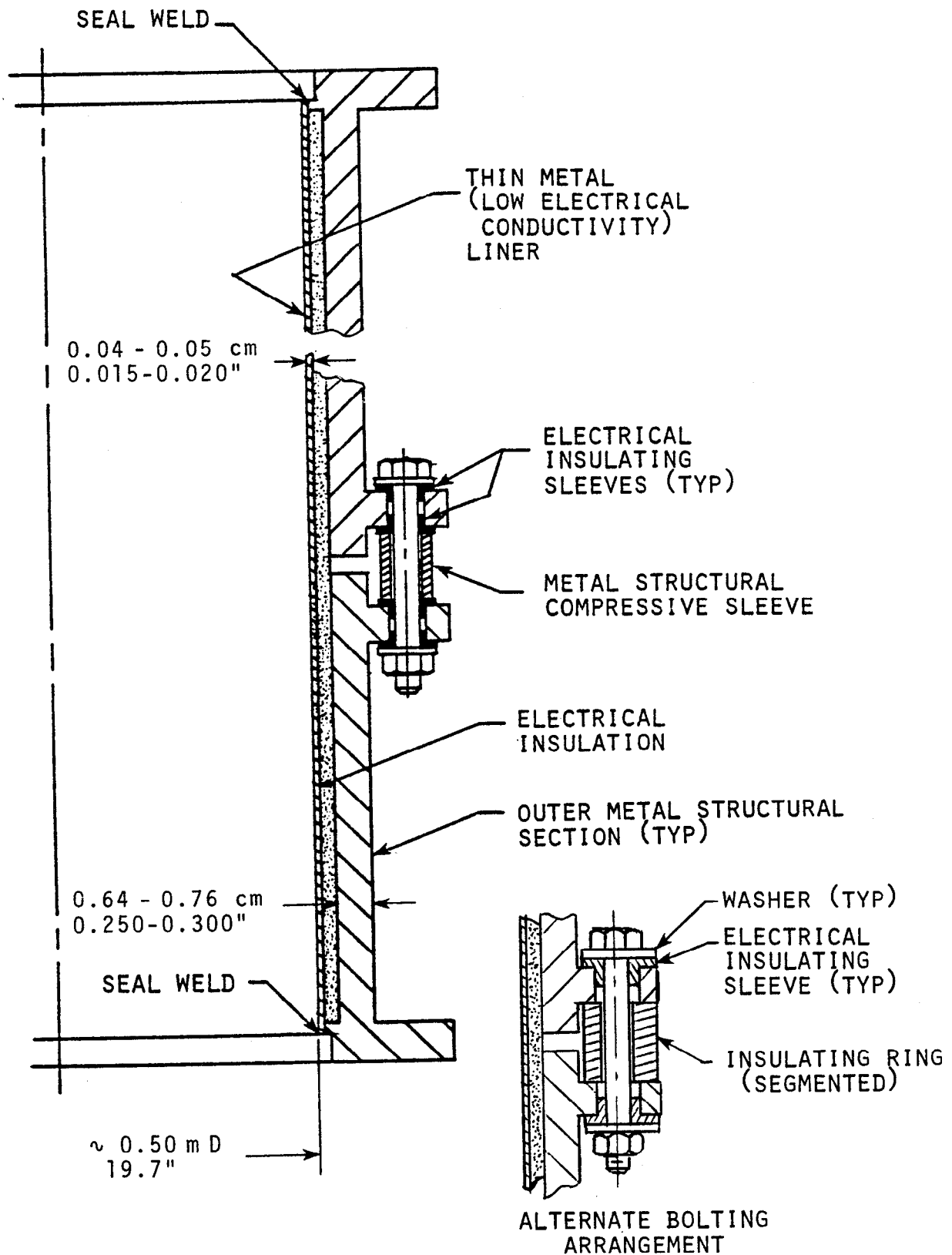
FIG. IV.C-1. Concept for electrically insulated pipe section for the
liquid metal cooled TMHR blanket.

induced currents in the structure are minimized by the presence of the insulating material. Axial currents in the pipe are minimized by the relatively thin liner, which reduces the conductivity of the pipe section as compared to a full thickness outer section necessary to carry the full pressure of the liquid lithium coolant. In addition, the outer section is split around the circumference of the pipe section as shown to insulate the outer pipe from induced currents in the axial direction.

To maintain the structural integrity of the pipe with respect to axial loads and any pipe bending moments, an insulated flanged joint is provided. Structural compressive metal sleeves are loaded by tensioned bolts with appropriate electrical insulating sleeves loaded in compression. An alternate bolting arrangement also shown in the figure utilizes an insulated ring in lieu of the metal compressive sleeves. The insulating ring could be made of a ceramic or similar material which would be structurally efficient since it is loaded in compression. To simplify fabrication, the insulating ring could be made in segments.

Some candidate materials for pipe sections which appear to have potential for achieving suitable insulating properties are:
- Duct Material - 316 SS
- Candidate Insulation Materials:
  - Al_2O_3, Detonation Gun (D-Gun) Plated
  - Al_2O_3 + Intermediate Layer to Accommodate Expansion - D-Gun or Plasma Spray Plated
  - REFRASIL®.

Alumina has been suggested as a result of discussions with Union Carbide[11] and Metco Inc., Flame and Plasma Spray equipment suppliers[12] representatives because of its excellent electrical insulating properties and resistance to thermal shock. Alumina has been successfully used as coating on stainless steels, carbon steels, Inconel X and other materials for applications at temperatures ranging from 650°C to above 1000°C. UCC reports[11] that these materials were subjected to 150 hour tests in the above range and several rapid heating and cooling cycles before failure of interface

---

® Produced by HITCO Materials Division Subsidiary of ARMCO Steel Corporation.

bond between the alumina and metal occurred. It should be noted that a UCC alumina coating has an expansion coefficient very similar to type 440 C stainless steel, suggesting the possibility that intermediate coatings of sprayed metal or another composition of ceramic material can be used to reduce the effect of the mismatch in expansion coefficients of the base material of the piping and the final coating layer.

The third alternate insulating material possibility is REFRASIL textile high temperature insulation. REFRASIL textiles are high temperature "continuous filament amorphous silica products with thermal performance of a refractory material." The insulation is available as fabric, tape, sleeving or cordage. It could be inserted between the inside of the structural pipe diameter and the thin metal liner. If necessary, the liner could be expanded by pressurization after assembly to remove any excess clearance.

Finally, another possibility shown in Figure IV.C-2, consists of a corrugated inner liner instead of the thin cylindrical liner discussed above. In the event of a local bond failure of the insulation, the electrical conductivity between the two pipe and internal corrugations would be minimized since the contact area is relatively small. This concept however, requires additional study and analysis to determine whether a practical corrugation configuration can be developed.

IV.C.1.c. Overview and Comments. Based on the above alternates, it appears reasonable to conclude that a design solution to the duct insulation problems can be achieved. Spray coating is a well developed art and material samples could be readily obtained and evaluated without an expensive test program. The effects of a radiation environment on coatings have not been addressed at this time, and should be included in future efforts once the best material combinations have been selected based on thermal and mechanical cyclic testing of candidate materials.

IV.C.2 Structural Materials Considerations

IV.C.2.a. First Wall/Blanket Structural Materials. In addition to the concerns associated with elevated temperature operation in general, the primary structural materials used for the first wall and most of the blanket structure will be subjected to radiation damage due to fast neutrons. This

~ 0.50 m D
19.7"

THIN CORRUGATED METAL (LOW ELECTRICAL CONDUCTIVITY) LINER

.040-.050 cm
.015-.020"

0.64-0.76 cm
0.250-0.300"

SECTION A-A
ENLARGED

ELECTRICAL INSULATING SLEEVES (TYP)

METAL COMPRESSIVE SLEEVE

ELECTRICAL INSULATION

A   A

OUTER METAL STRUCTURAL SECTION (TYP)

SEAL WELD
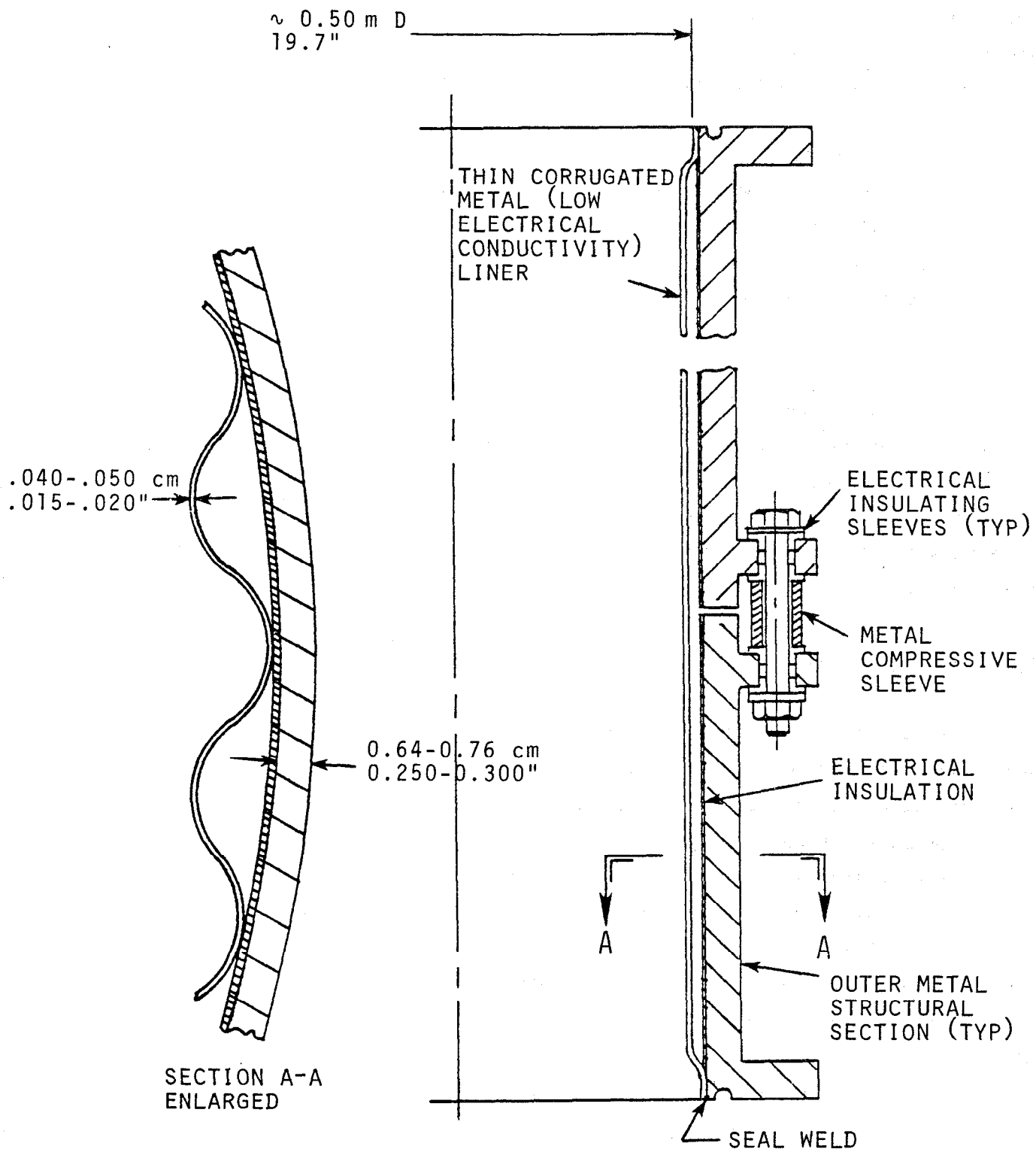
FIG. IV.C-2. Alternate corrugated liner concept for electrically insulated pipe section for the liquid metal cooled TMHR blanket.

IV-31

aspect of the service environment carries with it the concerns of dimensional stability and adverse effects on mechanical properties. For the reference TMHR design, the first wall service conditions include:

Operating Temperature   400-450°C
Fusion Neutron Wall Loading   2 MW/m^2
Annual Neutron Fluence $\sim 1.3 \times 10^{26}$ n/m^2 [E > 0.1 MeV]
Incident Heat Flux ~ 0.01 MW/m^2
Steady State Operation   (i.e. noncyclic loading during normal operation)

The operating temperature range and expected annual neutron fluence are typical of the values normally anticipated for magnetic fusion energy systems. The purpose of the current section is to briefly describe the rationale which led to the selection of first wall/blanket structural materials and to present a description of the projected effects of the service environment on these materials.

Materials Selection

The current activities of the Office of Fusion Energy's "Alloy Development for Irradiation Performance (ADIP)" program emphasize the qualification and data base development for two types of structural alloys for near-term applications in magnetic fusion reactors. These two types are the austenitic stainless steels, typified by compositions close to that of type 316, and the high temperature ferritic/martensitic steels, represented by such alloys as HT-9 (a Cr-Mo-V steel). Major research and development efforts have been initiated to characterize and, ultimately, optimize alloys of these general classes for service in the harsh irradiation environments of fusion reactors.

In the case of the austenitic stainless steels, designated as Path A alloys under the ADIP program, the major efforts are currently focused on chemical and metallurgical variations of a composition designated as the "Prime Candidate Alloy" (PCA) which is a modified version of 20% cold-worked type 316 stainless steel. The major modifications involve additions of titanium and slightly adjusted values of Ni, Cr and Mo. Each of these changes

is intended to confer greater metallurgical stability - i.e. to control
void-induced swelling and to minimize radiation-induced phase changes and/or
precipitation. Irradiation experiments to date on this type of Ti-modified
type 316 stainless steel indicate a greater than tenfold decrease in swelling
compared to 20% CW 316 SS for fluences to about 1.3×10^{27} n/m^2 [E > 0.1
MeV].

The ferritic/martensitic steels, designated the Path E option in the ADIP
program, have been less well characterized for fusion reactor radiation
service than have the Path A stainless steels. However, these alloys, in
particular the HT-9 composition, have demonstrated impressive radiation damage
resistance in fast test reactor irradiations for the LMFBR program and have
recently been given broader attention and consideration for fusion reactor
applications. In addition to enhanced radiation resistance, these alloys have
thermophysical properties which result in lower thermal stresses (from
temperature gradients caused by high incident heat loads) than the austenitic
stainless steels. This latter factor is particularly important for pulsed
loading scenarios since this reduces the tendency for fatigue-related
phenomena or failures. Major remaining concerns with the Path E alloys are
associated with their more limited fabricability/weldability characteristics
(e.g. pre- and post-weld heat treatments of moderate and heavy section welds
are required) and the increase in the (impact energy) ductile-brittle
transition temperatures due to neutron irradiation.

A comprehensive discussion of the tradeoffs involved in selection between
the Path A and Path E alloys has been provided recently in support of the
STARFIRE commercial tokamak reactor design.[5] For the STARFIRE design the
assumption of steady state operation, even for a tokamak reactor with an
incident surface heat flux of 0.85 MW/m^2, permitted the selection of
austenitic stainless steel for the first wall and blanket structures. This
selection reflects a general consensus of the materials community; viz, that
if both an austenitic stainless steel or a ferritic steel appear adequate for
a given application the austenitic stainless steel is preferred on the basis
of greater experience and ease of fabrication and joining. In addition, from
a corrosion standpoint, liquid lithium is compatible[13] with 316 SS as long
as the operating temperature does not exceed 450°C for any appreciable time.

There are no peculiar or special characteristics of the central cell
region of the TMHR which imply more severe conditions than are expected in the

STARFIRE reactor. Hence, a modified 316 SS (or a version of the PCA composition) was selected for the first wall/blanket structural material of the TMHR.

IV.C.2.b. Radiation Effects and Component Lifetime. The first wall in the central cell region of the TMHR will operate between 400 and 450°C. For a nominal neutron wall loading of 2.0 MW/m^2 and a duty factor of 0.7, the annual fluence accumulated is therefore equivalent to 1.4 MW-yr/m^2. In terms of neutron fluence, this value is equal to approximately $1.5-2 \times 10^{26}$ n/m^2/year [E > 0.1 MeV], and will produce about 16 dpa and 200 appm helium in the PCA alloy.

In the STARFIRE design study[5] for an incident heat flux of 0.85 MW/m^2 and a steady state neutron wall loading of 3.5 MW/m^2, it was concluded that the PCA alloy could successfully achieve a lifetime fluence of 20 MW-yr/m^2 at a nominal maximum temperature of about 450°C. This conclusion was based on a careful analysis of the swelling and total plastic strain which would occur as the result of the combined thermal and neutron radiation. As noted previously, the very low incident heat loads anticipated in the central cell region of the TMHR imply less severe thermal stresses/strains than for the STARFIRE first wall. Hence, it is likely that the 20 MW-yr/m^2 fluence equivalent should be attainable in the TMHR. This predicts a service lifetime of about fourteen years for the central cell first wall and blanket structure due to radiation damage.

Based on the analyses reported in the STARFIRE study, Table IV.C-1 summarizes the expected response of the TMHR first wall to the radiation environment.

Barring some unforeseen or off-normal event which could cause the metal temperature to exceed about 600°C for a period of time greater than about an hour, the helium produced by irradiation is not expected to compromise the mechanical integrity of the first wall/blanket structural material.

TABLE IV.C-1. Predicted response of the first wall material to the radiation environment.

| Service Time (yrs) | Approx. Fluence | | Response | |
	MW-yr/m^2	n/m^2 [>0.1 MeV]	Swelling $\Delta V/V$ (%)	appm He
5	7.0	$\sim 7.5 \times 10^{26}$	0.25	1015
7	9.8	$\sim 1.0 \times 10^{27}$	0.5	1420
10	14.0	$\sim 1.5 \times 10^{27}$	0.95	2030
14	20.0	$\sim 2.0 \times 10^{27}$	1.6	2900

IV.D. NUCLEAR FUEL PRODUCTION AND POWER GENERATION

IV.D.1 Methods and Codes

A variety of approaches were taken in the nuclear analysis of the liquid metal cooled blanket, but the primary tool was the Monte Carlo transport code TARTNP[14,15] developed at LLNL. TARTNP is capable of transporting both neutrons and neutron-induced gammas. In this application only neutrons were transported and photon energy was assumed to be deposited locally. TARTNP provides a flexible multi-dimensional geometry modeling capability and, in the case of the TMHR liquid metal blanket, a two-dimensional cylindrical model was used.

A large number of different neutron tallies can be generated with TARTNP. These include all the different reaction rates (i.e., expected collisions) for individual nuclides, energy transported into a zone, zone surface fluxes, and many angular distributions. The reaction rate tallies and energy deposition per zone were of greatest interest in the TMHR analysis. In some instances surface fluxes were also generated. TARTNP allows up to 110 zones, and reaction rate profiles can be easily generated.

Batch statistics in each zone for each tally type (i.e., total reaction rate tallies, energy depositions, or surface flux) are calculated by TARTNP. These help to optimize the total numbers of neutron histories required and determine whether any particle splitting (i.e. biasing) from zone to zone is necessary. For reaction rates or flux spectrums in deep penetration problems the particle splitting technique is necessary, but for most of the analysis done for TMHR blankets, acceptable reaction rate statistics do not require particle splitting. As few as 5000 particle histories were used for scoping cases, and as shown in Table IV.D-1, 20,000 histories usually produced results sufficiently precise for design.

Acceptable statistics result for relatively few histories because most reactions which are significant to blanket performance (i.e., tritium breeding, fissile fuel production, fissions, overall energy deposition) occur with large frequency (i.e., 0.01-1.0 per fusion neutron) in large spatial zones. Shielding and some radiation damage calculations (e.g., displacements per atom and gas generation in Hastelloy) require a greater number of histories or Monte Carlo biasing techniques to achieve an acceptable level of

TABLE IV.D-1. Typical TARTNP reaction statistics.

	Reaction		
	$^6Li(n,\alpha)T$	$^7Li(n,n'\alpha)T$	$^{233}Th(n,\gamma)$
Number of Fusion Neutrons	20,000	20,000	20,000
Number of Reactions	7,800	13,200	10,600
Percent Standard Deviation*	1.1	0.87	0.97

*defined as (number of reactions)$^{-1/2}$ according to Poisson counting statistics

accuracy. Also, the division of a problem into a large number of smaller zones requires an increase in the total number of particle histories followed in order to get precise reaction rate profiles in each zone.

TARTNP is part of the UCRL-50400 series which is an integrated, computer-oriented system for the production of neutronics and photonics constants and analysis of radiation transport problems. Another product of this system, the ENDL library[16] of neutron and photon constants, is the basis of multigroup set which TARTNP uses. The TARTNP cross section set of 175 neutron and 143 photon energy groups was processed using the ENDL library and the CLYDE code[17]. In most cases, the source ENDL library set is similar to the better known ENDF/B-V library[18]. However, in the case of the lithium/molten salt blanket, a slightly lower $^7Li(n,n't)$ cross section ($\sim 25\%$) and some other less significant differences are included.

In general, for the lithium blanket analysis, it is felt that the ENDL cross section set and the TARTNP code have produced a precise set of reaction rate and flux spectrum estimators. Further discussions of variations in the cross section data set are in Sections IV.D.3. A brief description of the various nuclear analyses which were done as part of the TMHR study follows. Most of this work is treated in greater detail elsewhere. A summary of the nuclear analysis by section of this report includes:

- Lithium blanket design and scoping analysis (IV.D)
- Beryllium blanket design and scoping analysis (V.B)
- Beryllium radiation damage studies (V.C)
- Hastelloy neutron damage studies (IV.G)
- UO_2 fertile fuel option for beryllium blanket (V.G)
- Isotopic generation studies for safety analysis (VI)
- Actinide buildup and decay studies for fuel cycle analysis (VII)
- Neutronics performance of alternate designs (Appendices A and B)

IV.D.2. Reference System Performance

The reference blanket concept utilizing liquid lithium and molten salt was initially analyzed in a one-dimensional configuration with the TARTNP Monte Carlo code to estimate the nuclear performance. A schematic diagram of this one-dimensional cylindrical geometry model and the material volume fractions of the various zones are shown in Figure IV.D-1. The lithium in this blanket was depleted to 0.2% ^{6}Li, and the molten salt composition was 72 mole percent LiF, 16 mole percent BeF_2, and 12 mole percent ThF_4, with the lithium in the molten salt also being depleted to 0.2% ^{6}Li. Because of the importance of the ^{7}Li (n, n' t) breeding reaction in this blanket design, all the TARTNP calculations were performed with a recently evaluated (Dec. 1980) data set that included the revision of the ^{7}Li cross section to a lower value than was used in previous studies. A sufficient number of neutron histories were run with TARTNP to produce statistics of a few percent or less.

The results for this one-dimensional calculation at beginning-of-life (BOL), i.e. with no ^{233}U present in the blanket, gave the following results for F (the net number of fissile atoms produced per fusion neutron), T (the tritium breeding ratio), E (the energy deposited in the blanket per incident fusion neutron), M (the energy multiplication factor = E/14.1), and the leakage per fusion neutron:

$$T = 1.13$$
$$F = 0.51$$
$$T+F = 1.64$$
$$E = 17.0 \text{ MeV}$$

Plasma

200 cm →

63.35 cm

1.6% Steel

98.4% Li

15 cm

6.7% Steel

93.3% Salt

65 cm

100% Salt

Steel
Wall,
0.76 cm

Steel
Wall,
0.89 cm

Steel
Wall,
3.8 cm
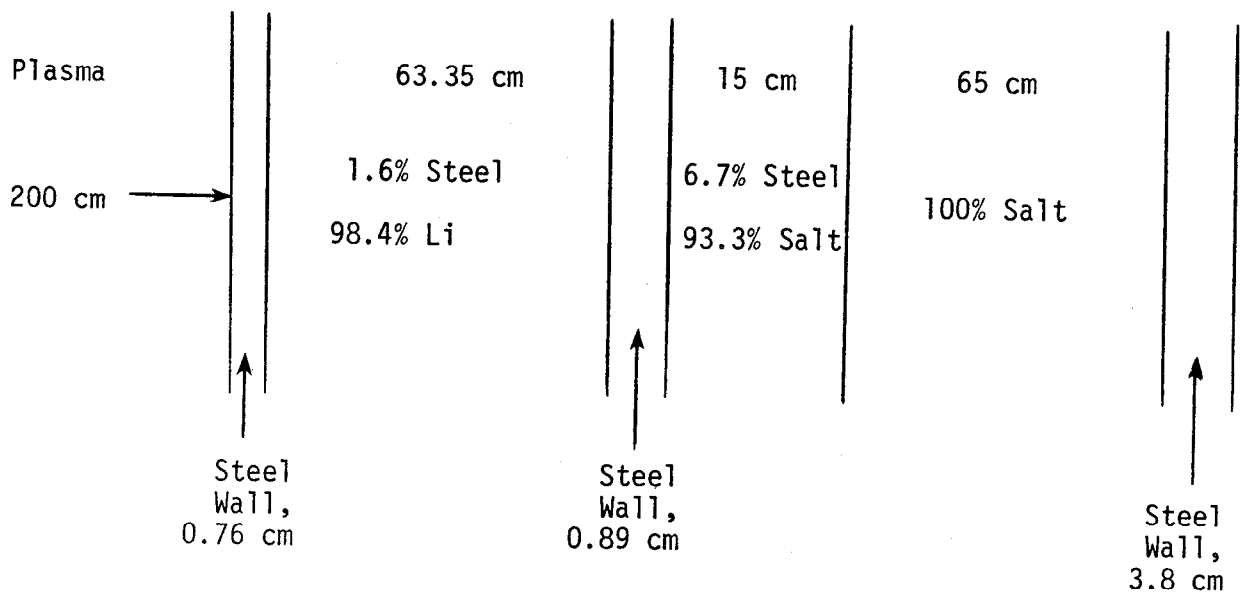
FIG. IV.D-1. Schematic Diagram of one-dimensional neutronic model used for TARTNP neutronics calculations (not to scale).

M = 1.21

Leakage = 0.0002

The tritium production from the ^{7}Li was T_7 = 0.66 and from ^{6}Li was T_6 = 0.47, including a tritium production of 0.05 from the lithium in the molten salt, almost all of which was from ^{6}Li. Since this blanket has too high a T value, various adjustments in the zone thickness and/or material compositions would be required. For example, decreasing the front lithium zone thickness from the 63 cm assumed in the analysis would decrease T and allow F to increase by increasing the neutron leakage into the salt zone. However, such modifications were not pursued for the one-dimensional analysis because the reference module concept with its non-axially symmetric configuration clearly required a two-dimensional analysis. As discussed below, a new TARTNP geometry model was established and used for further neutronic analyses of the reference blanket.

The TARTNP two-dimensional geometry model and zone material compositions used to analyze the reference module configuration are shown in Figure IV.D-2. As the figure shows, an individual blanket module of length 6.4 m was modeled in cylindrical geometry with a 50 cm thick lithium zone, a 0.5 cm thick first wall of stainless steel, and a 0.8 cm thick stainless steel wall between the lithium and molten salt zone. The molten salt zone was 80 cm thick, with the first 15 cm containing 6.7% (by volume) steel to account for structural ribbing. The salt zone was centered in the module with a width of 490 cm, as shown in the figure, with lithium inlet manifold zones of width 75 cm on either side of the salt zone. These manifold zones are two-thirds void due to the discrete lithium inlet and outlet pipes, which may result in a potential loss of neutrons out the back of module. For the TARTNP calculations a reflecting boundary condition was imposed on the left and right surfaces of the module in Figure IV.D-2, and a vacuum boundary was used at the rear of the module behind the final 4 cm thick wall. For the analysis, all lithium including that in the molten salt was depleted to 0.2% ^{6}Li; and the salt composition was 72 mole percent LiF, 16 mole percent BeF_2, and 12 mole percent ThF_4.

Because the molten salt blanket allows the continuous reprocessing and removal of the bred ^{233}Pa and ^{233}U produced, there will be some equilibrium concentration of the Pa and U in the salt that will be built-up
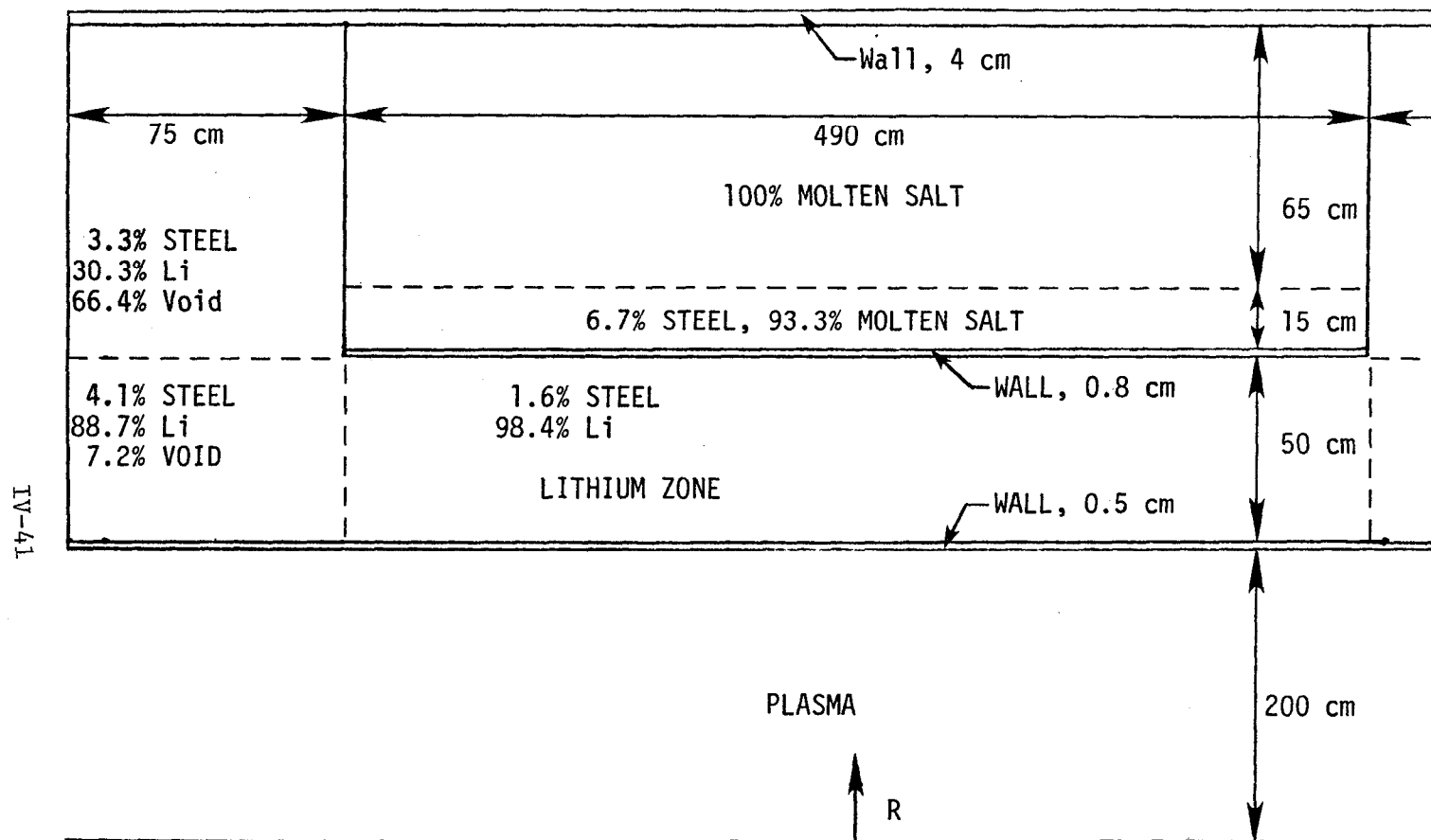
FIG. IV.D-2. TARTNP 2-D module geometry for the molten salt-lithium blanket concept (not

and then maintained. This concentration or enrichment will be dependent on such parameters as the irradiation time before the removal process is initiated, the rate of salt removal from the blanket for processing, and the salt inventory in pipes and hold-up tanks outside the blanket. While these parameters are variable so that the equilibrium Pa and U values can be adjusted, a typical set of conditions as outlined below resulted in an equilibrium concentration of 0.11 percent ^{233}U in Th as the reference blanket operating condition. This is equivalent to a salt composition of 0.013 mole percent ^{233}UF$_4$.

IV.D.2.b. <u>Fissile Production and Tritium Breeding</u>. A summary of the calculated neutronics performance for the two-dimensional geometry model is shown in Table IV.D-2. As the table shows, the calculated tritium breeding ratio T is 1.04 for the geometry and composition shown in Figure IV.D-2, and the net fissile production F is 0.53. The neutron leakage is fairly high at 0.07 neutron per incident fusion neutron. These values can be compared with the one-dimensional results discussed previously, which gave T+F = 1.64 and a leakage of 0.0002. The lower T+F value of 1.57 for the two-dimensional calculation appears to be primarily due to the increased leakage, since the tritium production, or neutron "multiplication", from the ^{7}Li reactions is the same for both calculations, as would be expected since the composition of the front lithium zone is nearly the same.

A breakdown of the calculated neutronics performance by major regions for the two-dimensional geometry calculation is shown in Figure IV.D-3. As the figure shows, the center region of the front lithium zone results in T = 0.74, while the two end regions have T = 0.21 and the two manifold end regions give T = 0.04. The tritium production from the molten salt region is 0.05, eighty percent of which is from ^{6}Li; and the net fissile production value F is 0.53. A breakdown of the neutron balance for this blanket configuration at beginning-of-life (zero ^{233}U enrichment) is shown in Table IV.D-3. As the table shows, there is a fairly low amount of parasitic absorption in the SS structure and other materials which is just about offset by neutron multiplication through (n,2n) and (n,3n) reactions in the same materials.

Although the 2-D results for a single reflected module discussed above would be correct for a cylindrical blanket of infinite extent, the TMHR blanket is 95 m long and the significant neutron leakage out the vacuum vessel

$T = 0.04$

$T_6 = 0.04$
$T_7 = 0.01$
$T = 0.05$
$F = 0.53$

MOLTEN SALT
ZONE

$T_6 = 0.07$
$T_7 = 0.14$
$T = 0.21$

$T_6 = 0.25$
$T_7 = 0.49$
$T = 0.74$

LITHIUM ZONE

PLASMA

R

FIG. IV.D-3. Neutronics performance breakdown by zone for the molten salt-lithium bla

TABLE IV.D-2. Neutronics performance for the reference lithium-molten salt blanket.

	Calculated	Adjusted*
^{233}U enrichment	0.11%	0.11%
T_6	0.382	0.389
T_7	0.661	0.661
T	1.043	1.050
^{232}Th (n,γ)	0.555	0.519
^{233}U (n,γ)	0.004	0.004
^{233}U fissions	0.024	0.024
F = net fissile	0.527	0.491
T + F	1.570	1.541
E	21.3 MeV	21.3 MeV
M	1.51	1.51
Leakage	0.069	0.069

*See later discussion

to the end cells requires modeling. As shown in Table IV.D.4, both T and F (for a blanket geometry similar to, but not identical to the blanket shown in Figure IV.D-2) decrease for a non-reflected case which considers end cell leakage.

The above results may be used to better predict the expected performance of the lithium/molten salt blanket. In particular, adjusting the calculated value of T+F value of 1.57 for end leakage by the ratio of the unreflected to reflected T+F (i.e., 1.50/1.53) gives an improved estimate of T+F = 1.541.

Two additional adjustments are required to better define the necessary tritium breeding ratio. First, for the axicell end plug configurations being considered, about 80 MW of fusion power is produced in the plugs. Since no tritium breeding blanket is assumed to exist in this region, additional tritium must be produced in the central cell blankets. For a 3000 MW fusion central cell the excess tritium breeding factor would 1.027 (= 3080/3000). Finally, some excess tritium is required to account for losses and

TABLE IV.D-3. Neutron balance table for the lithium-molten salt blanket at beginning-of-life conditions (all values are per fusion neutron).

Neutron Sources

Plasma Fusion Neutron	1.0
Th, Be, F, Li, SS* (n,2n) & (n,3n)	0.115

Neutron Sinks

^{6}Li (n,α) T	0.383
^{232}Th (n,γ)	0.532
Leakage	0.069
^{232}Th fissions	0.0026
SS* absorptions	0.111
F, Be, ^{7}Li absorptions	0.022

*SS = stainless steel, composed of Fe, Ni, Cr, and Mo.

Table IV.D-4. Lithium blanket end cell streaming.

END CELL MODEL	T	F	FISSIONS	END CELL LEAKAGE	BACK WALL LEAKAGE	M_F	T+F
Reflected	1.232	.294	.0052	---	.02	1.24	1.53
Non-Reflected	1.225	.273	.0055	.0442	.02	1.22	1.50

uncertainties. If we assume that 2.2% net excess tritium is required, then the central cell tritium breding ratio requirement is 1.050. Subtracting the required tritium breeding ratio from the adjusted T+F value above results in a decreased F value of 0.49.

These adjusted performance parameters are presented in Table IV.D-2 and are used throughout the report. Relating these results back to the calculational model, a very minor design iteration is required to achieve performance very close to the adjusted values. Namely, the ^{6}Li enrichment would be enriched slightly (to perhaps 0.25% from 0.20%) to provide a 1.05 tritium breeding ratio after end leakage. The expected fissile breeding ratio would be 0.49, the adjusted value.

The power densities during operation can be computed from the neutronics results for an assumed value of the neutron wall loading. For example, the average power density in the lithium front zone is about 2.8 W/cm^3 and the peak is about 4.5 W/cm^3 for a first wall loading of 2 MW/m^2. The power density in the first wall is about 20 W/cm^3, and in the wall between the lithium and the molten salt it is about 5.2 W/cm^3. The average power density in the molten salt region is comparatively low at approximately 1.3 W/cm^3.

A critical feasibility issue of the reference design is the ability to maintain a frozen layer of molten salt on the walls of the zone for protection of the surfaces from corrosion. To determine the feasibility of maintaining this layer, the power density in the first two centimeters of the salt zone was estimated as a function of irradiation time. The results are shown in Figure IV.D-4. While the overall salt zone power density is relatively low at about 1.3 W/cm^3, the power density in the first 2 cm of the salt zone is initially around 5 W/cm^3, (as shown in the figure) and increases steadily with irradiation time as the ^{233}U builds up. These power densities were then used in the thermal hydraulic design calculations discussed in Section IV.E to estimate the feasibility of maintaining and controlling the frozen salt layer.

IV.D.2.c. Energy Deposition. The two dimensional calculation results shown in Table IV.D-2 indicated a total energy deposition E in the blanket of 21.3 MeV per incident fusion neutron for a fusion neutron energy multiplication factor M of 1.51. The total power produced in the reactor can then be calculated from the M value and an assumed value for the total device fusion
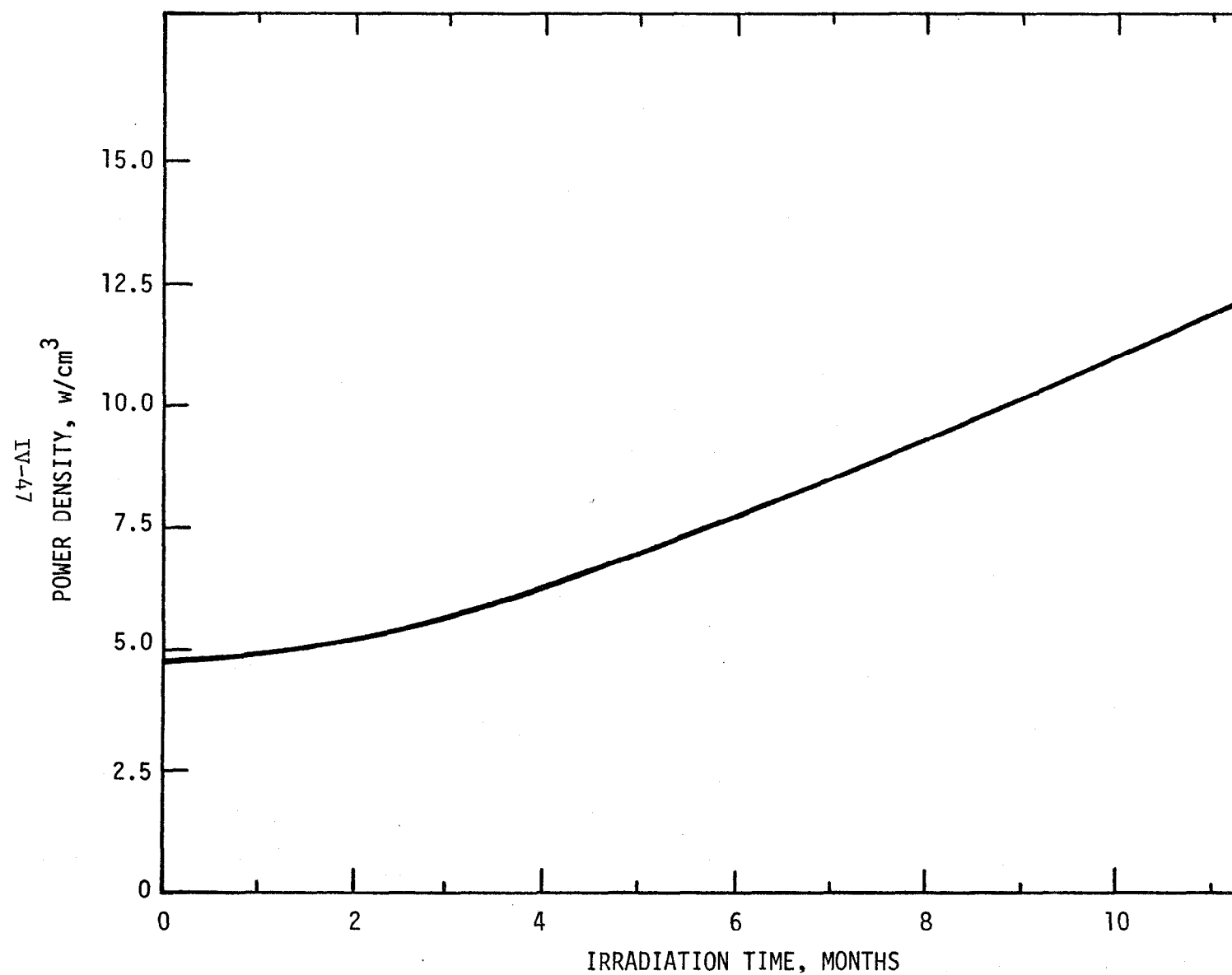
FIG. IV.D-4. Effect of neutron exposure on the power density in the frozen salt laye
(2 cm thick frozen layer assumed).

power produced, P_{fus}. Also, from the TARTNP calculation the power production from the various zones can be estimated, which is an important factor in the design of the heat transport system as discussed in Section IV.E. The total reactor nuclear or thermal power is calculated as:

$$P_{nucl} = 0.2 \times P_{fus} + P_{neut} \times M$$

where $P_{neut} = 0.8 \times P_{fus}$ = D-T fusion neutron power.

For example, with M = 1.51 and P_{fus} = 3000 MW, P_{neut} = 2400 MW and P_{nucl} = 4220 MW. The calculation from TARTNP indicated that about 39% of the total energy deposition is in the molten salt zone and the walls around the zone, while the remaining 61% is deposited in the inner lithium zone and the first wall. Furthermore, about 21% or 4.6 MeV of the total energy deposited (21.3 MeV) comes from fission reactions in the Th and ^{233}U, with the remainder resulting from exothermic reactions mainly in the Th and ^{6}Li. The total power production and a breakdown by region is shown in Table IV.D-5 for two different assumed fusion power levels, 2000 MW and 3000 MW. For a neutron wall loading of 2 MW/m^2, the central cell length is 64 m for a fusion power of 2000 MW, and the total nuclear power is 2820 MWt. Using the adjusted T and F value, such a reactor would produce fissile material in the form of ^{233}U at the rate of 2970 kg/yr with the reference blanket concept. The larger size reactor with 3000 MW of fusion power produces 4220 MWt nuclear and 4452 kg/yr of ^{233}U. The above values assume a 70% average plant capacity factor. Detailed parametric systems studies based on this reference lithium-molten salt blanket concept are presented in Chapter IX of this report.

IV.D.2.d <u>Variations with Enrichment.</u> The two-dimensional neutronics results presented thus far have been for an enrichment of 0.11% ^{233}U in Th. This value is dependent on a number of parameters, such as the salt processing rate, the irradiation time before the processing is initiated, and the total salt inventory both in the blanket and in pipes and hold-up tanks outside the blanket. For a 96 m long central cell with 3000 MW of fusion power consisting of fifteen blanket modules, the blanket molten salt volume is about 1050 m^3. If there is in addition about 10% of the blanket volume in piping and tanks external to the blanket, then the total salt inventory is about 1150 m^3, or about 3860 MT. The rate of ^{233}Pa production from this reactor with

TABLE IV.D-5. Total reactor power production from the lithium-molten salt blanket for two different fusion powers.

Fusion Power, MW	2000	3000
Neutron Wall Loading, MW/m^2	2.0	2.0
Central Cell Length, m	64	96
Fusion Neutron Power, MW	1600	2400
Alpha Power, MW	400	600
Blanket Multiplication M	1.51	1.51
Total Nuclear Power, MWt	2820	4220
Power in Lithium Zone, MWt	1470	2210
Power in Molten Salt Zone, MWt	942	1410
Power from Th + U Fissions, MWt	524	786

3000 MW of fusion power is about 0.202 g/s. Using these values, the production and decay of the key isotopes in the chain

$$^{232}Th \ (n,\gamma) \longrightarrow \ ^{233}Th \ \xrightarrow{22.2 \ m} \ ^{233}Pa \ \xrightarrow{27 \ d} \ ^{233}U$$
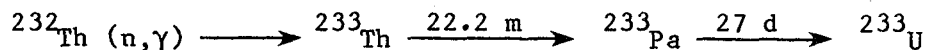
were calculated by solving the applicable differential equations to compute the density and enrichment variations as a function of irradiation time.

Two cases are of interest. In the first case, the TMHR operates without molten salt reprocessing to recover the bred ^{233}U for a fixed period of time. This case, shown in Figure IV.D-5, corresponds to a batch irradiation which represents the time period required to reach isotopic equilibrium conditions before the reprocessing plant is activated. As shown in the figure, under these conditions about 6 months are required to breed in the design basis ^{233}U concentration of 0.11% in thorium. As shown in the detailed insert of the above figure, ^{233}Pa builds up and equilibriates very quickly while about 2 months are required before the concentration of the ^{233}U daughter is greater than that of the ^{233}Pa parent.

In the second case, the TMHR operates from the time of initial startup with molten salt reprocessing to recover bred ^{233}U only (i.e., the
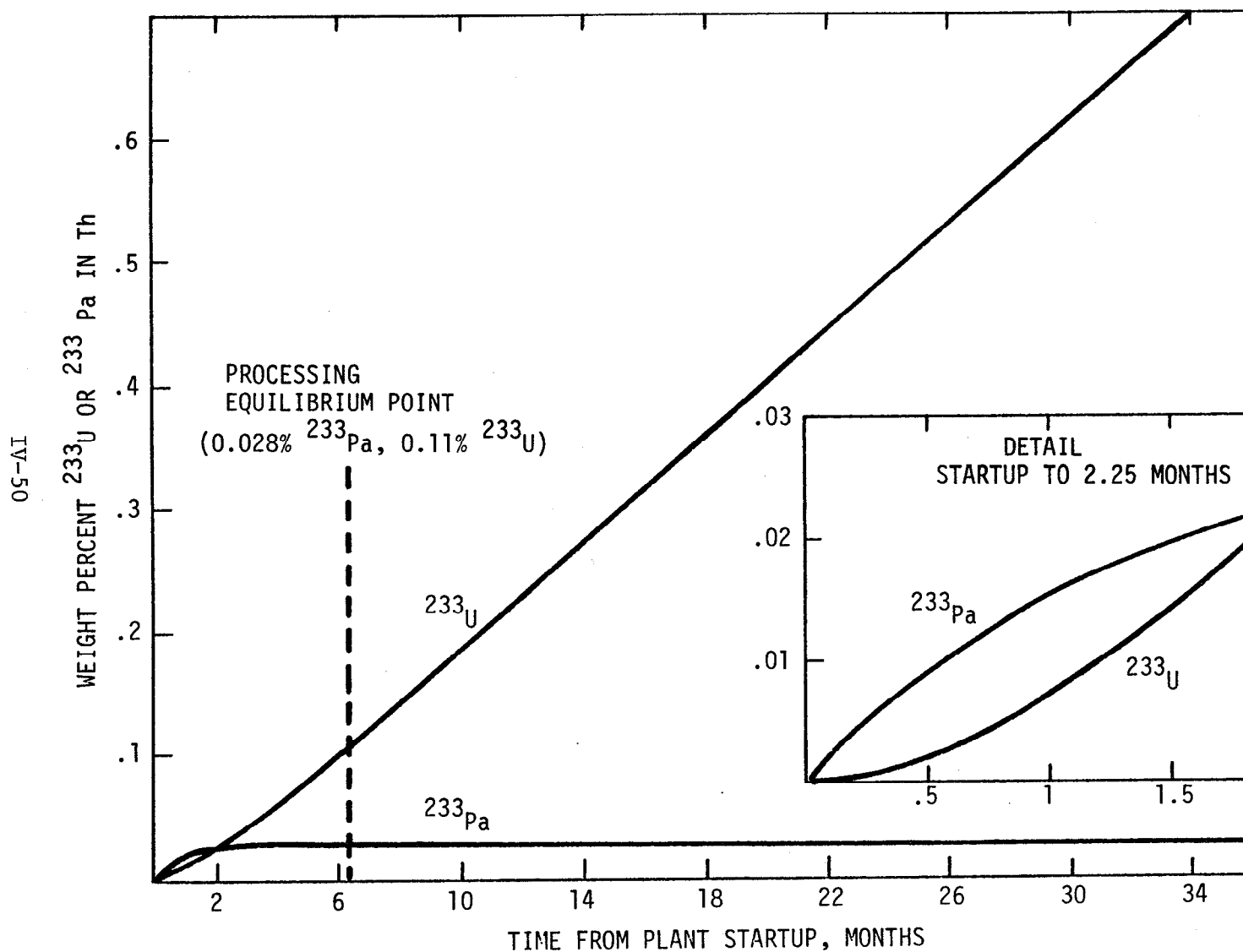
FIG. IV.D-5. Molten salt blanket enrichment as a function of time (70% average plan capacity factor, no molten salt reprocessing).

flourination only reprocessing plant discussed in Section VII.B). The results from this analysis more fully described in Chapters VI and VII indicate that the ^{233}Pa builds up quickly to an equilibrium value of about 0.03% in thorium while the ^{233}U requires about 2 years to reach the equilibrium design basis of 0.11% in thorium. A process rate of 0.46 m^3/hr (maximum recovery efficiency = 75%) is required to achieve the above equilibrium point. Since a continuous, or quasi-continuous, reprocessing mode minimizes the required inventories of ^{233}U ($\sim$ $80/gm) and molten salt ($\sim$ $1.66 x 10^5 per m^3) relative to a batch reprocessing mode, the former is perceived to be economically advantageous.

From the discussions above, it is clear that the enrichment values at equilibrium can be varied by making different assumptions regarding the salt processing rate and exposure time. While an enrichment of 0.11% was chosen for this study as the equilibrium point, it was also of interest to compute the blanket neutronics performance at other enrichment values to see if the total blanket breeding rate (T+F) was significantly impacted. The results from the two-dimensional analyses with three different enrichments - zero, 0.11% (reference), and 0.83% ^{233}U in Th - are compared in Table IV.D-6. As the table shows, there is no change in the T+F values as the enrichment varies, although there clearly is an increase in the energy multiplication. The leakage increases only slightly as the enrichment is increased. The reason the net F value remains constant is that the larger Th capture rate due to increased neutron production from fissioning of ^{233}U is offset almost exactly by the increased neutron absorptions in the ^{233}U itself, so that the net fissile atom production rate stays the same.

Hence it appears that the equilibrium enrichment value that is chosen will not change the fuel production rate, although clearly it will affect the power production from the reactor.

IV.D.3 Sensitivity and Uncertainty Effects

Some discussion about uncertainty and sensitivity effects in the lithium blanket is useful to reveal what cross section uncertainties are important in the lithium blanket, and what directions of future work will be useful. Three key uncertainties are especially important: the ^{7}Li(n,n't) ^{232}Th(n,γ), and ^{6}Li (n,t) cross sections. Obviously, the values of these three cross sections will determine the key blanket performance indices: T and F.

TABLE IV.D-6. Variation in performance of the lithium-molten salt blanket with different fissile enrichments.

	Enrichment, ^{233}U in Th		
	0.0	0.11%	0.83%
T_6	0.38	0.38	0.39
T_7	0.66	0.66	0.65
T	1.04	1.04	1.04
F (Net)	0.53	0.53	0.53
T + F	1.57	1.57	1.57
Leakage	0.069	0.069	0.076
M	1.21	1.51	1.73

The $^7Li(n,n't)$ cross section is very important in the lithium blanket because the major portion of the tritium breeding takes place in ^7Li. The ENDL cross section set used in the analysis of the lithium blanket contains a revised (smaller by about 25%) $^7Li(n,n't)$ cross section and this results in about 10% less total breeding than a model based upon ENDF/B data. This also indirectly affects other aspects of blanket performance because less tritium breeding takes place in ^7Li and neutron absorption in ^6Li is increased. Future work should concentrate on ^7Li cross section uncertainties to determine the sensitivities of individual designs to variation in the $^7Li(n,n't)$ reaction.

IV.D.4. Additional Neutronics Studies Performed

Two main additional neutronics studies were performed for the purpose of understanding the key sensitivities in the reference design described previously, and for the purpose of attempting to improve the neutronics performance over the reference concept. The first study simply involved a deletion of the first wall in order to determine how much the performance could be improved in an "ideal" case. The second study involved the use of some beryllium (Be) in the blanket in an attempt to increase the blanket performance by improved neutron multiplication.

The results for the hypothetical zero thickness first wall are compared
with the reference case performance with an equivalent wall thickness of 0.5
cm in Table IV.D-7. Both cases were done with the two-dimensional module
geometry shown in Figure IV.D-2, and all zone thicknesses and compositions
were identical except for the deletion of the first wall. As the table shows,
for no first wall the T value increases to 1.11, mainly because of the higher
^{7}Li tritium production value T_7. The T+F value increases by 0.08, so that
the F value at the same T of 1.04 increases by about 15% for the zero wall
case. Hence there clearly is a strong motivation for decreasing the first
wall to as thin a value as possible consistent with thermal hydraulic and
structural constraints. From Table IV.D-7, the sum of T+F plus the leakage is
about 1.72, which is within about 4% of the theoretical maximum[19] of
approximately 1.8 for an infinite medium of depleted lithium with no
structural material. This slight difference between the no first wall case
and the theoretical limit is due to the presence of some structure in the
blanket, particularly the 0.8 cm equivalent thickness wall between the lithium
and molten salt zones. Hence, the reference blanket design performance is
very nearly the highest possible consistent with mechanical and thermal design
considerations. The limiting factor in the neutronic performance is really
the neutron "multiplying" properties of the ^{7}Li (n, n' T) reaction.
Therefore, an attempt was then made to improve the performance by using a
better neutron multiplier, namely Be.

TABLE IV.D-7. Effect of zero first wall thickness on the performance of
the lithium-molten salt blanket.

| | First Wall Thickness, cm | |
	0.0	0.5
T_6	0.39	0.38
T_7	0.72	0.66
T	1.11	1.04
F (Net)	0.54	0.53
T + F	1.65	1.57
F with T = 1.04	0.61	0.53
Leakage	0.072	0.069

The study with Be added involved a TARTNP analysis in the two-dimensional geometry configuration in which the first 20 cm of the lithium zone just behind the 0.5 cm thick first wall was replaced with a layer of 20 cm of solid Be. The results from this case gave T = 1.26 and F = 0.24, for T + F = 1.50. Hence, the performance was actually decreased from the reference case where T + F = 1.57. This decrease with the Be zone was not due to a larger leakage, since the leakage value of 0.031 was only about half that in the reference case. The reason the performance was decreased was that an extremely high number of neutrons, nearly 0.5, were being absorbed in the first wall. This was because the neutrons being produced in the Be layer via the (n,2n) reactions were then moderated by the Be and a large number of them simply were reflected back toward the first wall where they were absorbed. There was a large amount of neutron multiplication with the Be, so that the total number of neutrons available in the blanket was close to 2.0, which would be a significant increase over the reference blanket performance using ^{7}Li. However, the problem is to get these neutrons to be absorbed in Li and Th and not in the structure or wall. A method for accomplishing this would be to put a small amount of Li or Th in the Be zone to absorb the neutrons before they can be reflected and absorbed in the first wall. This technique leads to a single zone type of blanket configuration which is similar to the approach used for the helium cooled blanket with Be discussed in Chapter V. A possible blanket of this type employing a packed bed blanket with a beryllium multiplier and using liquid metal coolant is briefly discussed in Appendix A. Alternate ways to improve the performance of the reference blanket concept using Be would be to have a relatively thin (perhaps 5 to 10 cm thick) layer of lithium between the first wall and the Be zone. Such approaches should allow the neutrons to be absorbed in the lithium and not in the wall, providing that thermal and mechanical design constraints could be met for the blanket design. Due to time restrictions, such blankets were not pursued further within the scope of this year's study. However, they should be the subject of future analyses to determine the viability of this approach. Possible additional methods to improve the performance of the reference concept other than using beryllium are discussed in the following subsection.

IV.D.5. Overview and Additional Studies Required

The neutronics analyses of the lithium-molten salt blanket concept has shown that for a 50 cm thick front zone of lithium depleted to 0.2% ^{6}Li, the calculated tritium breeding ratio (T) was 1.04 and the fissile atom production per fusion neutron (F) was 0.53. For an equilibrium enrichment of 0.11% ^{233}U in Th in the molten salt, the blanket energy multiplication (M) is about 1.5. It was also found that the nuclear fuel production performance did not change with the enrichment, although the blanket M did change slightly. While the blanket performance of T + F = 1.57 was adequate, it would be desirable to increase this if possible. Possible improvements through the use of a better neutron multiplier, e.g. Be, were discussed in the previous subsection. Aside from this, the most fruitful way to attempt to improve the performance of the reference blanket concept would appear to be to reduce the neutron leakage from the back of the blanket.

The design currently has a leakage of about 0.07 neutrons. If this leakage could be prevented so that these neutrons could be absorbed in thorium, the F value could be increased by up to 13 percent. The principal reason for this leakage is the lithium manifold (piping) regions on both ends of the module, which effectively allow many neutrons to stream out of the blanket after penetrating through 50 cm of lithium. If a moderating material such as graphite could be incorporated in these piping regions, it is likely that the leakage would be decreased and the breeding performance would improve. The possible use of moderating materials to decrease the leakage should be the subject of additional studies.

There are various other techniques that could be explored to attempt to optimize the blanket performance. For instance, a lower ^{6}Li isotopic concentration in the front zone, possibly coupled with a thicker front lithium zone, may slightly improve the performance[2]. Also, the use of a different molten salt with higher ThF$_4$ composition might be beneficial. Both of these variations would likely result in only very small improvements, but they should be the subject of additional studies to optimize the performance of the reference blanket. As discussed in the previous subsection, the blanket performance is relatively sensitive to the first wall thickness; hence, any possible reduction in the wall thickness should also be explored.

IV.E.   THERMAL HYDRAULIC DESIGN

Introduction

Thermal hydraulic calculations were performed to support the development of the reference liquid metal cooled-molten salt blanket concept. Special attention was given to the effect of the magnetic fields on the liquid lithium pressure losses because of the important impact the coolant pressure has on the blanket structural requirements, which in turn has significant effects on the neutronic performance. Detailed thermal analysis was performed on the characteristics of the frozen salt layer, a key consideration in protecting the blanket molten salt containment structure from the corrosive action of the molten salt.

A simplified schematic diagram of the flow systems of the liquid metal cooled blanket TMHR is presented in Figure IV.E-1 along with the system state points. The system state points and other related blanket parameters are summarized in Table IV.E-1.

IV.E.1.   Liquid Lithium Primary Loop

The liquid lithium primary loop consists of the inner zone of the blanket, the lithium-sodium intermediate heat exchanger, the lithium pump and the associated piping. The maximum lithium temperature exiting from the blanket was set at 390°C. This was based on both temperature limitations in the stainless steel module wall and on the need to maintain a frozen salt layer whose thickness is a function of the lithium temperature. The coolant temperature rise was set at 170°C. This was the maximum possible, given the melting point of lithium of 180°C. It is desired to maximize the lithium coolant temperature rise so that the coolant velocity, and hence the MHD losses, can be minimized.

IV.E.1.a.   Pressure Drop in the Liquid Lithium Loop. It is commonly recognized that the use of liquid lithium as fusion reactor blanket coolant/tritium breeder has a large number of advantages; however, it is also known that its use in magnetically confined fusion reactors would encounter serious difficulties because of the magnetohydrodynamic losses that could result in high coolant pressures and high coolant pumping power. Both factors
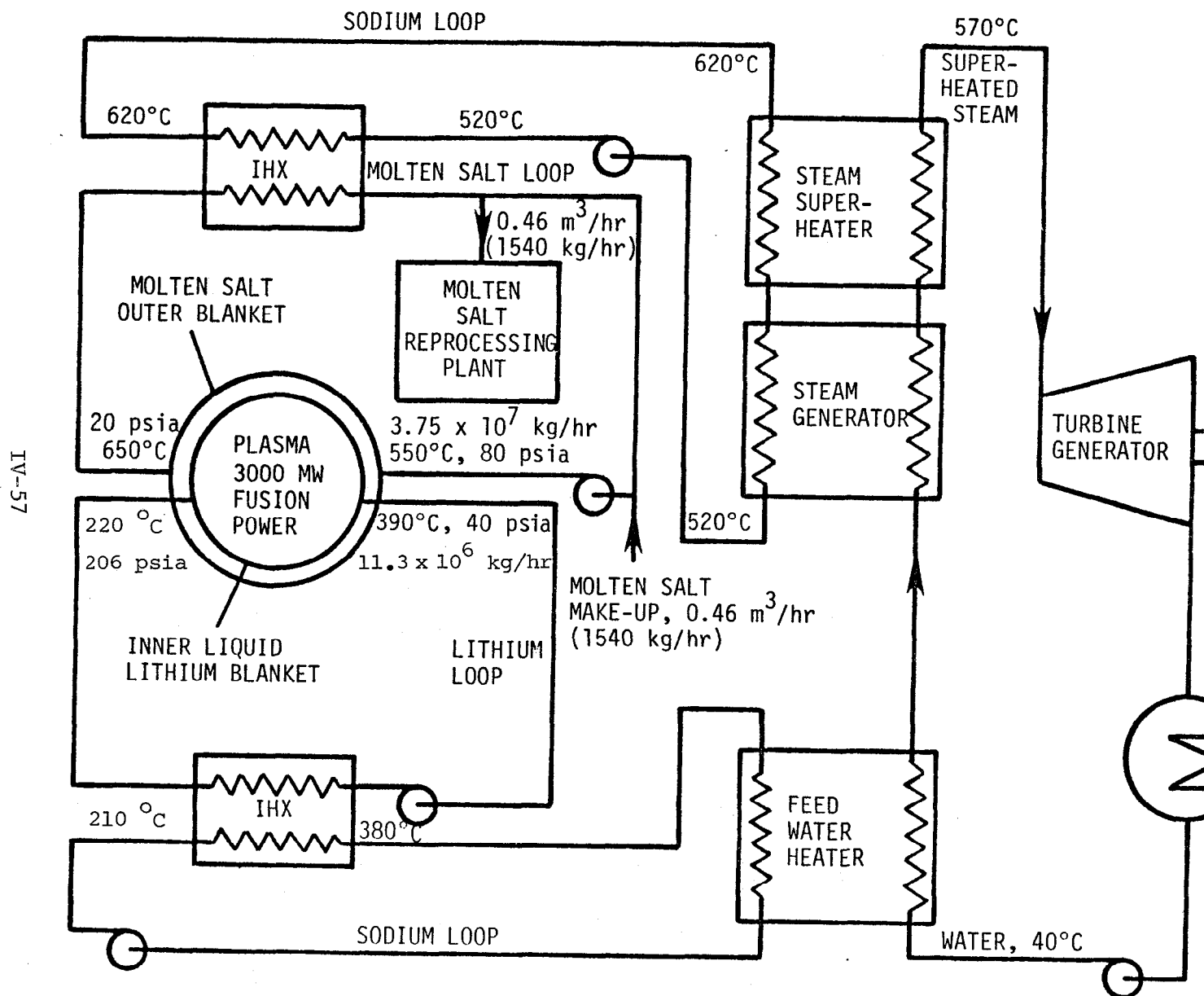
FIG. IV.E-1. Simplified system flow diagram for the TMHR liquid lithium-molten salt blan

TABLE IV.E-1. Preliminary primary loop & BOP system state points for the liquid metal cooled blanket

---

Molten Salt

Blanket Inlet Temperature	=	550°C
Blanket Exit Temperature	=	650°C
Blanket Inlet Pressure	=	∿ 20 psia
Blanket Exit Pressure	=	∿ 80 psia

Liquid Lithium

Blanket Inlet Temperature	=	220°C
Blanket Exit Temperature	=	390°C
Blanket Manifold Inlet Pressure	=	206 psia
Blanket Manifold Exit Pressure	=	40 psia
Total Pressure Drop Through Blanket	=	166 psi

Steam Cycle (Double Reheat)

Steam Temperature	=	570°C
Steam Superheat	=	217°C
Steam Pressure	=	2500 psia
Condenser Pressure	=	1 psia

---

have significant impacts on the economics of the reactor. The first is of concern because the structural requirements would cause penalties on the neutronics performance. Early studies have been more concerned about the large pumping power requirements. Subsequent work by Hunt and Hancox on fusion reactors[20] and by Rose, et al. on a tokamak hybrid reactor[21] have shown that while the blanket can be designed to require reasonably low lithium pumping power, the lithium pressures were found to be excessive. W. M. Wells studied the pressure losses of conducting fluid flow in a Thermonuclear Reactor Blanket[22] and concluded that both the coolant pumping power and the coolant pressure can be reduced by innovative design.

IV.E.1.b. <u>Overview and Methods.</u> In general, electrical eddy currents are generated whenever there is a finite value of the electromotive force around a closed path in a conducting medium. For a conducting fluid flowing across magnetic field lines, the steady state electromotive force is proportional to $\vec{u} \times \vec{B}$, where $\vec{u}$ is the local fluid velocity and $\vec{B}$ is the magnetic field strength. Therefore, in any conducting region where $\int (\vec{u} \times \vec{B}) \, d\vec{\ell}$ is non-zero, eddy currents can be expected to develop.

A transverse magnetic field (i.e. perpendicular to the flow velocity) can increase the pressure drop of an electrically conducting fluid in four ways:

1) Electrical eddy currents flow in the fluid in a plane perpendicular to the fluid velocity, causing thinning of the side-wall boundary layers and increased wall friction.

2) If the channel walls are electrically conducting, eddy currents generated in the fluid can return through these walls, resulting in a net electromagnetic body force in the fluid which opposes its motion.

3) Electrical eddy currents flow in "end regions" in a plane perpendicular to the magnetic field or where there are gradients of magnetic field strength. These eddy currents also result in a net retarding electromagnetic body force, and

4) Turbulence suppression. This effect generally tends to laminarize the flow and for the parallel field cases reduces the pressure drop. For transverse fields, effects 1, 2 and 4 are usually all present so that the pressure drop may be increased or decreased.

<u>Pressure Drops.</u> The last factor above suggests that, because of the possibility of having relatively long lithium flow paths parallel to the magnetic field in the central cell of a TMHR, one might be able to design a TMHR blanket using liquid lithium that could yield reasonable pressures and coolant pumping power.

Preliminary parametric scoping analysis showed that the pressure drop due to flow parallel to the magnetic field is indeed very low; however, mechanical design considerations and service and maintenance requirements suggested the design for one blanket module for every two solenoidal coils.

The total pressure drop through the blanket, ΔP_T, is made up of a number of terms that include the following:

ΔP_{IO} — pressure drop due to flow into and out of the magnetic field

$\Delta P_{\underline{1}}$ — pressure drop due to radial flow perpendicular to the magnetic field,

ΔP_c — pressure drop due to circumferential flow perpendicular to the magnetic field,

ΔP_a — pressure drop due to flow parallel to the magnetic field.

ΔP_o — other losses in the blanket such as those due to turns and contactions/expansions, and

ΔP_e — pressure drop through the liquid lithium loop outside the magnetic field.

Thus,

$$\Delta P_T = \Delta P_{IO} + \Delta P_{\underline{1}} + \Delta P_c + \Delta P_a + \Delta P_o + \Delta P_e \qquad (1)$$

MHD Effects

ΔP_{IO} — The pressure drop due to flow into and out of a magnetic field is normally expected to be relatively high for uninsulated (electrical insulation) flow duct walls. For insulated duct walls, Wells[22] recommended the following semi-empirical equation for flow into or out of a magnetic field:

$$\Delta P_{IO} = 0.062 \ V_r b \ B^2 \ \sigma \qquad (2)$$

Where: V_r is the liquid metal velocity entering/leaving the magnetic field
b   is the half width of a square duct, or the radius of a round pipe
B   is the magnetic field, and
σ is the electrical conductivity of the liquid metal.

$\Delta P_{\perp}$ – For flow through a conductive pipe or duct with length L across a uniform transverse magnetic field, the general equation for the pressure drop is given by Hoffman and Carlson[23] to be:

$$\Delta P_{\perp} = \frac{1.3\ \mu\ V_{\perp} L}{r^2}\ [H + H^2\ (\frac{c}{1+c})] \tag{3}$$

Where   r is the pipe radius, or square duct half width,

$V_{\perp}$ is the velocity for flow perpendicular to the field,

H is the Hartman number, where $H = rB\ \sqrt{\sigma/\mu}$

μ is the viscosity of the liquid metal, and

c is the wall conductivity ratio, where

$$c = \frac{\sigma_w\ \delta_w}{\sigma\ r} \tag{4}$$

δ_w is the wall thickness

ΔP_c – The pressure drop equation for this component is identical to that given by Equation 3 with the suitable values for L and the replacement of $V_{\perp}$ by V_c, the circumferential flow velocity (through the flow distributor).

ΔP_a – For flow parallel to a magnetic field, it is known that turbulence tends to be suppressed so that the transition Reynolds number is extended to higher Reynolds numbers for increasing magnetic fields. Carlson[24] recommended the following criterion:

$$\frac{R_{et}}{R_{eo}} = \frac{H}{7} \tag{5}$$

Where R_{et} is the transition Reynolds number in a parallel magnetic field, and R_{eo} is the transition Reynolds number in the absence of a magnetic field, assumed to be 2000. Then

$$\frac{R_{et}}{H} = 286 \tag{6}$$

From the definition of the Hartman Number, Equation 6 reduces to

$$\frac{\rho V_t}{\sigma B} = 286 \tag{7}$$

Thus for a given magnetic field and a given liquid metal, the critical velocity (transition velocity) is fixed. For liquid lithium,

$$V_t = 71.32 \text{ m/s}$$

This is a very high velocity. For reasonable design velocities and well designed blankets, liquid lithium flow parallel to the magnetic field is expected to be well in the laminar flow reqime, where the pressure drop equation is

$$\Delta P_a = \frac{32 \mu V_a L}{d^2} \tag{8}$$

ΔP_o - Other losses are primarily due to the turns in the flow paths. These can be treated like the pressure drop due to flow into and out of a magnetic field (ΔP_{IO}) drop.

Non-MHD Effects

ΔP_e - This pressure drop is dependent on a detailed plant layout; consequently, it is subject to a detailed design and in the absence of MHD effects permits significant flexibility.

IV.E.1.c. Pressure Drops and Pumping Power. The reference parameters (either specified or calculated) needed to calculate the total pressure drop are listed in Table IV.E-2. The lithium pressure drops, pumping power and pressures calculated are summarized in Table IV.E-3. It should be noted that the pressure having the greatest impact on the blanket neutronic performance is that affecting the first wall, or 120 psia. The total pressure drop through the liquid lithium loop calculated is about 200 psi. The maximum

TABLE IV.E-2. Liquid lithium reference parameters.

Thermal power production in the lithium zone	= 2210 MW
Thermal power produced in the molten salt zone	= 1410 MW
Lithium blanket inlet temperature	= 220°C
Lithium blanket exit temperature	= 390°C
Total lithium flowrate through blanket modules	= 3129 kg/s
Number of blanket modules	= 15
Number of lithium inlet and outlet ducts (to each header)	= 20
Diameter of inlet ducts	= 0.5 m
Duct structural wall thickness	= 0.762 cm
Duct inner wall thickness	= 0.05 cm
Maximum magnetic field encountered by liquid metal coolant	= 3 Tesla
Lithium velocity through the radial flow ducts perpendicular to the magnetic field	= 0.105 m/s
Total length of lithium ducts in radial flow direction, perpendicular to the magnetic field, per module	= 7.44 m
Lithium velocity in axial flow, parallel to the magnetic field	= 0.06 m/s
Total length of axial flow paths per module	= 10 m
Lithium velocity in the circumferential flow direction	= 0.0524 m/s
Length of circumferential flow path (inlet and outlet)	= 0.4 m

lithium pressure, at the outlet of the EM pumps, is 226 psia. The liquid lithium pumping power calculated is 8.2 MW. This is based on an EM pump efficiency of 80% and on EM pumps with conducting walls. For advanced EM pumps with insulated walls, a pump efficiency of 90% has been indicated in prototype tests at Westinghouse.[25]

TABLE IV.E-3. Summary of liquid lithium loop pressure drop, pumping power, and pressures.

		Reference	Alternative[a]
ΔP_{IO}	– pressure drop due to flow into and out of the magnetic field, psi	6(6)[b]	6(6)
$\Delta P_{\perp}$	– pressure drop due to radial flow, perpendicular to the magnetic field, psi	44(138)	8(119)
ΔP_c	– pressure drop due to circumferential flow, perpendicular to the magnetic field, psi	4 (4)	4 (4)
ΔP_a	– pressure drop due to axial flow, parallel to the magnetic field, psi	0.7 (0.7)	0.7 (0.7)
ΔP_o	– pressure drop due to turns in the blanket module (assumed), psi	111 (111)	36 (36)
ΔP_e	– pressure drop in the lithium flow loop external to the blanket and outside the magnetic field, psi	40 (40)	40 (40)
ΔP_T	– total lithium loop pressure drop, psi	206 (300)	95 (206)
Back pressure, assumed, psi		20 (20)	20 (20)
P_p	– lithium pumping power (hydraulic power), MW	9.3 (13.5)	4.3 (9.3)
Pump efficiency (pumps with conducting walls)		0.8 (0.8)	0.8 (0.8)
P_p	– lithium pumping power (electric power), MW	11.6 (16.9)	5.4 (11.6)
Lithium pressure at outlet of EM pump, psi		226 (320)	115 (226)
Lithium pressure at blanket inlet manifold, psi		206 (300)	95 (200)
Lithium pressure at first wall, psi		123 (170)	68 (136)
Lithium pressure at blanket outlet manifold, psi		40 (40)	40 (40)
Lithium pressure at EM pump inlet, psi		20 (20)	20 (20)

a) Alternative design (shown in Figure IV.B-5) features pipes around rather than under magnets.

b) Numbers in ( ) are if insulated pipes are not used in straight radial sections.

IV.E.1.d. <u>Overview and Comment</u>. It should be noted that both the maximum
lithium pressure and the lithium pumping power are relatively small in con-
trast to significantly larger values reported in previous studies for tokamak
reactor applications. This stems from several factors, two of which are
unique to the TMHR: the relatively low magnetic field (3 Tesla maximum vs. 8
to 12 Tesla maximum in tokamak reactors) and the availability of relatively
large flow cross-sectional areas for flow perpendicular to the magnetic field
(as a result of the relatively long central cell $\sim$ 95 m). Finally, the pro-
posed insulated ducts provide a practical solution to minimizing the pressure
drops due to flow perpendicular to the magnetic field. These factors permit
the serious consideration of the use of liquid lithium as blanket coolant in a
magnetically confined fusion reactor.

The total pressure drop due to MHD effects calculated here represent a
first approximation for a number of reasons. The use of Equation 8 to calcu-
late the pressure drop for flow parallel to the magnetic field assumes fully
developed flow through a channel with a smooth wall. This assumption neglects
the entrance effects and the effects of the corrugated first wall. Either
effect is expected to lead to higher pressure drop than those calculated.
Such effects are not readily amenable to analytical solutions; however, a
factor of 10^4 greater pressure drop than the pressure drop calculated using
Equation 8 was assumed to account for these two phemonena. In view of the
relatively low pressure drops calculated from this contribution, large errors
in the estimated pressure drop can be tolerated. Experimental testing will be
needed ultimately to confirm this expectation.

As shown in Table IV.E-3, a 94 psi increase in the pressure drop is
obtained if insulated pipes are not used in the reference piping arrangement.
This increase is entirely attributable to the pressure drop due to radial flow
perpendicular to the magnetic field ($\Delta P_{\parallel}$). Although the 94 psi decrease
is highly desirable with respect to improving the neutronic efficiency of the
design, the development of insulated piping is not a critical feasibility
issue for this blanket design.

In contrast to the reference design, the alternative piping arrangement
(see Figure IV.B-5) can reduce the pressure drop by 111 psi (see $\Delta P_{\parallel}$ and
ΔP_{o} terms). This occurs due to fewer (one versus three) turns in the
coolant flow within the field. The primary loop pressure drops for the

alternative arrangement with and without insulated piping are 95 and 206 psi respectively. Therefore, if the pressure drop in the blanket were to become an important determinate regarding blanket performance, a number of options exist to minimize its effect.

IV.E.2.   Molten Salt Primary Loop

The molten salt primary loop includes the molten salt outer zone of the blanket, the molten salt-sodium intermediate heat exchanger, the molten salt pump and the flow loop components. The molten salt selected, LiF - BeF$_2$ - ThF$_4$, consists of 72 Mole % LiF, 16 Mole % BeF$_2$ and 12 Mole % ThF$_4$. Its melting point is 500°C.* The blanket inlet temperature for the molten salt was specified to be 550°C and the molten salt temperature rise was set at 100°C to yield a blanket exit temperature of 650°C. This maximum temperature was set based on anticipated strength limitations of Hastelloy-N, the material for molten salt containment in low neutron flux regions outside of the blanket.

IV.E.2.a.   Frozen Salt Layer Control. The unique feature of the molten salt blanket is the use of a frozen layer of the salt to protect the stainless steel containment walls (wherever they are used in the blanket) from corrosion by the molten salt. The major design issue was therefore the thickness of the protective frozen salt layer. Since the molten salt is the heat source with the highest temperature, there is a natural tendency to lose heat from the molten salt to its environment. Thus if any heat sink that interfaces with the molten salt operates at temperatures below the freezing point of the salt, a frozen layer of salt can theoretically be maintained. The analysis of the frozen salt layer thickness is complicated by the nuclear behavior of the salt. In particular the frozen salt layer will experience a transient build-up of ^{233}U and ^{233}Pa resulting in increasing fission power density with irradiation. Increases in the power density in the frozen layer are expected to decrease the thickness of the frozen salt layer until some equilibrium thickness is attained. The thinnest layer is expected at locations where the molten salt is at its highest temperature and where the adjacent heat sink (lithium) temperature is also the highest.

The actual thicknesses of frozen salt required for stainless steel wall protection is unknown. Nevertheless, in the event that the thicknesses following neutron irradiation are inadequate, the remaining frozen salt can be replaced periodically with a fresh layer that contains a lower fissile concentration and hence a lower power density. There are several ways in which the frozen salt layer can be removed. The simplest method is to raise the molten salt inlet temperature (through the use of the auxiliary heater) while simultaneously decreasing the molten salt flowrate with the reactor operating. The rate at which the frozen salt is removed can be determined through detailed transient thermal analyses.

IV.E.2.b.   Temperature Profiles.   Figure IV.E-2 presents the temperature distributions through the lithium-molten salt interfacial region, which includes the lithium-molten salt common wall. The analysis was performed with a one-dimensional TAP-A model.[27] The boundary conditions and salt properties used in the analysis are listed in Table IV.E-4. A peak molten salt temperature of 650°C and nominal lithium temperature of 290°C were selected in this analysis. This represents the worst case, where the thickness of the frozen salt layer is expected to be at a minimum. The location of the freezing point of the salt (500°C) determines the edge of the frozen layer and hence its thickness. The minimum thickness of the frozen salt layer is thus determined to be 0.63 cm at the beginning-of-life (BOL, before neutron irradiation).

IV.E.2.c.   Time Dependent Considerations.   The increase in frozen salt power density with irradiation time (with increasing fissile concentration) is illustrated in Figure IV.D-4. The results were based on a TARTNP model with an assumed uniform 2 centimeter thick frozen salt layer. It is noted that the initial power density of the frozen layer is $\sim$ 4-5 W/cm^3 but increases steadily with neutron irradiation. The effect of the increase in the power density on the thickness of the frozen salt layer was analyzed, again using the one dimensional TAP-A model. The results are presented in Figure IV.E-3 for the worst case with the initial temperature profile given in

---

* The thermal-physical properties of this material, used in the design and analysis of the molten salt blanket, were obtained from Reference 26.
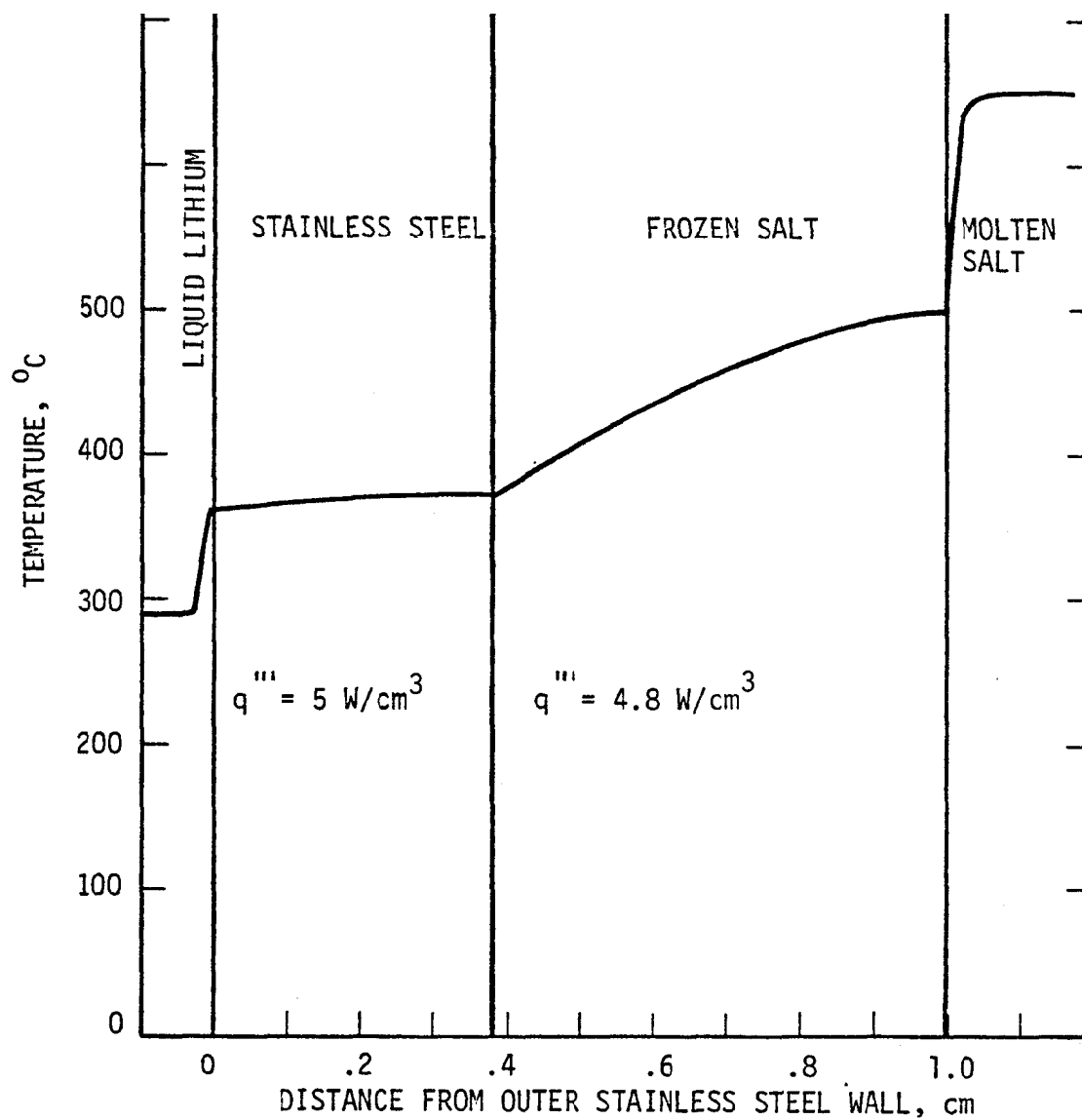
FIG. IV.E-2. Temperature distributions through lithium-molten salt interface region (temperature distribution at BOL with nominal 290°C lithium temperature and 650°C molten salt temperature).
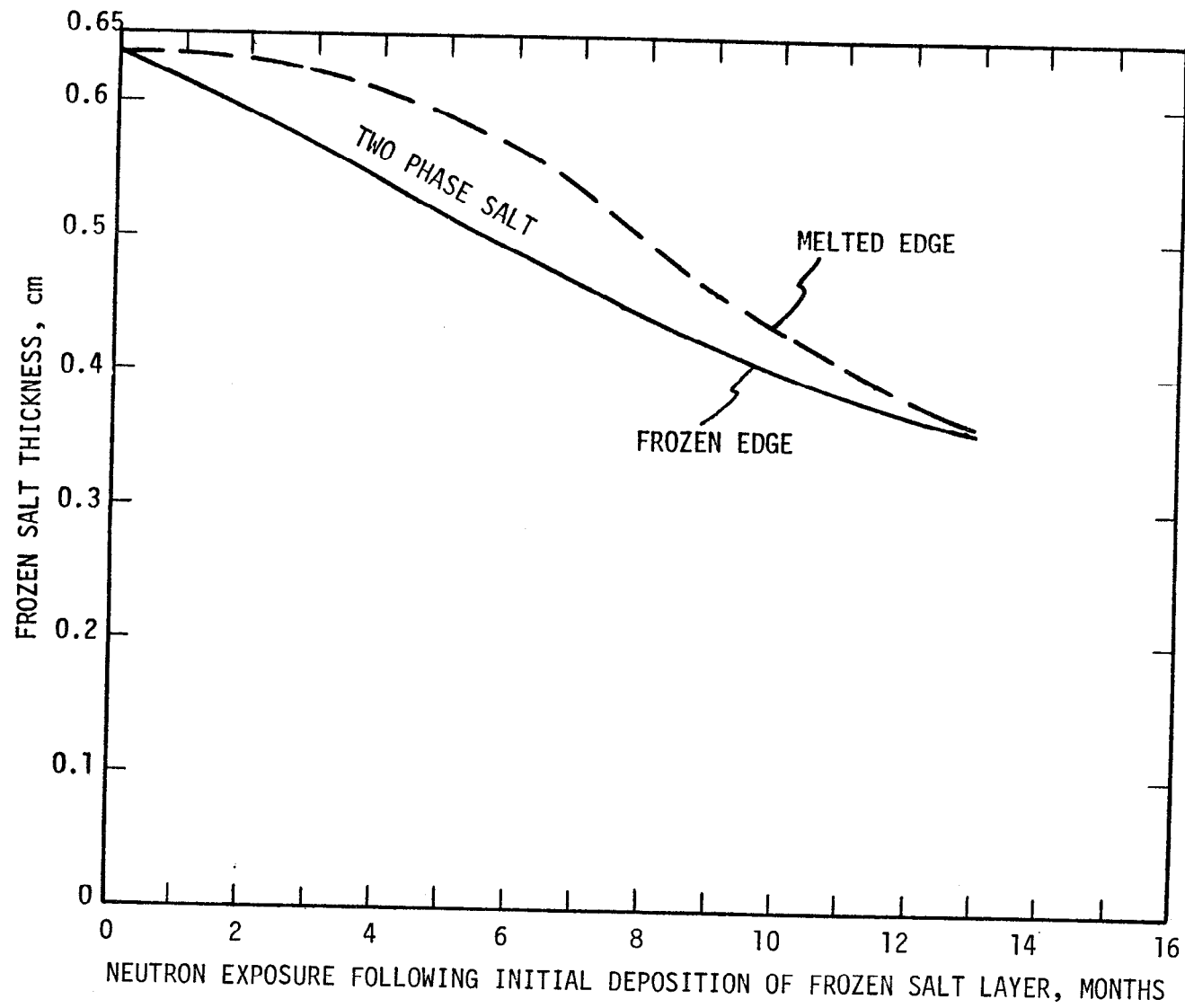
FIG. IV.E-3. Effect of neutron exposure on the thickness of the frozen salt (650°C molten salt, 290°C liquid lithium).

IV-69

TABLE IV.E-4. Boundary conditions and assumptions used for temperature
distributions in lithium-molten salt interface region.

Liquid Lithium Temperature (nominal)	290°C
Molten Salt Temperature	650°C
Molten Salt Viscosity	12 centipoise
Estimated Liquid Lithium - Stainless Steel Structure Interface Heat Transfer Coefficient	2000 W/m^2-°C
Estimated Molten Salt - Frozen Salt Layer Interface Heat Transfer Coefficient	1280 W/m^2-°C
Melting Temperature of Frozen Salt Layer	500°C
Latent Heat of Salt	63 cal/g
Thermal Properties of Frozen Salt	
Density	3.35 g/cm^3
Specific Heat	0.33 cal/g-°C
Thermal Conductivity	1.1 W/m-°C

Figure IV.E-2. It is seen that the thickness of the frozen salt layer
decreases with increasing fissile build-up to about 0.35 cm in 130 days. For
longer irradiation periods it appears that the frozen salt thickness would
reach a minimum equilibrium thickness in the range of 0.25 cm. The maximum
thickness of the frozen salt layer is found at the molten salt inlet end of
the blanket, where both the molten salt and the liquid lithium are at the
lowest temperatures (550°C and 190°C, respectively). Here the BOL layer
thickness is estimated to be roughly three times greater than that at the hot
end, or approximately 1.8 centimeters.

It should be noted that the above analysis assumes a zero fissile
enrichment in the initial frozen layer whereas, to correspond with the
equilibrium processing rate for the molten salt fuel, the initial composition
of the layer is expected to contain 0.14% fissile material (including ^{233}Pa)

in thorium (see Section IV.D). Since the frozen salt layer next to the stainless steel wall accumulates fissile material at the rate of about 0.05%/month in thorium, it is appropriate to translate the data in Figure IV.E-3 by approximately 3 months (i.e., subtract 3 months from the absissa). The result will be a prediction of the thickness vs. time for a frozen salt layer formed from an equilibrium enrichment salt. Assuming the above conditions, the thickness would decrease to about 0.33 cm after one year of irradiation beyond the initial equilibrium point.

The above analyses apply to the frozen salt on the module walls that are common to the liquid lithium which provides active, forced convective cooling. In the back wall regions of the molten salt blanket, the walls are not in direct thermal contact with a heat sink. As a consequence, heat losses from the external surface are primarily by thermal radiation. Calculations show that under such conditions, typical thicknesses of the frozen salt are less than or equal to 0.5 mm. Although the actual thickness required for effective wall protection is unknown, 0.5 mm might be too thin. Accordingly, it is proposed that consideration be given to having the back walls constructed of Hastelloy N unless later anlaysis or data indicate that an adequate frozen salt layer can be developed by either passive or active cooling of the back walls. It should be noted that Hastelloy N material has been proposed at the outset for molten salt containment everywhere outside the blanket; consequently, its use on the back walls is simply an extension of that application. The behavior of Hastelloy-N in the radiation environment is discussed in Section IV.G.

IV.E.2.d. <u>Other Critical Components</u>. Other critical components contacting the molten salt include the molten salt intermediate heat exchanger, the molten salt dump tank valve, the dump tank and various components in the reprocessing plant. The dump tank and valve are described in Section VI.C and the reprocessing plant components discussed in Section VII.B. Both active heating and active (or passive) cooling are required for the dump tank and the dump tank valve if the latter is designed to be of the melt-out plug type design. Some of the components can be relatively complex when the need for both heating and cooling are taken into consideration. However, the design of such components can, to a large extent, be adapted from the molten salt breeder reactor program.

IV.E.2.e. Overview and Comment. It has been pointed out that the actual thickness of frozen salt required for stainless steel protection is unknown, however, the minimum frozen salt thickness calculated is on the order of 0.30 cm (at the hot end of the molten salt zone). This thickness can be increased simply by reducing the maximum molten salt temperature. The maximum molten salt temperature used in this calculation was initially assumed to be 650°C for the purpose of maximizing the power conversion efficiency. It is noteworthy that the 100°C molten salt temperature rise resulted in a low average flow velocity of 0.12 m/s and low pressure drop. Consequently, a significant reduction in the maximum molten salt temperature is feasible with minimal penalty on the power conversion efficiency.

There remain a number of unknown factors and issues involving the frozen salt concept. They are the following:

1) The adherency of the molten salt layers.

2) Short term corrosion characteristics of stainless steel exposed to the molten salt

3) Actual thicknesses required for effective stainless steel wall protection.

4) The rate of diffusional exchange.

5) Possibility of self regeneration.

6) Procedures for initial frozen salt deposition and frozen layer removal.

The first 4 issues are subject to resolution by experimental testing, while the last issue can be resolved by more detailed design and analysis.

Analysis has shown that the thickness of the frozen salt layers tend to decrease with increasing irradiation because of the increase in the fissile content and power density. However, in the limit of an assumed zero thickness, a new layer, with a thickness equal to that at BOL, should be formed. Consequently, it would be expected that a self-regulated, regeneration process will take place so that a finite, equilibrium thickness is maintained. The model of such a process requires a more detailed approach to thermal analysis, and meaningful experimental testing requires simulation of the heat generation in the frozen salt layer.

It is noteworthy that the use of molten salt as blanket coolant and fluid fuel had been considered in several previous studies[1,28-30]. A recent review of previous molten salt blanket concepts for fusion hybrid reactors[31] listed all the major disadvantages and did not recommend its use in fusion hybrids. The major and critical objections are eliminated in the proposed molten salt blanket concept through a combination of factors that include the following unique features:

1) The possibility of using a thick region of liquid lithium as an effective neutron multiplier (depleted of ^{6}Li).

2) The adoption of the concept of fission suppression with fertile dilution in a Th-U fuel cycle.

3) The avoidance of the use of high nickel content alloys for molten salt containment through the use of a protective layer of frozen salt (over stainless steel).

IV.E.3. Thermal Insulation and Heat Tracing Considerations

IV.E.3.a. Blanket Thermal Insulation Requirements. It was recognized that thermal insulation may be required around the relatively high temperature blanket to minimize heat losses. However, the installation of thermal insulation materials could reduce the blanket space available for tritium breeding and/or fissile breeding. Moreover, thick insulation may be difficult to accommodate. Consequently, it would be desirable to minimize the insulation thickness. An evaluation was therefore made on the thickness of a typical insulation material. For this purpose, MIN-K® Type 108 produced by the Johns Manville Corp. was determined to be a flexible, high temperature insulation ideally suited to the blanket application. The thermal conductivity (k) of the material is a function of the average material temperature (T) and the average thickness (δ) of the material. Consequently, an iterative calculation is required. For an assumed ΔT of 550°C (the worst case) and 0.5% heat loss, the converged solution was as follows:

$$k = 5.4 \times 10^{-4} \ W/cm\text{-}°C$$

$$\overline{T} = 375°C$$

$$\delta = 0.3 \ cm \ (\sim 1/8 \ inch)$$

The total area assumed to be insulated is 1875 m^2 and the total heat loss from all the blanket modules is estimated to be ~20 MW. This does not include the heat transferred from the molten salt to the liquid lithium across common walls, because this heat can be recovered. The heat transferred across the lithium-molten salt common wall was estimated to be also ~ 20 MW. The relatively thin insulation thickness calculated suggests that there should be little difficulty in the installation of the material around the blanket.

IV.E.3.b. <u>Auxiliary Heating and Heat Tracing Systems</u>. As in the Molten Salt Reactor Experiment (MSRE), the Molten Salt Breeder Reactor (MSBR) and all liquid metal fast breeder reactors (LMFBR's), auxiliary heating and heat tracing systems are required for the liqiud lithium-molten salt TMHR blanket. In this case, the auxiliary heating and heat tracing systems are required for both primary loops because the melting points of the two fluids are substantially higher than normal ambient temperatures. Since the blanket itself provides the largest volume in the primary loop and will not contain trace heating systems, the molten salt must be circulated continuously at a low rate through the heated primary loop piping. A similar situation applies to the liquid lithium coolant. However, the molten salt in the blanket requires a protective frozen layer on the stainless steel wall to prevent corrosion. Therefore, if the lower temperature lithium flow were stopped, the molten salt would be drained to its Hastelloy dump tank where heating or cooling of the salt would be accomplished.

IV.E.3.c. <u>Reactor Start-Up Considerations</u>. Auxiliary heating and heat tracing systems are also required for start-up and restart operations; no basic feasibility questions are anticipated in the design of such systems. They are simple electric resistance type heaters. Auxiliary heaters for the lithium and molten salt loops are needed to melt the initial charges of lithium and salt to start up the reactor. Blanket fill-up with liquid lithium and molten salt is conceived to proceed as follows: liquid lithium is heated in an auxiliary heater prior to entering the blanket. The heated liquid lithium is thus used to heat up the blanket to about 350°C. Molten salt is then introduced into the blanket. The relatively high blanket temperature

will prevent a total freeze-up of the molten salt as it fills the molten salt zone of the blanket. A frozen layer (of varying thickness) will quickly form on the surfaces of the module walls. Trace heating of liquid lithium and molten salt pipes and ducts will prevent any freeze-up. Since all of the piping and flow loop components are insulated, relatively little power is expended for heat losses during auxiliary and trace heating. Once the reactor has become operational, trace heating can be gradually reduced as the fission product afterheat increases.

IV.F. TRITIUM BREEDING

IV.F.1. Overview and Material Choice

The liquid lithium cooled molten salt blanket concept breeds nearly all
of the tritium required for reactor operation from the lithium front zone,
with a small amount being bred in the molten salt. The lithium in both
regions is depleted to 0.2% ^{6}Li in order to enhance the tritium producing
reaction in the ^{7}Li. The lithium also serves as a coolant and thus is
continuously circulated in a heat transport loop, as described in the previous
section. As the lithium is circulated, it is processed to recover the
generated tritium and the helium that is also produced.

An important consideration in the design of the lithium processing system
is to limit the blanket tritium inventory to a fairly low value so that it
does not add appreciably to the tritium inventories in the plasma fueling and
vacuum systems. This is important because of considerations such as safety,
decay losses of tritium, permeation of tritium through blanket structures, and
makeup requirements for tritium fuel before the reactor-bred tritium becomes
available from the lithium processing. The ability to maintain a small
blanket tritium inventory will depend largely on the lithium processing rate
and on the capability of the extraction process to recover the tritium from
the lithium at fairly low concentrations.

IV.F.2. Tritium Processing and Inventory Analysis

A model for the tritium inventory of the reactor and the performance and
cost of a molten salt extraction process for liquid lithium systems[10,32] is
given below. This model is based upon work performed at Argonne National
Laboratory. As a function of the total tritium inventory desired, the lithium
inventory, and the tritium production rate, the model calculates the lithium
flow rate to the extraction system required to maintain the given tritium
inventory or concentration. The lithium flow rate determines the number of
extractor units required. The cost and power requirements of the extraction
system are directly proportional to the number of extractor units.

The fraction of the total lithium inventory that must be circulated
through the tritium extraction system per unit time is given by

$$X = \frac{R_g}{I_{ss}} \cdot \frac{\epsilon D_v \eta + 1}{\epsilon D_v \eta}$$

where R_g = tritium generation rate which may include unburned as well as bred tritium

I_{ss} = steady-state tritium inventory

ϵ = efficiency of tritium recovery from the salt

D_v = volumetric distribution coefficient of tritium between the lithium and the salt

η = efficiency factor that accounts for non-equilibrium tritium distribution during contacting.

Typical values for ϵ, D_v, and η are 0.9, 2.0, and 0.3, respectively.

The lithium flow rate to the tritium extraction system is then

$$F = X I_L / \rho_L \qquad cm^3/s$$

where I_L = lithium inventory, g

ρ_L = lithium density, g/cm^3

The number of extractor units required in parallel for a single stage operation is

$$N = F/3200$$

where F is in cm^3/s. This is based on a capacity per extractor unit of 23 m^3/h (lithium plus salt) used in a process where equal volumes of salt and lithium are contacted. Each extractor draws 3.73 kW_e for continuous operation and costs on the order of one million dollars.

A summary of key parameters related to the blanket lithium and tritium inventories is shown in Table IV.F-1 for two different values of the reactor fusion power, 2000 MW and 3000 MW. As the table shows, at 3000 MW of fusion power the tritium production rate is 476 g/day, and the blanket Li inventory is 388 MT. For this system a total tritium inventory of 1 kg may be achieved

for a lithium processing rate of about 43 m^3/hr. At this rate, the four
required extractor units cycle the entire lithium inventory in about 18
hours. The direct cost of the tritium extractor units is about $4 million and
they are expected to consume a negligible amount of electrical power. Since
the extraction process has been demonstrated at tritium concentrations on the
order of 1 wppm, lower inventories than 1 kg tritium are possible.

TABLE IV.F-1. Key parameters related to the lithium and tritium
inventories for the lithium-molten salt blanket.

Fusion Power, MW	2000	3000
Neutron Wall Loading, MW/m^2	2.0	2.0
Blanket Li Inventory, kg	2.59×10^5	3.88×10^5
T Production Rate, g/day	317	476
T Inventory in lithium, g	1000	1000
T Concentration in Li, wppm	3.9	2.6
Li Processing Rate, m^3/hr	18.9	42.6
Time to Circulate Entire Blanket Li Inventory, hr	43.7	17.7
Number of Extractors Required	2	4

Although the amount of tritium bred in the molten salt is quite low ($\sim$
0.05 per fusion neutron) recovery and reuse in the fusion fuel cycle is
anticipated. A technology to efficiently perform this separation has been
proposed and is discussed in detail in the 1979 TMHR final report[3].
Briefly, this process involves a sparging gas (principally helium) which is
bubbled through the molten salt to remove tritium and fission product gases.
A series of holdup and filtration processes follow. Finally, the tritium is
separated from Kr and Xe fission product gases by a Palladium Diffusion
Separation Process or a process involving conversion to tritiated water
followed by electrolysis.

As noted previously, the lithium used in the blanket design is depleted
to 0.2% ^{6}Li, whereas natural lithium is composed of 7.5% ^{6}Li. As shown in
Table IV.F-1, the lithium inventory for 3000 MW of fusion power is 3.88 x

10^5 kg. A possible concern with this design might then be the cost for this depleted lithium. A study by McGrath[1] determined the amount of separative work required to isotopically separate lithium, but it was difficult to calculate the actual cost because the cost of a unit of separative work was not known. By doing a parametric study, it was estimated[1] that the cost for the lithium depleted to 0.2% ^{6}Li might be in the range of $100-$200/kg ($160/kg reference value). Hence, the capital cost for the blanket lithium inventory for 3000 MW of fusion power would be in the range of $60M. While this is not a prohibitive cost, it would be desirable to perform future studies to attempt to more accurately estimte the cost of highly depleted lithium.

IV.G ALTERNATIVE MATERIALS AND CONFIGURATION OPTION FOR REFERENCE CONCEPT

This section will describe irradiation effects on Hastelloy in a molten salt TMHR and an alternative design option for a molten salt zone utilizing graphite. Hastelloy as a structural material in the molten salt zone is an important option because of its resistance to salt corrosion. The addition of graphite behind, or in, the salt zone is addressed because it may lead to increased or equivalent performance with reduced fissile and fertile fuel inventories. Both of these options are important because they are possible paths for design improvement and will be investigated in greater detail in later studies.

IV.G.1 Hastelloy Structural Materials for the Lithium/Molten Salt Blanket

IV.G.1.a Introduction. Structural materials in fusion reactors experience a harsh and hostile irradiation environment. Since the economics of a fusion power plant depend to a large degree on the lifetime of materials in this irradiation field, radiation damage to structural materials can result in reduced plant factors and increased capital costs due to shut-downs resulting from material failures and scheduled replacement. The remote handling facilities and expanded storage required to handle large volumes of radioactive materials compound this problem. Therefore, there is strong motivation to choose structural materials with reasonably long lifetimes.

One of the basic requirements of a structural material in a molten salt environment is its resistance to chemical corrosion by the salt. Selective chromium leaching by some salts is a primary corrosion mechanism. In a salt environment, iron base alloys are more easily oxidized by the salts than nickel alloys. Hastelloy-N was therefore specifically developed for use as a structural material for molten salt systems. In particular, a Nb-modified Hastelloy N alloy (Ni; 16% Mo, 7% Cr, 5% Fe, 1 to 2% Nb, 0.5% Si; 0.05% C) has been shown to be more resistant than unmodified or Ti-modified Hastelloy to tellurium embrittlement (see discussion in Section VII.B). This alloy is proposed for use as a back wall blanket material, heat transport loop material,

and chemical processing plant material for the reference lithium/molten salt blanket TMHR.

In this section the results of the development of an empirical design equation and its application to the TMHR lithium/molten salt blanket are presented.

IV.G.1.b. <u>Development of an Empirical Design Equation for Hastelloy in the TMHR Environment</u>. Characterization of the performance of Hastelloy in the lithium/molten salt TMHR requires consideration of operating temperatures, dpa production rates, helium production, applied stresses, and alloy composition. In the present design, the high energy neutron flux will be moderated by the thick lithium zone. In comparison with a typical fusion environment near the first wall, this will dramatically reduce damage due to both atomic displacement and helium production. In contrast, however, the high operating temperature in the molten salt zone ($\sim$ 650°C) will shorten the Hastelloy lifetime; primarily through the process of creep rupture.

The approach to the development of a Hastelloy design equation[1] was to consider experimental evidence and empirical correlations based upon current theoretical predictions of irradiation damage. Two primary effects are seen in nickel based alloys: neutron irradiation-enhanced void swelling and irradiation embrittlement. Both of these have been extensively considered in reference 1, and their effects will be briefly summarized here.

Void swelling involves the nucleation and growth of cavities in the metal matrix. The principal variables which have been found to influence the growth of cavities is the migration and capture of excess vacancies at nucleation sites. Neutron collisions with the atoms of the metal matrix are the source of the most of the vacancies which agglomerate in the voids. The principal variables which have been found to influence void swelling are the displacement damage rate (proportional to flux), total dose (proportional to fluence), irradiation temperature, helium content, alloy composition, and type of bombarding particle. Once voids are nucleated and growing, the density and volume of the matrix are changed. This can induce significant stresses in structural members.

In the design equation which has been developed, void swelling is predicted as a function of the above parameters.

In a real radiation environment, irradiation creep could act to relieve some of the stresses induced by void swelling. A detailed analysis, in fact, would consider the interplay of operating stresses, irradiation creep, void swelling, and design stress-strain limits. We feel, however, that the present void swelling limit approach taken here is conservative.

Irradiation embrittlement occurs because of two processes: the nucleation and growth of helium filled cavities on grain boundaries and the pinning of dislocations or helium bubbles in the grain matrix. Grain boundary cavities weaken the grain boundaries and decrease the stress to rupture. Pinning of dislocations hardens the matrix. The simultaneous hardening of the matrix and weakening of the grain boundaries is the cause for the loss of ductility and the reduction of the time-to-rupture (t_R) under irradiation. Embrittlement is a function of alloy composition, temperature, helium content, and applied stress. These factors have been included in a design equation which predicts t_R as a function of operating temperature, helium content, and applied stress. Figure IV.G-1 shows the operating curve for a helium does rate of 33.8 appm/yr at 650°C with a design stress limit for 5 ksi. The time to rupture in this example is about 4 years.

For most postualed operating conditions, failure occurs by the high temperature helium irradiation embrittlement mechanism. Void swelling limits were found to be a lesser constraint at high temperatures. The reader is referred to reference 1 for a more complete discussion.

IV.G.1.e Radiation Damage Lifetime Analysis for Hastelloy in the Lithium/ Molten Salt Blanket. The previously described model of irradiation effects on Hastelloy predicts swelling and embrittlement as a function of helium production, dpas, temperature, and design stress. In the analysis presented in this section, a design stress of 5 ksi and an operating temperature of 650°C were assumed. Neutron transport calculations were done for the lithium/molten salt blanket to predict helium production and atomic displacement damage as a function of irradiation time and varying lithium region thickness. Stress, temperature, helium production, and atomic
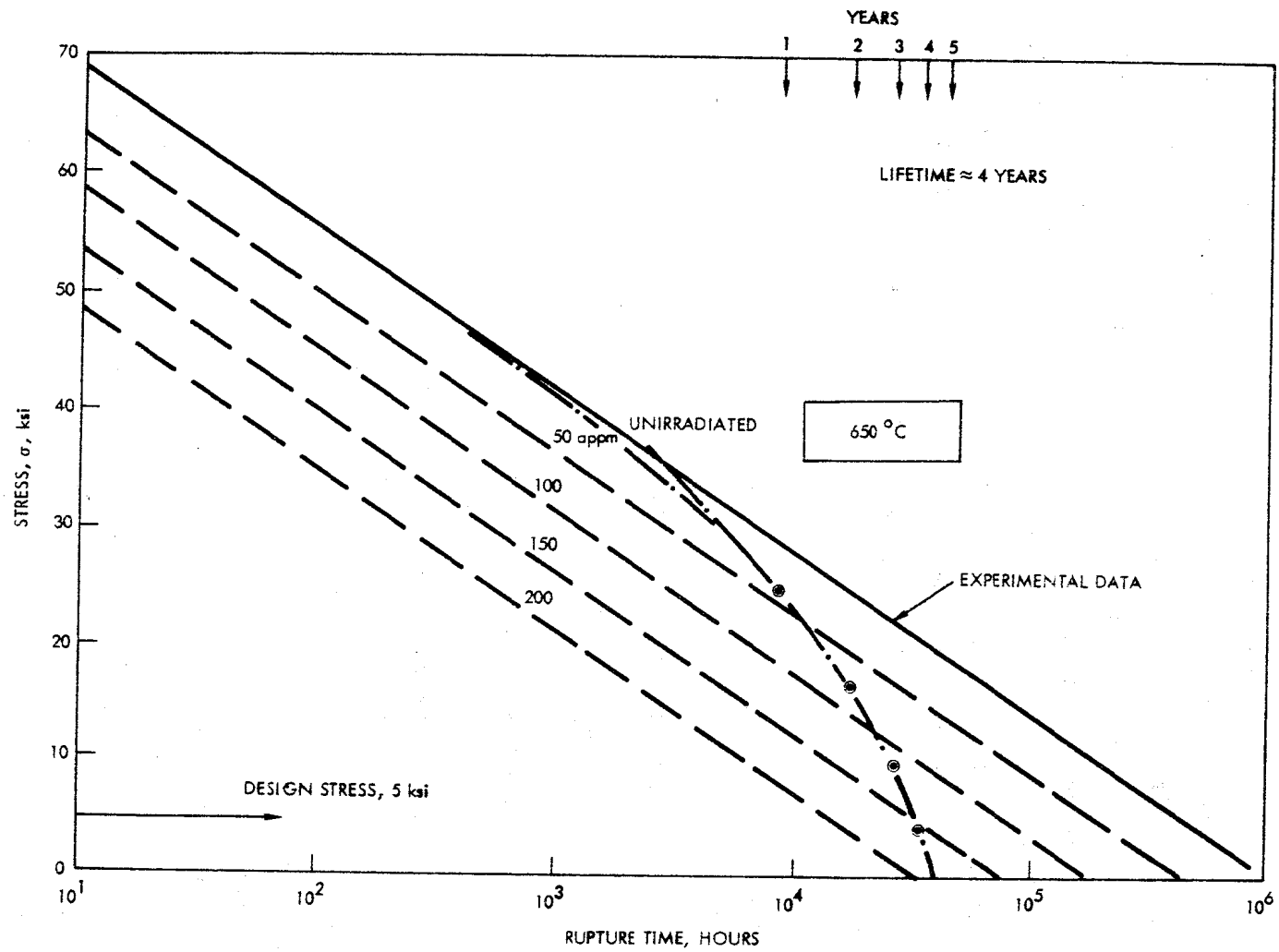
FIGURE IV.G-1. Hastelloy lifetime versus design stress and helium production at 650°C.

displacement damage were then combined using the design equation, and
lifetimes were predicted.

Figure IV.G-2 shows the blanket geometry and composition which
were used in a TARTNP simulation of the lithium/molten salt blanket.
Flux tallies were taken in the first Hastelloy region, and the resulting
energy dependent spectrum was combined with MACKLIB-IV [2] displacement
cross section data. The result was a prediction of atomic displacements
per atom per year in the first Hastelloy zone.

Helium production was derived directly from the reaction rate tallies
produced by TARTNP. Most of these reactions are threshold type (n, α)
reactions, and the majority of helium production comes from reactions in
^{58}Ni. Additional helium [3] will be produced from a reaction with ^{10}B
impurities

$$^{10}B + n \rightarrow {}^{7}Li + {}^{4}He \text{ (3000 barns)}$$
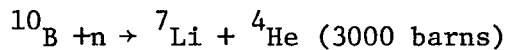
and from a low neutron energy chain reaction with ^{58}Ni

$$^{58}Ni + n \rightarrow {}^{59}Ni + \gamma \text{ (4.4 barns)}$$
$$^{59}Ni + n \rightarrow {}^{56}Fe + {}^{4}He \text{ (13 barns)}.$$
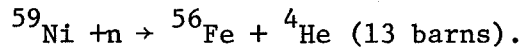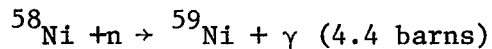
The cross sections above are estimates for a thermal flux. For the
lithium zone thicknesses of interest, the thermal ^{58}Ni chain reaction
produces very little helium [4] and was not considered. The 40 appm
^{10}B impurities were assumed to all be converted to helium early in the
irradiation lifetime.

Figure IV.G-3 shows the helium and dpa production rates as a function
of lithium zone thickness. A 70% capacity factor was assumed. Figure
IV.G-4 shows the ratio of helium production to displaced atoms, again
as a function of lithium zone thickness. In the calculation of total
helium production, the 40 appm helium from the ^{10}B impurities was assumed
to be produced in the first year of operation. After one year, both
helium and dpas are linear in time. Figure IV.G-5 shows the buildup
of helium and displaced atoms with irradiation time.

The data shown in Figure IV.G-3 for the production of helium and
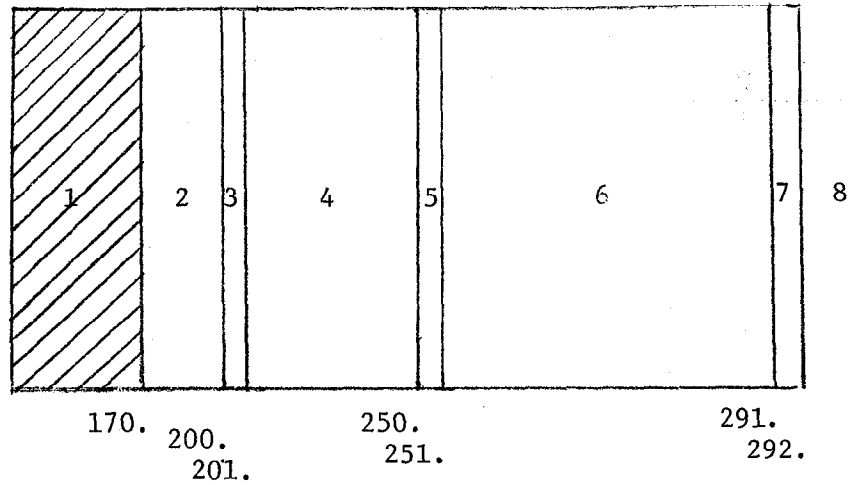
ZONE	DESCRIPTION
1	PLASMA
2	VACUUM
3	Fe FIRST WALL
4	LITHIUM REGION
5	HASTELLOY
6	MOLTEN SALT
7	HASTELLOY
8	LEAKAGE ZONE

FIGURE IV.G-2. TARTNP cylindrical simulation of lithium/molten salt blanket for hastelloy damage calculation.
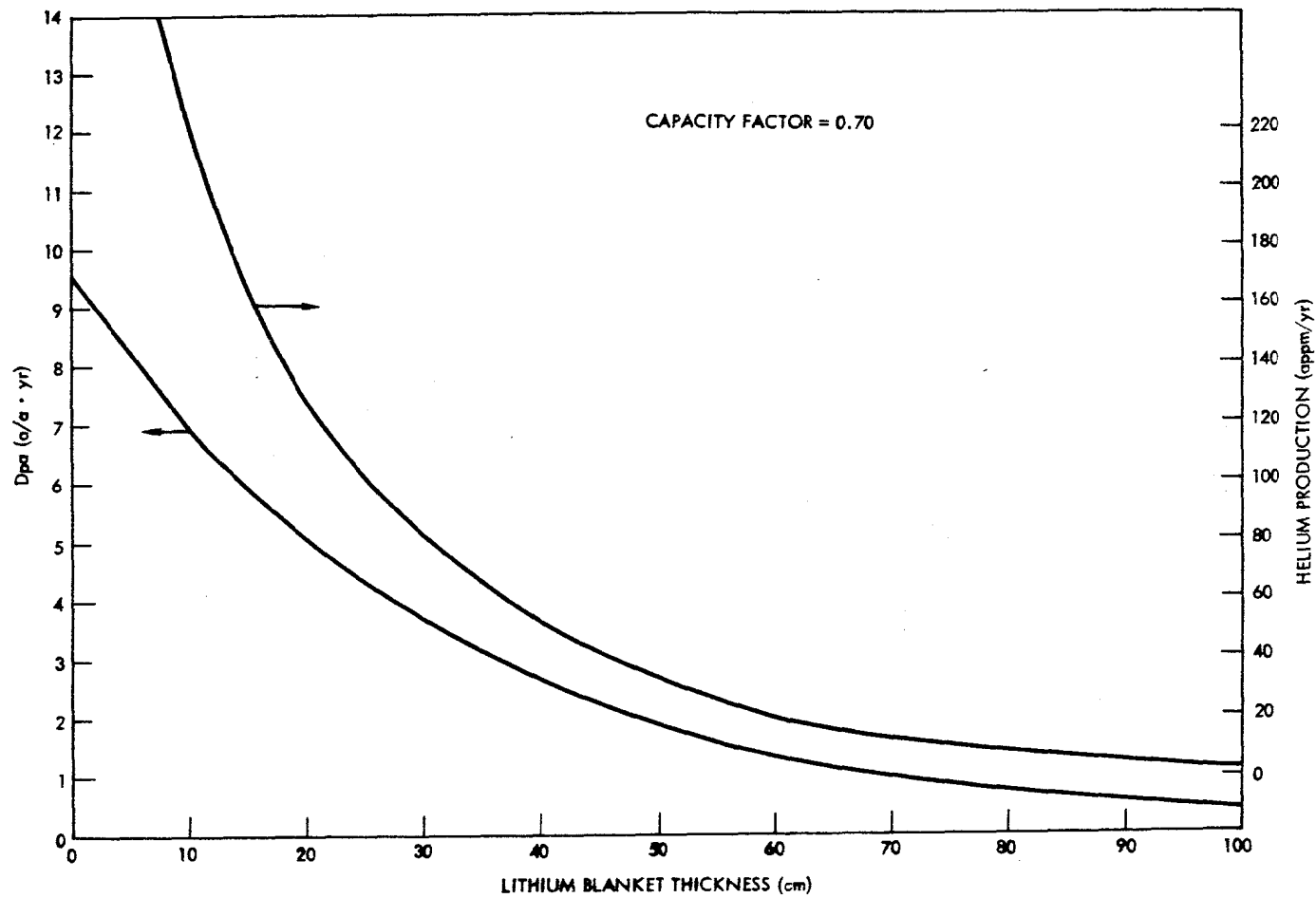
FIGURE IV.G-3.   Hastelloy damage as a function of lithium zone thickness.
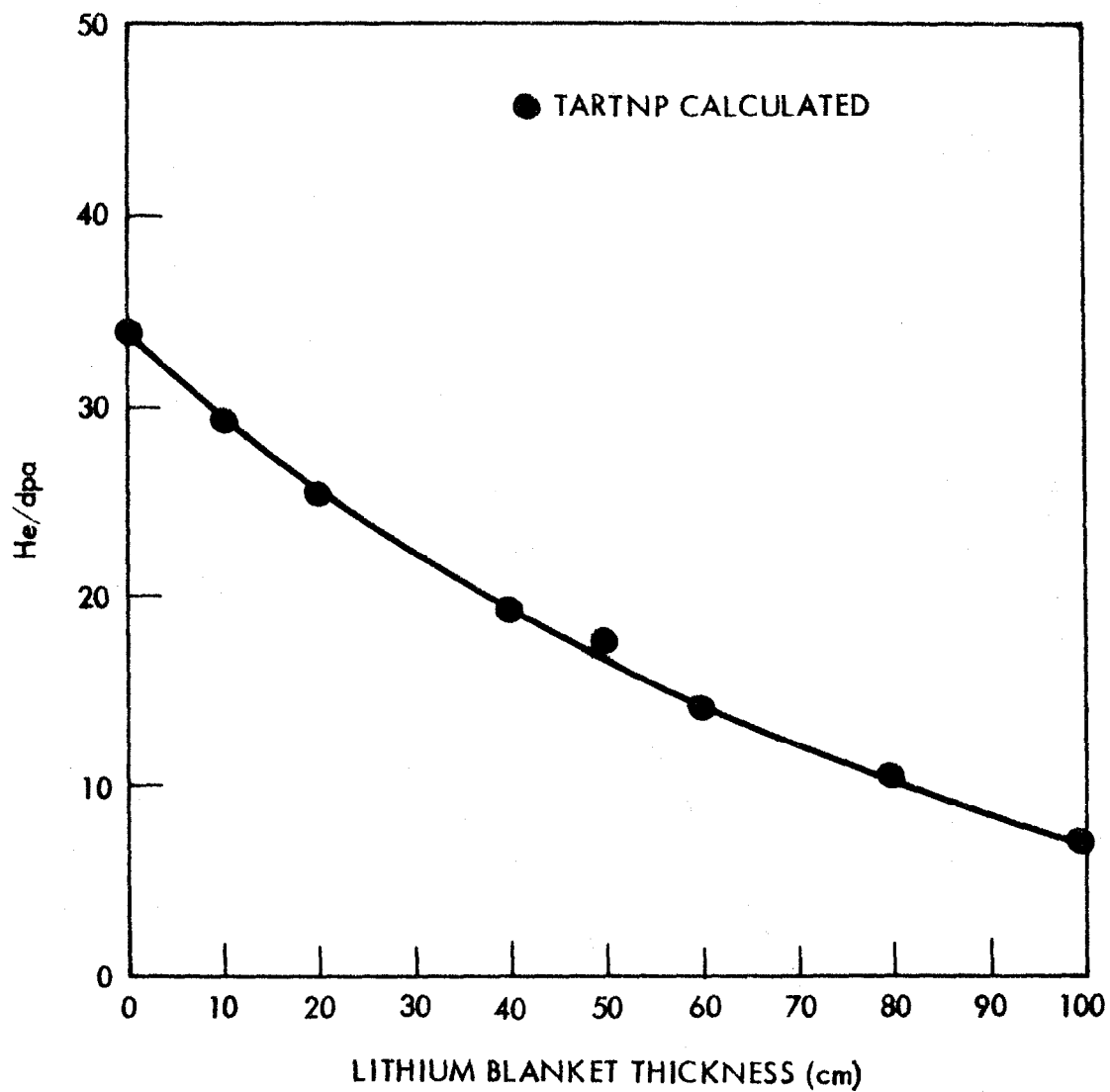
FIGURE IV.G-4. He/dpa as a function of lithium blanket thickness.
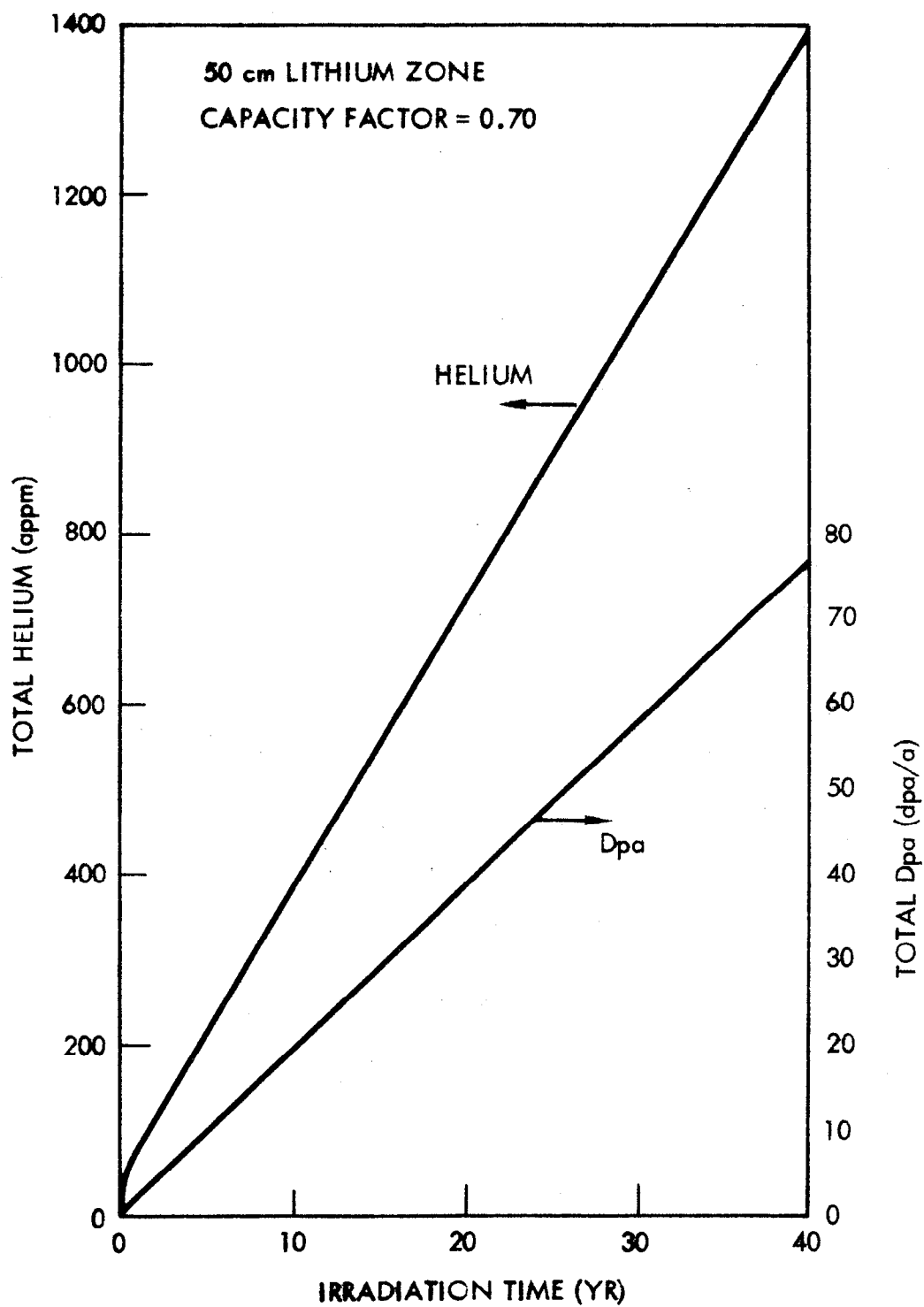
FIGURE IV.G-5. Total helium and dpa's as a function of irradiation time.

displaced atoms as a function of lithium zone thickness can be used to predict Hastelloy lifetimes as a function of lithium zone thickness. In particular, a set of curves similar to Figure IV.G-1 can be constructed for each lithium zone thickness such that the time to reach the design stress can be obtained. The results for 650°C are shown in Figure IV.G-6. A nominal lithium zone thickness of 50 cm gives a lifetime of about 4 years, which is identical to the result in Figure IV.G-1.

Thicker lithium zone thicknesses result in longer predicted Hastelloy lifetimes of 5 years for 60 cm of lithium, 6 years for 70 cm of lithium, 8 years for 80 cm of lithium, and 10 years for 90 cm lithium.

Concerning the back wall of the molten salt zone, an approximation (presumably conservative) of protection from the fast flux is that a given thickness of molten salt (80 cm in this case) is equivalent to half as much lithium. In this case, the equivalent lithium thickness would be 50+(80/2) = 90 cm of lithium and the expected lifetime would be 10 years. Taking safety and reliability into account, a design lifetime of 7 years is suggested by the data. This appears to be the limiting lifetime in the blanket (see section IV.C.2.b).

In summary, this work indicates that a reasonable lifetime for a Hastelloy structure in the fusion environment can be obtained behind a lithium zone. However, several factors, relating to this particular blanket environment should be stressed. The primary irradiation damage effects are limited by the thick lithium zone which both moderates high energy neutrons and acts as a sink for low energy neutrons (due to useful absorption in ^{6}Li), but further work should be done if the molten salt option is pursued. Better modeling of the ^{58}Ni(n,γ) and ^{59}Ni(n,α) cross sections in a fusion environment is required; especially for thicker lithium zones. Also, more refined estimates of ^{10}B impurities are needed. Analysis of final design configurations should be carried out since the flux spectrum is extremely sensitive to the physical layout. Lastly, the role of the molten salt in limiting irradiation damage to the back wall should be addressed.
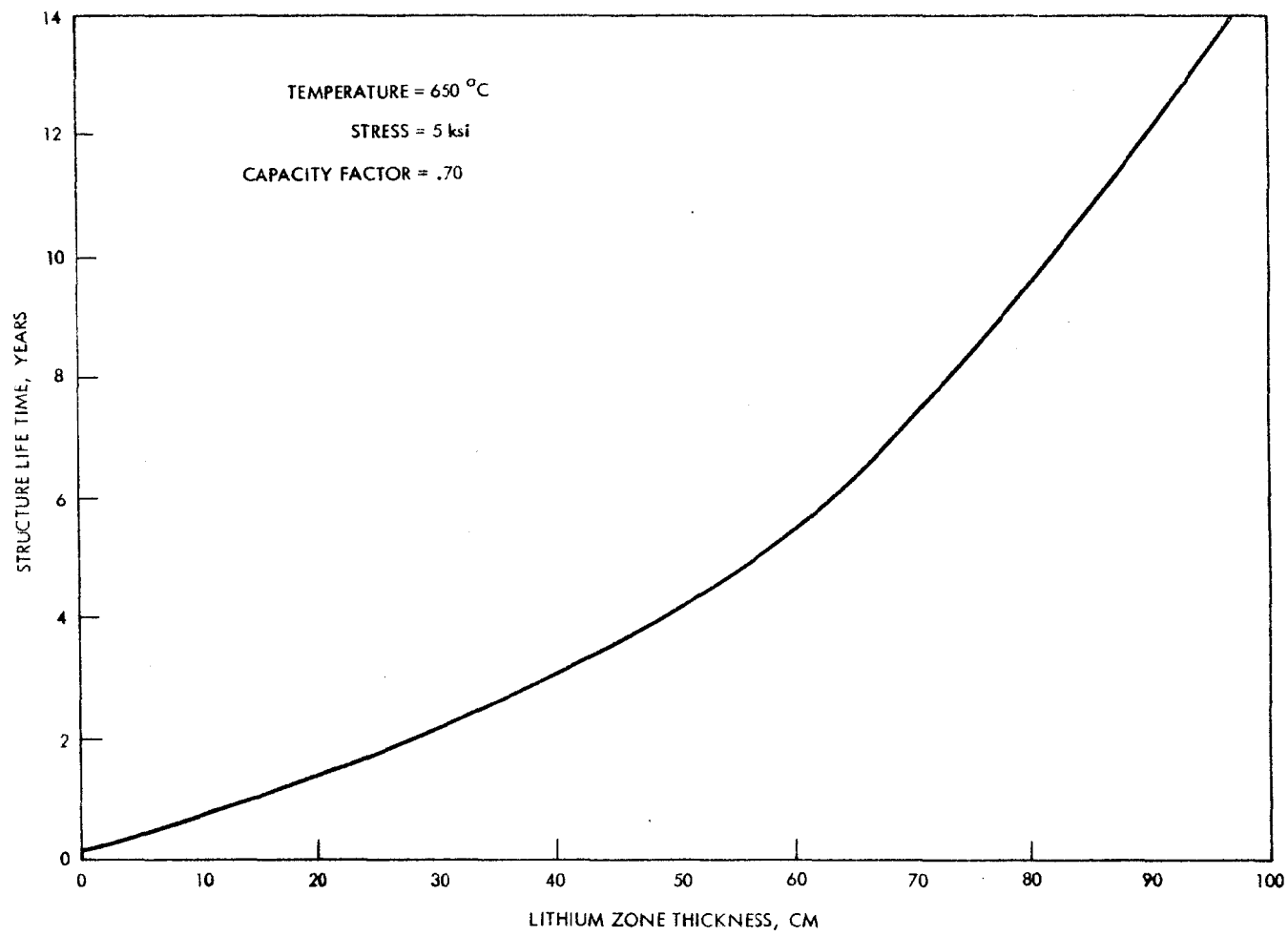
FIGURE IV.G-6. Hastelloy structure lifetime as a function of lithium zone thickness at 650°C.

IV.G-2 Description of a Possible Alternate Lithium/Molten
        Salt Configuration

In comparison with the beryllium/thorium oxide blanket (chapter V)
and a previous molten salt blanket design [5], the reference molten salt
blanket has several disadvantages related to the quantity of salt in the
blanket. These disadvantages are as follows:

   • Large molten salt inventory (1150 m^3) has an associated direct
cost of $192 million

   • Large salt inventory results in a large fissile inventory since
the ^{233}U concentration in thorium is fixed (see section VII.A discussion)

   • Relatively high buildup of several important actinides (e.g.,
^{232}U, ^{228}Th) results from fast spectrum in molten salt zone and irradiation
of the original salt for 30 years

As a result, if an effective method to reduce the salt inventory (and
possibly soften the neutron energy spectrum) could be found, the potential
savings would be substantial.

One possible method is the use of graphite - either as a reflector
or within the blanket itself as a diluent. Graphite is compatible with
the salt and use would be expected to decrease the salt inventory in the
blanket by more than 50% while decreasing the overall breeding performance
only marginally. This option deserves further study.

IV.H. BLANKET TECHNOLOGY ASSESSMENT

IV.H.1. Blanket Technology

The liquid lithium technologies for the lithium-molten salt blanket have a reasonably well developed technology base. Liquid lithium technology has been under development as a part of the overall fusion power program. Moreover, many of the technologies developed for sodium in the liquid metal fast breeder reactor program (e.g. trace heating, liquid metal safety, power conversion systms) are directly applicable here. The principal areas where additional technological developments are needed involve the effects of MHD on pressure losses under actual blanket flow configurations and the development of an electrically insulated liquid metal flow channel. Although a significant data base exists as a result of MHD power generator and electromagnetic pump developmments, these cannot be readily extrapolated to some of the design problems unique to the fusion hybrid blanket. However, with the possible exception of electrically insulated coolant ducts, the technological developments required are not expected to involve go/no-go feasibility issues; rather, they are primarily needed to resolve uncertainties and to establish design margin requirements.

Liquid lithium and lead-lithium mixtures as potential coolants have been investigated for other reactor studies[36-38] and successes in any development involving liquid lithium technologies can be applied to non-hybrid reactor applications as well. In view of the fact that liquid lithium and lead-lithium mixtures provide very attractive tritium breeding performance among potential lithium compound materials, the experimental resolution of the uncertainties involving liquid lithium MHD losses should serve the long-term interest of the overall fusion development program.

Molten salt as a fluid fuel had been extensively developed under the Molten Salt Reactor Experiment (MSRE) and the Molten Salt Breeder Reactor (MSBR) Program where many of the critical feasibility issues had been resolved satisfactorily. However, additional new uncertainties unique to the hybrid blanket, have appeared in the present application. Those feasibility issues that require experimental resolution to support further consideration of this blanket concept are as follows:

- The adherency of frozen salt layers on stainless steel walls.

- The rate of molten salt/stainless steel corrosion and the actual, minimum, thickness of frozen salt layers required to protect stainless steel walls from molten salt corrosion (as a function of wall temperature).

From a corrosion standpoint type 316 stainless steel is satisfactory structural material for containing liquid lithium in the environment for the reference design molten salt blanket. Hastelloy can be used for the blanket outer zone walls to contain the molten salt in the event that the outer walls cannot be adequately cooled.

The intermodule sealing problem may be generic to many blanket designs. Although concepts may not have been developed and tested, it appears reasonable that adequate seals can be developed if given the proper priority and funding.

Except for the issue of adequate corrosion protection of the stainless steel from the molten salt and the possible substitution of Hastelloy for the stainless steel, all of the above issues pertain to both hybrid and non-hybrid reactor options. Although molten salts have been proposed in both hybrid and fusion electric concepts[39], the salts considered for fusion electric coolant applications were usually lower melting point flibe salts (e.g., $47LiF-53BeF_2$ melts at 363°C) which are compatible with stainless steels. In these cases the salts functioned primarily as the coolants. In such cases, a frozen salt layer would provide no benefit to the design since it would impair the efficiency of heat removal from the cooled blanket walls. It may be possible however, that any developments relative to structural material compatibility or protection may be extrapolatable to non-hybrid designs.

REFERENCES FOR CHAPTER IV

1. R. T. McGrath, "Conceptual Design and Neutronics Analysis of a Flowing Lithium/Molten Salt Blanket Fusion Hybrid Breeder Reactor," Ph.D. thesis, University of Michigan (1980).

2. J. A. Maniscalco, et al., "Laser Fusion Breeder Design Study Final Report," DOE Contract DE-AC08-79DP40-11, TRW (1980).

3. R. W. Moir, et al., "Tandem Mirror Hybrid Reactor Design Study Final Report," Lawrence Livermore National Laboratory Report UCID-18808, (1980).

4. W. R. Grimes Oak Ridge National Laboratory, Personal Communications (1981).

5. "STARFIRE - A Commercial Tokamak Fusion Power Plant Study," Argonne National Laboratory Report ANL/FPP/80-1, (Vol. I) September 1980.

6. G. A. Carlson, B. Arfin, W. L. Barr, "Tandem Mirror Reactor with Thermal Barriers," Lawrence Livermore National Laboratory Report UCRL-52836, September 1979.

7. Private Communications. June 1981, Discussions between J. S. Karbowski of Westinghouse Fusion Power Systems Department and W. S. Neef, Jr., of Lawrence Livermore National Laboratory.

8. R. W. Werner, "ORNL Fusion Power Demonstration Study: Arguments for a Vacuum Building in Which to Enclose a Fusion Reactor," Oak Ridge National Laboratory Report ORNL/TM-5664, December 1976.

9. "Recent Development in FINTOR 1 Design," in Proceedings of the 9th Symposium on Fusion Technology, Garmisch-Partenkirchen, Germany, June 14-18, 1976, p. 375-380, Pergamon Press, New York, 1976.

10. W. F. Calaway, "Electrochemical Extraction of Hydrogen from Molten LiF-LiCl-LiBr and Its Application to Liquid Lithium Fusion Reactor Blanket Processing," Nucl. Tech., 39, 63, 1978.

11. Private Communications, June 1981. Discussions between J. S. Karbowski of Westinghouse Fusion Power Systems Department and G. Wahl, Union Carbide Co., Linde Division, New Castle, Pennsylvania.

12. Private Communication, June 1981. Discussion between J. S. Karbowski of Westinghouse Fusion Power Systems Department and J. Schuler, METCO Inc., Westbury, L. I., New York.

13. J. H. DeVan, "Compatibility of Structural Material with Fusion Reactor Coolant and Breeder Fluids, Journal of Nuclear Materials, 85 & 86, pp. 249-256 (1979).

14. J. Kimlinger and E. Plechaty, TARTNP User's Manual, UCID-17026, February 9, 1976.

15. E. Plechaty and J. Kimlinger, TARTNP: A coupled Neutron-Photon Monte Carlo Transport Code, Lawrence Livermore National Laboratory Report UCRL-50400, Vol. 14, July 4, 1976.

16. R. J. Howerton R. C. Haight, M. H. Macgregor, E. F. Plechaty, and S. T. Perkins, "An Integrated System for Production of Neutronics and Photonics Calculational Constants " Vol 15, The LLL Evaluated Nuclear Data Library (ENDL): Evaluation Technique, Graphical Displays and Descriptions of Individual Evaluations, Lawrence Livermore National Laboratory Report UCRL-50400 (September 1975).

17 R. J. Doyas, R. E. Dye, R. J. Howerton. and S. T. Perkins, "An Integrated System for Production of Neutronics and Photonics Calculational Constants," Vol. 5, Rev. 1, CLYDE, A Code for the Production of Calculational Constants from Nuclear Data, Lawrence Livermore National Laboratory Report UCRL-50400 (September 1975).

18. D. Garber, C. Dunford, and S. Pearlstein (eds.), "Data Formats and Procedures for the Evaluated Nuclear Data File ENDF/B-V," National Nuclear Data Center, Brookhaven National Laboratory Report BNL-NCS-50496/ENDF-102 (1979).

19. R. W. Moir, "Hybrid Reactors", Lawrence Livermore National Laboratory Report UCRL-84826, Rev. 1, March 1981.

20. J. C. R. Hunt and R. Hancox, "The Use of Liquid Lithium as Coolant in a Toroidal Fusion Reactor Part I. Calculation of Pumping Power," CLM-R115, October 1971.

21. R. P. Rose, "Design Study of a Fusion-Driven Tokamak Hybrid Reactor for Fissile Fuel Production," Westinghouse Electric Corporation Project RF-47-1-3 Final Report, EPRI Report ER-1083, May 1979.

22. W. M. Wells, "Experiments and Calculations on the Feasibility of Pumping Liquid Lithium in a Thermonuclear Reactor Blanket," Lawrence Livermore National Laboratory Report UCRL-50544, February 1969.

23. M. A. Hoffman and G. A. Carlson, "Calculation Techniques for Estimating the Pressure Losses for Conducting Fluid Flows in Magnetic Fields," Lawrence Livermore National Laboratory Report UCRL-51010, February 1971.

24. G. A. Carlson, "Magnetohydrodynamic Pressure Drop of Lithium Flowing in Conducting Wall Pipe in a Transverse Magnetic Field: Theory and Experiment," UCRL-75307, 1st Topical Meeting on the Technology of Controlled Nuclear Fusion, April 1974.

25. C. C. Alexion, Westinghouse R&D Center, Private Communications, July 1, 1981.

26. S. Cantor, Ed., "Physical Properties of Molten-Salt Reactor Fuel Coolant, and Flush Salts," Oak Ridge National Laboratory Report ORNL/TM-2316, August 1968.

27. B. L. Pierce and H. J. Stumpf, "TAP-A: A Program for Computing Transient or Steady State Temperature Distributions," Westinghouse Astronuclear Laboratory Report WANL-TME-1872, December 1969.

28. F. H. Tenney, "A Tokamak Hybrid Study in US-USSR Symposium on Fusion-Fission Reactors," Livermore, CA, July 13-16, CONF-760733, July 1976, pp. 71-80.

29. D. T. Aase, M. C. C. Bampton, T. J. Doherty, et al., "TCT Hybrid Preconceptual Blanket Design Studies," Battelle Pacific Northwest Laboratories Report, PNL-2304, January 1978.

30. V. L. Blinkin and J. M. Novikov, "Optimum Symbiotic System of Fission-Fusion Molten Salt Reactors," I. V. Kurchatov Institute of Atomic Energy, IAE-2819, 1977.

31. J. W. H. Chi and R. P. Rose, "Fusion Fission Feasibility-Blanket Data Requirement," Westinghouse Electric Corporation Report WFPS-TME-81-007, December 1980.

32. V. A. Maroni, et al., "Some Preliminary Considerations of a Molten Salt Extraction Process to Remove Tritium from Liquid Lithium Fusion Reactor Blankets," Nucl. Tech., 25, 83 (1975).

33. N. Ghoneim and R. H. Whitley, "Hastelloy Irradiation Damage Studies for the TMHR Liquid Lithium/Molten Salt Blanket," Draft TRW Report (Reference TRW-TMHR-120), November 1981, May be obtained from R. Whitley, TRW, One Space Park, Redondo Beach, CA.

34. Y. Gohar and M. A. Abdou, "MACKLIB-IV, a Library of Nuclear Response Functions Generated with the MACK-IV Computer Program from ENDF/B-IV", Radiation Shielding Information Center, DLC-60, March 1978.

35. D. R. Olander, Fundamental Aspects of Nuclear Reactor Fuel Elements, University of California, TID-26711-P1 (1976).

36. W. M. Wells, "Lithium as a Blanket Coolant," in <u>Proceedings from the Seventh Symposium on Engineering Problems of Fusion Research</u>, Vol. II, Knoxville TN., October 25-28, 1977, pp. 1707-1712, Institute of Electrical and Electronics Engineers, New York, 1977

37. J. T. D. Mitchell and J. A. Booth, "Comparison of Direct and Indirect Cooling of Fusion-Reactor Blanket Containing Lithium," In <u>Proceedings of the Seventh Symposium on Fusion Technology</u>, Grenoble, France, EUR-4938, October 24-27, 1972, pp. 125-130.

38. B. Badger, et al., "WITAMIR-1: A University of Wisconsin Tandem Mirror Reactor Design," University of Wisconsin Report UWFDM-400 (1980).

39. "Fusion Reactor Blanket/Shield Design Study," Argonne National Laboratory Report ANL/FPP-79-1 (1979).

CHAPTER V

REFERENCE GAS COOLED BLANKET DESIGN

V.A. DESIGN OVERVIEW

V.A.1. Concept Description and Motivation

The General Atomic beryllium/thorium oxide suspension blanket is a
two zone design which is helium cooled, uses beryllium as a neutron
multiplier, thorium oxide as a fertile fuel, and $Li_{17}Pb_{83}$ as a tritium
breeding and heat transfer material. A perspective view of the reference
blanket is shown in Figure V-1.

As a result of the use of beryllium as a neutron multiplier, this
design achieves excellent breeding performance (fissile breeding ratio
of 0.73 for tritium breeding ratio of 1.05) with a very low fission rate
($\sim$ 0.03 per fusion). Fast and thermal fissioning in the beryllium/thorium
oxide suspension blanket is suppressed in several ways (see section V.B).
Most importantly, the concept of fertile dilution is used. In particular,
the thorium oxide volume fraction in the blanket is less than 3%. As a
result, the macroscopic fast fission cross section for thorium above the
fission threshold energy ($\simeq$1.2 MeV) is only a small fraction of the total
macroscopic cross section above the threshold (which in this case is
dominated by ^{9}Be(n,2n). Below the fast fission threshold (i.e., in the
resonance region) the thorium (n,γ) cross section is large enough however,
to provide the desired level of fissile breeding at very low thorium
concentrations. Fast fissioning is also reduced due to the strong neutron
energy moderation properties of the beryllium multiplier.

Fissioning of ^{233}U in this blanket is suppressed in three ways.
First, the fissile fuel bred in the blanket is discharged at very low
concentration (typically 0.5% ^{233}U in thorium). Second, for a fixed
fissile discharge enrichment, a consequence of fertile dilution is a very
low concentration of fissile material (e.g., 0.5% x 3% = 0.015% by volume)
in the blanket. Third, in the reference system, the above fissile discharge
enrichment can be achieved during a 1-2 month fuel residence time. As a
result, ^{233}Pa($T^{1/2}$=27d) does not reach isotopic equilibrium during the fuel
residence time and, consequently, most of the bred material ($\sim$60%) prior
to discharge from the blanket, will be in the form of ^{233}Pa rather
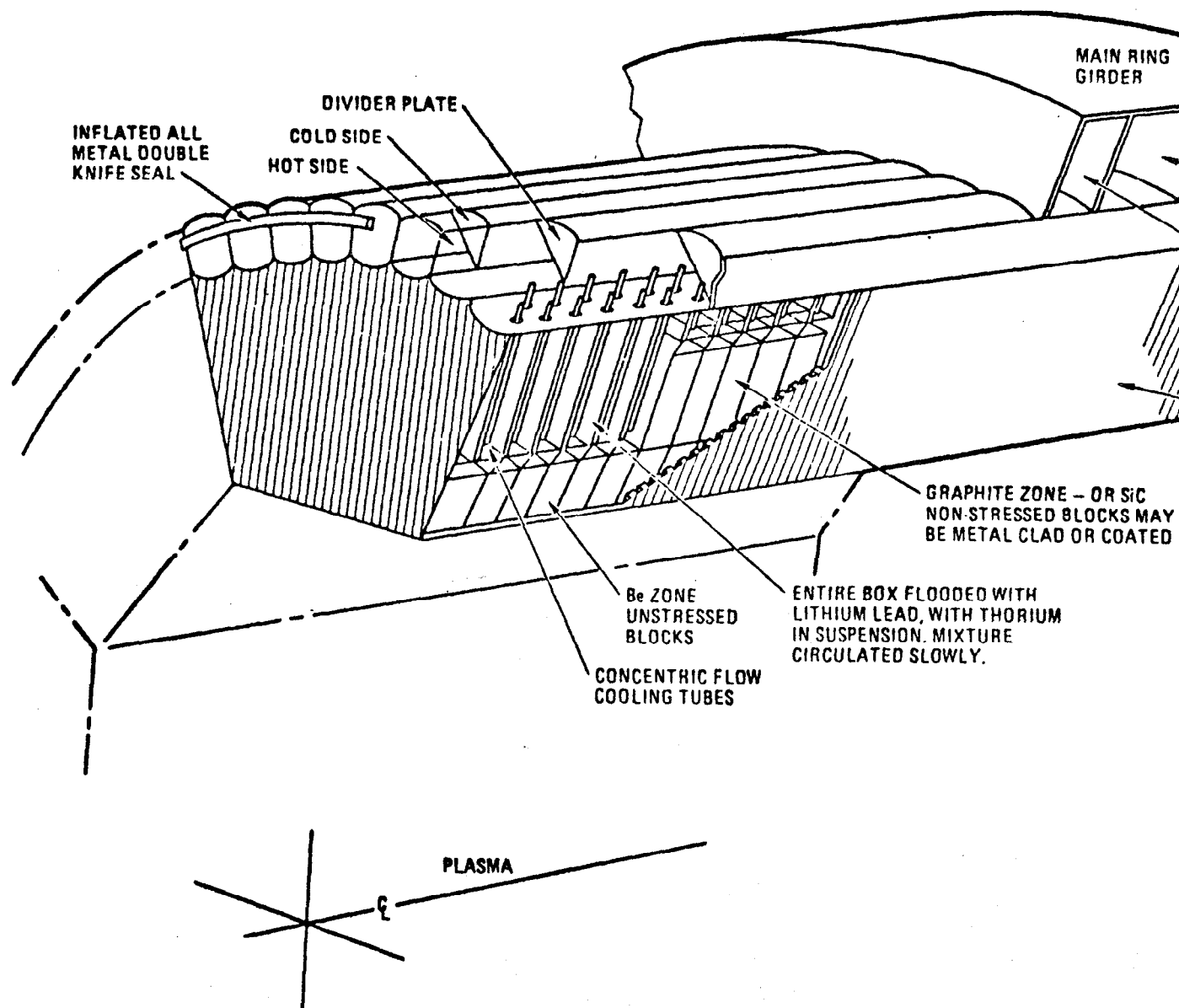
FIGURE V-1. Reference Beryllium/Thorium Oxide Suspension Blanket

than ^{233}U. This effect reduces the amount of thermal fissioning and improves the net fessile breeding ratio.

In addition to its suppressed fission characteristics, this concept introduces several novel design features. To begin, pressurization of the entire blanket module is not required (see sections V.D. and V.E.) Rather, the helium coolant is confined to annular high pressure ($\sim$50 Atm) tubes which penetrate the blanket. The coolant flows from the inlet manifold through the center of each tube, turns near the first wall, and exits to the outlet manifold along the outside annulus of each tube. This concept results in a considerable savings in structural materials and improved neutronics and safety aspects relative to previous pressurized module designs.[1] The average thickness of the corrugated first wall is only 0.3 cm and the volume fraction of HT-9 ferritic steel in the blanket is only 4%.

Anoher novel design feature is the use of beryllium and the lead-lithium eutectic/thorium oxide suspension in this design. Since beryllium is predicted to swell up to 10% by volumr during a 10 year irradiation at 2 MW/M^2 wall loading(see section V.C.), space must be provided to accommodate such swelling. The suspension solves four problems. First, it fills the entire void between the fixed beryllium blocks and the pressurized coolant tubes. Seocnd, it provides conductive heat transfer between berylium blocks, thorium oxide fuel, and the coolant tubes. Third, it provides an excellent breeding material for both tritium and ^{233}U. Finally, it is expected that the lead-lithium density can be closely matched to that of thorium oxide so that the physical characteristics of the suspension can resemble those of a liquid if only a modest recirculating flow is incorporated into the system. During the lifetime of the blanket, the

beryllium blocks will swell and will displace 50% of the original volume of the suspension. Nevertheless, as discussed in section V.B, the heat transfer and breeding characteristics of the blanket can be preserved. The latter is accomplished by varying both the volumetric concentration of thorium in the suspension as well as the ^{6}Li enrichment in the lithium component of the suspension.

A unique advantage associated with this design is the use of materials which are not chemically reactive with water or other common materials

while achieving excellent breeding performance. Therefore, safety and design concerns normally associated with liquid metal and some solid lithium compounds (e.g., Li_7Pb_2) are avoided.[2]

V.A.2 Blanket Design and Performance Overview

Table V-1 is an overview of several key design and performance parameters for the beryllium/thorium oxide suspension TMHR blanket. These parameters are discussed in more detail throughout this chapter. Additional data relating to a reference TMHR based upon the beryllium/ thorium oxide suspension blanket is presented elsewhere in this report.

TABLE V-1. Key design and performance parameters for the reference beryllium/thorium oxide suspension blanket.

(Design Basis: 3000 MW fusion)

Mechanical Design

Central cell length	96 m
First wall radius	2 m
Number of blanket modules	24
Number of blanket submodules per blanket module[a]	8
First wall thickness[b]	0.3 cm (ave)
Beryllium multiplier zone thickness[c]	30 cm
Silicon carbide reflector zone thickness[c]	30 cm
Total blanket thickness	63 cm
Shield thickness	120 m
Magnet inner bore (diameter)	7.9 m
Magnet width	50 cm
Magnet pitch	4 m
Blanket structural material	HT9 steel

TABLE V-1 (Continued)

Power Flow and Thermal Hydrualic Design

Central cell fusion power	3000 MW
First wall surface heat load[d]	0.01 MW/m^2
First wall neutron loading	2.0 MW/m^2
Total thermal power removed by helium coolant[e]	4500 MW
Helium inlet/outlet temperatures	250/450°C
Helium coolant pressure[f]	50 atm (735 psia)
Pressure tube pitch separation	$\sim$4 cm
Number of pressure tubes per unit area	$\sim$800/m^2
$Li_{17}Pb_{83}/ThO_2$ suspension operating temperature	663°C
Beryllium operating temperature[f]	596°C
HT9 pressure tube operating temperature[f]	514°C
HT9 first wall operating temperature[f]	600°C

Nuclear Design and Performance[g]

^6Li enrichment in lithium component of lead-lithium	10-25%
Tritium breeding ratio[h]	1.05
^{233}U discharge enrichment in thorium[i]	$\sim$0.20%
^{233}Pa discharge enrichment in thorium[i]	$\sim$0.38%
Net fissile breeding ratio	0.73
Net fissile production rate[i]	9475 kg/yr
Fuel residence time[i]	36 days
Fissions in ^{232}Tn per fusion[j]	0.007
Fission in ^{233}U per fusion[j]	0.019
Fission power[j]	840
Blanket energy multiplication[j]	1.86

[a]These are aximuthally oriented and make the first wall octagonal in shape

[b]Effective thickness for corrugated first wall

[c]Also contains $Li_{17}Pb_{83}/ThO_2$ suspension for breeding and heat transfer

[d]Dominated by Bremsstrahlung radiation

[e]Includes first wall surface heat contribution

[f]Maximum strady state quantities

[g]Includes 2-D leakage and other adjustments to 1-D calculations

TABLE V-1   (Continued)

[h]Must breed at least 1.027 to compensate for breeding losses due to 80 MW
fusion power in end plugs

[i]At 100% plant capacity

[j]Average over blanket lifetime

V.A.3   Overview of Blanket Design Issues

The beryllium/thorium oxide blanket design described in the following
sections has several attractive design and performance characteristics.
The reference design results in an efficient capability for fissile fuel
production as well as an excellent potential for reactor safety. For
this design, excellent breeding performance results from both the use of
beryllium as a neutron multiplier as well as a novel design configuration.
In particular, the pressure tube blanket concept results in a low structural
volume fraction and the fertile dilute lead-lithium/ThO_2 suspension permits
adequate fissile breeding, but effectively limits fissioning in the blanket.
Attractive reactor safety characteristics result because of the low fission
rate and because of the use of non-reactive materials (e.g., helium coolant
and lead-lithium eutectic).

In this chapter, several design issues are explored in some detail,
but others will require further resolution in future studies, and/or
development programs. These are briefly described below.

The first set of issues requiring further resolution relates to the
behavior of un-stressed beryllium blocks upon irradiation (section V.C.1).
In particular, the physical integrity of the blocks considering an
accumulation of 10% or more swelling (by volume) must be confirmed.
These blocks will also be subject to a large temperature gradient as well
as some temporal cycling due to power level adjustment, start-up, and
shutdown (similar to that occuring in LWR fuel rods). The solution to
this problem will require an experimental program.

A second set of issues concerns design solutions to accomodate the
failure of one or more high pressure coolant tubes. Two issues are involved.
First, due to the large number of coolant tubes ($\sim 800/m^2$) small leaks

may occur (in analogy to the small fraction of coolant tubes in a steam generator which are expected to leak at any given time). There is a reasonable level of confidence that such leaks can be accommodated routinely, without having to shut the system down, by providing a purge relief mechanism at the back of the blanket.

A second concern involves a gross failure of a coolant pipe near the first wall which could result in a sudden over pressurization of a local area of the blanket module followed by a rupture of the module. This situation is a particular concern since the module itself is designed for low pressure operation, the lead-lithium eutectic is a heavy and incompressable fluid, and the flow area in the neighborhood of the first wall is constricted by the corrugated wall and the beryllium blocks. It seems possible to remedy this situation via the use of simple burst tubes (see section V.D), however the number and location of such tubes and the actual behavior of the tubes (i.e., they might fill with lead-lithium before helium) requires further study and, possibly, an experimental program.

A third set of issues concerns the lead-lithium/ThO_2 suspension. In particular, the suspension requires a balance in the densities of the lead-lithium and the ThO_2. This balance must exist under the conditions of accumulated neutron fluence, different temperature regimes in different parts of the blanket, temporal cycling, and limited convective flow. Another issue concerning the suspension is related to chemical compatability issues (section V.C) which require resolution. For example, contact between the beryllium blocks and ThO_2 might be detrimental.

A fourth set of issues concerns heat transfer in the blanket (section V.E). The predicted first wall temperature of 600°C is acceptable but a multidimensional thermal analysis is required to better predict these temperatures. As a result, the design wall loading of 2 MW/m^2 might need to be reduced to limit the first wall temperature.

A fifth set of issues concerns fuel reprocessing for this design. Most importantly, as discussed in sections VII.A and VII.B, an inexpensive ($\gtrsim$ \$200/Kg thorium) THOREX reprocessing technology for low burn-up ($\sim$100 MWD/MT), high surface/volume ratio, un-clad ThO_2 particle fuels must be identified. A key question relating to the economics of

such a process is the ability to adequately dissolve ThO_2 with minimal additions of fluorine – a highly corrosive agent.

Two secondary reprocessing issues are also of importance. The first concerns tritium bred in the lead-lithium eutectic that reacts with the thorium oxide or otherwise becomes entrapped within thorium oxide fuel that is to be reprocessed. The magnitude of this transfer and its effect upon the reprocessing plant require additional study. Finally, separation of ThO_2 particles from the lead-lithium carrier fluid prior to reprocessing requires study to determine if this step would adversely impact overall economics.

In conclusion, the gas cooled beryllium/thorium oxide blanket features attractive performance and safety features, but several technological issues must be explored in greater depth before the attainment of this level of performance is assured in a feasible design.

V.B.1   Methods and Codes

The primary tool used in the nuclear analysis of the beryllium/thorium oxide blanket was the one-dimensional S_N neutron transport code, ANISN.[3] The problem was modeled in cylindrical geometry and the P_3S_6 scattering approximation was used. The data base used for this analysis, ENDF/B-IV,[4] was processed into ANISN type multigroup format using the AMPX system.[5] Table V-2 shows the energy group structure which was used. The 25 group set for all nuclides except thorium was created from the 100 group set called DLC-37[6] using the group collapse routines in AMPX and a 1/E spectrum to weight the 100 group set. The thorium nuclear data are from the DLC-41[7] library and were also collapsed into the same group structure. MACKLIB-IV,[8] also based on ENDF/B-IV, was the source of reaction rate and energy deposition data. This activity data was collapsed from 171 groups to the energy group structure shown in Table V-2 using the same 1/E spectrum and was incorporated into the ANISN activity table format. ANISN was then able to produce reaction rates and energy depositions as a function of zone or meshpoint. Note that the gamma-ray energy released from the Th(n,γ) reaction is to be assumed to deposit entirely in the thorium material since the gamma production cross section for thorium is not available at this time.

ANISN is a widely used and well documented code which is capable of providing highly accurate estimates of the flux and reaction rates for one-dimensional scoping analysis. However, the above model has known shortcomings in two areas. First, the TMHR central cell is long (∿96 m), but finite in extent. As a result, neutron leakage out the two ends is a 2-D concern and an adjustment to the 1-D ANISN results is required to account for such losses. This adjustment and others are described in more detail in Section V.B.3.e.

Second, although the ENDF/B data is widely used, the [9]Be(n,2n') evaluations in ENDF/B-IV and the more recent ENDF/B-V are known to produce excessive neutron multiplication in thick assemblies of beryllium (such as the blanket described in this chapter). This effect is fully described in Section V.B.2 (benchmark results) and Section V.B.4 (sensitivity and uncertainty analysis).

TABLE V-2.   Neutron 25 energy group structure (in eV).

| Group | Group Limits (eV) | | |
	E (Top)	E (Low)	E (Midpoint)
1	1.4918 (+7)	1.3499 (+7)	1.4208 (+7)
2	1.3499 (+7)	1.2214 (+7)	1.2856 (+7)
3	1.2214 (+7)	1.1052 (+7)	1.1633 (+7)
4	1.1052 (+7)	1.0000 (+7)	1.0526 (+7)
5	1.0000 (+7)	9.0484 (+6)	9.5242 (+6)
6	9.0484 (+6)	8.1873 (+6)	8.6178 (+6)
7	8.1873 (+6)	7.4082 (+6)	7.7979 (+6)
8	7.4082 (+6)	6.7032 (+6)	7.0557 (+6)
9	6.7032 (+6)	6.0653 (+6)	6.3843 (+6)
10	6.0653 (+6)	5.4881 (+6)	5.7787 (+6)
11	5.4881 (+6)	4.4933 (+6)	4.9907 (+6)
12	4.4933 (+6)	3.6788 (+6)	4.0860 (+6)
13	3.6788 (+6)	3.0119 (+6)	3.3453 (+6)
14	3.0119 (+6)	2.4660 (+6)	2.7390 (+6)
15	2.4660 (+6)	1.3534 (+6)	1.9097 (+6)
16	1.3534 (+6)	7.4274 (+5)	1.0481 (+6)
17	7.4274 (+5)	4.0762 (+5)	5.7518 (+5)
18	4.0762 (+5)	1.6573 (+5)	2.8667 (+5)
19	1.6573 (+5)	3.1828 (+4)	9.8778 (+4)
20	3.1828 (+4)	3.3546 (+3)	1.7591 (+4)
21	3.3546 (+3)	3.5358 (+2)	1.8541 (+3)
22	3.5358 (+2)	3.7267 (+1)	1.9542 (+2)
23	3.7267 (+1)	3.9279 (+0)	2.0597 (+1)
24	3.9279 (+0)	4.1399 (−1)	2.1718 (+0)
25	4.1399 (−1)	2.2000 (−2)	2.1800 (−1)

As discussed in Section V.B.3.e, 0.05 should be subtracted from the total tritium plus fissile breeding to compensate for excessive breeding predicted by the ENDF/B data set.

In summary, the use of ANISN and ENDF/B produces satisfactory estimates of blanket performance, especially for scoping studies. However, two important adjustments must be kept in mind: (1) end cell effects somewhat reduce tritium breeding performance/ and (2) ^{9}Be(n,2n') performance is over-estimated in ENDF/B and produces optimistic estimates of blanket breeding. Both of these factors are addressed in the following sections and a lumped estimate of performance for the reference system is provided in Section V.B.3.e.

V.B.2 Beryllium Blanket Benchmarks Comparing ENDL and ENDF/B Data Bases

As discussed in Section V.B.1, recent ENDF/B cross section evaluations are expected to overestimate both neutron multiplication and tritium and fissile breeding[9] — particularly due to differences in the representation of the ^{9}Be(n,2n') reaction. In contrast, ^{9}Be(n,2n') evaluations in the LLNL ENDL[10] data set and a recent modification of the ENDF/B representation for ^{9}Be(n,2n') performed by LASL[11] are expected to provide more conservative estimates of integrated quantities such as tritium production and fissile breeding. In this section, data base effects using ANISN[3] and ENDF/B data versus the TARTNP Monte Carlo code[10] and ENDL data are compared. Additional benchmark results comparing ANISN and ENDF/B data versus ANISN with the same ENDF/B data but using the LASL evaluation for ^{9}Be are presented in Section V.B.4 (where a more complete discussion of this evaluation is presented).

The one-dimensional geometry used for the benchmark comparison is shown in Fig. V-2. It is important to note that this geometry (unlike that considered in Section V.B.4) does not correspond to the final design concept, but is representative of suppressed fision blankets featuring beryllium multiplication. Table V-3 shows the results of the benchmark analysis. Note that ^{233}U has been added in three of the cases to simulate fissile buildup during irradiation. The ANISN cases use the DLC-37 and DLC-41 libraries collapsed to 25 groups. Both the TARTNP calculations use the newest ENDL data. Tritium and fissile breeding are lower in the TARTNP/ENDL analysis. The TBRs differ by ~3% for the 0% ^{233}U case. Net fissile breeding differs by ~7.5%. Total breeding (T+F) differs by ~5.2%. ^{9}Be(n,2n) reactions vary by ~5.0%. M is also lower by ~5.6%.

In conclusion, the use of ENDF/B data in ANISN type format results in higher ^{9}Be(n,2n') reaction rates. This results in slightly higher total breeding rates than predicted using TARTNP and ENDL data.
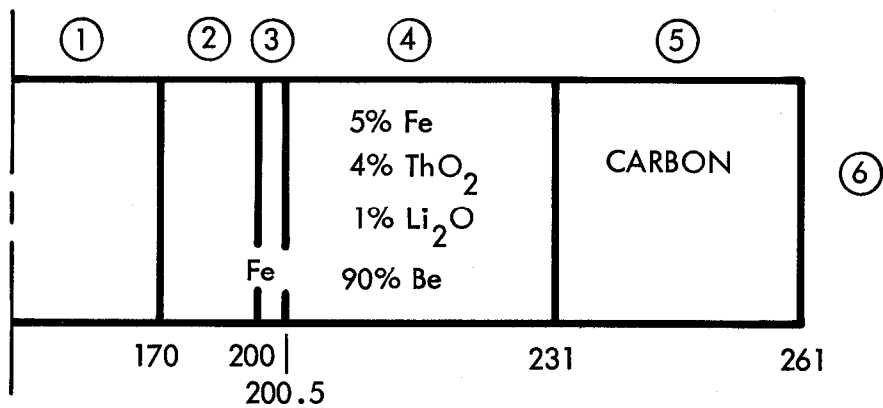
TARTNP CYLINDRICAL CROSS SECTION SIMULATION

ZONE	DESCRIPTION
①	PLASMA
②	VACUUM
③	Fe FIRST WALL
④	FUEL REGION
⑤	REFLECTOR
⑥	LEAKAGE

FIGURE V-2. Beryllium blanket neutronics benchmark.

TABLE V-3. Beryllium blanket benchmark calculation: ANISN/ENDF versus TARTNP/ENDL comparison.

	TARTNP 0% ^{233}U	TARTNP 0.25% ^{233}U	Case ANISN 0% ^{233}U	ANISN 0.1% ^{233}U	ANISN 2% ^{233}U
Tritium, T	0.981	0.996	1.01	1.03	1.18
^{6}Li(n,t)	0.977	0.991			
^{7}Li(n,n't)	0.004	0.005			
Net fissile bred, F	0.86	0.85	0.93	0.92	0.86
Total fission rate	0.007	0.038	0.0068	0.023	0.38
Be(n,2n)	1.32	1.32	1.39	1.39	1.50
Leakage	0.08	0.09			
M=E_{DEP}/14.1	1.51	1.93	1.6	1.8	6.6
T+F	1.84	1.845	1.94	1.95	2.04

V.B.3 Reference System Performance

V.B.3.a Overview. As far as the beryllium hybrid blanket performance is
concerned, there are several important parameters to be considered, namely
the beryllium zone thickness, the volume fraction of lithium lead suspension
liquid in the blanket, the volume fraction of fertile material in the sus-
pension liquid and the ^{6}Li enrichment in lithium. We performed a parametric
investigation which considered the above parameters and took the mechanical,
thermal-hydraulic and beryllium design aspects into consideration. A final
blanket design was derived from this preliminary investigation and is dis-
cussed in this section.

Figure V-3 shows schematically the one-dimensional blanket model for the
gas-cooled TMHR blanket design. The blanket structure is made of HT-9 ferritic
steel. It consists of a 3 mm thick first wall, a 0.3 m beryllium zone, a
0.3 m SiC reflector zone and a helium plenum zone which is a pressure vessel
and simulated by a net HT-9 ferritic steel plate of 30 mm in the neutronic
model. The beryllium zone at the beginning of blanket life is composed of
4% ferritic steel, 10% helium coolant, 66% beryllium, and 20% suspension
liquid, all by volume. The beryllium blocks in this zone are made of sintered
products of beryllium and the density of the beryllium is about 80% of the
theoretical density. After several years of neutron irradiation, the beryllium
swells and the volume increases to a saturation value of about 76% assuming
an average swelling of 10% in the blanket as will be discussed later in
Sec. V.C. The corresponding beryllium density drops to about 70% of the
theoretical density. The blanket volume fraction for the suspension liquid
in the beryllium zone thus is reduced to 10% at the stage close to the end
of blanket life (about 10 years). The material composition in the SiC
reflector zone is constant. It consists of 4% ferritic steel, 10% helium
coolant, 78% SiC and 10% suspension liquid, again all by volume.

The ThO_2 fertile fuel content in the suspension liquid and the percent
^{6}Li in lithium are important variables in the blanket for obtaining an opti-
mized blanket operation since the suspension liquid volume fraction in the
blanket decreases with increasing neutron fluence. To determine the ThO_2
and ^{6}Li contents in the suspension liquid, the neutronic performance, namely
fissile and tritium production rates, and the fissile enrichment rate, which
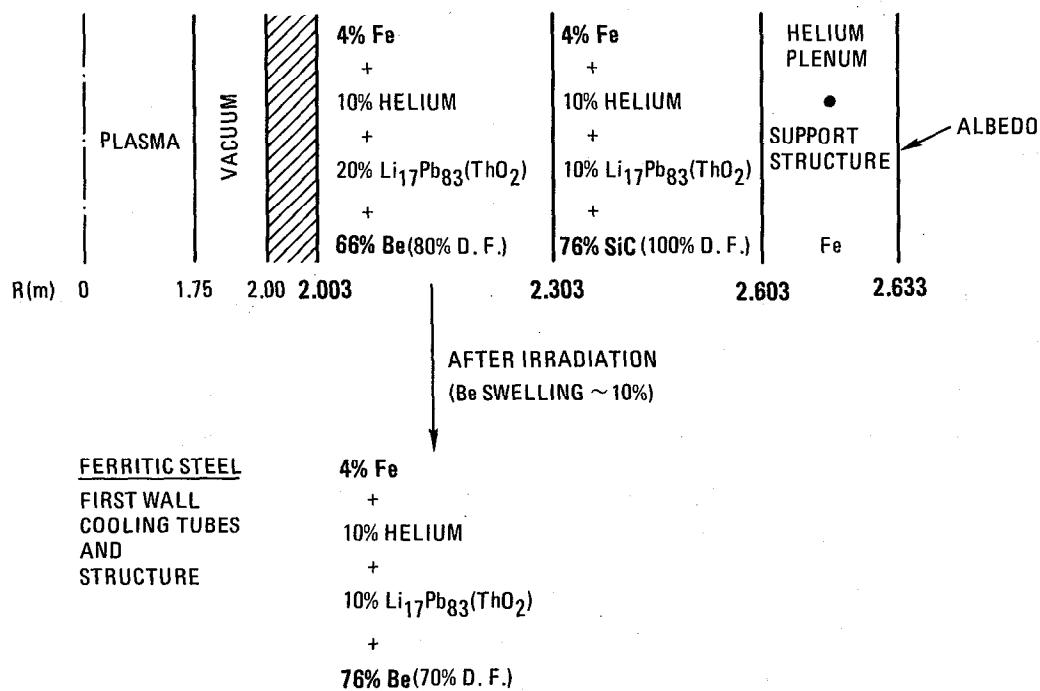
FIGURE V-3. Schematic of the final beryllium blanket configuration for neutronic calculations.

The figure shows the radial configuration with the following labeled regions along R(m):

PLASMA | VACUUM | (hatched first wall region) | region 1 | region 2 | HELIUM PLENUM

R(m): 0   1.75   2.00 2.003   2.303   2.603   2.633

Region 1 (2.003–2.303):
4% Fe
+
10% HELIUM
+
20% $Li_{17}Pb_{83}(ThO_2)$
+
66% Be(80% D. F.)

Region 2 (2.303–2.603):
4% Fe
+
10% HELIUM
+
10% $Li_{17}Pb_{83}(ThO_2)$
+
76% SiC (100% D. F.)

HELIUM PLENUM / SUPPORT STRUCTURE (2.603–2.633):
HELIUM
PLENUM
•
SUPPORT STRUCTURE
Fe

ALBEDO

AFTER IRRADIATION
(Be SWELLING ~10%)

FERRITIC STEEL
FIRST WALL
COOLING TUBES
AND
STRUCTURE

4% Fe
+
10% HELIUM
+
10% $Li_{17}Pb_{83}(ThO_2)$
+
76% Be(70% D. F.)

is inversely proportional to the ThO_2 concentration in the suspension liquid, must be considered. The amount of ThO_2 material in the suspension liquid is a tradeoff between the fissile fuel production rate and the enrichment rate. The amount of ^6Li in lithium, however, is controlled by the required tritium breeding ratio (which was assumed to be 1.12* tritons per D-T neutron in the 1-D design calculations) and the amount of ThO_2 fuel in the suspension liquid. For a suspension liquid containing less ^6Li, the corresponding ThO_2 content is smaller and therefore the total (fissile + tritium) breeding rate is reduced due to increased parasitic absorptions. To achieve the maximum total breeding rate, increases in ^6Li in lithium and ThO_2 in the suspension liquid are preferred until neutron capture in the non-fertile materials is unimportant.

Figure V-4 displays the calculated $^{232}Th(n,\gamma)$ reaction rate for a fixed tritium breeding ratio of 1.10 tritons per D-T neutron as a function of the ThO_2 volume fraction in the blanket and the ^6Li enrichment in lithium. These are given for the blanket at beginning of life and at end of life. A design of 15% ThO_2 by volume in the $Li_{17}Pb_{83}$ suspension liquid is found to be the best composition at the beginning of life. The corresponding ^6Li content in lithium is also about 15% to produce the required tritium breeding ratio of 1.12 tritons per D-T neutron. At the end of blanket life, the suspension liquid in the beryllium zone reduces to 10% by volume. The suggested volume fraction of the ThO_2 fertile fuel becomes 25% and the corresponding ^6Li fraction in lithium is found to be 25% meeting the tritium breeding requirement. If lower tritium breeding rates are desired, the ^6Li fraction would be slightly reduced with the result that fissile breeding would increase slightly. Table V-4 summarizes the blanket configuration and the material composition by zone for the reference design. The calculated fissile (U + Pa) production rate in this blanket is found to be about 0.8 atoms per D-T neutron both at beginning and end of life. The fissile concentration in the blanket accumulates as the fertile material resides in it and the blanket nuclear heating increases due to thermal fissioning in the bred uranium. One of the attractive features of the blanket concept proposed in this design study is the rapid buildup of fissile material concentration

---

*Later revised to 1.05 based upon 2-D design calculations as discussed in Section V.B.3.e.
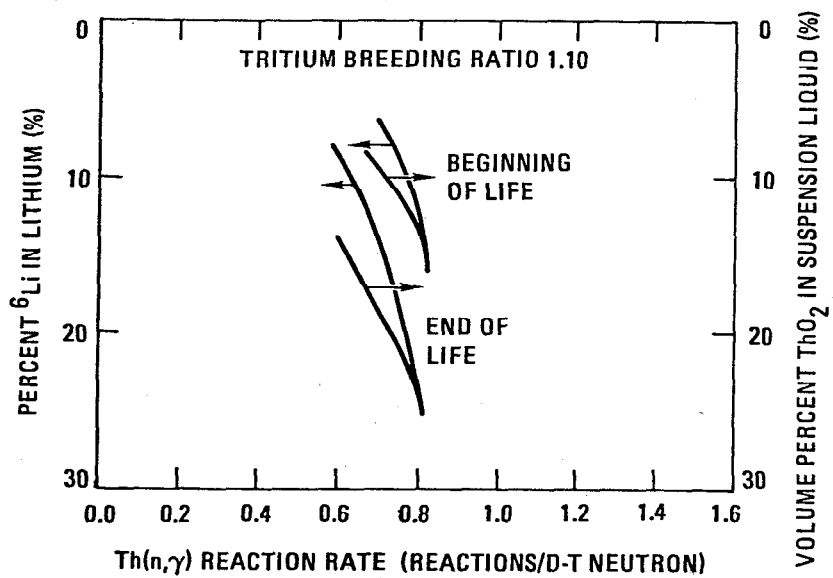
FIGURE V-4.   Fissile production rate in the beryllium
hybrid blanket as functions of ^{6}Li enrichment
in lithium and ThO$_2$ volume fraction in the
suspension liquid.   The tritium breeding
ratio is 1 — 10 tritons per D-T neutron.

TABLE V-4.   Summary of the blanket configuration and material composition by zone for the reference TMHR design.

	Beginning of Life	End of Life
Beryllium zone (Neutron multiplication)	4% ferritic steel 10% helium 66% beryllium (80% dense) 20% suspension liquid	4% ferritic steel 10% helium 76% beryllium (70% dense) 10% suspension liquid
SiC zone (reflector)	4% ferritic steel 10% helium 76% SiC 10% suspension liquid	4% ferritic steel 10% helium 76% SiC 10% suspension liquid
Composition of suspension liquid	15% ThO_2 + 85% $Li_{17}Pb_{83}$ (15% ^6Li in lithium)	25% ThO_2 + 75% $Li_{17}Pb_{83}$ (25% ^6Li in lithium)

in the fertile material. The high thorium capture rate (0.73 per fusion neutron*) and the low ThO_2 inventory (2.5 volume %) result in a rapid buildup of fissile concentration. After only 34 days residence time in the blanket, ThO_2 is enriched to about 0.6% fissile material. Because of the rapid buildup, most of the fissile material is still in the form of ^{233}Pa, the 27 day half-life precursor of ^{233}U. By slowly circulating the Li-Pb suspension liquid through the blanket such that the ThO_2 residence time is 34 days, the discharge ^{233}Pa and ^{233}U concentrations are 0.4 and 0.2%, respectively. The ^{233}Pa will decay to ^{233}U outside the blanket, giving an effective fissile concentration of 0.6%, yet during its residence time in the blanket the average ^{233}U concentration is only ~0.1%, giving excellent suppression of thermal fissions.

---

*Adjusted for 2-D leakage effects as discussed in Section V.B.3.e.

The above analysis assumes a plant capacity factor of 100% (i.e., base-load operation) during the fuel residence time. If the blanket experiences a 70% capacity factor during the fuel residence time, the ^{233}Pa/^{233}U ratio will decrease. In this case, the design ^{233}U level of 0.2% would be achieved in 44 days, but the overall fissile discharge enrichment would decrease to 0.5%. Since expensive fuel reprocessing costs are inversely proportional to the overall fissile discharge concentration, this blanket will benefit from a high average availability factor during the fuel residence time. This may be accomplished by scheduling maintenance operations on either side of the batch irradiation period whenever possible.

The neutronic calculations for the above-mentioned blanket were performed. The breeding performance, nuclear heating, and characteristics for this blanket both at beginning and end of blanket life are displayed in Figs. B-5 through V-7 and tabulated in Tables V-5 through V-7. They are also discussed in more detail in the following subsections.

V.B.3.b <u>Fissile Production</u>. Table V-5 lists the major nuclear reaction rates in the gas-cooled TMHR blanket at both beginning and end of life. For these particular suspension liquid compositions and for discharge ^{233}U concentration, the calculated neutron capture reactions in thorium are 0.838 and 0.829 reactions per D-T neutron, respectively. For the continuous flow fuel cycle, the bred fissile atoms undergo fission, capture and other transmutation reactions which result in a decrease of the fissile production rate. The net fissile (U + Pa) production rates at beginning and end of life are 0.823 and 0.812 atoms per D-T neutron, respectively. Note that most of the fissile destruction reactions are due to fissioning as shown in Table V-6. The decrease of fissile production rate due to neutron reactions with the accumulated protactinium (~0.4% in thorium) is expected to be small and is not included here since at the time of the neutronics calculations, ^{233}Pa reaction cross sections are not available.

Figure V-5 shows the spatial distribution of the Th(n,γ) reaction rate in the suspension liquid at beginning and end of life. From this figure it may be seen that the fissile production rate varies by more than one order of magnitude from the front to the back of the blanket. The "enrichment" rates or rates of buildup of fissile material in thorium are 0.05% per day

TABLE V-5. Major nuclear reaction rates in the beryllium TMHR blanket at beginning and end of blanket life, with discharge ^{233}U concentration (0.2% ^{233}U in thorium).

	Beginning of Life	End of Life
Tritium Breeding (T/n)		
^{6}Li(n,α)T	1.0743	1.0917
^{7}Li(n,n'α)T	0.0070	0.0033
Be(n,T)	0.0161	0.0176
Tritium breeding ratio	1.0974	1.1126
Thorium Reactions (R/n)		
Th(n,2n)	0.0218	0.0214
Th(n,3n)	0.0048	0.0045
Th(n,fission)	0.0068	0.0066
Th(n,γ)	0.8384	0.8287
Uranium Reactions (R/n)		
U(n,2n)	1.41×10^{-5}	1.39×10^{-5}
U(n,3n)	6.97×10^{-7}	6.48×10^{-7}
U(n,fission)	0.0136	0.0149
U(n,γ)	0.0019	0.0021
Net Fissile Production (U + Pa/n)	0.8229	0.8117
Neutron Multiplication Reactions (R/n)		
Be(n,2n)	0.9968	1.1370
Pb(n,2n)	0.1744	0.0894
Fe(n,2n)	0.0404	0.0424
Parasitic Absorption Reactions (R/n)		
Fe(n,γ)	0.1218	0.1455
Pb(n,γ)	0.0119	0.0067
Be(n,γ)	0.0058	0.0074
Si(n,γ)	0.0162	0.0136
High Energy Neutron Reactions (R/n)		
Fe(n,p)	0.0160	0.0174
Fe(n,α)	0.0091	0.0097
Be(n,p)	6.16×10^{-5}	6.72×10^{-5}
Be(n,α)	0.1076	0.1187
Si(n,p)	0.0162	0.0184
Si(n,α)	0.0077	0.0104
C(n,α)	0.0054	0.0074
C(n,n')3α	0.0055	0.0074
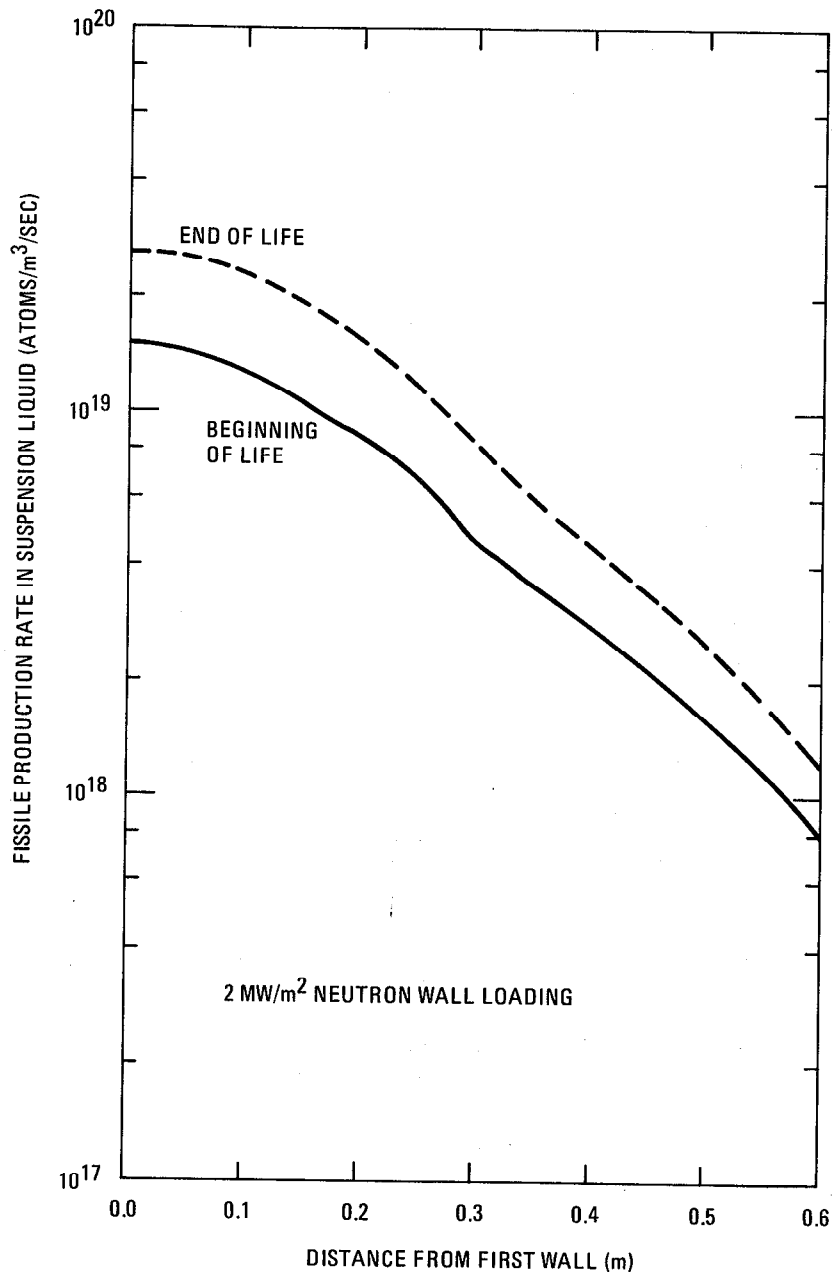
FIGURE V-5. Fissile production rate in the suspension
liquid at beginning and end of life.

and 0.002% per day, respectively, in the region behind the first wall and in front of the plenum. The blanket average enrichment rate is 0.018% per day.

V.B.3.c Tritium Breeding. Table V-5 also shows the tritium breeding performance in this TMHR blanket at beginning and end of life. The tritium breeding ratio is adjusted to not exceed the quantity needed by varying the ThO_2 and ^6Li concentrations. As shown in Table V-5, the calculated tritium treeding ratios are 1.10 and 1.11 tritons per D-T neutron at beginning and end of life, respectively, of which about 98% is contributed by the $^6Li(n,\alpha)$ reaction. The production of tritium from Be(n,T) reaction constitutes about 1.6% of the total tritium breeding. These would be decreased to about 1.05 in a design iteration by slightly decreasing the ^6Li enrichment.

Figure V-6 displays the spatial distribution of the tritium production (or ^6Li consumption) rate in the suspension liquid. The tritium production rate, very similar to the Th(n,γ) reaction rate, also varies by more than one order of magnitude from the first wall to the plenum region. The maximum ^6Li consumption rate occurs in the region close to the first wall and is 0.3% per day. However, the blanket average ^6Li consumption rate is about 0.12% per day. When considering the 30 day average fuel residence time, the total average ^6Li consumption during each cycle is 3.6% which must be supplied by makeup ^6Li in the suspension liquid to maintain adequate tritium breeding.

V.B.3.d Energy Deposition. Tables V-6 and V-7 list the blanket nuclear heating by zone and by element for the gas-cooled TMHR blanket at beginning and end of life, respectively. These tables reveal that the total blanket energy multiplication is high for this blanket and is 1.84 and 1.89 at beginning and end of life, respectively. The contribution from the bred uranium thermal fissioning is about 10% of the total blanket heating. Note that most of the blanket nuclear heating is produced by or deposited in beryllium, thorium, ^6Li, bred uranium and lead. Note also that more than 85% of the total blanket heating is deposited in the beryllium zone.

Figure V-7 displays the volumetric nuclear heating in the blanket at beginning and end of life. The average volumetric heating and the volumetric heating in the blanket components, namely the beryllium and suspension liquid
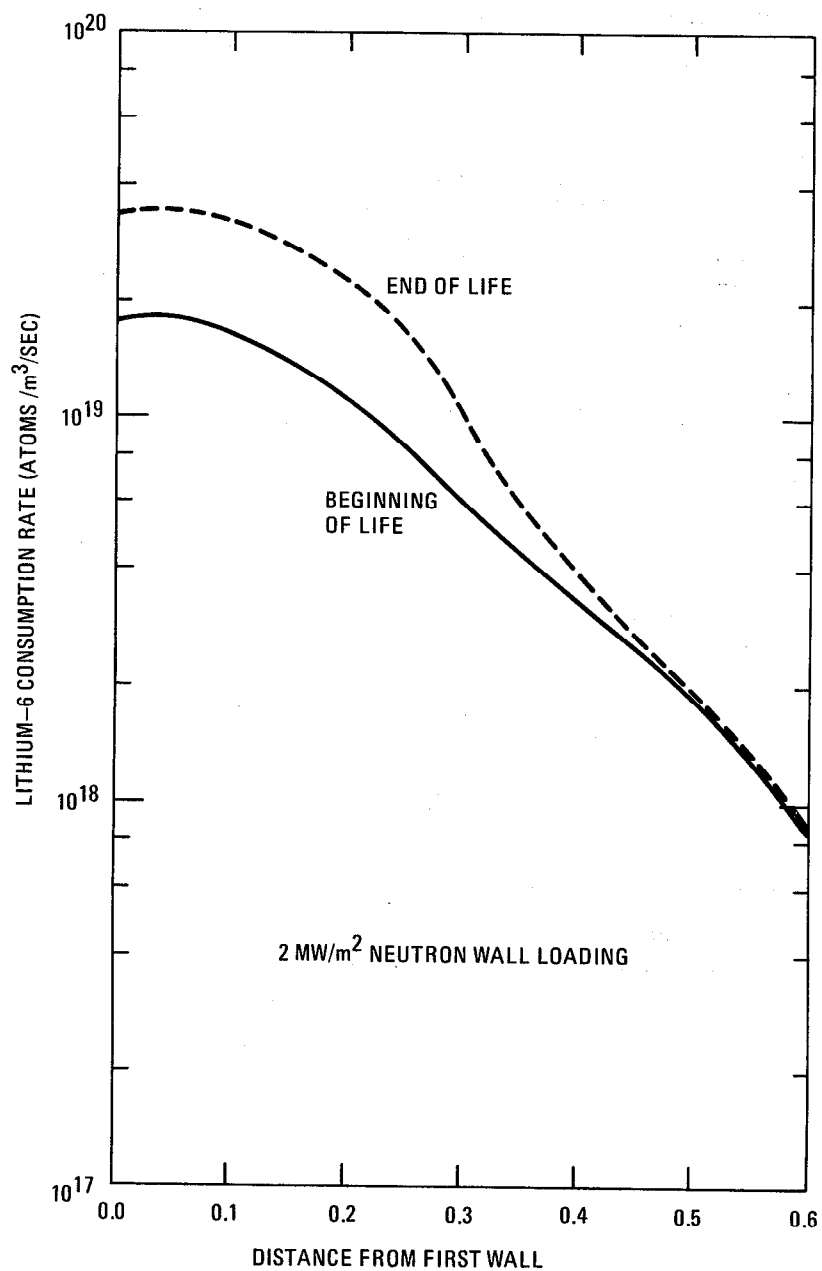
FIGURE V-6. ^{6}Li consumption rate in the
TMHR blanket at beginning
and end of life.

TABLE V-6. Nuclear heating by zone and element in the beryllium TMHR blanket at beginning of life (0.2% ^{233}U in thorium).

Element	Nuclear Heating (MeV/D-T Neutron)				
	First Wall	Beryllium Zone	SiC Zone	Plenum	Sum
Oxygen	---	0.1333	0.0074	---	0.1407
Carbon	---	---	0.3845	---	0.3845
Iron	0.3380	0.4542	0.0716	0.0728	0.9366
Lead	---	2.2438	0.2752	---	2.5190
Lithium-6	---	4.6180	0.5466	---	5.1646
Lithium-7	---	0.0864	0.0042	---	0.0906
Thorium	---	5.4032	0.5774	---	5.9806
(Fission)	---	(1.2385)	(0.0467)	---	(1.2852)
(Capture)	---	(4.1647)	(0.5307)	---	(4.6954)
Uranium	---	2.3120	0.2812	---	2.5932
Beryllium	---	7.6722	---	---	7.6722
Silicon	---	---	0.5299	---	0.5299
Sum	0.3380	22.9231	2.678	0.0728	26.0119

$$\text{Blanket energy multiplication} = \frac{26.01}{14.1} = 1.84$$

TABLE V-7. Nuclear heating by zone and element in the beryllium TMHR blanket at end of life (0.2% ^{233}U in thorium).

| Element | Nuclear Heating (MeV/D-T Neutron) | | | | |
	First Wall	Beryllium Zone	SiC Zone	Plenum	Sum
Beryllium	--	8.5438	--	--	8.5438
Carbon	--	--	0.5049	--	0.5049
Iron	0.3565	0.5756	0.0991	0.0799	1.1111
Lead	--	1.4417	0.3435	--	1.7852
Lithium-6	--	4.5685	0.6764	--	5.2450
Lithium-7	--	0.0379	0.0043	--	0.0422
Oxygen	--	0.1273	0.0166	--	0.1439
Silicon	--	--	0.7111	--	0.7111
Thorium	--	4.9328	0.9656	--	5.8984
(Fission)	--	(1.1514)	(0.1066)	--	(1.2580)
(Capture)	--	(3.7814)	(0.8590)	--	(4.6404)
Uranium	--	2.4159	0.4134	--	2.8293
Sum	0.3565	22.5162	3.7349	0.0799	26.6875

$$\text{Blanket energy multiplication} = \frac{26.68}{14.1} = 1.89$$
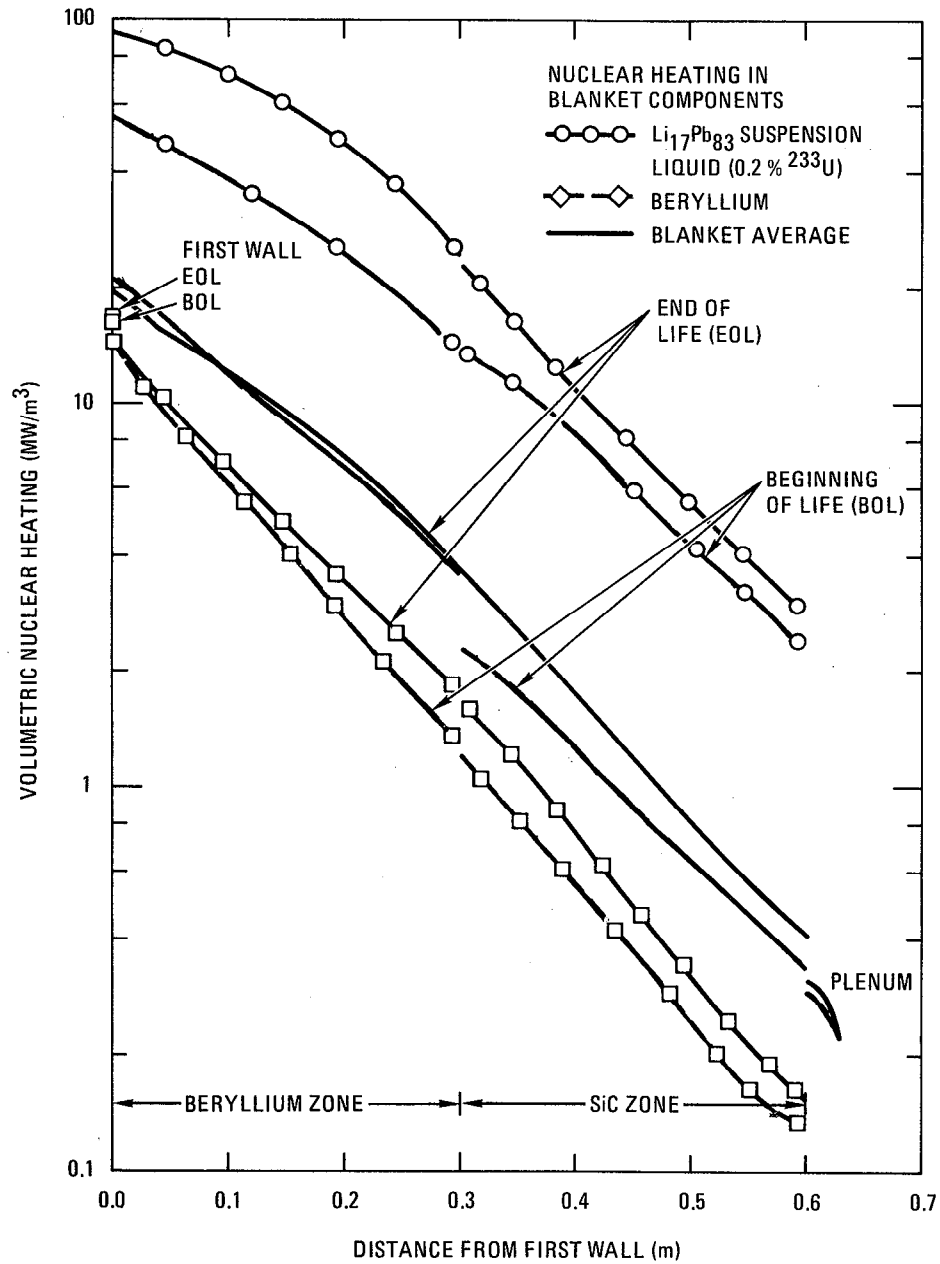
FIGURE V-7. Volumetric nuclear heating in the
blanket and blanket components at
beginning and end of life.

as well as the first wall, are all given in this figure. It can be seen that the average volumetric nuclear heating in the blanket and in the beryllium component are about the same at beginning and end of life. However, the nuclear heating in the suspension liquid varies quite appreciably at beginning and end of life, and their maximum values are about 56 and 90 MW/m^3, respectively. This is due to the change of the available volume in the blanket for the suspension liquid during blanket life since the nuclear energy produced or deposited in the suspension liquid remains about the same as seen in Tables V-6 and V-7.

V.B.3.e <u>Breeding Adjustments Due to 2-D Leakage and Other Effects</u>. Although the 1-D ANISN results presented in the preceding sections are adequate for blanket design purposes, some adjustments to the calculated breeding rates are required to account for geometric, nuclear data, and end plug effects which cannot be modeled adequately using ANISN and the ENDF/B-IV data. These effects include the following:

● Reductions in beryllium multiplication resulting from improved modeling of the ^{9}Be(n,2n) inelastic levels.

● Reductions in tritium and fissile breeding resulting from neutron leakage out the ends of the 96 m central cell (2 m first wall radius, 2 MW/m^2 neutron loading, 3000 MW fusion power).

● Adjustments in required tritium breeding to make up for fusions in the end plug region (where there is no breeding blanket) and a marginal net excess of tritium to account for uncertainties and process losses.

Considering the beryllium multiplication issue first, several evaluators have noted the fact that the present ENDF/B evaluation over-emphasizes the number of (n,2n) reactions resulting from excitation of the lowest inelastic level and correspondingly under-emphasizes the higher levels (see Section V.B.4.b). The result is an over-estimate of the energy of first emitted neutron with the result that an excessive number of additional (n,2n) reactions are predicted. Since the levels are more correctly modeled in a TARTNP/ENDL transport calculation, such a calculation for a benchmark case (see Section V.B.2) has been used to develop a calibration for this effect. The results of this calculation, although not conclusive, indicate that total breeding (i.e., T+F) will decrease by at least 0.05 when the

improved beryllium model is used. Consequently, the calculated 1-D T+F
value of 1.917 (average of BOL and EOL) is reduced to 1.87 to account for
improved modeling of beryllium cross section.

Since the TMHR blanket is long (96 m) but finite in extent, the sig-
nificant effect of neutron leakage out the vacuum vessel to the end cells
requires modeling. As shown in Table V-8, both T and F (for a blanket
geometry similar to, but not identical to the blanket shown in Fig. V-2)
decrease for a non-reflected case which considers end cell leakage.

TABLE V-8. Beryllium blanket end cell streaming.

END CELL MODEL	T	F	T+F	FISSIONS	M_F	END CELL LEAKAGE	BACK WALL LEAKAGE
Reflected	1.328	.618	1.95	.0054	1.40	----	.08
Non-Reflectd	1.262	.593	1.86	.0053	1.38	.062	.07

The above results may be used to better predict the expected performance
of the beryllium/thorium oxide blanket. In particular, adjusting the
above T+F value of 1.87 for end leakage by the ratio of the unreflected to
reflected T+F (i.e., 1.86/1.95) gives an improved estimate of T+F = 1.78.

Two additional adjustments are required to better define the necessary
tritium breeding ratio. First, for the axicell end plug configurations
being considered, about 80 MW of fusion power is produced in the plugs.
Since no tritium breeding blanket is assumed to exist in this region, addi-
tional tritium must be produced in the central cell blankets. For a 3000 MW
fusion central cell, the excess tritium breeding factor would be 1.027
(= 3080/3000). Finally, some excess tritium is required to account for
losses and uncertainties. If we assume that 2.2% net excess tritium is
required, then the central cell tritium breeding ratio requirement is
1.050. Subtracting the required tritium breeding ratio from the adjusted
T+F value above results in a decreased F value of 0.73.

These adjusted performance parameters are presented in Table V-9 and
are used throughout the report. Relating these results back to the

TABLE V-9. Adjusted breeding performance for the reference beryllium/thorium oxide blanket.

	AVERAGE 1-D ANISN RESULTS	ADJUSTED
Tritium Breeding		
^{6}Li (n,α)T	1.083	1.028
^{7}Li (n,n'α)T	0.005	0.005
Be (n,T)	0.017	0.017
TBR	1.105	1.050
Fissile Breeding		
^{232}Th(n,γ)	0.834	0.751
^{233}U (n,γ)	0.002	0.002
^{233}U (n,f)	0.019	0.019
Net fissile prod.	0.812	0.730

calculational model, a very minor design iteration is required to achieve performance very close to the adjusted values. Namely, the ^{6}Li enrichment would be decreased slightly (by perhaps 5%) to provide a 1.05 tritium breeding ratio after end leakage. The expected fissile breeding ratio would be 0.73, the adjusted value.

V.B.4 Summary of Beryllium Blanket Sensitivity and Uncertainty Analysis

The uncertainty analysis was concentrated on the effect of uncertainties in the Be(n,2n') cross section on the breeding performance of the beryllium blanket. The reason for this is that there is controversy over the value of the Be(n,2n') cross section and its representation in the ENDF/B format. Also, beryllium is a very significant material in the blanket because its neutronic performance affects both tritium and uranium breeding. Finally, other pure fusion and hybrid fusion designs rely on beryllium in the blanket to enhance performance. In these respects, the decision to concentrate the analysis on the beryllium cross section will produce results (including an operational methodology) which are both significant and timely.

The uncertainty analysis consisted of two parts: a discussion of the controversy surrounding the beryllium (n,2n') cross section and a direct evaluation of the effects of several different evaluations on breeding performance. The problem with the ENDF/B Be(n,2n') cross section is that the energy/angle correlation implicit in the representation is inadequate. ENDF/B represents the ^{9}Be(n,2n') reaction as up to four time-sequential processes which can decay through four discrete excitation levels of 1.68 MeV, 2.43 MeV, 6.76 MeV, and 11.28 MeV. This representation has been shown to be inadequate. Recent measurements by Drake et al.[12] have shown that while integrated experimental values for the (n,2n') reaction are in good agreement with ENDF/B-IV evaluation at 5.9, 10.1, and 14.2 MeV, the differential cross section, $\sigma(E \rightarrow E',\mu)$, is not. The investigations of Purser[13] and Basu[9] also support Drake's conclusions. Drake found that the low lying states in the ^{9}Be(n,2n') decay process are substantially over-emphasized. In addition, the ENDF/B format does not allow the incorporation of new ^{9}Be(n,2n') measurements since only four levels can be described.

A recent evaluation of ^{9}Be cross sections has been carried out by Young and Stewart (LASL-1979), and a modified ENDF/B format has been used to update and represent the ^{9}Be(n,2n') reaction.[11] Young and Stewart allow for up to 33 energy excitation bins which are based on a cluster of real ^{9}Be levels[12,14] near 2.43 MeV and a continuum representation[12] of the energies around 2.43 MeV. These energy bins implicitly represent the angular distribution of existing neutrons and are better able to do so because there are

33 rather than 4 levels. The integrated values of the (n,2n') cross section are still very similar to the unmodified ENDF/B values. It is the energy-angle correlation which has been improved.

The second part of the uncertainty evaluation involves the direct assessment of the different ^{9}Be(n,2n') representations by an application to the beryllium blanket. Tritium and ^{233}U breeding ratios were calculated using ANISN in cylindrical geometry (P_3S_4) with 25 neutron energy groups. The details of the reference blanket geometry are contained in Section V.B.3. Three different ^{9}Be(n,2n') evaluations were used: ENDF/B-IV (Be-IV), ENDF/B-V (Be-V), and LASL (Be-LASL). To minimize the sources of variation in the calculated breeding ratios, the ENDF/B-IV data base was used in all three cases for other materials present in the blanket. A summary of the results is shown in Table V-10.

In the Be-LASL evaluation case, both the uranium breeding ratio (R_u) and the tritium breeding ratio (R_{Li}) have decreased by 4.4% as compared to the corresponding values in the Be-V evaluation case. Consequently, the total breeding ratio ($R_u + R_{Li}$) has decreased by the same amount. Note that the decrease in Th(n,γ) and ^{6}Li(n,α) reaction reates becomes smaller farther from the first wall since neutron multiplication through ^{9}Be(n,2n') reactions mainly occurs in regions closest to the plasma where neutrons are energetic. In addition, the Th(n,γ) and ^{6}Li(n,α) reactions are competing with one another. The simultaneous decrease in both reaction rates upon using Be-LASL evaluation can only be explained by the decrease in the number of neutrons available for breeding. This becomes apparent when the neutron balance in the two evaluations are examined. The following three conclusions may be drawn:

1)   Neutron multiplication comes mainly from (n,2n') reactions which are dominated by the contribution from the ^{9}Be(n,2n') reaction (43.5% of total number of available neutrons per D-T neutron in the Be-V evaluation case; 41% in the Be-LASL evaluation case).

2)   Most of neutron absorption reactions are in ^{232}Th and ^{6}Li. The fraction of the available neutrons contributing to breeding is ~84% in both the Be-V and Be-LASL evaluation cases. The lower value for $R_u + R_{Li}$ in the Be-LASL evaluation case (-4.4%) is due to the decrease in the total number of available neutrons per D-T neutron, M_n, by the same amount ($M_n = 2.31$ in Be-V case, $M_n = 2.21$ in Be-LASL). Thus, the change in breeding is largely dominated by the changing contribution of the ^{9}Be(n,2n) reaction.

TABLE V-10. Breeding ratios in the beryllium blanket using three different evaluations for ^{9}Be.

Breeding Parameters	Be-ENDF/B-V Evaluation	Be-LASL Evaluation	(%) Decrease	Be-ENDF/B-IV Evaluation
Uranium Breeding Ratio, R_u				
Zone 3	3.234-1	3.047-1	5.8	3.143-1
Zone 4	2.493-1	2.374-1	4.8	2.468-1
Zone 5	1.557-1	1.509-1	3.3	1.588-1
Zone 6	6.057-2	5.998-2	0.9	6.312-2
Zone 7	3.670-2	3.700-2	0.8	3.996-2
SUM	8.257-1	7.900-1	4.4	8.238-1
Tritium Breeding Ratio, R_{Li}				
R_{6Li} Zone 3	4.231-1	3.994-1	5.6	4.195-1
Zone 4	3.438-1	3.274-1	4.8	3.399-1
Zone 5	2.197-1	2.124-1	3.3	2.227-1
Zone 6	7.605-2	7.481-2	0.9	7.948-2
Zone 7	4.314-2	4.313-2	0.8	4.634-2
Sub-Sum	(1.1058)	(1.0571)	4.4	(1.1004)
R_{7Li} Zone 3	4.391-3	4.058-3	7.6	4.376-3
Zone 4	1.789-3	1.629-3	8.9	1.803-3
Zone 5	7.742-4	7.087-4	8.5	7.915-4
Zone 6	1.729-4	1.647-4	4.7	1.990-4
Zone 7	4.207-5	4.071-5	3.2	4.367-5
Sub-Sum	(7.168-3)	(6.601-3)	7.9	(7.193-3)
SUM	1.113	1.064	4.4	1.107

3) The results for the Be-IV evaluation case are essentially the same as the Be-V evaluation case since the ^{9}Be(n,2n') cross section is the same in the two evaluations.

The last two conclusions emphasize that the present Be(n,2n') evaluation in ENDF/B-V overestimates neutron multiplication. A decrease of $\sim$ 9% in the ^{9}Be(n,2n') reaction rate is observed upon using the correct energy-angle correlation for the secondary neutrons. [Basu[9] estimates an M_n which is larger by 25% but this is because his experiment utilized 100% beryllium. Other multiplying reactions occur in our blanket e.g., Pb(n,2n'), Fe(n,2n'), Th(n,$\nu\sigma_f$), ^{233}U(n,$\nu\sigma_f$)].

It is of interest to note that the decrease in M_n occurs although the total ^{9}Be(n,2n') cross section is almost the same in both the ENDF/B-V and the LASL evaluations. The corrected LASL energy-angle correlation for the secondary neutrons tends to transport the high energy secondary neutrons in the forward direction. Since these secondary neutrons strongly contribute to the production of excess neutrons in the beryllium zone via additional (n,2n') reactions, overall multiplication and breeding drop when the LASL evaluation is used. On the other hand, the relative increases in the high energy neutrons scattered to the back zone of the blanket results in a slight increase in the multiplying reactions in the SiC$_4$ and the shielding zones (e.g., Fe(n,2n'), Si(n,2n'), ^{11}B(n,2n'). However, the overall neutron multiplication decreases since it is dominated primarily by neutron multiplication reactions in beryllium.

The above discussion focused on the impact of uncertainties or controversy in the value and representation of the ^{9}Be(n,2n') cross section. The second part of this study considered the sensitivity of the beryllium blanket nuclear performance to errors in the neutron cross sections of the blanket materials. First order perturbation theory was used and the concept of the relative integrated sensitivity coefficient was employed as an indicator of the sensitivity of a design parameter (either tritium or uranium breeding) to changes in a particular cross section type. The objective was to identify the elements and reaction types which contribute the most to uncertainties in the design parameters (particularly tritium and uranium breeding). The baseline analysis was done with the Be-LASL evaluation since it is generally believed that its evaluation of the ^{9}Be(n,2n') cross section is the most

correct. Processing of cross section data for the sensitivity analysis codes "SWANLAKE"[15] and ANISN used the DLC-41C/VITAMIN-C cross section library and the AMPX[5] system. The processing of the modified format of the LASL ^{9}Be(n,2n') evaluation required special consideration and modification of the elements of AMPX.

$$R_K = <\Sigma_r, \phi> \tag{V-1}$$

due to uncertainties in a given multigroup cross section set, $\delta\Sigma_i^g$, is evaluated from the expression

$$\frac{\delta R_K}{R_K} = \sum_g P_{\Sigma_{i,k}}^g \left(\frac{\delta\Sigma_i^g}{\Sigma_i^g} \right), \tag{V-2}$$

$P_{\Sigma_{i,k}}^g$ is the sensitivity profile coefficient for group g for material i relative to design parameter k. The $P_{\Sigma_{i,k}}^g$ are calculated by SWANLAKE, a first order perturbation theory code for sensitivity analysis. It requires special cross section data and forward and adjoint fluxes from ANISN. With estimates of cross section uncertainties, $\delta\Sigma_i/\Sigma_i$, $\delta R_K/R_K$ can be derived using the single sum in Eq. (V-2). Another parameter of interest, the relative integrated sensitivity coefficient, $S_{\Sigma_i}^k$, can also be derived.

$$S_{\Sigma_i}^k = \sum_g P_{\Sigma_{i,k}}^g \tag{V-3}$$

This is interpreted as the percent change in the design parameter of interest, $\delta R_K/R_K$, due to a simultaneous 1% increase in the group cross section $\Sigma_{i,k}^g$ in all energy groups, g, which assumes full correlation between all energy groups.

$S_{\Sigma_i}^U$ and $S_{\Sigma_i}^{6Li}$ have been calculated based upon SWANLAKE results. Several conclusions can be drawn:

- A 1% increase in the ^{232}Th(n, total) cross section at all energies results in $\sim$ 0.68% increase in R_u and $\sim$ 0.47% decrease in R_{6Li}.

- A 1% increase in the ^{6}Li(n,total) cross section at all energies results in a 0.18% increase in R_{6Li} and a 0.15% decrease in R_u.

- Neither ^{232}Th or ^{6}Li contribute significantly to the total neutron multiplication, which is dominated by ^{9}Be(n,2n') reactions.

- ^{9}Be(n,2n') has a positive sensitivity coefficient for both R_u and R_{6Li}. However, increasing ^{9}Be(n,total) by 1% will decrease R_u by ∿ 0.2% and will increase R_{6Li} by ∿ 0.6%. R_u has a positive sensitivity coefficient for ^{9}Be(n,2n') but the total sensitivity is dominated by the negative ^{9}Be(n,elastic) cross section coefficients.

Equation (V-2) couples sensitivity profiles and cross section uncertainty estimates. Typical cross section uncertainty estimates are contained in Table V-11. Note that the cross section compensation is carried out such that the total cross section remains unchanged since its value is usually known to better accuracy than its partial cross section. Therefore, it is often more realistic to vary at least two partial cross sections at the same time.

The results of the evaluation of Eq. (V-2) for the cross section uncertainties listed in Table V-11 are shown in Table V-12. The uncertainty associated with the uranium breeding ratio is due primarily to uncertainties in the beryllium cross sections. The present uncertainties in the ^{6}Li, ^{7}Li, and Pb cross sections have insignificant contributions to $\delta R_u/R_u$. The uncertainty associated with the tritium breeding ratio is due primarily to the same cross sections. The expected uncertainty in the total breeding ratio due to the present uncertainty estimates for the thorium and lithium-6 cross sections are small (~2%) due to cancellation of error signs. It is interesting to note that increasing the Th(n,fission) cross sections decreases both R_u and R_{6Li} and that the decrease is small.

Table V-13 contains estimates which quantify the maximum expected adverse effect on total breeding due to variations in cross sections. If each cross section type is independently varied to decrease the overall breeding as shown, then the effect on total breeding for each partial cross section and for each element can be found. When these breeding variations are summed, the total effect on breeding (i.e., tritium plus fissile) is 0.14 or a decrease of 7.53% with respect to the nominal value of 1.847.

TABLE V-11. Uncertainty estimates for various partial cross sections.

Element	Cross Section Type Varied	Energy Range	Percent Change in Varied Cross Section	Cross Section Type Varied To Compensate
Thorium[a]	$(n, \nu\sigma_f)$	>5 MeV	11%	(n,2n')
		3 MeV–5 MeV	6%	(n,elastic)
		<3 MeV	7%	
	(n,γ)	>5 MeV	20%	(n,2n')
		3 MeV–5 MeV	20%	
		1 MeV–3 MeV	20%	(n,elastic)
		4 eV–1 MeV	12%	
		<4 eV	8%	
Beryllium[c]	(n,2n)	>13.5 MeV	20%	(n,p)
		11–13.5 MeV	20%	(n,t)
		2 MeV–11 MeV	20%	(n,elastic)
		<2 MeV	––	–––––
Lithium-6[b]	(n,α)t	1.7–14.1 MeV	10%	(n,elastic)
		1–1.7 MeV	15–10%	
		0.7–1 MeV	15%	
		0.5–0.7 MeV	15–10%	
		0.3–0.5 MeV	5–10%	
		0.1–0.3 MeV	5%	
		10 KeV–0.1 MeV	1–2%	
		0.1 eV–10 KeV	1%	(n,total)
		<0.1 eV	0.5%	
Lithium-7[b]	(n,n')αt	All energies	20%	(n,elastic)
Lead[c]	(n,2n')	All energies	20%	(n,inelastic)

[a]From Reference 16.

[b]From Reference 17.

[c]Uncertainties are assumed.

TABLE V-12.   Estimated changes for the uranium breeding ratio, $\delta R_u/R_u$, and the tritium breeding ratio from ^{6}Li, $\delta R_{6_{Li}}/R_{6_{Li}}$.

Element	Cross Section Type Varied or Compensated	$\delta R_u/R_u$ (%)	$\delta R_{6_{Li}}/R_{6_{Li}}$ (%)
Thorium	$(n, \nu\sigma_f)$	−7.49−2	−7.25−2
	(n,γ)	7.96	−5.6
	$(n,2n')$	−7.00−2	−7.90−2
	$(n,\text{elastic})$	−8.13−4	−1.69−2
Sub-Sum		7.82	−5.76
Beryllium	$(n,2n')$	5.69	5.87
	(n,p)	7.79−4	7.71−4
	(n,t)	3.46−2	3.40−2
	$(n,\text{elastic})$	0.60	0.58
Sub-Sum		6.32	6.48
Lithium-6	$(n,\alpha)t$	−0.16	0.17
	$(n,\text{elastic})$	2.54−4	2.36−5
	(n,total)	−0.13	0.14
Sub-Sum		−2.89−2	3.10−2
Lithium-7	$(n,n')\alpha t$	3.13−2	2.95−2
	$(n,\text{elastic})$	−3.25−2	2.07−2
Sub-Sum		−1.12−3	5.03−2
Lead	$(n,2n')$	0.36	0.41
	$(n,\text{inelastic})$	0.42	0.39
Sub-Sum		0.78	0.80

TABLE V-13. Maximum uncertainty estimates for the total (T+F) breeding ratio.

Element	Type and Direction of Cross Section Varied	Compensating [b] Cross Section Type	$\delta R_B = \delta R_u + R_{6_{Li}}$
Thorium	$(n, \nu\sigma_f)$ increased		-0.1358×10^{-2}
		$(n,2n')$	-0.0492×10^{-2}
		$(n,\text{elastic})$	-0.0016×10^{-2}
	(n,γ) decreased		-0.3692×10^{-2}
		$(n,2n')$	$+0.0896 \times 10^{-2}$
		$(n,\text{elastic})$	$+0.0172 \times 10^{-2}$
	δR (SUM)		-0.449×10^{-2}
Beryllium	$(n,2n')$ decreased		-10.70×10^{-2}
		(n,p)	-0.0014×10^{-2}
		(n,t)	-0.0633×10^{-2}
		$(n,\text{elastic})$	-1.0871×10^{-2}
	δR (SUM)		-11.852×10^{-2}
Lithium-6	$(n,\alpha)t$ decreased		-0.0533×10^{-2}
		$(n,\text{elastic})$	-0.0002×10^{-2}
		(n,total)	-0.0453×10^{-2}
	δR (SUM)		-0.0988×10^{-2}
Lithium-7	$(n,n')\alpha t$ decreased		-0.0559×10^{-2}
		$(n,\text{elastic})$	$+0.0038 \times 10^{-2}$
	δR (SUM)		-0.052×10^{-2}
Lead	$(n,2n')$ decreased		-0.7178×10^{-2}
		$(n,\text{inelastic})$	-0.7440×10^{-2}
	δR (SUM)		-1.462×10^{-2}
	δR (TOTAL)		-13.914×10^{-2}
	$\delta R/R$ [b]		-7.53%

[a] $R \simeq R_u + R_{6_{Li}} = 1.847$ where $R_u = 0.7$ and $R_{6_{Li}} = 1.057$.

[b] Compensating cross sections are varied to preserve the total cross section.

Note that the maximum adverse effect corresponds to a decrease in all cross sections except ^{232}Th$(n,\nu\sigma_f)$, which would adversely effect the total breeding if it were increased.

As an extension of this work, several suggestions can be made. The covariance information in the ENDF/B-V error files can be used in a statistical manner. This should produce better error estimates. However, currently only error files for total cross sections are included in ENDF/B-V, but theories exist to implement uncertainties in secondary neutron energy distributions and differential cross sections. Finally, the sensitivity and uncertainty analysis could be extended to include the heat disposition rate and radiation damage to the first wall.

V.C MATERIALS ISSUES

V.C.1 Beryllium Feasibility Assessment

V.C.1.a <u>Introduction</u>. Beryllium has been selected as the candidate material for use as the neutron multiplier component in the Tandem Mirror Hybrid Reactor (TMHR) design which incorporates the features of suppressed fission and of blanket cooling using helium. To better understand the use of beryllium in this function an assessment of feasibility issues was performed.

There are a few issues associated with production. First, can the requirement for a substantial quantity of beryllium be met considering current availability of the mineral resource and present milling and associated production capacity for the metal? The issue of beryllium production demands has been of general interest over the last few years as blanket designs have evolved and the potential need for a substantial quantity of beryllium has been identified. Second, the issue of whether industry experience with beryllium, considering fabrication and usage to date, supports fabrication practicality is relevant. In the hybrid blanket application high volume production of a straightforward beryllium-component configuration is contemplated and cost is an important consideration. Third, safety is an issue throughout the production of beryllium due to the toxicity of the particulate and vapor even at very low level concentration in air. These three issues were investigated and are reported on.

Another series of feasibility questions pertain to the material design aspects of beryllium components for use at elevated temperature ($\sim$600°C) where deformation by creep mechanisms can occur. The use of beryllium in a neutron irradiation environment (fluence $\sim$4 x 10^{27} n/m^2, $\sim$20 MW-yr/m^2 at the first wall) with energies ranging from thermal to 14 MeV adds to the complexity of design and causes difficulty in the prediction of radiation damage effects. Further, blanket materials contacting the beryllium under these conditions must be considered carefully to account for possible interactions. The impurities in the beryllium may be an important factor in assessing material compatibility with the thermal contact medium and with the transmutation species, Li and T, formed in the beryllium during irradiation.

Finally, because of the large inventory of beryllium and high cost, recycling is preferred and necessary. This will occur either at the end of reactor life, or on a shorter timescale if irradiation imposes a shorter limit on the life of beryllium components and/or the blanket structure. For example, this might occur due to swelling or cracking. It is therefore relevant to consider if the beryllium can be economically recycled and refabricated for use. The activation of beryllium and the impurities in beryllium could prevent direct refabrication and impose a remote handling process shielded from gamma radiation.

The beryllium feasibility assessment resulted in the identification of additional issues requiring further study, tests, and investigations. However, sufficient literature was available on the use of beryllium for applications of neutron moderation, reflecting and multiplying to enable a good assessment of the feasibility for using beryllium in the TMHR concept. Two review articles, by Beeston[18] and by Simnad[19] survey the general subject of beryllium for use in a radiation environment. Our results and recommendations are discussed below.

V.C.1.b <u>Beryllium Configuration for the Neutron Multiplier.</u> The conceptual design of a blanket module is presented in Fig. V-1. The shorter length blocks immediately behind the first wall form the beryllium neutron multiplier component. A single beryllium block will, in principle, have a configuration like the block shown schematically in Fig. V-8. The overall length of 30 cm may also be comprised of a stack of shorter length blocks. The triangular cross section and spacing sequence permits linear expansion of 3% (9.27 volume %) during the service life of the beryllium. If the blocks swell and touch, the steel tubes and beryllium still remain apart from one another. A liquid metal eutectic of 83 at % Pb-17 at % Li (99.7 wt % Pb-0.3 wt % Li) is present in the gap region and provides the necessary thermal conduction from the nuclear-heated beryllium to the helium-cooled steel tubes. Breeding of tritium occurs in the liquid alloy, and fissile fuel is produced in the fertile particulate of thorium oxide suspended in it. At the beginning of blanket life, the liquid eutectic accounts for 20% volume fraction in the blanket. After irradiation and swelling by the beryllium blocks, the liquid eutectic volume fraction may be reduced to

GAPS BETWEEN STEEL TUBES AND Be BLOCKS
TUBES PERMITS ≤ 10 VOL % SWELLING IN Be.

14 mm
DIA.

ℂ SPACING

36 mm

ARRAY REPEATS
THROUGHOUT
BLANKET

550°C

500°C

Be
BLOCK

CYLINDRICAL HOLE ASSISTS RELEASE OF
HELIUM AND TRITIUM FROM Be.

RE-ENTRANT TYPE HEAT EXCHANGER. 50 Atm.
HELIUM COOLANT. HT 9 FERRITIC STEEL TUBES.
T ≤ 550°C.

0.3 m

SLOW CIRCULATION THROUGH GAP OF LIQUID
METAL ~ 550°C AND 1 Atm. EUTECTIC ALLOY OF
83 AT % Pb – 17 AT % Li. PROVIDES THERMAL
CONTACT; BREEDS TRITIUM; SUSPENDS FERTILE
ThO$_2$ PARTICLES OF ≤ 0.5 mm DIAMETER

700°C AT ℂ
OF BLOCK

650°C

CORRUGATED FIRST WALL – HT 9 FERRITIC
STEEL. A SiC SPACER SEPARATES Be FROM
STEEL WALL.

PLASMA

14 MeV
NEUTRONS

FIGURE V-8. Materials and component design for neutron
multiplier in TMHR blanket.

about 10%. The tubes account for 3% volume fraction and the cylindrical central hole in each block accounts for 0.5%. The volume of space (inside the steel tubes) for the helium required to cool the blanket is about 10% by volume. The beryllium blocks occupy the remaining 67% of the blanket volume.

A first approximation of the required amount of 100% dense beryllium is therefore equal to the volume of a cylinder described by an R_1 = 2.0 m and an R_2 = 2.3 m and a central cell length of 96 m (3000 MW fusion, 2 MW/m^2 neutron wall loading) multiplied by the reduction factor of 0.67 (= 1 - 0.2 - 0.2 - 0.03) taking into account the aforementioned considerations for gaps, liquid metal, helium coolant and tubing structure. The net volume of beryllium is: Vol Be = 389 m^3 × 0.67 = 261 m^3. For hot pressed beryllium manufactured to have a density of only 80% of theoretical, the overall dimensions of the beryllium blocks are the same and the weight of Be = 0.8 × 261 × 1,850 kg/m^3 = 386,650 kg ≃ 387 metric tons per TMHR.

Currently, the intent is to design the entire neutron multiplier component using interchangeable, symmetrical blocks. This approach should permit economical mass production of the beryllium blocks with minimal or no expensive secondary machining opertions.

V.C.1.c Berylium Resource Availability and Production Considerations.

Availability. During the last decade in the U.S., the general subject of strategic materials availability has received particular interest and discussion. Beryllium reserves and resources have been identified by the U.S. Bureau of Mines,[20,21] and in a U.S. Geological Survey.[22] Also, since fusion requirements for beryllium could be large, recent studies on a fusion economy[23] and the STARFIRE reactor design[24] have included the current status and outlook for beryllium in their assessment of materials availability in the future. Of interest in this report is the impact of the beryllium requirement for TMHR considering the current domestic and world resources of beryllium bearing ore. Table V-14 summarizes the situation using terminology consistent with that of the U.S. Bureau of Mines. Data from the U.S. Geological Survey[22] is included for comparison. Their categorization and terminology differ somewhat from the USBM, so a direct comparison is difficult. In Table V-14 reserves are defined as the amount of beryllium present in discovered deposits which are considered to be mineable and

TABLE V-14. Availability of beryllium and impact of TMHR requirements.

	United States		World	
	Reserves (metric tons)	Resources[b]	Reserves (metric tons)	Resources[b]
Percentage represented by one TMHR using (a) data	25,000[a]	72,000[a]	380,000[a]	1,105,000[a]
	1.5%	0.5%	0.1%	0.04%
	55,000[c]	282,000[c]	84,000[c]	679,000[c]

Note: Beryllium requirement for one TMHR = 387 metric tons, (80% dense material), for a fusion plant of 3000 MW fusion.

(a) Ref. 4, U.S. Bureau of Mines.
(b) Includes reserves.
(c) Ref. 5, U.S. Geological Survey.

processible through the use of existing technology. Also, reserves are generally identified with production capacities which exist or are planned. Resources, however, include discovered ores and potential areas of ore possibility based on strong geological evidence. Resource figures, as a result, are helpful in assessing long-term availability. The 387 metric tons of beryllium necessary for one TMHR would require approximately 1.5% of the domestic reserve of beryllium, a substantial amount, but likely a quantity of sufficient incentive to encourage interest and expansion by the metals industry. The quantity would be considered overwhelming if the need was immediate but not so as part of a TMHR program with many years for planning and developing a commercial size reactor. The amount of beryllium needed for one TMHR is close to the current domestic production capacity for beryllium metal in one year. However, beryllium production currently is well below the production capacity level.

In a scenario for introduction of TMHRs to support light water reactors (20:1 nuclear support ratio for LWRs/TMHR), presented in Ref. 25 and Chapter X, construction of commercial plants commences in 2005 to produce

^{233}U to satisfy the world's demand for LWR fuel (^{233}U). Using the same rate of introduction for reference purposes, the need for beryllium can be plotted accordingly as presented in Fig. V-9. As shown, the TMHR beryllium requirement through 2038 of about 31,000 MT represents 43% of the USBM resource estimate. As shown in Chapter X, this amount of beryllium, when utilized in 80 TMHRs is sufficient to fuel an LWR economy of about 1600 GW$_e$ to provide about 50% of the electrical demand in the 2050 time frame.

Beryllium is obtainable from the mineral beryl located in pegmatite deposits in a number of locations in the U.S. However, current production and interest lies with low-grade nonpegmatite deposits in Utah and Alaska; the only significant domestic production currently is in Utah. The ore mineral described is termed Bertrandite. In this deposit the USBM has estimated a reserve of 25,000 metric tons of beryllium. Brush-Wellman Company mills and processes the ore through the final stages of beryllium metal production.

An important factor to consider in the use of beryllium in fusion applications will be the incentive for recycling following a specified degree of swelling or change in material property. Since recycling of the beryllium blocks will be needed to limit resource requirements, reprocessing and refabrication of blocks (radioactivity remains) seems appropriate, logical and likely cost effective.

Production and Cost of Neutron Multiplier Blocks. The configuration of the beryllium block in the subject design would, if made today in modest quantities, be produced as a hot-pressed product form and the tooling would be designed to achieve near-net or net shape. The cost for such a product could be in the vicinity of $1000/kg at current day prices. However, the mass production associated with the needs projected for a TMHR calls for re-thinking through all stages of metal production. During an informal assessment of the quantity needed with Brush-Wellman Company metallurgists, the idea of extruding ingots of cast beryllium appears to be a candidate approach for the mass production of beryllium blocks. The anisotropic mechanical properties of extruded beryllium could be tolerated in the neutron multiplier components. From the extrusion, the operation of
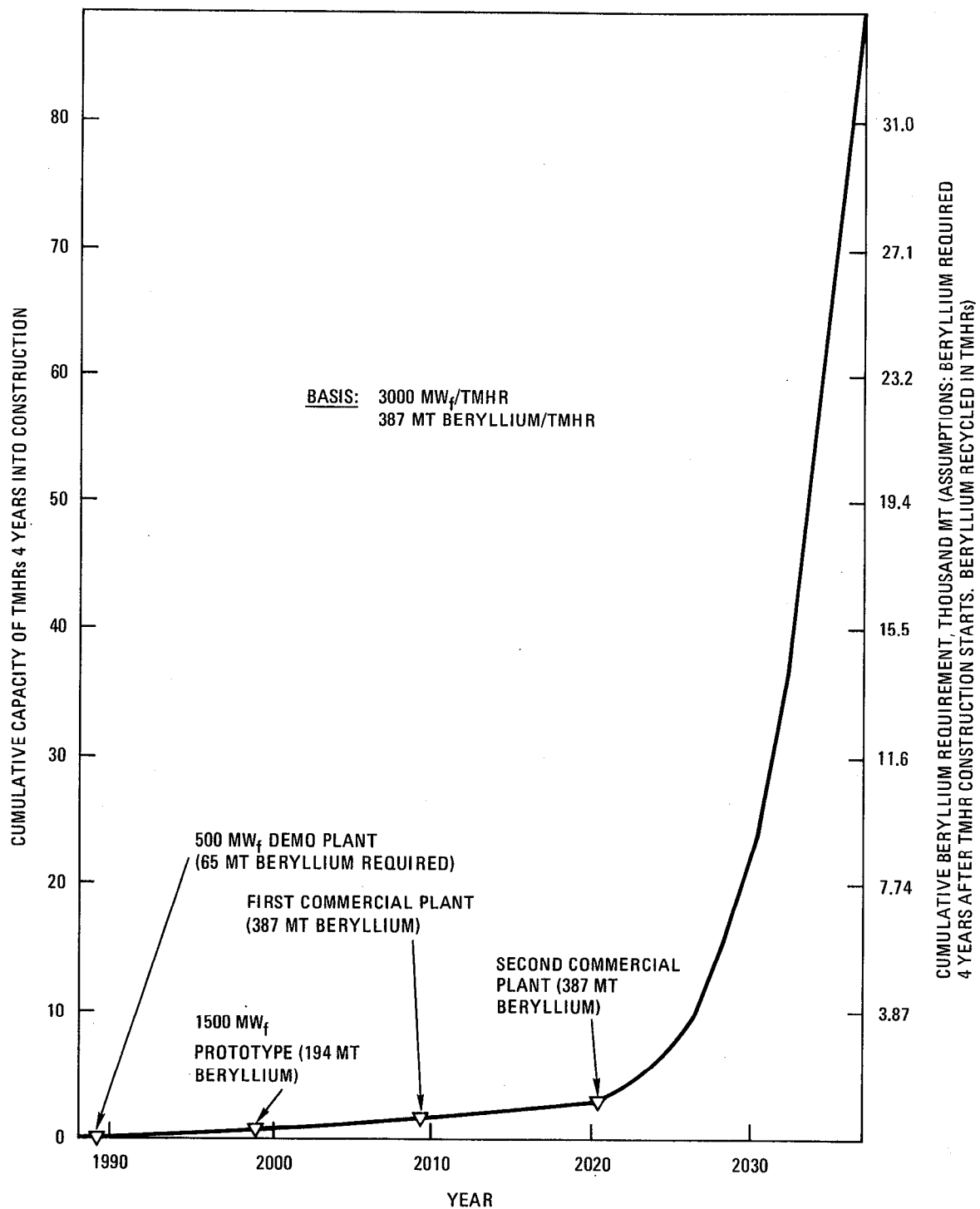
FIGURE V-9. Beryllium requirement for the neutron multiplier component in TMHRs according to the Chapter X deployment scenario.

cutting the blocks to length would be straightforward. By this production method substantial cost reduction should be a reasonable assumption. Without analysis, an unofficial cost of $374/kg was arrived at as a number for cost estimating at this time. Using the quantity requirement of 387 metric tons for a TMHR, the expected cost of the beryllium would be $145 million. However, at this time, no ideas have been conceived which justify using the lower $374/kg price for the 80% dense powder metallurgy product form. For 100% dense extruded beryllium, considering the 20% increase in weight and assuming the same volume, the cost would be $181 million.

V.C.1.d Fabrication of Beryllium Components. Safe industrial experience with beryllium over the last 15 — 20 years has demonstrated that beryllium components can be safely fabricated and handled directly.[26] There is no need to fear using beryllium just because of its toxic effect under certain conditions. With due regard to the health hazard of beryllium particulate, fumes and salts, appropriate facilities can be established which permit safe, hands-on operation of many typical fabrication steps including machining, cutting, drilling, chemical etching and forming.

Health Safety. Beryllium diseases may be divided into two major groups, dermal and respiratory. Contact dermatitis can occur during contact with bertain beryllium compounds. Allowing for reasonable precaution, handling solid beryllium is not a problem. A wound containing beryllium will not heal and requires removal of the trapped metal pieces.

Inhalation of vapor containing fine particulate can cause serious respiratory disease. Recognition of these facts in the late 40s and 50s led to studies of hygiene in conjunction with beryllium manufacturing. The established allowable concentration of beryllium in air was set at 2 $\mu g/m^3$ for a work period of 8 hours. This regulation is still in effect today. Employees of a beryllium fabrication facility are examined medically on a periodic basis to ensure against the contraction of illness associated with beryllium.

Fabrication Facility. The requirement of low beryllium concentration in
air has been met effectively by using appropriate ventilation and filtering
as well as localized exhaust systems near the area of contaminent generation.
Further, machining of beryllium using liquid coolants will aid in the retention
of particulates generated. Air sampling is used to monitor all operational
steps in a fabrication facility. Some operations, however, such as working
with beryllium powder and grinding must be conducted inside an enclosure
which is kept under a negative pressure. Facilities for the fabrication of
beryllium components are kept at a slight negative pressure and all air is
exhausted through filtering systems.

Direct Fabrication. Quite possibly the beryllium block as shown in Fig. V-9
could be fabricated directly to final shape by the beryllium producer.
Brush-Wellman Company can produce product forms made by vacuum hot-pressing
of powder and sintering and by the hot extrusion of ingots. A design goal,
for cost effectiveness, would be to produce a part to net shape and size;
if extruded, only cutting to length would be required. Installation would
simply involve direct insertion in the blank module.

Recycling Beryllium Block Material. Removal of post-service beryllium
blocks will not be straightforward because of the radioactivity associated
with the module components. Once removed from the blanket module, each
block, extremely brittle from irradiation, can, however, be pulverized and
annealed to remove the tritium and helium trapped internally. Lithium, formed
by neutron reaction, should also be removed from the beryllium along with any
Pb-Li entrapment on the surface. At 827°C the vapor pressures for Be, Pb and
Li are 3.0×10^{-8} atm, 6.4×10^{-4} atm and 2.1×10^{-2} atm, respectively. Vacuum
distillation at higher temperatures might well be a sufficient method for re-
moval of Li and Pb from beryllium during reprocessing of the beryllium. The
beryllium particles can then be refabricated again into blocks. Likely, part
of the reprocessing effort will have to be conducted remotely with adequate
shielding of personnel from the γ-radiation emitted from the radionuclides
from the impurity elements associated with the beryllium. At this time,
production of beryllium with low impurity concentration (e.g., <1 ppm of
Fe, Ni, Cr, W, etc.) is considered to be prohibitively difficult, costly,

and is inconsistent with the earlier mentioned requirement of low-cost, mass production of blocks. A more practical impurity level in beryllium metal for the above elements collectively is about 1000 ppm. The only long term radionuclide associated with beryllium is ^{10}Be which is a β-emitter and by itself would not require the more extensive shielding for γ-radiation. However, following decay of impurity radiation over 50 years (to be discussed later), the blocks may be of low enough activity to permit safe handling of individual blocks.

Certain steps of reprocessing may not be that impractical even with the requirement of remote handling and γ-radiation shielding considering that beryllium products are produced today with many steps automated and within an enclosure to prevent exposure of the attending personnel to the fumes and/or particulates.

Radioactivity and Dosage. Beta emitting ^{10}Be has a half life of 2.5×10^6 years. The post-shutdown radioactivity and biological dosage were calculated using the fusion radioactivity calculation code DKR[27] and decay chain data library DCDLIB.[28] The neutron flux input for the DKR code was obtained from an ANISN calculation (see Section V.B). The activity level of this nuclide in pure beryllium after about 10 MW-yr/m^2 of D-T fusion neutron activation of beryllium is about 10^{-6} curies/cc and it will maintain at this level for at least a few million years. Refabrication of a material containing beta emitting radionuclide with this level of radioactivity does not, in general, impose any serious problem other than those associated with the material before irradiation. However, as indicated previously, the beryllium material normally carries in it approximately 1000 ppm impurities (such as Fe, Ni, Cr, and W). Considering these impurities, we have conducted an analysis to estimate the biological dosage working personnel will be exposed to when refabrication of the beryllium blanket with irradiated beryllium is encountered.

A radioactivity analysis was performed for 1 ppm Fe incorporated in otherwise pure beryllium material and the aforementioned neutron exposure. The results shown here could be indicative of other impurity elements such as Ni, Cr and W. With 1 ppm iron in beryllium, the specific radioactivity in the beryllium material due to the impurity only is about 36 μCi/cc one

day after shutdown. The dominating contributors are ^{55}Fe (2.7 yr half life) and ^{56}Mn (2.6 hr half life). It drops to about 26 and 2.3 μCi/cc one yr and ten yr after shutdown, respectively. The most important radioisotope within this time interval is ^{55}Fe which emits bremsstrahlung when it decays into stable ^{55}Mn through electron capture process. At about 50 yr after shutdown, the radioactivity level reaches about 10^{-6} μCi/cc which is acceptable for hands-on processing.

The induced biological dose rate to fabrication plant personnel due to a 1 ppm iron impurity in the beryllium material is on the order of 400 mRem/hr on the plasma side and behind the beryllium blanket, assuming the following conditions hold: (1) the surrounding structure (HT-9 steel) is new (replaced) and unactivated, and (2) the replacement beryllium material was recycled one yr after the TMHR service shutdown discussed above. The dose rate drops to about 30 mRem/hr if irradiated beryllium is refabricated after 10 years. However, if the recycle time is about 50 yr, the dose rate will be of the order of 10^{-5} mRem/hr.

Considering the practical impurity level of about 1000 ppm, the dose rate in the reactor assembly could be on the order of 30 Rem/hr if the recycle time is 10 years. If the recycle time is 50 years, the dose rate will be no more than 10^{-2} mRem/hr. Hence, we may conclude that contact refabrication of the irradiated beryllium is only possible if we maintain an impurity level below about 1000 ppm and a recycle time of about 50 years or more. Obviously, more detailed calculations accounting for more representative impurity species and levels in beryllium are desired. However, for refabrication periods on the order of 10 yr remote and shielded fabrication facilities will be required. Economic analysis indicate that early recycling is most likely required.

V.C.1.e <u>Metallurgical Changes Anticipated in Beryllium During TMHR Service.</u>
The beryllium blocks will, in their function as the neutron multiplier, experience a high fluence of high energy 14 MeV neutrons. The gradient of neutron fluence and temperature within the beryllium parts is expected to cause metallurgical changes of differing degree along the component length. Irradiation experiments on beryllium and associated analyses have provided a basis for predictions and estimations. Unfortunately, irradiation tests

have been limited to temperature and fluence levels lower than anticipated for the TMHR application. As usual, the available radiation effect data is derived from fission reactor experience and is representative of fast neutrons of $E \geq 0.8$ MeV but much lower in energy than the 14 MeV fusion source energy.

Swelling. The swelling characteristics and mechanical properties of neutron-irradiated beryllium have been investigated and typical interest has focused on the viability of beryllium as a structural material in applications for neutron multiplication, moderation and reflection.[18,19,29—31] The nuclear transmutation of beryllium by fast neutrons causes extensive atom displacement damage, however, without formation of voide.[29,30] Helium atoms are formed which cluster into 100 Å diameter bubbles and swelling can result at temperatures high enough for sufficient thermally activated processes to occur. Thermal activation is sufficiently high at temperatures of TMHR interest (500° to 700°C to permit diffusion of He atoms and bubbles, growth and colescence of bubbles, and the formation of holes.[29]

The neutron radiation environment of the reference beryllium blanket is depicted in Fig. V-10 where the neutron fluxes are given as a function of distance from the first wall at a wall loading of 2 MW/m^2. This figure shows the 14 MeV (first group, 13.5 — 14.9 MeV) group neutron flux, the integrated (i.e., total) neutron flux and the flux above 0.8 MeV. The 14 MeV group flux is about 5×10^{25} n/m^2/year at the first wall while the integrated flux and the flux above 0.8 MeV are about 4.6×10^{26} and 1.3×10^{26} n/m^2/yr, respectively. A calculation was made of the amount of helium which will be produced in the beryllium along the 0.3 m long blocks using the neutron flux obtained with the reference beryllium blanket. The conditions used and results are presented in Table V-15. Figure V-11 further displays the calculated helium generation rate in the beryllium.

Prediction of swelling from the irradiation test data available is not straightforward in all regions of the block since tests have not been conducted at all the temperatures, fluence or energy levels of interest. However, predictions were made from irradiation test results of beryllium by Andriyevski, et al.[31] and from post-irradiation annealing experiments by Rich, et al.[29] A prediction of a ~30% ceiling on volume increase due to He formation in beryllium was made by Barnes.[30,34] Metallic fuels of
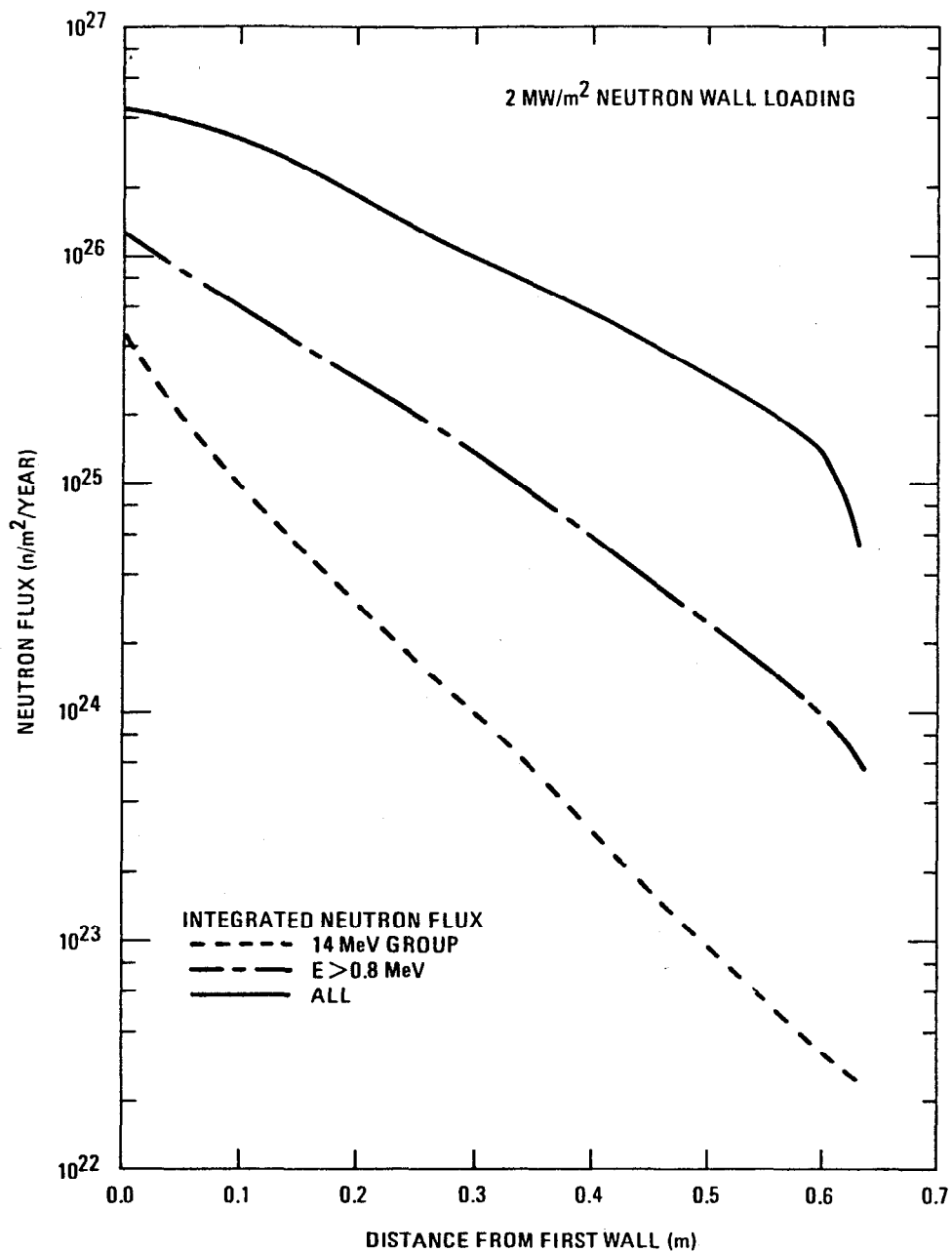
FIGURE V-10. Neutron flux distributions in the reference
             beryllium blanket. Note that the neutron
             wall loading is 2 MW/m^2.

TABLE V-15. Prediction of helium formation and swelling in beryllium neutron multiplier during service in TMHR.

| Parameters | Beryllium Block (of Fig. V-8) | | | |
| | End Nearest First Wall | | End Furthest from First Wall[1] | |
	1 yr	10 yr	1 yr	10 yr
Be temperature (at surface/centerline)	650/700°C		500/550°C	
Thermal contact medium[2] between Be and cooling tube	Liquid Pb-Li		Liquid Pb-Li	
Neutron Fluences (n/m^2)				
13.5 MeV $< E < 14.9$ MeV	5×10^{25}	5×10^{26}	1.1×10^{24}	1.1×10^{25}
$E > 0.8$ MeV	1.3×10^{26}	1.3×10^{27}	1.4×10^{25}	1.4×10^{26}
$E > 2.2 \times 10^{-2}$ eV	4.6×10^{26}	4.6×10^{27}	1.0×10^{26}	1.0×10^{27}
Helium formed: (appm)	7.5×10^3	75×10^3	0.6×10^3	6×10^3
cm^3 He/cm^3 Be (N.T.P.)	37	370	3	30
Swelling: $\frac{\Delta V}{V} 100\%$ *	[4]16%	[4][3]30%	[4]2%	[4]9%
**	4%	10%	1%	2%

(1) Length of Be block = 30cm.
(2) 83 at % Pb - 17 at % Li.
(3) Assumption that volume increase maximum is reached at approx. 30%. Bubbles touch and provide release path along grain boundaries.
(4) Assumption: Use model prediction of R. A. Andriyevskii, et al., (Ref. 14). Increase by an estimated factor of 2 to account for: higher fluence, E ~14 MeV and possibility of enhanced swelling from formation of voids.

*Very conservative estimate.
**Conservative engineering estimate for GA design concept.
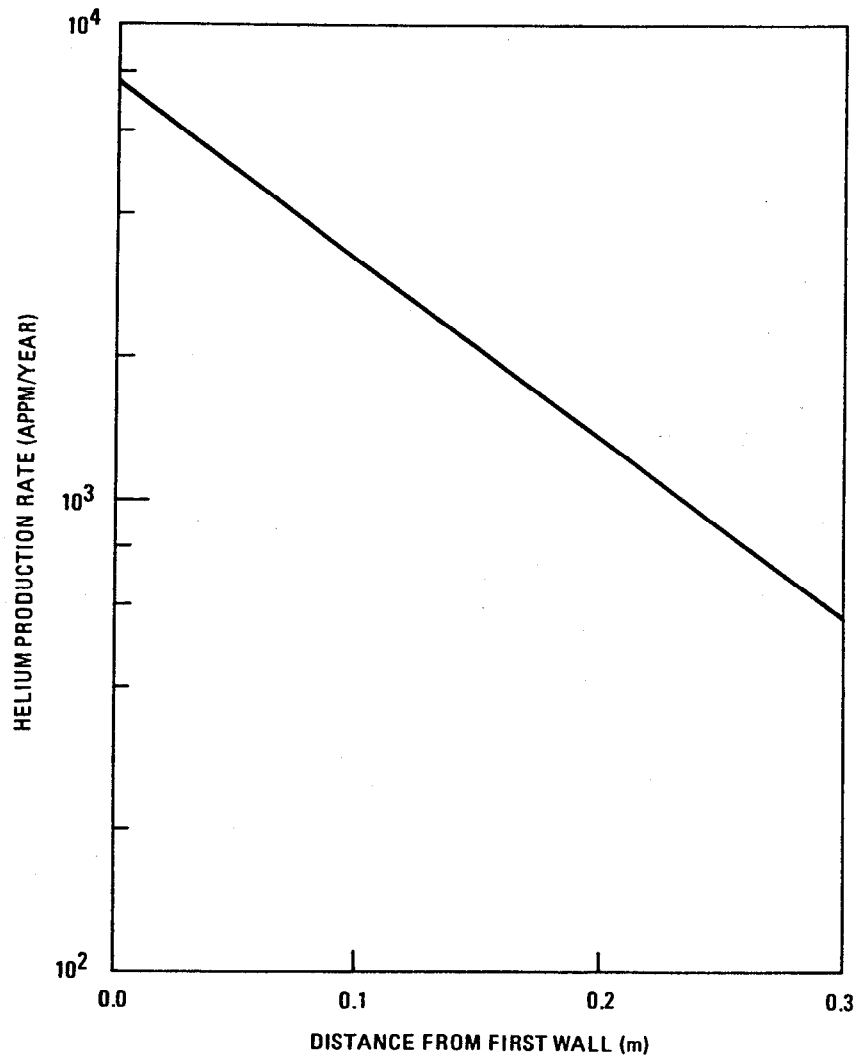
FIGURE V-11. Helium production rate in beryllium blocks as a function of distance from the first wall. The neutron wall loading is 2 MW/m².

U and U-Pu alloys have, upon swelling to ~33%, shown rapid release of fission product gases.[35] For irradiated beryllium which was subsequently annealed between 900°C to 1100°C, swelling was observed to reach ~30%.[29] However, in spite of the very high fluence of 1.3×10^{27} n/m^2 (E > 0.8 MeV) and helium formation (Table V-15) predicted after 10 years, an estimate of 30 vol. % swelling (at 700°C) does not seem warranted. This position is based on swelling observations by Andriyevski, et al., for beryllium irradiated in the range of 450° - 480°C.[31] For an integrated neutron flux of 1.3×10^{26} n/m^2, for E ≥ 0.8 MeV, swelling was ≤ 0.5 vol. %. And, the highest value of swelling observed in their test program was 6.2 vol. % for beryllium irradiated at 7×10^{25} n/m^2 at temperatures of 650° - 700°C. It is with this test data that the very conservative swelling prediction of 30% appears unjustified for irradiation of high fluence over the temperature range of 500° and 700°C in the TMHR. Instead, a conservative engineering estimate of swelling was made for the TMHR design and these values are also presented in Table V-12. Two other factors which might enhance swelling would be the formation of voids due to higher atom displacement damage from the high fluence and higher neutron energy. However, regarding the higher E ~ 14 MeV energy, for low atomic number materials, including beryllium, work by Myers[36] has predicted that use of irradiation data typical of a fission neutron spectrum (E ≤ 2 MeV) may in fact offer a reasonably close approximation for damage by the higher energy (E ~ 14 MeV) neutrons.

Microstructural Change During Irradiation. The microstructural changes anticipated in the beryllium blocks during irradiation in the temperature range of 500°C to 700°C are described in Fig. V-12. The summary model presented incorporates the test observations, analytical modeling, and diagnostic analyses reviewed which included observation of He bubbles and holes by electron transmission microscopy. Bubble growth and coalescence are the cause of swelling up to ~3%. Extensive swelling observed during annealing at ≥ 800°C was attributed to the formation of irregular shaped holes of ~5 μm in size at grain boundaries where adjacent grains have large differences in number and sizes of helium bubbles. With consideration for the anisotropic nature of beryllium crystals, the hole formation phenomenon has been attributed to the difference in stresses induced at these grain boundaries.[29] Of

Operating Conditions: (for 10 yrs
$650°-700°C - 1.3 \times 10^{22}$ n/cm^2,
$500°-550°C - 1.3 \times 10^{21}$ n/cm^2,

Swelling: $(\frac{\Delta V}{V} = 100\%)$ <1%   <3%   4-30%

Microstructure:
  Be grains and
  He bubbles

5 μm holes
at G.B.

1 μm bubbles
in grains

Mechanism
Model:

- 20Å-100Å dia. He
  bubbles nucleate
  at vacancies.

    He pressure = $\dfrac{2(\text{surface energy})}{\text{bubble radius}}$

- Interstitials and
  vacancies form from
  DPA.

- Bubbles grow to ~600Å
  (0.05μm) by assimilating
  vacancies and by
  coalescing.

- Bubbles at grain boundar-
  ies coarsen and migrate
  toward higher temperature
  zone.

- Swelling occurs as bubbles
  coarsen >100Å and number
  increases.

- Increase in numb
  of He bubbles a1
  boundaries.

- Irregular shapec
  in grain boundar
  to grains with 1
  differences in r
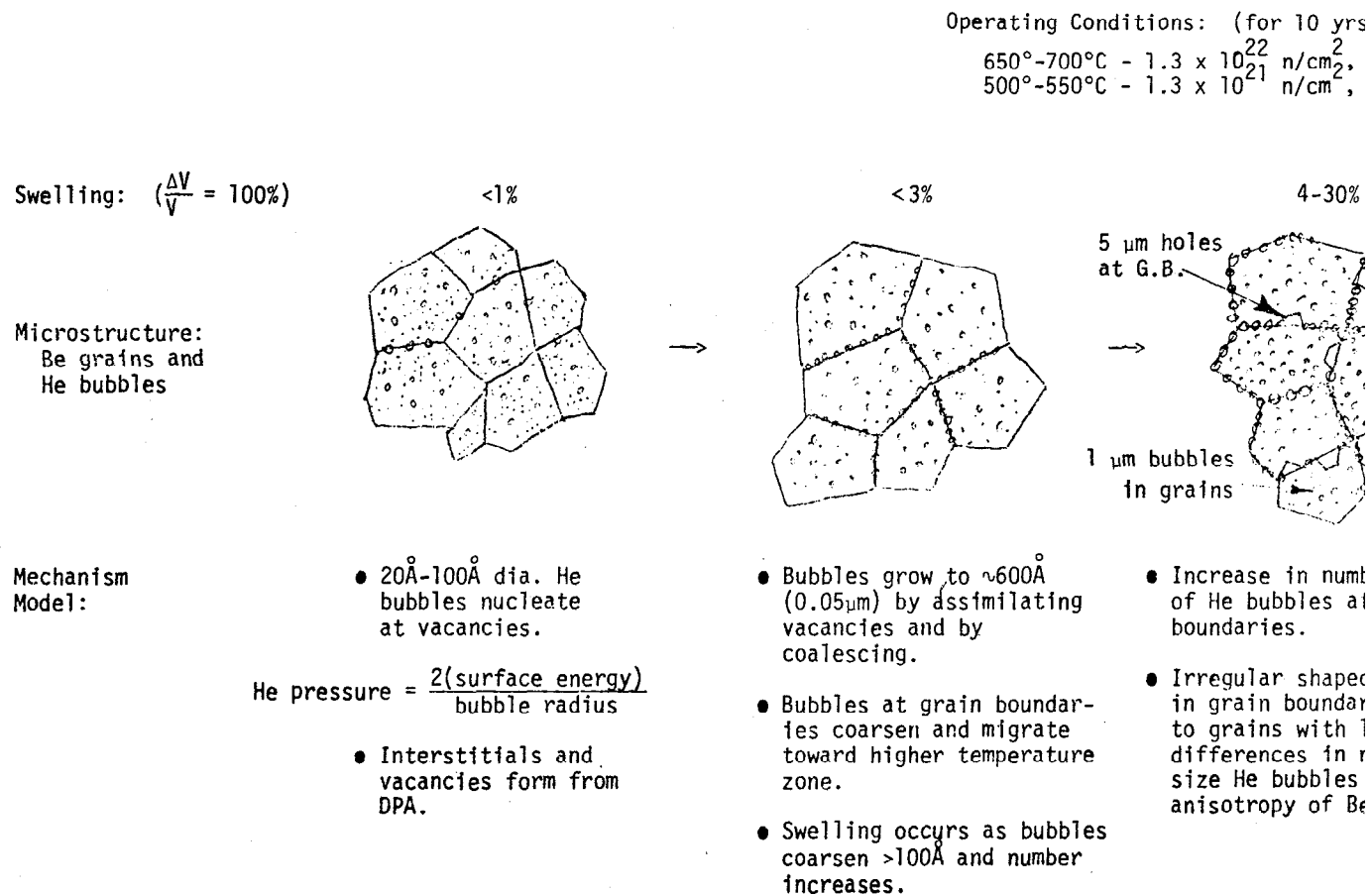 size He bubbles
  anisotropy of Be

FIGURE V-12. Microstructure changes anticipated in beryllium during irradiation in

important engineering significance is the ability of beryllium to swell without internal cracking or fragmenting when no external constraint is imposed on the material.

Release of Helium From Beryllium. The aforementioned swelling ceiling of ~30 vol. % in metals are thought to be the condition at which the He bubbles in the grain boundaries have grown and migrated and finally touched allowing a release path to form for the entrapped helium gas, tritium, and subsequently formed He.[29,30] Some of the tritium gas formed in the beryllium by the neutron reactions may escape with the He unless, of course, the tritium is dissolved in the zones of lithium (liquid) which is also formed by neutron reactions in the beryllium. A key factor for inducing migration of He bubbles is the presence of a temperature gradient. The beryllium blocks will have an increase in temperature in a direction toward the longitudinal centerline and also along the block length. The bubbles migrate toward the higher temperature region. Having a central hole in the beryllium block should permit a path of escape for He and T reaching this surface. This design feature has been used in solid fissile fuels to aid in the release of fission product gases.

Changes In Mechanical Properties. Irradiation of the beryllium will cause formation of point defects and formation of He which will cluster into fine helium bubbles initially, as discussed previously. These defects collectively will diminish the ability of beryllium to plastically deform the slip and twinning mechanisms. The resulting effects are the reduction in ductility and increases in tensile yield, ultimate strength and hardness.[29,32,33] Essentially, the embrittlement negates any practical consideration for localized yielding. Ductility is restored only upon annealing at high temperatures $\geq 950^{\circ}$C where extensive coarsening of the He bubbles can occur.[29] In the current design concept the beryllium blocks are not constrained and stress should be limited to that induced internally. Strains due to differential swelling, which occur gradually, may be however, alleviated by irradiation-induced creep in the temperature range of operation for the TMHR. In this situation the occurrence of creep is beneficial.

Materials/Design Concerns. Two principal concerns identifiable with swelling which might be a cause of failure result from the temperature and irradiation gradients and the resultant differential in swelling induced in the beryllium blocks. These concerns are presented in Table V-16, and, as noted, arise even though the blocks are not under applied stress. The first is associated with the generation of high localized strain if swelling varies greatly along the length of the block. Localized cracking and fracture of a block might result. The second concern is tied to the very high fluence of high energy neutrons, a condition heretofore untested. This concern is aggravated by a moderate temperature of irradiation which is below the temperature for annealing. If the swelling is high, the possibility of internal cracking and fragmenting is of concern.

These two concerns for the possibility of fracture are diminished, however, when consideration is given to observations presented earlier. First, the annealing of beryllium specimens after irradiation by Rich, et al., demonstrated that substantial swelling occurred only at temperatures $\geq 800^\circ$C.[29] And in the studies by Andriyevski, et al., a maximum swelling of 5% was reported after an 800°C annealing treatment of beryllium irradiated

TABLE V-16. Swelling of beryllium: materials/design concerns in TMHR.

Operating Condition: 500°-700°C and no applied stress on Be blocks

Concern	Reason for and Location of Concern
Localized cracking/ fracture of block	Differential swelling causing high localized strains; mid-way between ends.
Internal cracking/ fragmenting	High swelling during irradiation and low ductility at any location

Optimistic Viewpoint (diminishing the concerns):

● Irradiation-induced creep and temperature of operation may permit swelling and strain relief without cracking.
● Temperature and temperature gradients assist migration of He bubbles to and along grain boundaries to provide a release path for He and as a result less swelling.

at 480°C (1.3×10^{22} n/cm^2 for $E \geq 0.8$ MeV).[31] In the same investigation, beryllium irradiated at $650°$ $-$ 700°C (7×10^{21} n/cm^2 for $E \geq 0.8$ MeV), swelling was 6.2 vol. %. The above data suggests that swelling of the beryllium may not be excessive in the TMHR and $\leq$ 10 vol. % engineering estimate may still be conservative. Further, deformation by irradiation-induced creep at $500°$ $-$ 700°C may permit sufficient strain relief to accommodate the regions of swelling differential instead of causing localized cracking.

The presence of a temperature gradient through the beryllium blocks, both radially and longitudinally, will accommodate migration of He bubbles along the grain boundaries and reduce the degree of swelling compared to that which might be anticipated under isothermal conditions.

V.C.1.f The Compatibility of Beryllium With Other Blanket Materials. The blanket module will be comprised of a number of materials, but some of the materials will not make contact with each other by design. Specifically, the beryllium blocks will be situated to both allow for growth due to swelling and will also be spaced or supported (possibly on SiC) to avoid contact with the HT-9 or 316SS steel framework, first wall and heat exchanger tubes. This design feature is necessary to avoid rapid alloying between Be and Fe or Ni-base alloys which would be expected to occur upon contact at the operating temperatures of $500°$ $-$ 700°C.[18,37]

Compatibility is predicted between the beryllium and the liquid Pb-Li alloy (which is present for good thermal transfer between the beryllium and the heat exchanger tubes). The Pb-Li alloy temperature will be 550°C typically. The compatibility anticipated between Pb-Li and beryllium is based on test data showing good corrosion resistance. With Pb at 600°C good corrosion resistance was found but at 800°C, beryllium was reported as incompatible with Pb.[38] Unfortunately, a phase diagram for the Pb-Be binary system cannot be located in the literature. Beryllium was reported to be compatible with Li at 593°C[38] and at 816°C.[37]

Compatibility is anticipated for the thoria particles which are suspended in the Pb-Li eutectic (83 at % Pb) liquid. However, some concern exists for the compatibility of Be with ThO_2 and UO_2 based on the studies by Hanna[39] in which attempts were made to produce cermets consisting of

particles of UO_2 or ThO_2 dispersed in Be. The mixtures were compacted at
$600°C$ in vacuum. Subsequent exposure at $600°C$ and $800°C$ in argon resulted
in continual swelling with time. Reaction products were UBe_{13}, BeO and U
in the Be-UO_2 cermet and $ThBe_{13}$ and BeO in the Be-ThO_2 cermet. Swelling
was greater than predicted for a theoretical volume change and was attributed
to a pronounced Kirkendall effect in which Be diffused preferentially.

Concern was raised by Migge[40] for the use of beryllium in a fusion-
blanket design (at $727°C$) using Li as the coolant, beryllium spheres as the
neutron multipliers, and a framework (canning) of vanadium. He pointed out
the possibility of slow dissolution of Be and V by Li with the subsequent
formation of vanadium beryllides which would then deposit likely on the V.
His recommendation was to coat the Be with VBe_2 (40 µm thickness) to achieve
a higher probability of compatibility in the blanket system. A second con-
cern raised by Migge was the possibility of formation of the double oxide
$2BeO·Li_2O$, which undergoes a eutectic reaction with BeO at ~$727°C$. The BeO
phase is present as fine precipitates in the Be. Li_2O would be present as
an impurity of the Li. The consequence of the eutectic reaction at $727°C$
would be selective removal of block material which would then float or be
suspended in the Pb-Li medium. These phenomena should be avoidable in the
reference design of lower temperature.

To minimize the possibility of ThO_2 particles adhering to the Be blocks,
the particles might be coated with a thin layer of BeO. The BeO would be
stable and provide a barrier to alloying between the Be and ThO_2 and UO_2.
The technique for Chemical Vapor Deposition (CVD) coating UO_2 particles in
a fluidized bed was developed years ago at Battelle.[42,43] Another coating
protection concept might be to coat the ThO_2 particles with a buffer coating
of pyrocarbon and follow with a thin coating of TiC. This concept is
analogous to the encapsulation design used by General Atomic Company in
coating nuclear fuel particles, e.g., porous pyrocarbon buffer coating with
an outer coating of SiC. TiC is compatible with Li at $816°C$.[37] TiC would
likely be compatible with Be between $500° - 700°C$.

It is not anticipated that contact between the SiC reflectors and the
Be blocks will result in any interaction at the temperatures of operation
based on the lack of metallurgical reaction observed at $600°C$ in a CO_2
environment for 2000 hours reported by Vickers.[41]. Concern exists, however,

for the compatibility between Li and SiC and Al_2O_3 based on tests by Hoffman which showed rapid attack on these ceramics by Li at $816^\circ C$ after 100 hours of exposure.[37] However, Pb at the same temperature was compatible with each of the ceramics and with the reduction of activity for Li in the Pb-Li alloy, compatibility may be satisfactory at the TMHR operating temperatures.

The tritium formed will have very low solubility both in the Be and Pb-Li eutectic but will be highly soluble in the Li formed within the Be by nuclear transmutation. No reaction is anticipated between the Be and tritium.

V.C.1.g Recommendations. In review of the feasibility of using beryllium for the neutron multiplier the need for additional studies and tests were identified.

It is important to separate the effects which are specific to the block shape Be product of the subject design from designs of smaller size different shape and different operating conditions. For example small (1 cm diameter) spheres of beryllium would not experience a temperature gradient or neutron fluence gradient to the extent of the blocks. The spheres would, however, contact neighboring structure and would have to be coated to avoid diffusion bonding.

The following subsections describe investigation warranted for continuation of the reference design configuration. Any change of the design configuration or materials could require a modification in the type of tests and emphasis.

Swelling of Beryllium. A need exists for developing test data in the range of $400^\circ - 700^\circ C$ under irradiation exposure which enables a more rigorous prediction of swelling of beryllium for a helium production 75,000 appm (a fluence of 1.3×10^{27} n/m^2 of interest for the reference design) using fast neutrons and preferably of the high energies anticipated for the fusion environment. Further, the irradiation test exposures at a high fluence will also help determine if a threshold is reached where swelling is enhanced due to formation of voids. This phenomenon has not been observed in beryllium for the irradiation studies reviewed.

In addition, an experiment is warranted to establish the effectiveness of a temperature gradient in reducing the occurrence of swelling in the same temperature range and fluence. These investigations would establish whether cracking or fragmenting occur in the beryllium (with no externally applied stress). The effect of anisotropic properties characteristic of beryllium will need to be addressed in the investigation.

Fabrication of Beryllium Blocks. The extensive amount of beryllium necessary for the neutron multiplier component makes the issue of fabrication and cost a key consideration for the TMHR. Additional studies appear warranted to further identify methods and details for the production of beryllium blocks (Fig. V-8). To achieve a reasonable estimate on component cost and the impact on the U.S. beryllium industry an appreciable commitment would be necessary on their part. All phases of beryllium production would be involved because of necessary capital-intensive expansion.

Compatibility Testing. The Pb-Li alloy may offer appreciable improvement over Li (also investigated) for the thermal contact medium from the standpoints of materials compatibility and safety. This point requires verification. As with Li or Na liquid metal systems, the question of mass transport of C, O, N, and other elements in the Pb-Li liquid alloy system must be addressed. (In the reference design, the slow flow rate and relatively low temperature gradients favor low rate of mass transport.) A phase diagram for the Pb-Be binary should be developed. Also, the ability of thoria to remain suspended in the Pb-Li and not be reduced by the Be requires investigation. Use of a BeO coating on ThO_2 particles should be investigated as a means of preventing contact between beryllium and ThO_2. Other coating systems such as pyrocarbon buffer coating followed by an outer coating of TiC should also be investigated. The compatibility between the ceramics SiC and Al_2O_3 and Be at $700^\circ C$ in the presence of Pb-Li alloy also warrants investigation.

V.C.2 Other Material Issues

V.C.2.a Pirst Wall and Structural Materials. The first wall of the blanket
module, in general, suffers the most intensive radiation damage from both
neutron energy and fluence. Material swelling is one of the most important
effects of neutron irradiation. Changes of mechanical properties such as
strength, ductility are also important. Candidate structural first wall
materials and their mechanical properties in the radiation environment have
been discussed extensively.[1,44,45] Type-316 stainless steel, the primary
candidate alloy (PCA), Inconel 718 alloy and ferritic/martensitic steels
are among the most suitable alloys for fusion blanket first wall applica-
tions under consideration. For the reference gas-cooled beryllium blanket
[because of the use of liquid lithium lead ($Li_{17}Pb_{83}$) eutectic, which is
flooding the entire blanket module as the tritium breeding and heat con-
duction medium] the primary concerns relating to the choice of the blanket
first wall and structural materials are material compatibility and metal
swelling.

The ferritic/martensitic steel, HT-9, was chosen as the first wall and
structural material because: (1) it was found to be more corrosion resistive
at temperatures below $600^\circ C$ than austenitic steel and nickel-based Inconel
alloys;[46] (2) the material swelling due to neutron irradiation for the HT-9
ferritic steel was also found to be very low in the temperature range of
$500^\circ - 600^\circ C$;[47] and (3) the loss of ductility and creep rate are within a
practical range at the temperatures and fluence of interest. Figure V-13
shows the helium and hydrogen production rates and atomic displacement rate
in the HT-9 steel as a function of distance from the first wall. Together
with the neutron fluence distributions shown in Fig. V-10, they serve as
parameters for the determination of the blanket lifetime. Lifetime analyses
done for a helium cooled, pressurized blanket and a liquid $Li_{17}Pb_{83}$ eutectic
cooled fusion blanket showed that the blanket lifetime with the HT-9 steel
first wall is no less than 10 MW-yr/m^2 with the effect of in-reactor creep
as the dominating limiting feature.[46,47] Considering the reference gas-
cooled beryllium blanket, due to the idea of the low pressure blanket design,
the blanket lifetime can be further extended and is no less than 20 MW-yr/m^2,
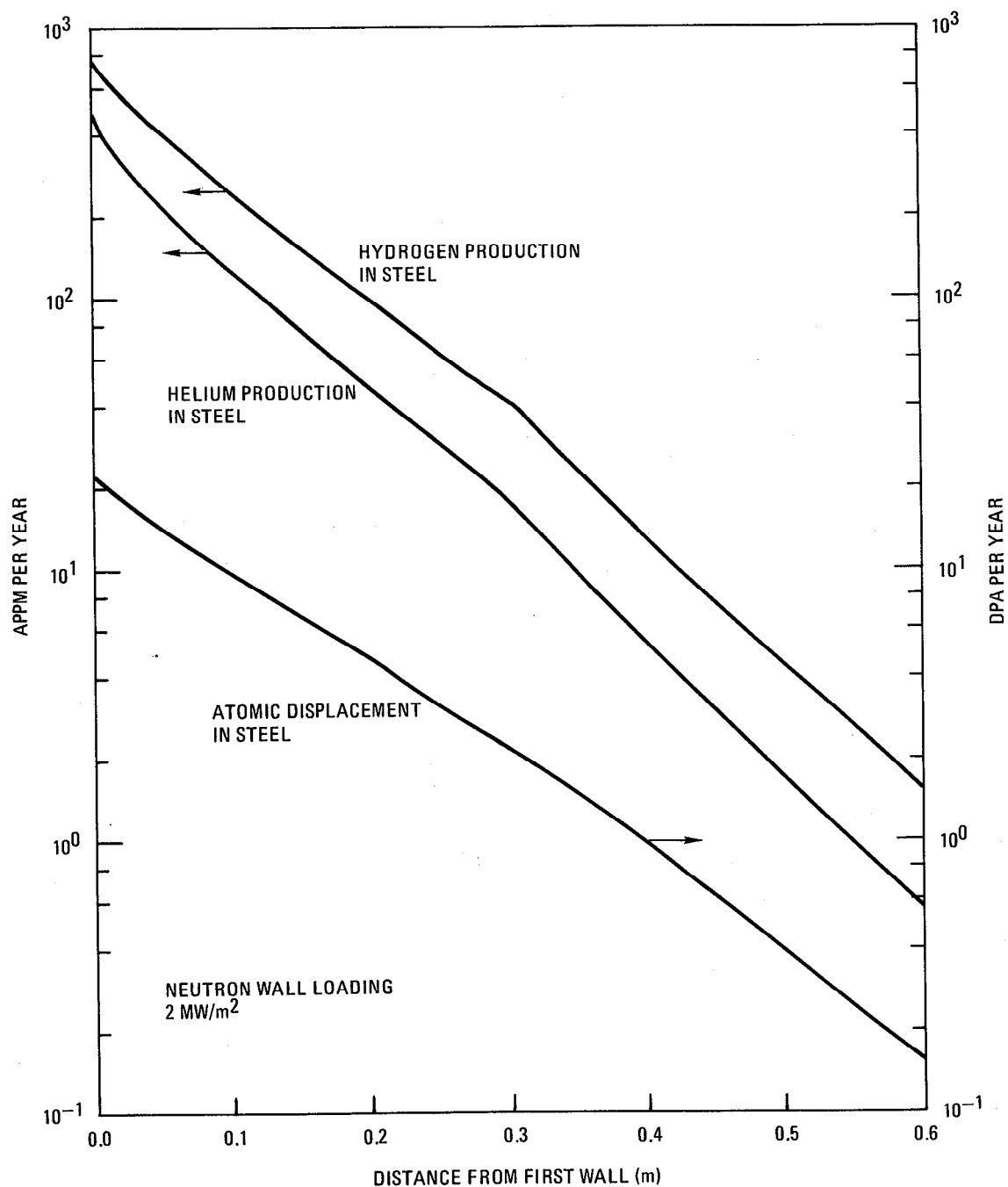or 10 years at a neutron wall loading of 2 MW/m^2.

FIGURE V-13. Gas production and atomic displacement rates as a function
of distance from the first wall for the structural metal in
the reference beryllium blanket. Note that the neutron wall
loading is 2 MW/m^2.

Static Magnetic Forces on Blanket Walls. Because the ferritic/martensitic
steel HT-9 is ferromagnetic with a saturation induction around 1.9 tesla, it is
to be expected that significant magnetic forces will appear on blanket walls.
The determination of the exact distribution of these forces is a matter of some
complexity and was not attempted in this study. Instead an estimate of the
total magnetic force and thereby an average surface force density on a flat
piece of blanket wall was computed by means of the magnetic Maxwell tensor:

$$\vec{T}_{ij} = \mu_o \left\{ \vec{H}_i \vec{H}_j - \frac{1}{2} \delta_{ij} H^2 \right\} \quad,$$

where the delta function δ_{ij} is equal to one if the Cartesian coordinates i and j
are the same; else $\delta_{ij} = 0$. H is the external magnetic field intensity and μ_o is
the permeability of vacuum. The stress tensor obtained from the above expression
is multiplied by unit normal vector $\vec{n}$ and integrated over a suitable envelope
surface around the magnetic body. The components of the surface force density
so obtained are

$$f_n = \frac{1}{2} \mu_o \left(H_n^2 - H_t^2 \right) \quad \text{normal to the surface, and}$$

$$f_t = \mu_o H_n H_t \quad \text{tangential to the surface.}$$

These (fictitious) force components conform with the notion that there is a
tension of magnitude $1/2 \ \mu_o H^2$ acting along the field lines and a pressure of
equal magnitude at right angles to them. If the envelope contains no sources
(currents or magnetized matter) the surface integral is zero. When sources are
included the external field, which in this case is created by a sparcely spaced
set of axisymmetric coils, is modified by the magnetized material. The net
forces F_n and F_t are a summation of the components f_n and f_t over a suitable
envelope defined by many field points.

The components of the total external field were computed for the outer walls
only because the field magnitudes and gradients are highest in the vicinity of
the coils. The well known 3-dimensional field code GFUN[6] was employed to com-
pute the total field and a post processor was developed to integrate the Maxwell
stresses over a close fitting closed rectangle surrounding the center cross
section of the wall under study.